Electronic and Vibrational Spectroscopies Applied to Organic/Inorganic Interfaces

Dietrich R. T. Zahn,* Gianina N. Gavrila, and Georgeta Salvan

Institut für Physik, Technische Universität Chemnitz, 09107 Chemnitz, Germany

Received June 30, 2006

Contents

10.1021/cr050141p CCC: $65.00
Published on Web 04/11/2007

Dietrich R. T. Zahn received a diploma in Physics from the RWTH Aachen in 1986 and a Ph.D. in Physics from the University of Wales Cardiff in 1988. After a post-doc period at the Technical University in Berlin, he became Professor of Semiconductor Physics at the Chemnitz University of Technology in 1993. His research focuses on the spectroscopic characterization of semiconductor interfaces and thin films, with particular emphasis on organic/inorganic hybrid systems, low dimensional systems, e.g., quantum dot superlattices, as well as advanced interconnects in micro-/nanoelectronics. He is author or coauthor of more than 400 related publications. Since 2006 he has been chairman of the Thin Film Division of the German Physical Society and Vice President for Research at the Chemnitz University of Technology.

Gianina N. Gavrila was born in 1976 in Romania. She studied technological physics at the Babes-Bolyai University in Cluj-Napoca, Romania. In 2000 she received her B.Sc. A year later she obtained an M.Sc. degree at the same university and in collaboration with the Semiconductors Physics Department at the Chemnitz University of Technology, Germany. In 2005, in the same group from Chemnitz, she received her Ph.D. with a thesis focusing on the electronic properties and chemistry of organic heterostructures. Since 2004, she has been a postdoctoral researcher in the group of Prof. D. R. T. Zahn, with activities mainly at BESSY, in Berlin. Her current research focuses on the characterization of semiconductor interfaces and thin films, with particular emphasis on organic/inorganic hybrid systems, using synchrotron radiation.

Georgeta Salvan was born in 1975 in Romania. She received a M.Sc. degree at the Babes-Bolyai University in Cluj-Napoca in 1999 and a Ph.D. at the Chemnitz University of Technology in 2003. She then spent 6 months as a postdoctoral research assistant at the University of Wales Aberystwyth. In December 2003 she became Juniorprofessor for Organic Semiconductors at the Chemnitz University of Technology. Her current research activities include magneto-optical investigations on organic films as well as on organic/inorganic hybrid structures.

1. Introduction

In recent years enormous progress was made in the investigation of organic semiconductors both experimentally and theoretically. The research interest in these materials is driven by the manifold applications such as organic light emitting devices (OLEDs), organic field effect transistors (OFETs), and organic photovoltaic cells (OPVCs). Some experimental techniques such as photoemission spectroscopy, which has been one of the major surface science techniques in the field of inorganic semiconductor research for decades, have also been successfully applied to study organic semiconductors and their interfaces for quite some time. Other experimental techniques such as Raman spectroscopy are less widely used for studying organic semiconductor interfaces. However, this optical spectroscopy technique, which probes the vibrational modes and may thus also be called vibrational spectroscopy, also can provide very valuable information about interface properties such as geometric structure, band bending, and interfacial chemistry. It is the intention of this review to illustrate that the combination of techniques, namely vibrational and electron spectroscopies, is extremely powerful in the field of organic interface characterization and that it provides complementary information and an improved insight in organic interface formation.

There are two groups of organic semiconductors based on either polymers or so-called "small" molecules. This review deals exclusively with the latter class, and within this, two examples from the class of perylene derivatives were chosen, 3,4,9,10-perylenetetracarboxylic dianhydride (PTCDA) and *N*,*N*′-dimethyl 3,4,9,10-perylenetetracarboxylic diimide (DiMe-PTCDI). The molecular structures of these two molecules are quite similar. Still the "minor" change of the functional groups of these molecules has dramatic effects on both molecular orientation on inorganic substrates and interfacial chemistry when an interface with the organic semiconductor is formed by depositing a metal on top of the organic semiconductor. These dramatic effects motivate the choice of these two molecules. They are excellently suited to demonstrate how minor changes of molecular structures can be utilized to influence interfacial and layer properties. At the same time, they allow the sensitivity of the major experimental techniques used in this review, Raman and photoemission/NEXAFS spectroscopies, to be benchmarked.

In fact, PTCDA is an archetype organic molecule and has already been studied on a variety of inorganic substrates by a large number of experimental and theoretical methods[1−4] with scanning probe techniques being the ones most widely used. The most commonly used substrate materials have been metals, highly oriented pyrolytic graphite, and insulators (NaCl, SiO_2, Al_2O_3)[1] while investigations using the more reactive surfaces of common inorganic semiconductors such as silicon and gallium arsenide (GaAs) have been scarce. In this review, GaAs is the substrate of choice due to the

emphasis in our work on inorganic/organic semiconductor heterostructures.

On clean GaAs(100)[5,6] or Si(100)[7] surfaces a strong chemical interaction occurs between the anhydride groups of the molecules at the interface and the substrate, predominantly with the dangling bonds and defects. This usually results in the formation of small crystalline domains, in nearly random azimuthal orientation. Improved structural order is observed when the semiconductor substrate surface is passivated, e.g., by reaction with chalcogen or hydrogen atoms in the case of GaAs or Si substrates, respectively. The passivation induces a reduction of chemically active sites by saturating dangling bonds.[8,9]

Substrate temperature is a further important parameter that influences the structural order in the organic film. The crystallite size drastically increases with the temperature in the case of PTCDA deposited on Si(100) covered with natural oxide[10] as well as in the case of hydrogen-passivated Si(100) substrates[11,12] and sulfur-passivated GaAs(100) substrates[13] when varying the temperature from room temperature to 140 °C. The same trend was observed for DiMe-PTCDI films on S-GaAs(100) substrates.[14] The organic layers decribed in this review were all prepared at room temperature, leading to polycrystalline but mostly homogeneous layers with the lowest degree of roughness observed on these inorganic semiconductor substrates. These characteristics correspond to the requirements for organic layers in organic-based electronic devices. Besides the conventional methods for the study of the crystalline nature of the films, such as X-ray diffraction,[10] Raman spectroscopy was proven to provide valuable information as well.[11,13,14]

Numerous studies are dedicated to the deposition of organic molecules onto single-crystal metallic substrates, since these are excellently suited for studying growth mechanisms.[15−19] For example, Marchetto et al.[18] investigated by UV-excited photoelectron emission microscopy (UV-PEEM) the microscopic growth behavior of PTCDA on a Ag(111) single crystal from the submonolayer range up to 5 layers or more. A detailed investigation of the interface bonding of PTCDA on Ag(111) and Ag(110) surfaces by a combination of structural and electronic techniques (SPA-LEED, STM, TPD, UPS, HR-XPS, and NEXAFS) was made by Zou et al.,[19] thus obtaining a consistent picture of the adsorption behavior of PTCDA on silver in the monolayer regime.

The deposition of metals onto organic layers, which is a step often required in the fabrication of vertically stacked organic-based devices, is less investigated. Only a few studies, mainly performed by means of electron spectroscopies, are reported, and they are in some cases controversial. Photoemission spectroscopy (PES) studies revealed that silver deposition onto PTCDA leads to the formation of an abrupt, nonreactive interface.[20] Regarding the interface formation of indium with the perylene derivatives, there still is a controversy: PES studies indicate a strong reaction between In and PTCDA via the C═O bonds,[21] whereas more recent near-edge X-ray absorption fine structure revealed the presence of a fractional charge transfer between the PTCDA or DiMe-PTCDI molecules and indium.[22] Nakamura et al.[23] evidenced a strong interaction when In is deposited onto very thin films of PTCDA (i.e., 0.2 nm Å). On the other hand, our recent PES results (not included in this review) show that the strength of interaction depends on the film morphology, i.e., the size of the organic island and/or surface smoothness.

Most of the work devoted to the vibrational properties of metal/PTCDA interfaces refers to molecular thin films deposited on either low-index single-crystal or rough metal substrates. Representative for the case of single-crystal metal substrates are the studies of PTCDA on Ag(111) and Ag(110) by means of high-resolution electron energy loss spectroscopy (HREELS) and electron energy loss spectroscopy (EELS).[24−27] These studies revealed a breakdown of selection rules of the internal vibrational modes attributed to the presence of a charge transfer between the molecules and the metal substrate. The only Raman spectroscopy studies of PTCDA on Ag(111) report frequency shifts much lower than those observed in the HREELS experiments but provide no explanation for this discrepancy.[28,29] The rough substrates were found to induce surface-enhanced Raman scattering (SERS) for PTCDA[30,31] as well as for other perylene derivatives.[32] We have recently shown that the spectral changes occurring during the metal deposition onto the organic films are related to different SERS mechanisms and therefore can be exploited to extract information not only about the chemical but also about the structural properties of the interface.[33]

This review is organized as follows. Section 2 introduces the molecules and their properties with particular emphasis on the molecular crystals. In section 3 the sample preparation and the experiments with the related data analysis are described together with a brief introduction to density functional theory calculations which are very helpful for interpreting the experimental results. Section 4 deals with the initial adsorption of the molecules on GaAs surfaces. Both Raman and photoemission spectroscopies reveal that there is a submonolayer amount of molecules preferentially adsorbing on defect sites and leading to a reduction of inhomogeneities in substrate band bending. The energy level alignment between the GaAs substrates and the organic semiconductors is determined, and a method is proposed for how the transport gap can be derived by measuring the interface dipole as a function of varying substrate electron affinity. Section 5 deals with the properties of thin organic films, beginning with the molecular orientation in such films. For this purpose, NEXAFS as well as Raman measurements are employed. In addition, another type of vibrational spectroscopy, namely infrared spectroscopy, is introduced as a tool for the determination of molecular orientation. Moreover, it is shown that a dispersion of the occupied electronic valence states can be measured for well-ordered organic films. Finally, the transport gap is evaluated from the combination of direct and inverse photoemission spectroscopy. In section 6 the metal deposition on organic layers is discussed. Raman spectroscopy becomes very sensitive to the metal/organic interface due to surface-enhanced Raman scattering effects, allowing information about interfacial reactivity and indiffusion of the metals to be derived. A thorough understanding is obtained by taking core level photoemission spectra into account. Both methods reveal that the change of the functional groups drastically influences the interfacial reactivity. Finally, the metal morphology on organic films as substrates is discussed. Concluding remarks describing the potential of the two methods and their complementarity and a pictographic summary comprising the electronic, structural, and chemical properties of the systems investigated in this review are given in section 7.

2. Properties of Organic Semiconductors: Perylene Derivatives

2.1. Electronic Structure of Organic Semiconductors

Organic semiconductors are made of polyatomic molecules that consist largely of carbon, oxygen, nitrogen, and hydrogen atoms. The bonds between the atoms in the molecule are covalent with binding energies in the range of 1 eV, similar to the case of inorganic crystals. For comparison, the binding energy per valence electron in silicon is 1.16 eV.[34] The interactions between the atomic orbitals (AOs) of the bonding atoms within the molecule lead to the formation of delocalized π bonds and/or localized σ bonds. Single bonds exhibit σ symmetry while double bonds exhibit both symmetries, σ and π. The C−C interaction in large conjugated molecules, for example, yields localized σ bonds and/or highly delocalized electrons in π bonds composed of $2p_z$ states. In most cases, the energetically highest π state gives rise to the highest occupied molecular orbital (HOMO) while the lowest π^* state is known as the lowest unoccupied molecular orbital (LUMO).

2.1.1. Organic Molecular Solids: Energy Levels

In the solid state the molecular orbitals (MOs) are superimposing, producing the so-called HOMO and LUMO "bands" that are comparable to the valence and conduction bands, respectively, encountered in inorganic semiconductors. However, in organic semiconductors, the term "band" must be regarded with care. The overlap between the wave functions centered on neighboring molecules in an organic solid is small, leading to bandwidths of the HOMO and LUMO typically up to 200 meV (see section 5.3—Transport Gap of PTCDA and DiMe-PTCDI). This quantity is small compared to the bandwidth of the valence and conduction bands in inorganic semiconductors, which is on the order of several electronvolts. The energy dispersion and relevant energy levels are shown in Figure 1.

Figure 1a shows the highest occupied and lowest unoccupied energetic levels, which define the band gap of a semiconductor. The band dispersions of an organic semiconductor are represented by the solid lines while the valence band and conduction band dispersions are represented by the dotted lines. Even though the two semiconductors have the same band gap, the different bandwidths lead to strong differences, e.g., in electronic transport. The large bandwidths in inorganic semiconductors indicate that electrons and holes are delocalized. Due to delocalization, the addition or removal of a charged particle will induce electronic polarization effects in the range of a few millielectronvolts. For organic semiconductors, due to the very narrow bandwidths, the electrons and holes are considerably more localized and the bandlike transport exhibited by the inorganic semiconductors is no longer present. The conduction occurs via tunneling and hopping mechanisms between localized states. Consequently, the addition or removal of a charged particle will induce much more pronounced electronic polarization effects. These effects play an important role in the electronic properties (energy levels) of organic solids and are thoroughly discussed in the following.

The band gap of a semiconductor determines most of the (opto-)electronic properties of the solid. Two types of band gaps need to be considered in semiconductors: the transport

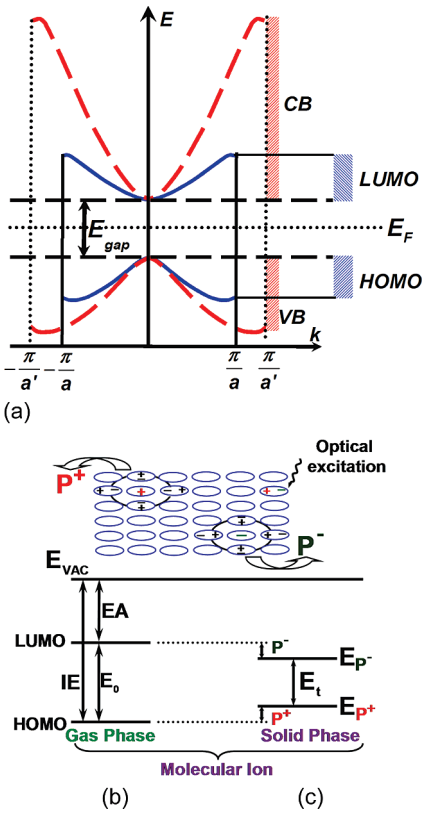

Figure 1. Schematic plot showing (a) the energy dispersion of an arbitrarily chosen inorganic (dashed lines) and an organic semiconductor (solid line) with the same band gap, (b) the highest occupied molecular orbital (HOMO) and the lowest unoccupied molecular orbital (LUMO) of a gas-phase molecule with an energy gap E_0, and (c) the energy levels of a charged molecule in a crystal including the polarization energies P^- and P^+. (After I. Hill et al.[35])

gap, E_t, and the optical gap, E_{opt}, and it is important to make a clear distinction between them. The transport gap, E_t, is the energy necessary to create spatially well-separated electrons and holes. In organic semiconductors, this is similar to a complete removal of an electron from the HOMO of one molecule and addition of it directly into the LUMO of another molecule. The optical gap, E_{opt}, corresponds to the formation of a correlated electron−hole pair, known as an exciton. For inorganic semiconductors, this exciton is known as the Wannier exciton, and due to the small polarization and good carrier screening efficiency, its binding energy is only a few millielectronvolts. Therefore, the charge separation energy, $E_t - E_{opt}$, or in other words the exciton binding energy, E_{ex}, is usually negligible for inorganic semiconductors. The band gap can thus often be obtained from the onset of the optical absorption spectra, and E_t equals, to a good approximation, the optical gap E_{opt}. In the case of an organic solid, E_{opt} corresponds to the formation of a Frenkel exciton with the electron−hole pair on the same molecule or a change transfer (CT) exciton with the electron and the hole on two adjacent molecules. Considering the excitons in organic materials, measurements employing electron energy loss provided an interesting correlation between the length of the molecule and the size of the exciton.[36] It was reported that in conjugated polymers the exciton binding energy is small (~200 meV) while in small molecules such as C_{60} the exciton binding energy is larger than 1.5 eV. However, the issue of the exciton binding energy continues to be a controversial one. Detailed experimental information on the exciton properties, in particular their dispersion, is not

available to date despite the tremendous importance of such data as a basis for a complete understanding of the various phenomena in organic molecular solids.

As a consequence of the large exciton binding energy, E_t cannot be derived from optical absorption measurements for organic semiconductors. The molecular polarization and charge localization complicates the situation. When a charge carrier is brought into the molecular solid, its field polarizes the surrounding molecules. A secondary polarization field created by polarized molecules contributes to the total self-consistent polarization clouds that surround each charged particle. The formation of these polarization clouds, illustrated at the top right of Figure 1, is associated with the stabilization energy P^+ for cations and P^- for anions. Their influence on the transport gap is illustrated in Figure 1b and c and is discussed in the following. The HOMO and LUMO of a gas-phase molecule are separated by the energy gap E_0. E_0 is equal to the difference between the ionization energy (IE) and the electron affinity (EA) of a molecule in the gas phase. The energy gap of a system in the solid phase will differ from that in the gas phase. In the solid phase, the HOMO corresponds to the position of the lowest energy hole state created by the promotion of a hole from the electrodes or by the photoemission of an electron. Because of the polarization energy P^+ induced in the surrounding medium by the (photo)induced hole, the HOMO level shifts toward the vacuum level (E_{VAC}) to its new position E_{P^+}, as depicted in Figure 1c. Similarly, the LUMO corresponds to the position of the lower energy electron state created by electron injection from the electrodes or by a time-reversed photoemission process. The induced polarization energy P^- will shift the LUMO level toward higher energies (E_{P^-}), as shown in Figure 1c. Consequently, the transport gap E_t of an organic solid and the relation between E_t and the polarization energy $P = P^+ + P^-$ is given by the following equation:

$$E_t = E_0 - (P^+ - P^-) \quad (1)$$

Since Coulomb interactions are long-ranged, polarization clouds can extend over many lattice constants and the polarization energy is significantly different in the bulk, in thin organic layers, at a free surface, and near a metal/organic interface. Because of the existence of a smaller number of nearest neighbor molecules, the induced polarization is smaller at the surface than in the bulk. Furthermore, near a metal interface, due to the high polarizability of the metal, the induced polarization increases compared to the bulk value, leading to a decrease of the transport gap.[37,38]

Knowledge of the transport gap is essential for constructing reliable energy diagrams for carrier injection and transport. Since the transport gap of an organic solid corresponds to the difference in the energies related to the removal of an electron from the HOMO and the addition of an electron into the LUMO, the combination of valence band photoemission spectroscopy (VB-PES) and inverse photoemission spectroscopy (IPES) represents one of the methods that can be used to determine the transport gap in molecular films.[39,40] Comparison of the energy difference between the hole-induced state and the electron-induced state with the energy of formation of an electron−hole pair (E_{opt}) leads to an approximation of the exciton binding energy ($E_{ex} = E_t - E_{opt}$). However, the evaluation of the exciton binding energy is beyond the main interest of this review.

The energy levels relevant in constructing energy diagrams are defined in the following way. The vacuum level, E_{VAC}, shown in Figure 1b, is defined as the energetic level at which electrons can escape from the solid into the vacuum. The ionization energy, IE, is the energy necessary to bring the electrons from the uppermost occupied states, i.e., HOMO or valence band maximum (VBM), to just outside the surface with zero kinetic energy:

$$IE = E_{VAC} - E_{HOMO(VBM)} \quad (2)$$

while the electron affinity, EA, is defined as the energy difference between the lowest unoccupied states, i.e., LUMO or conduction band minimum (CBM), and E_{VAC}:

$$EA = E_{VAC} - E_{LUMO(CBM)} \quad (3)$$

The work function, ϕ, not shown in Figure 1, is defined as the energy difference between the Fermi level, E_F, and E_{VAC}:

$$\phi = E_{VAC} - E_F \quad (4)$$

2.2. Characterization of Molecular and Crystalline Structure

2.2.1. Molecular Structure

The two molecules which are the object of this work belong to the class of heteroaromatic systems, more specifically to the group of perylene derivatives (Figure 2): 3,4,9,10-perylenetetracarboxylic dianhydride (PTCDA) and *N*,*N*′-dimethyl 3,4,9,10-perylenetetracarboxylic diimide (DiMe-PTCDI).

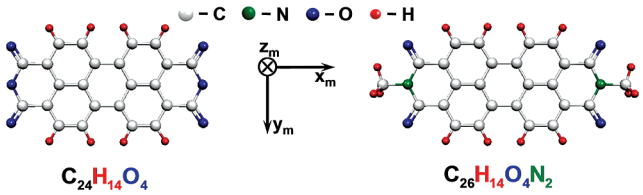

Figure 2. Chemical structures of PTCDA and DiMe-PTCDI. The molecular coordinate system is defined such that the x_m and y_m axes are parallel with the long and short axes of the molecules, respectively, and the z_m axis is perpendicular to the molecular planes. The molecular mass is 392 atomic mass units (amu) and 418 amu for PTCDA and DiMe-PTCDI, respectively.

PTCDA is one of the most intensively studied organic molecular semiconductors, e.g., for investigations of structural ordering during growth. This is because PTCDA is thermally stable, and very pure, well-ordered thin films can be fabricated by organic molecular beam deposition (OMBD) on various inorganic substrates. The structural formula of PTCDA is shown in Figure 2. PTCDA has a planar rectangular geometry consisting of a perylene core (22 carbon atoms, 8 hydrogen atoms) terminated by two electron-withdrawing anhydride (O═C−O−C═O) groups. Three C_2 axes of symmetry can transform the molecule into itself upon rotation by 180°, three planes show reflection symmetry ($\sigma(xy)$, $\sigma(xz)$, $\sigma(yz)$) and an inversion center *I* is present. The symmetry of all molecular orbitals can be described by the irreducible representations of the D_{2h} point group. All the symmetry classes that are even/odd with respect to the inversion center will be labeled with the indices *g* (*gerade*)/*u* (*ungerade*). Following Suzuki,[41] the orbitals are usually denoted by lower-case letters, and states by capital letters. As an example, the symmetry of the HOMO is $a_u(xyz)$, that of the LUMO is $b_{1g}(yz)$, and the corresponding states are A_u and B_{1g}. These states are singlet, and the usual notation found in the literature for the corresponding vibronic (electronic

Table 1. Unit Cell Parameters for PTCDA and DiMe-PTCDI

parameter	α-PTCDA[a]	β-PTCDA[a]	DiMe-PTCDI[b]
space group	$P2_1/c(C_{2h}^5)$	$P2_1/c(C_{2h}^5)$	$P2_1/c(C_{2h}^5)$
a (Å)	3.74	3.78	3.87
b (Å)	11.96	19.30	15.58
c (Å)	17.34	10.77	14.60
β (deg)	98.8	83.6	97.65
Z	2	2	2
d(102) (Å)	3.21	3.25	3.21

[a] From ref 1. [b] From ref 43.

plus vibrational) states is S_0 for the HOMO, S_1 for the LUMO, and S_2 for the next excited state accessible via a dipole-allowed transition. E_{0-0} designates the transition between the ground vibrational states of the electron ground state and the first excited state.

DiMe-PTCDI is very similar to PTCDA, and it consists of 26 carbon atoms, 14 hydrogen atoms, 4 oxygen atoms, and 2 nitrogen atoms. The replacement of the bridging oxygen atom of the anhydride group with the 3-dimensional methylimide group leads to a deviation from the planar geometry. The molecular structure is also shown in Figure 2. Two relative arrangements of the methyl groups are possible: in one of them, the hydrogen atoms face each other (C_{2v} molecular symmetry); in the other, they are rotated by 180° such that the molecule has an inversion center (C_{2h} symmetry). The electronic levels and vibrational frequencies are not influenced by the difference in the geometry; therefore, the C_{2h} group will only be considered further on for the ease of comparison with PTCDA.

2.2.2. Crystalline Structure

The fact that perylene derivatives often grow in a well-ordered mode, and sometimes even in a quasi-epitaxial mode when thermally evaporated under vacuum conditions, was experimentally verified on a variety of substrates ranging from metals to ionic insulators. An exhaustive review was made by Forrest in 1997.[1] In most cases, the monoclinic crystallographic system ($P2_1/c(C_{2h}^5)$) is preferred. For PTCDA two polymorphs are reported,[1] whereas for DiMe-PTCDI only one crystal structure is known so far. PTCDA molecules were found to lie almost flat on the substrates.[1] The crystal parameters are summarized in Table 1, and a graphic representation of the crystalline arrangement is depicted in Figure 3.

Both molecular crystals have two molecules per unit cell arranged in a herringbone packing in the (102) lattice planes. The inclination of the molecular plane with respect to the (102) plane amounts to ∼ 5° for PTCDA[42] and ∼ 8° for DiMe-PTCDI (calculated from the crystal data in ref 43). The distance between adjacent planes is ∼3.2 Å, which is small compared to the other lattice constants. This causes fairly strong interactions of the π-electron systems within the stacks perpendicular to the (102) plane.

Both the HOMOs and the LUMOs of perylene derivatives are mainly governed by the extended conjugated π-electron system composed of atomic $2p_z$ wave functions[44,45] of the perylene core. The charge contour of these orbitals can be found in section 2.4—Electronic Properties: Valence Band Structures. There it can be seen that the hydrogen atoms and the outer constituents hardly affect these orbitals. Transitions between the HOMO and the LUMO are dipole allowed and are well separated from the higher energy transitions, due to the large energy difference between the HOMO and lower lying occupied orbitals and between the LUMO and higher lying unoccupied orbitals. The symmetry and orientation of the transition dipole can be calculated from the direct product of the irreducible representations of the two states, following an algorithm described in ref 46. For example, $A_u \otimes B_{1g} = B_{1u}(x)$ for PTCDA and $A_u \otimes B_g = B_u(x)$ for DiMe-PTCDI. It follows that the dipole of the HOMO−LUMO transition lies along the x_m molecular axis in both molecules.

The experimental ultraviolet−visible (UV−VIS) absorption spectra of isolated molecules (monomer) obtained from diluted solutions of PTCDA in dimethyl sulfoxide (DMSO) and of DiMe-PTCDI in chloroform are very similar in terms of line shape.[47] In both cases, the vibronic progression of the S_0-S_1 transition with the E_{0-0} peak at 2.38 eV (PTCDA) and 2.36 eV (DiMe-PTCDI) dominates the spectra. It must be noted, however, that the E_{0-0} values are affected by the dielectric constant of the solvent. The E_{0-0} values for PTCDA monomers in an inert environment were determined by means of laser-induced fluorescence of PTCDA in He droplets to be 2.6 eV.[48] A comprehensive analysis of the PTCDA monomer absorption was carried out by Scholz et al.,[49] taking into account the participation of totally symmetric vibrations in the vibronic progression.

In thin films grown on quartz substrates, the E_{0-0} (S_0-S_1) transitions are red-shifted compared to those for monomers in solution and the first absorption peaks appear at 2.22

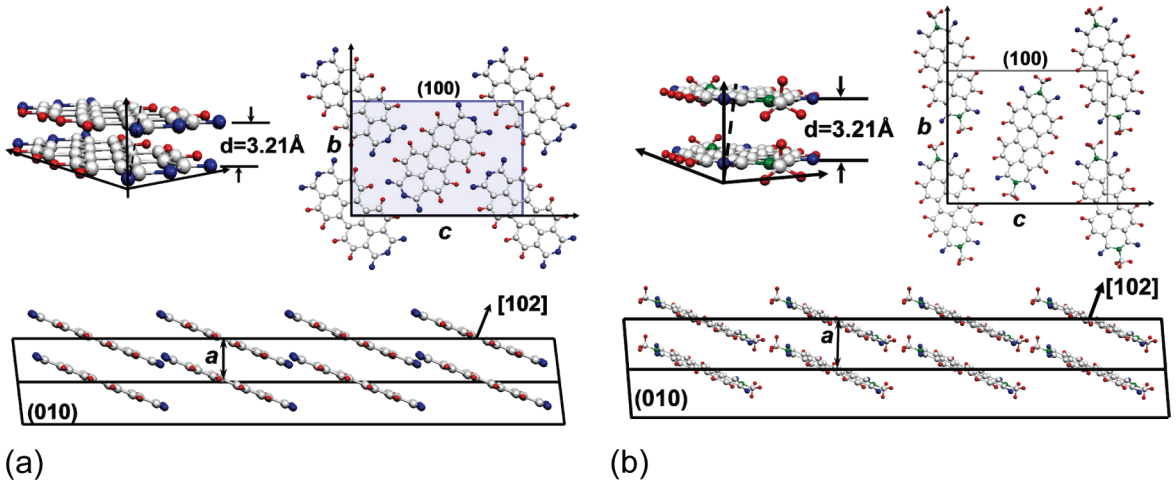

Figure 3. Three views of α-PTCDA (a) and DiMe-PTCDI (b) crystalline structures.

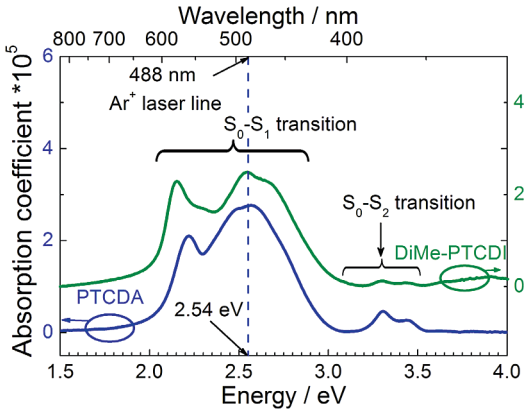

Figure 4. Absorption spectra of PTCDA (bottom) and DiMe-PTCDI (top) films (50 nm each) deposited on quartz substrates at room temperature. The energy position of the excitation line used in Raman experiments is indicated by the dashed vertical line.

eV (PTCDA) and 2.16 eV (DiMe-PTCDI) (see Figure 4). Moreover, the broadening is large so that the individual vibronic peaks are not resolved. The same holds for the S_0-S_2 transition, the dipole of which is oriented along the short molecular axis y_m. The change in the absorption line shape of films (crystal) compared to monomers in solution is known as crystallochromy and was observed for a large number of perylene derivatives.[47] For PTCDA, it was shown that this change can be related to the transfer of Frenkel excitons between neighboring molecules,[49] considering a regular arrangement of the molecules in the crystalline domains having finite size.

2.3. Vibrational Properties

A molecule consisting of N atoms exhibits $3N$ degrees of freedom, which means that $3N$ coordinates are necessary to specify the positions of all N atoms. Of these, three coordinates are employed to describe the translational movement of the molecule. Furthermore, for a nonlinear molecule, three additional coordinates (for example, Euler's angles) are necessary to specify the orientation of the molecule in space. Thus, $3N$(total) − 3(translational) − 3(orientational) = $3N - 6$ degrees of freedom remain available to describe the vibrations of atoms in the molecule. One can define a set of $3N - 6$ normal internal vibrations that sum up with different weights to describe a certain molecular vibration. Their corresponding spatial patterns are called normal coordinates. Even without considering the molecular dynamics, it is possible to classify the normal vibrations by applying the group theory.[46] Each normal vibration will have a symmetry corresponding to one of the irreducible representations of the molecular point group. If the molecule has a center of inversion, the vibrations that are symmetric with respect to it (labeled with the subscript *g*) are usually Raman active and those that are antisymmetric (labeled with the subscript *u*) show infrared activity. This is the case for PTCDA (D_{2h} point group) and for DiMe-PTCDI (C_{2h} point group) molecules. The irreducible representation, Γ, of their internal modes is presented below:

$$\Gamma_{PTCDA} = 19A_g + 18B_{1g} + 10B_{2g} + 7B_{3g} + 10B_{1u} + 18B_{2u} + 18B_{3u} + 8A_u \text{ (108 internal vibrations)} \quad (5)$$

$$\Gamma_{DiMe-PTCDI} = 44A_g + 22B_g + 23A_u + 43B_u \text{ (132 internal vibrations)} \quad (6)$$

Table 2. Raman Tensors for the Symmetry Classes of the D_{2h} and C_{2h} Point Groups in the Molecular-Axes Coordinate System

group	symmetry class			
D_{2h}	$A_g(xyz)$	$B_{3g}(xy)$	$B_{2g}(xz)$	$B_{1g}(yz)$
PTCDA	$\begin{pmatrix} a & 0 & 0 \\ 0 & b & 0 \\ 0 & 0 & c \end{pmatrix}$	$\begin{pmatrix} 0 & d & 0 \\ d & 0 & 0 \\ 0 & 0 & d \end{pmatrix}$	$\begin{pmatrix} 0 & 0 & e \\ 0 & 0 & 0 \\ e & 0 & 0 \end{pmatrix}$	$\begin{pmatrix} 0 & 0 & 0 \\ 0 & 0 & f \\ 0 & f & 0 \end{pmatrix}$

group	symmetry class	
C_{2h}	$A_g(xyz)$	$B_g(xyz)$
DiMe-PTCDI	$\begin{pmatrix} a & d & 0 \\ d & b & 0 \\ 0 & 0 & c \end{pmatrix}$	$\begin{pmatrix} 0 & 0 & e \\ 0 & 0 & f \\ e & f & 0 \end{pmatrix}$

The symmetry of a given vibrational mode is reflected in its corresponding Raman tensor R (Table 2).

When molecules are brought together to build a crystal, the total number of normal coordinates will be $Z(3N)$, where Z is the number of molecules in the unit cell. If the molecules in the unit cell are identical and the internal vibrations are not degenerate, each internal vibrational state must split into Z levels as a result of in-phase and out-of-phase coupling of identical vibrations among the molecules in the same unit cell. The effect is termed Davydov splitting or factor group splitting. A thorough description of the Davydov splitting will be given later in this section. The change in symmetry of a vibration upon the application of the crystal symmetry elements can be predicted employing the so-called correlation method.[46] This requires the knowledge of the symmetry of the site occupied by the molecule in the crystal. The procedure is to correlate the molecular point group to the site group and then to the factor group.

For example, PTCDA and DiMe-PTCDI have two molecules in the monoclinic unit cell (see Figure 3) and the site group of each molecule is C_i. In such a low-symmetry group, only the symmetry with respect to the inversion center is preserved; that is, all 54 vibrations of PTCDA which initially had *g* character (and were Raman active) become A_g symmetric (Table 3). In a unit cell with two molecules, each one contributes with 54 *gerade* vibrations; hence, the total number of A_g vibrations will be 2×54. Owing to the higher symmetry of the monoclinic factor group (C_{2h}^5) compared to the C_i site group, two symmetry classes are even with respect to the inversion operation: A_g and B_g. Accordingly, each of the 108 A_g vibrations in C_i transforms to an A_g or B_g vibration in C_{2h}^5 (Table 3). Similarly, all 54 *ungerade*

Table 3. Correlation Table for the Internal Modes of PTCDA and DiMe-PTCDI in a Monoclinic Crystal

molecule	point group D_{2h}	site group C_i	factor group C_{2h}^5
PTCDA	19 A_g	2×54 A_g	54 A_g
	18 B_{1g}		
	10 B_{2g}		54 B_g
	7 B_{3g}		
	8 A_u	2×54 A_u	54 A_u
	18 B_{1u}		
	18 B_{2u}		54 B_u
	10 B_{3u}		
DiMe-PTCDI	44 A_g	2×66 A_g	66 A_g
	22 B_g		66 B_g
	23 A_u	2×66 A_u	66 A_u
	43 B_u		66 B_u

vibrations in one molecule become A_u symmetric in the site group and will have either A_u or B_u symmetry in the crystal group.

A similar correlation can be done for DiMe-PTCDI (Table 3). The energetic separation between the vibrational levels depends on the strength of dipole and quadrupole interaction between the molecules in the unit cell. This issue will be addressed in the next sections.

For PTCDA and DiMe-PTCDI, the excitation light (488 nm line of an Ar^+ laser) used for the Raman spectroscopy experiments throughout this work falls in the S_0-S_1 absorption band (Figure 4). This provides favorable conditions for the resonant Raman effect. Since the S_0-S_1 transition dipole moment lies along the x_m axis mainly the vibrations with a large R_{xx} component of the Raman tensor will be enhanced during the process. For PTCDA, this condition is fulfilled by the 19 vibrations originating from the A_g modes of the isolated molecule. In the case of DiMe-PTCDI, only those A_g modes with low off-diagonal components in the Raman tensor will be resonantly enhanced by the 488 nm excitation line, i.e., those modes preserving the rectangular symmetry of the perylene core. Therefore, a similar number of vibrations is expected to occur in the resonant Raman spectra of DiMe-PTCDI.

The total number of degrees of freedom associated with internal vibrations is $Z(3N - 6)$. The other $6Z$ degrees of freedom determine the orientation of the Z molecules in space and can describe movements of entire molecules, i.e., lattice vibrations. These vibrations will be termed as external modes, or simpler phonons. As in inorganic crystals, three of the phonons have acoustic character. From the remaining $6Z - 3$ of optical origin, three have translational character and the rest involve rotations of the rigid molecules around their fixed axes. The symmetry of external vibrations is determined by irreducible representations of the crystal space group. As both PTCDA and DiMe-PTCDI belong to the same factor group with $Z = 2$, they have the same representation for the external modes:

$$\Gamma_{ext} = 3A_g + 3B_g + 3A_u + 3B_u \qquad (7)$$

Six of the optical phonons are symmetric with respect to the inversion center of the unit cell and are Raman-active, and those with B_u symmetry are infrared active. The acoustic phonons have A_u symmetry.

2.3.1. PTCDA

The first vibrational spectra of PTCDA films were reported in 1987 by Akers et al., who proposed an empirical assignment of internal modes.[50] Several theoretical works have been devoted in recent years to the study and identification of the vibrational modes. Scholz et al. used a density functional theory (DFT) code and compared the frequencies of the calculated A_g modes with those observed in thin PTCDA films.[44] A similar DFT time-dependent method was used in the Gaussian 98[51] package with several basis sets for the molecular wave functions. The correspondence between the resulting Raman active modes and the experimental ones is discussed in detail in ref 45. However, the calculations were all performed for nonresonant conditions, while the experimental spectra of films were obtained in resonance; therefore, a direct correspondence between the calculated cross sections and the experimental ones must be considered with care.

Polarization-dependent measurements performed on a single crystal using the 488 nm (2.54 eV) Ar^+ line enabled recently the first observation of the Davydov splitting in this system.[52] The Raman spectra from ref 52 are shown in Figure 5. For the determination of the Raman mode frequencies and

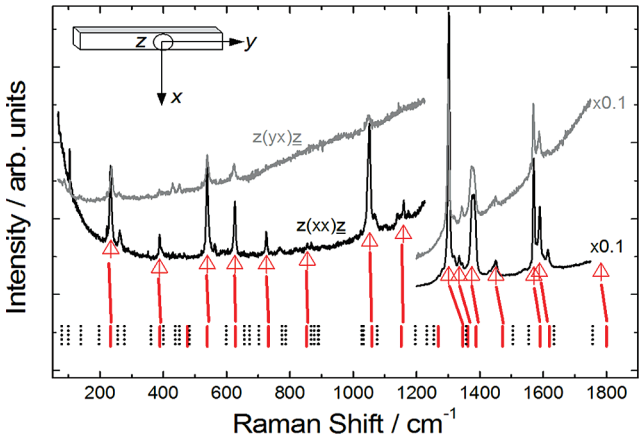

Figure 5. Raman spectra of a PTCDA single-crystal recorded at room temperature in the crossed (gray line) and parallel (black line) polarization configurations. The triangles represent experimental frequencies of A_g modes, and the vertical lines represent calculated frequencies of A_g (thick lines) and B_g (dotted lines) modes.

intensities in the spectra shown in Figure 5, a least-square fitting algorithm with Lorentzian peaks was employed. The Raman tensor for the A_g component of the Davydov doublet has three diagonal components of different magnitude and nondiagonal components, while the tensor of the B_g mode has only nondiagonal components (see Table 2). For the experimental geometry employed by Tenne et al.,[52] the B_g bands appear only in the crossed polarization geometry $z(yx)\bar{z}$ (see the description of this notation in section 3.2.2—Raman Spectroscopy), while the A_g modes are present in both configurations depending on the magnitude of their Raman tensor components.

Table 4 summarizes the assignments of the PTCDA modes observed under resonant conditions. The second and the third columns contain the frequencies of the Davydov components observed in a crystal,[52] and the fourth column gives the calculated frequencies in a free molecule.[45] The last two columns describe the symmetry of the corresponding vibrations in the isolated molecule and which part of the molecule is predominantly involved. As depicted in Figure 6, a PTCDA molecular breathing along the x_m axis gives rise to the lowest frequency internal mode (232.9 cm^{-1}) (see Table 5), while the mode at 1302.3 cm^{-1} (see Table 5) (with the largest cross section) is related to C−H bending vibrations. The stretching of C−C bonds governs the modes around 1580 cm^{-1}. There are two groups of modes, namely around ∼1150 cm^{-1} and between 1320 and 1360 cm^{-1}, where the assignment is still ambiguous due to their very similar cross section and polarization behavior.

The observation of external modes in PTCDA was reported in 2000[52,53] (Figure 11, left). The symmetry assignment was performed by analogy with the modes reported for β-perylene,[54] which has the same monoclinic structure as PTCDA and, therefore, for which similar intermolecular forces can be assumed. Considering the difference in mass

Table 4. Vibrational Modes for a PTCDA Single Crystal[52] and Calculated Vibrational Properties for an Isolated Molecule Using the B3LYP:3-21G Basis Set of Gaussian 98

	Raman shift (cm^{-1})					
PTCDA	(*xx*)	(*yx*)	B3LYP:3-21G (cm^{-1})	perylene*0.8 (cm^{-1})	symmetry	dominant character
external modes		37		*32*	B_g	libronic
	41			*42*	A_g	
	60			*67*	B_g	
	75			*75*	A_g	
		88		*81*	B_g	
	106			*96*	A_g	
internal modes	232.9	236.2	233		A_g	breathing along x_m
	262.2	259.3	255		B_{3g} (*xy*)	$\nu_{C=O}$
	388.2	387.6	389		A_g	δ_{C-O-C}, $\delta_{C=O}$
		430	437		B_{3g} (*xy*)	δ_{C-C}, δ_{C-O-C} in plane
		451	450		B_{2g} (*yz*)	δ_{C-O-C}, δ_{C-C} out of plane
	538.6	539.1	539		A_g	ν_{C-C} radial
	562		598		B_{3g} (*xy*)	δ_{C-C}, δ_{C-H}
	625.6	623.3	627		A_g	δ_{C-O-C}, δ_{C-C}, ν_{C-C} tangential
	725.7		732		A_g	δ_{C-C}, δ_{C-H}, δ_{O-C-C}
	855		853		A_g	δ_{C-C}, δ_{C-H}
	1052	1043.5	1059		A_g	d_{C-O-C}, d_{C-C}, d_{C-H}
	1072		1075		B_{3g} (*xy*)	δ_{C-C}, δ_{C-H}
	1141		1196		B_{3g} (*xy*)?	δ_{C-H}, δ_{C-C-C}
		1149	1151		A_g	δ_{C-H}, δ_{C-O-C}
	1159		1232		B_{3g} (*xy*)?	δ_{C-H}
	1302.3	1300.6	1346		A_g	δ_{C-H}
	1321					
		1349				
	1335		1356		B_{3g} (*xy*)	δ_{C-C}
	1375.4	1373	1363		A_g	δ_{C-H}
	1383.6	1381.8	1389		A_g	δ_{C-H}, ν_{C-C}
	1451		1472		A_g	δ_{C-H}, ν_{C-C}
	1572	1585	1591		A_g	ν_{C-C}, δ_{C-H}
	1589.1	1588.3	1620		A_g	ν_{C-C}, δ_{C-H}
	1615		1634		B_{3g} (*xy*)	δ_{C-C} along short axis
	1783		1800		A_g	$\nu_{C=O}$

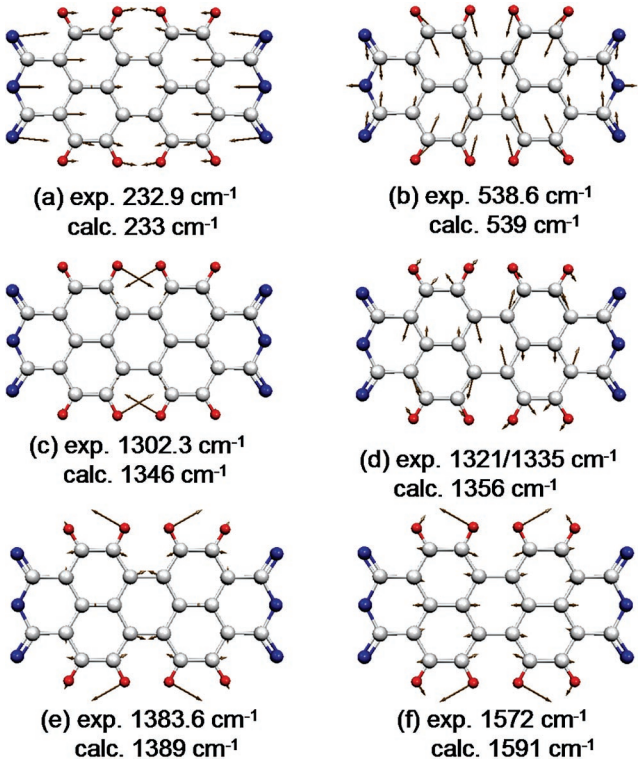

Figure 6. Elongation patterns of selected modes of a neutral PTCDA molecule obtained by DFT calculations with the B3LYP: 3-21G basis set of the Gaussian 98 package along with their calculated frequencies and the frequencies measured for a crystal in the parallel polarization configuration.

for the two molecules (m_{PTCDA} = 392 amu and $m_{perylene}$ = 252 amu), the frequencies of the PTCDA phonons were calculated using the proportionality relation of two harmonic oscillators with the same force constant:

$$\frac{\omega_{perylene}}{\omega_{PTCDA}} = \sqrt{\frac{m_{PTCDA}}{m_{perylene}}} = 0.8 \qquad (8)$$

The properties of phonons observed in PTCDA are summarized in the first six rows in Table 4. The frequencies calculated as described above are given in column five and are displayed in Figure 6. The assignment of the mode at 60 cm^{-1} is not clear, since, according to the comparison with the perylene phonons, it should be a B_g mode but, in PTCDA, it is observed in parallel polarization, as are the A_g modes. The lowest energy phonons employ rotations around the x_m axis of the molecules, while, for the higher energy ones, the molecules rotate around their z_m axis.[55] A sketch of the vibrational pattern for selected modes can be seen in Figure 7. It must be noted that DFT methods (B3LYP:3-21G) predict the existence of three out-of-plane (oop) internal modes below 150 cm^{-1}: one B_{2g} ($\delta_{C-C-C} + \delta_{C-O-C}$) mode at 78 cm^{-1} and two B_{1g} (δ_{C-C-C}) modes at 99 cm^{-1} and 138 cm^{-1}. In-plane (ip) and out-of-plane modes stem for vibrational elongations involving movement of atoms within the molecular plane and perpendicular to it, respectively.

Muck et al.[55] reported the presence of more than six modes below 125 cm^{-1} in Raman spectra measured at 20 K, with some of them showing a strong polarization dependence. They proposed a model that explains the large number of modes based on the coupling between internal and external modes mediated by pure van-der-Waals interactions. The number of the observed modes and their ordering are reproduced fairly well. However, the calculated frequencies are highly overestimated, in particular for the C—H and C═O

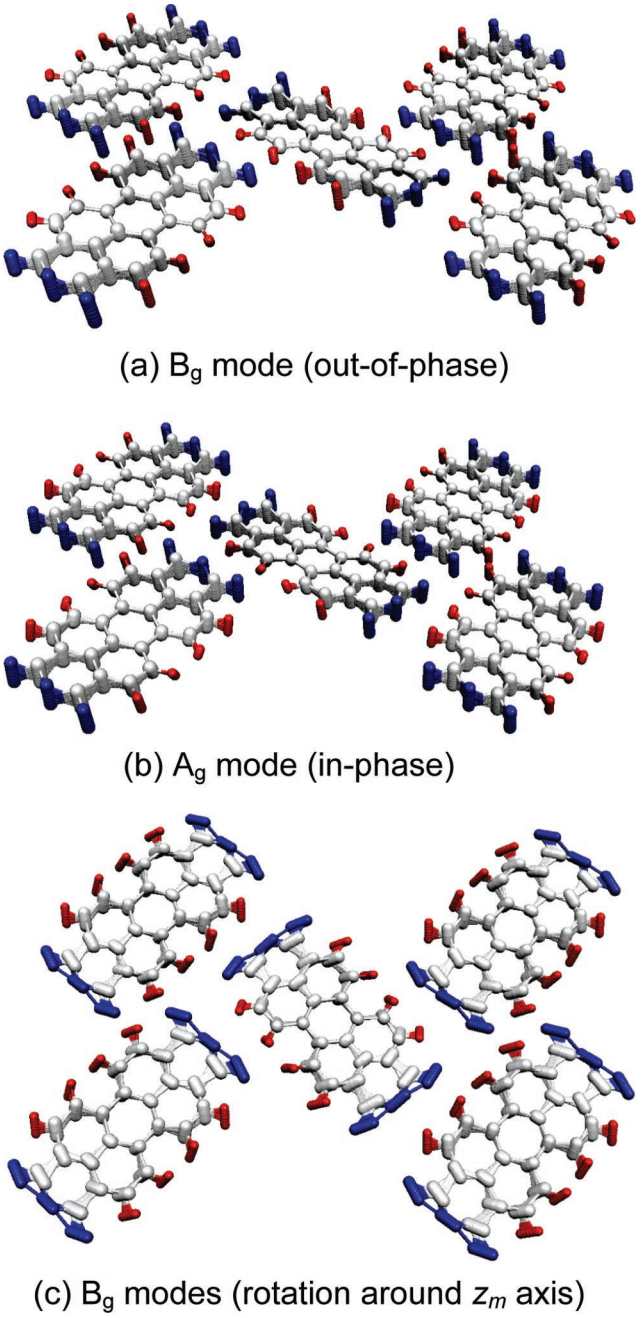

Figure 7. Elongation patterns of selected phonons of the α-PTCDA crystal: the lowest frequency phonons employ out-of-phase (a) and in-phase (b) rotations around the x_m axis of the molecules; in the highest frequency B_g phonon (c), the molecules rotate around their z_m axis.

related modes. No more accurate description is available to the best of our knowledge.

2.3.2. DiMe-PTCDI

The literature is less rich in works devoted to the vibrational properties of DiMe-PTCDI. Guhatathakurta-Gosch and Aroca were again the first to report Raman spectra of films and propose an empirical assignment.[56] Reports on theoretical investigations are still lacking. For the mode assignments used in this work, DFT was employed with the same basis set as that for PTCDA (B3LYP:3-21G).

As in the case of PTCDA, polarization measurements on a single crystal were performed under resonant conditions using an excitation energy of 2.54 eV (488) (Figure 8) and a resolution of 2 cm^{-1}.

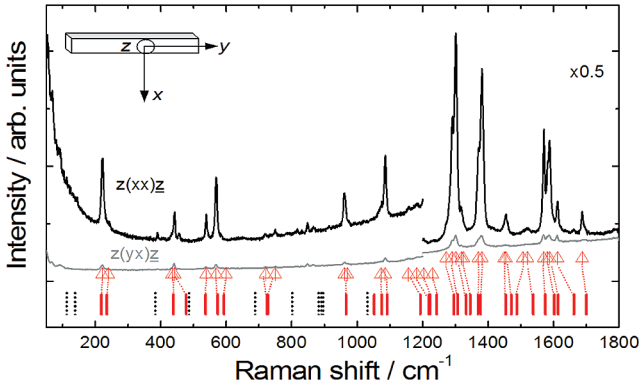

Figure 8. Raman spectra of a DiMe-PTCDI single-crystal recorded at room temperature in the parallel (black line) and crossed (gray line) polarization configurations. The triangles represent experimental frequencies of A_g modes, and the vertical lines represent calculated frequencies of A_g (thick lines) and B_g (dotted lines) modes.

A concept widely used in the literature dedicated to quantitative analysis of the sample polarization response is the depolarization ratio.[46] This is defined as the ratio between the Raman signals obtained in the crossed polarization configuration and those obtained in the parallel configuration:

$$\mathrm{Dep} = \frac{I_{yx}}{I_{xx}} \tag{9}$$

The frequencies obtained for the parallel and crossed polarization spectra are tabulated in the second and third columns of Table 5. In column five the intensities in parallel polarization relative to the strongest mode at 1301.4 cm^{-1} are provided. The experimental depolarization ratios are listed in column six. The calculated frequencies, the mode symmetry, and the character are listed in columns four, seven, and eight, respectively. Selected elongation patterns of several modes of a neutral DiMe-PTCDI molecule are displayed in Figure 9. No scaling factor was applied to the calculated frequencies for consistency with the model applied to PTCDA.[57]

A large number of similarities can be found between the vibrational spectra of DiMe-PTCDI and PTCDA, due to their perylene core which determines the rectangular symmetry of both molecules. For instance, the breathing mode at 220.5 cm^{-1} has the same character as the corresponding one in PTCDA and its frequency is a factor 0.95 lower compared to the 232.9 cm^{-1} (see Table 5) mode of PTCDA (Figure 10). This factor is very close to the scaling factor obtained approximating both molecules (m_{PTCDA} = 392 amu and $m_{\mathrm{DiMe-PTCDI}}$ = 418 amu) with linear oscillators having the same force constants:

$$\frac{\omega_{\mathrm{DiMe-PTCDI}}}{\omega_{\mathrm{PTCDA}}} = \sqrt{\frac{m_{\mathrm{PTCDA}}}{m_{\mathrm{DiMe-PTCDI}}}} = 0.97 \tag{10}$$

As in the case of PTCDA, a mode with out-of-plane character involving deformation of C−C and C═O bonds appears at 441.9 cm^{-1} (see Table 5). The C−H deformation modes with some contribution from CH_3 groups, and the C−N stretching or bending modes appearing around 1300 and 1380 cm^{-1} dominate the spectra. The C−C stretching modes accompanied by C−H deformations govern the region around 1600 cm^{-1}. There are a few modes originating exclusively from the methylimide groups (−N−CH_3) in the spectra: a shoulder at 239.3 cm^{-1} (see Table 5) stems from

Table 5. Vibrational Modes of a DiMe-PTCDI Single Crystal and Calculated Vibrational Properties for an Isolated Molecule Using the B3LYP:3-21G Basis Set of Gaussian 98

DiMe-PTCDI	Raman shift (cm^{-1}) (xx)	(yx)	B3LYP:3-21G (cm^{-1})	intensity (xx)	depolarization	symmetry	dominant character
external modes		30				B_g	libronic
	37	37		0.05	0.18	A_g	
	50	50		0.05	1.22		
	57			0.11	0	B_g	
	69	68		0.06	0.18	A_g	
	89	88		0.03	0.20	B_g	
		96				A_g	
internal modes	220.5	221.1	220	0.11	0.13	A_g	breathing along x_m
	239.3	238.2	238	0.06	0.04	A_g	ν_{N-C}
	390.4	391	403	0.01	0.30	A_g	core deformation + δ_{C-O-C} + $\delta_{C=O}$
	434.8		442	0.01	0.41	A_g	δ_{C-C} + δ_{C-O-C}
	441.9	440.6	457	0.04	0.24	B_g	δ_{C-O-C} + δ_{C-C}, oop
	538.9	539.1	542	0.03	0.30	A_g	core stretch, radial + $\delta_{C=O}$
	569.3	568.8	580	0.11	0.11	A_g	δ_{C-C} + δ_{C-H} + δ_{CH3}
	720.4	718.9	733	0.01	0.64	A_g	δ_{C-C} + δ_{C-N-C} + δ_{C-H}
	749.2	750.6	734	0.01	1.01	A_g	δ_{C-C} + δ_{C-N-C} + δ_{C-H}
	848.7	847.5	882	0.01	0.47	B_g	δ_{C-H}
	961.4	962	975	0.07	0.12	A_g	CH_3 rocking
	1085.9	1086.1	1103	0.11	0.07	A_g	CH_3 rocking + δ_{C-H}
	1157	1155.7	1173	0.07	0.03	A_g	CH_3 rocking
	1181.7	1184.1	1205	0.04	0.11	A_g	δ_{C-H}
	1203.2	—	1232	0.04	—	A_g	δ_{C-H}
	1290	1289.6	1320	0.49	0.08	A_g	δ_{C-H} + δ_{CH3} + ν_{C-N}
	1301.4	1301	1347	1.00	0.09	A_g	δ_{C-H} + ν_{C-C}
	1318.5	—	1358	0.04	—	A_g	core deformation
	1370	1369	1383	0.35	0.14	A_g	δ_{C-H} + δ_{CH3} + δ_{C-N-C}
	1381.4	1380.2	1391	0.91	0.09	A_g	δ_{C-H} + ν_{C-C} + δ_{CH3}
	1454.6	1452	1469	0.11	0.27	A_g	δ_{CH3} + δ_{C-H}
	1520	1517.4	1554	0.22	0.55	A_g	δ_{C-H} + ν_{C-C}
	1570.3	1568.9	1591	0.36	0.12	A_g	δ_{C-H} + ν_{C-C}
	1581.3	1581.1	1618	0.12	0.17	A_g	δ_{C-H} + ν_{C-C}
	1587.8	1587.2	1631	0.40	0.07	A_g	δ_{C-C} + δ_{C-H}
	1612.1	1610.8	1679	0.13	0.20	A_g	$\nu_{C=O}$
	1687.8	1689.0	1717	0.08	0.12	A_g	$\nu_{C=O}$ + δ_{CH3}

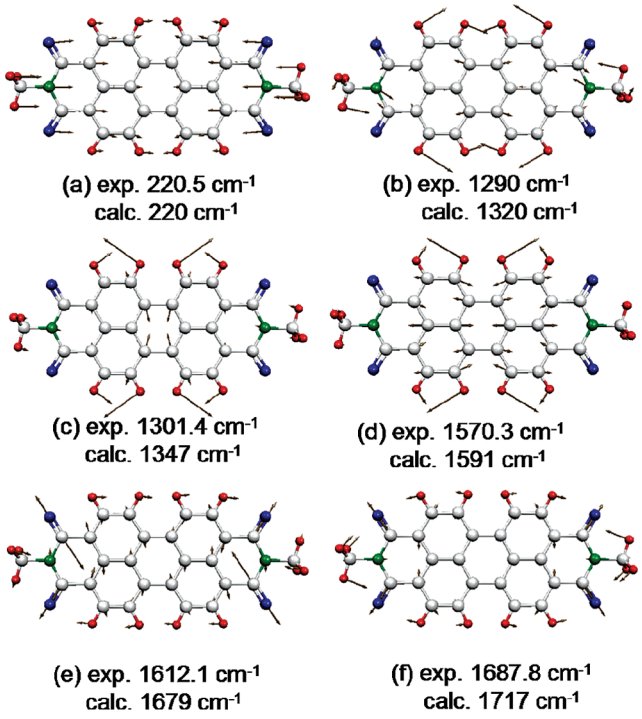

Figure 9. Elongation patterns of several modes of a neutral DiMe-PTCDI molecule calculated using DFT methods with the B3LYP: 3-21G basis set of the Gaussian 98 package along with their calculated and corresponding experimental frequencies.

the stretching of C−N bonds, and the modes at 961.4, 1085.9, and 1157 cm^{-1} (see Table 5) are due to the rocking of CH_3 groups.

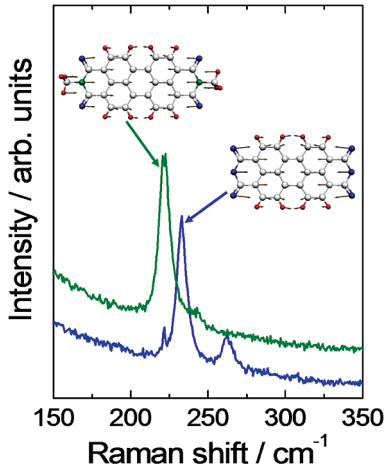

Figure 10. Raman spectra in the region of the breathing mode of PTCDA and DiMe-PTCDI together with the elongation pattern of this mode.

In crossed polarization configuration $z(yx)\bar{z}$, the internal modes almost vanish. This leads to low depolarization ratios (0.1−0.2) for most of the A_g modes involving vibrations of the perylene core. The few modes with depolarization above 0.5 have either oop (B_g) or ip C−H or C−N−C deformation character. The amount of Davydov splitting is generally less than that observed in PTCDA due to different relative orientations of the molecules in the unit cell, as will be shown in section 2.3.3—Davydov Splitting: Dipole−Dipole Approximation.

The external vibrational modes of DiMe-PTCDI were observed for the first time in a Raman experiment by our group in 2003.[58] Their observation in a femtosecond pump−probe experiment has recently been reported by Hasche et al.[59]

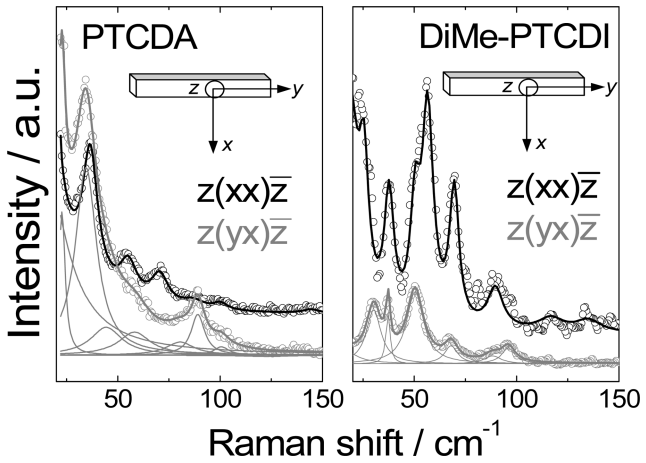

Figure 11. Raman spectra of PTCDA (left) and DiMe-PTCDI (right) crystals in the region of the external modes. The sketch of the measurement geometry is shown in the inset.

Table 6. Frequencies of Modes Observed below 125 cm^{-1} in a DiMe-PTCDI Crystal Compared with the Experimental Values from Ref 59[a]

crystal				ref 59	perylene	
$z(xx)\bar{z}$	$z(yx)\bar{z}$	$z(yy)\bar{z}$	$z(xy)\bar{z}$	(cm^{-1})	($\times$0.8 cm^{-1})	symmetry
25				4.7 + 25		B_g
	30	31	33	33	32	B_g
37	37			43	42	A_g
50	50	50		57	67	B_g
57			54			
69	68	67	69	71	75	A_g
89	88	88	89	89	85	B_g
	96	101	102	105	96	A_g

[a] The symmetry assignment is made following ref 59 by comparison to the molecular phonons of perylene. All values are in cm^{-1}.

Figure 11 shows the polarization dependence in the phonon region in both PTCDA and DiMe-PTCDI crystals for the experimental geometries shown in the insets. Even though the relative intensities are different for the two crystals, a clear polarization dependence is observed in both cases. Modes that are strong in parallel polarization become very weak or even vanish in cross polarization, enabling the symmetry assignment proposed for DiMe-PTCDI in Tables 2−6. When rotating the DiMe-PTCDI crystal around the *z*-axis, the polarization behavior changes and several modes appear at different frequencies. The frequencies are summarized for both situations in columns one to four of Table 6. In column five the frequencies reported in ref 59 are provided. Columns six and seven contain the frequencies and the symmetry assignment proposed[59] by comparison with the phonons reported for perylene.[54] The correspondence in number of modes and frequency positions is good, except for the presence of two modes at 4.7 and 25 cm^{-1}. These were assigned to a Davydov splitted internal mode with B_g symmetry which is predicted by DFT calculations to appear at 16 cm^{-1}. On the other hand, the B3LYP:3-21G methods predict the existence of four Raman active internal modes with B_g(oop) character below 125 cm^{-1}, but none of them has such a low frequency: 77, 86, 111, and 112 cm^{-1}.[60] The mode at 25 cm^{-1} is also observed in the Raman spectra.

Moreover, it was found that the three modes located at 50, 54, and 57 cm^{-1} correspond to the B_g mode at 57 cm^{-1} reported by Hasche et al.,[59] whereby the mode observed at 50 cm^{-1} behaves rather like an A_g mode. Also, the Raman modes at 96 and 101 cm^{-1} correspond to the same A_g mode in the time-resolved experiment. The large number of modes could be understood in the frame of the model proposed by Muck et al.[55] as originating from the coupling between internal and external modes. Since a comprehensive theoretical model is still lacking, the modes below 125 cm^{-1} will be considered as external modes according to the assignments in Table 4 (for PTCDA) and Table 6 (for DiMe-PTCDI) throughout this work, even though a contribution from the internal modes cannot be ruled out.

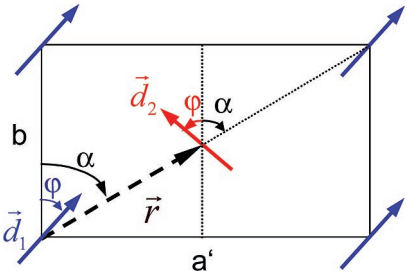

Figure 12. Geometrical arrangement of dynamic dipoles ($\vec{d}_1$ and $\vec{d}_2$) in the (102) plane of the monoclinic crystal of α-PTCDA.

Table 7. Relevant Geometrical Parameters for the Estimation of the Davydov Splitting δ_{norm}[a]

parameter	α-PTCDA	β-PTCDA	DiMe-PTCDI
space group	$P2_1/c(C_{2h}^5)$	$P2_1/c(C_{2h}^5)$	$P2_1/c(C_{2h}^5)$
a' (Å)	19.91	12.45	17.41
b (Å)	11.96	19.30	15.58
r (Å)	11.61	11.48	11.68
α (deg)	59	33	48
φ (deg)	42	52	18
δ_{norm}	2.8	2.2	1

[a] δ_{norm}, normalized to the value of splitting in DiMe-PTCDI.

2.3.3. Davydov Splitting: Dipole–Dipole Approximation

The following section is an attempt to explain the different amounts of Davydov frequency splitting observed in PTCDA and DiMe-PTCDI crystals. The splitting δ is considered to arise from pure dipole−dipole interaction of the vibration-related dynamic dipole moments ($\vec{d}_1$ and $\vec{d}_2$) of the molecules in the monoclinic unit cell:

$$\delta \propto \frac{d_1 d_2}{4\pi\epsilon_0\epsilon r^3}\left((\vec{e}_1\cdot\vec{e}_2) - \frac{3(\vec{e}_1\cdot\vec{r})\cdot(\vec{e}_2\cdot\vec{r})}{r^2}\right) \qquad (11)$$

where $\vec{d}_1 = d_1\vec{e}_1$ and $\vec{d}_2 = d_2\vec{e}_2$, with $\vec{e}_1$ and $\vec{e}_2$ being the unit vectors determining the directions of $\vec{d}_1$ and $\vec{d}_2$, considered to lie in the (102) plane, as shown in Figure 12. They form an angle $+\varphi$ and $-\varphi$, respectively, with the *b* crystallographic axis.

The $\vec{r}$ vector determines the distance between the dipole centers and forms an angle α with the *b*-axis. In the first approximation, the dipole absolute values are considered equal for both molecular crystals and only the geometrical differences are taken into account. All parameters of interest were calculated based on the crystal parameters given for PTCDA[1,42] and for DiMe-PTCDI[43] and are summarized in Table 7. The last row presents the amount of splitting normalized (δ_{norm}) to the splitting in DiMe-PTCDI, which has the lowest value. It can be seen that in the dipole approximation the splitting is expected to be almost three times larger in a PTCDA than in a DiMe-PTCDI crystal.

This qualitatively reproduces the experimental trend; that is, the splitting is 3.3 and 0.6 cm^{-1} for the Raman breathing mode or 1.7 and 0.4 cm^{-1} for the most intense

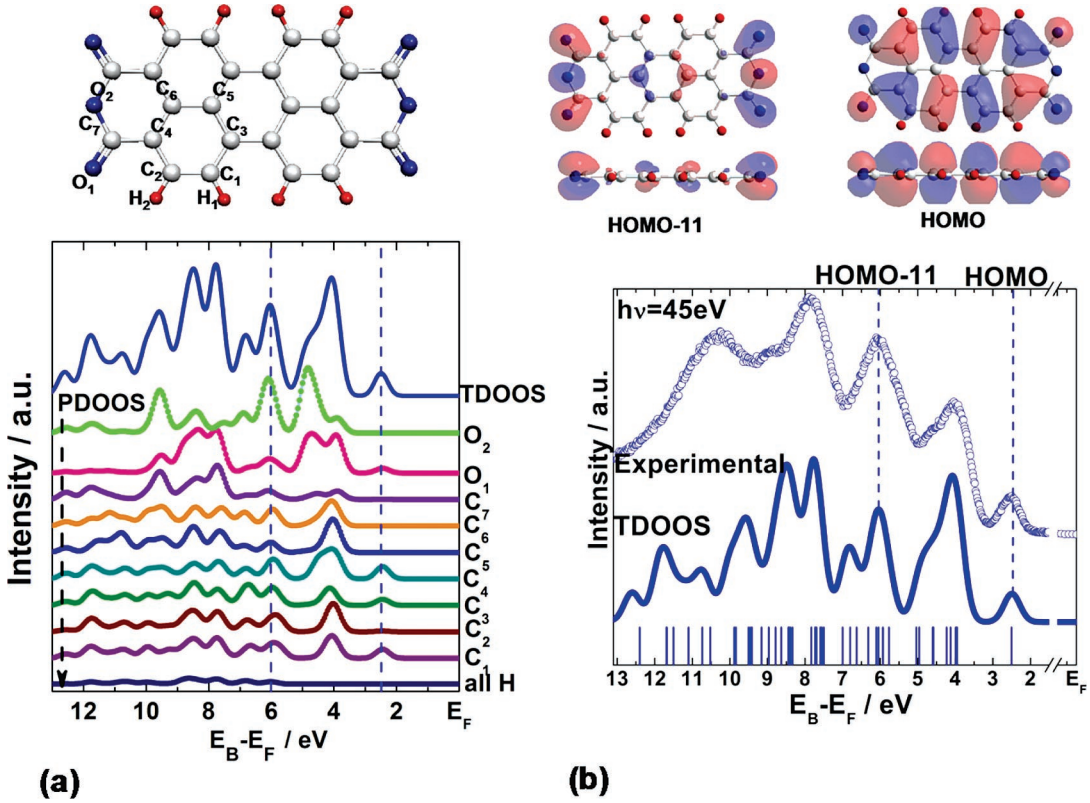

Figure 13. (a) PDOOS and TDOOS of PTCDA. (b) Valence band spectrum of a PTCDA thin film (symbols) along with the calculated TDOOS (line). The MO energies are shown by vertical bars. The HOMO and HOMO − 11 are π-derived states. Above: left, geometry of PTCDA with labels on the atoms for which the PDOOS is shown in part a; right, charge density contours of HOMO − 11 and HOMO.

δ_{CH} modes in PTCDA and DiMe-PTCDI, respectively. The maximum frequency splitting observed among the Raman modes amounts to 8.5 cm^{-1} (ref 52) for the A_g mode at 1052 cm^{-1} in PTCDA and 2.4 cm^{-1} for the A_g mode at 1181.7 cm^{-1} in DiMe-PTCDI. For the $\nu_{C=O}(y)$ infrared active modes at 1731 and 1743 cm^{-1} in PTCDA and 1649 and 1658 cm^{-1} in DiMe-PTCDI, the splittings are 12 and 9 cm^{-1}, respectively. The discrepancy between the values predicted by the crude model and the experiment may be caused by the presence of H bridges in the molecular crystals. Other factors influencing the experimental splitting could be the coupling between vibrations with different character, or even a mixture of crystalline phases. To date, there is no reported theoretical study that predicts the vibrational Davydov splitting for dimers consisting of such large molecules. The largest molecular system to our knowledge for which a prediction of the low-frequency Raman spectra and the splitting therein was attempted is benzene, modeled by V. Spiro and co-workers using the Hartree Fock approximation.[61]

The arrangement of the PTCDA molecules in the unit cell quasi-perpendicular to each other may lead to optical isotropy in the (102) crystalline planes even in a well-ordered crystal.[47] The low angle (36°) between the DiMe-PTCDI in the (102) unit cell results in a strong optical anisotropy within this plane in ordered systems. For this reason, some authors refer to DiMe-PTCDI as a quasi-1D system.[47,59]

2.4. Electronic Properties: Valence Band Structures

Detailed knowledge about transport and optical processes taking place in organic-based devices can be achieved through a fundamental understanding of the electronic structure of the individual molecules and of the molecular thin films. A comparison between the occupied and unoccupied electronic states measured via electron spectroscopic methods and those derived from DFT represents one good approach for providing fruitful information about the electronic structure. Moreover, analyzing the contribution of the electronic states of the individual atoms to a particular molecular orbital, one can also obtain the localization of the states. As mentioned in section 2.1—Electronic Structure of Organic Semiconductors, the molecular solids are characterized by strong covalent intramolecular bonds but weak van-der-Waals (vdW) intermolecular bonds. The overlap between the wave functions centered on neighboring molecules is small, leading to a weak intermolecular electronic coupling. Therefore, the electronic and optical properties of organic molecular films, in a first approximation, are close to those of the individual molecules. DFT calculations using the B3LYP method and the 6-31++G(d,p) basis set together with the AOMix software[62] were employed for the modeling of the electronic properties of the two perylene derivatives. A detailed description of the total (T) and partial (P) density of occupied states (DOOS) calculations is given in section 3.2—Experimental Methods and Data Analysis. The combination of these two methods gives an insight into the role the atoms play in determining the electronic structure of organic molecules.

2.4.1. PTCDA

The partial density of occupied states (PDOOS) spectra presented in Figure 13a for the marked atoms (see top left figure) provide a wide range of information. The total density of occupied states (TDOOS) displayed at the top of Figure 13a and the bottom of Figure 13b represents the sum of all contributions of the labeled atoms. This was obtained by

Gaussian broadening of each molecular orbital energy calculated for a single molecule using the Gaussian 98 B3LYP-6 31++G(d,p) basis set[51] and represented in Figure 13b by the vertical bars. The full width at half-maximum (fwhm) of the Gaussian function used for broadening is 0.5 eV and corresponds to the value determined from the fit of the experimentally observed HOMO spectral feature. An examination of the PDOOS of atoms contributing to the TDOOS reveals that the HOMO is mainly located over the perylene core. It has π character (see Figure 13b top right) and is well separated energetically from the rest of the occupied molecular orbitals. The advantage of the present method is that the identification of any molecular orbital is straightforward. For example, the next four bands are related to contributions with π character from the perylene core and to the molecular orbitals derived from oxygen $2p_x$ and $2p_y$ atomic orbitals. Moreover, the feature at 6 eV (HOMO − 11) is mainly assigned to the contribution of the $2p_z$ atomic orbitals of the anhydride groups. Any change in the electronic structure of the anhydride oxygen, as we shall see in section 6—Metals on Organic Layers, can therefore be associated with changes in the HOMO − 11 feature.

The calculated TDOOS of PTCDA, as indicated in Figure 13b, is similar to the experimentally measured one using an excitation energy of 45 eV. This excitation energy was chosen based on photoionization cross-section considerations. For comparison of the simulated DOOS and the measured valence band spectrum, the energy scale of the calculated spectrum was rigidly shifted by 0.65 eV toward higher binding energy in order to match the HOMO position observed experimentally. The mismatch in energy positions between the calculated and the experimentally observed features stems from the inaccuracy of the DFT calculations in predicting the band gap of materials and, along with it, energy positions (see section 3.3.1). Nevertheless, a good match between the experimental and theoretical line shapes can be achieved, enabling a reliable assignment of the spectral features

The IPES spectra showing the unoccupied molecular states of PTCDA are presented the Figure 14. As in the case of VB-PES measurements, the energy scale is given with respect to the Fermi level. Due to the rather poor instrumental resolution of the IPES spectra, a special data treatment was required. Details are described in section 3—Experimental Methods, Data Analysis, and Theoretical Calculations.

The calculated density of unoccupied states (DOUS) was obtained by Gaussian broadening of each orbital energy with a full width at half-maximum (fwhm) of 0.75 eV, which corresponds to the experimentally deconvoluted LUMO state. In order to compare the simulated DOUS with the measured IPES spectrum, the energy scale of the calculated spectrum was rigidly shifted by 0.87 eV toward the Fermi level. The fwhm after deconvolution is larger than the fwhm of the HOMO by about ~0.2 eV. This is an inherent property of IPES spectroscopy and is related to the lifetime of the final states.[63] As shown in Figure 14, the agreement between the experimental and theoretical line shapes is very good. Most of the states in the lowest unoccupied molecular levels, LUMO and LUMO + 1, are predominantly located on the perylene core.

2.4.2. DiMe-PTCDI

The PDOOS spectra of DiMe-PTCDI are presented in Figure 15 for the marked atoms (see top left figure). As for the case of PTCDA, they were obtained by Gaussian broadening of the atomic contribution with a fwhm of 0.5 eV. The TDOOS is the sum of all contributions of the labeled atoms. By examining the PDOOS of atoms contributing to the TDOOS, it can again be shown that the HOMO is mainly located over the perylene core and has π character (see Figure 15b top right). The HOMO appears as a separate feature while the remaining ones overlap. For comparison and in order to match the simulated DOS with the measured valence band spectrum, the energy scale of the calculated spectrum was rigidly shifted by 0.73 eV toward higher binding energy.

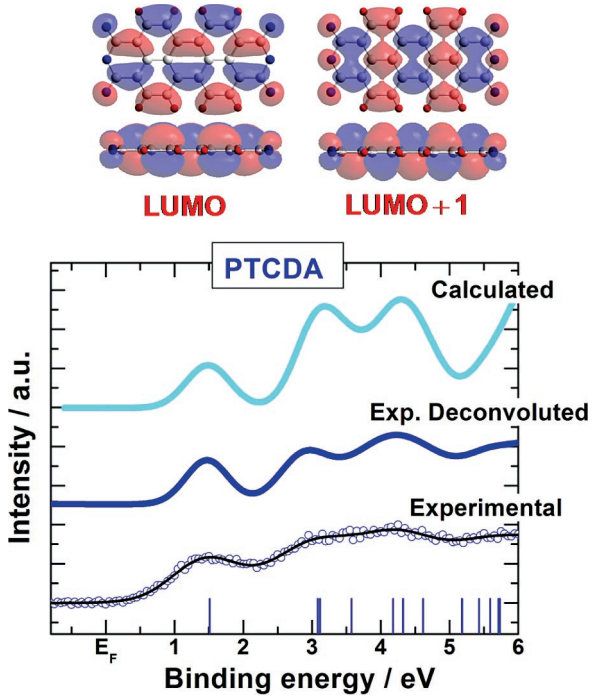

Figure 14. Experimental, deconvoluted, and calculated densities of unoccupied states of PTCDA. Above: the charge density contours of LUMO and LUMO + 1.

The very good match between the experimental and theoretical line shapes allows a reliable assignment of the spectral features to be made. The strong peak at a binding energy of about 4 eV is characteristic for DiMe-PTCDI and stems from both π and σ bonds in the methylimide and carboxylic groups. One of the contributing orbitals, for example HOMO − 8, is visualized in Figure 15 (top right). The methyl (CH_3) groups strongly contribute to the molecular orbital situated at about 8 eV. For binding energies above 10 eV, mainly molecular orbitals with σ character contribute to the spectra.

The IPES experimental spectra of DiMe-PTCDI and the deconvoluted ones are presented together with the calculated densities of unoccupied states in Figure 16.

The procedure for obtaining the calculated DOUS is the same as that for PTCDA. In order to compare the simulated DOUS with the measured IPES spectrum, the energy scale of the calculated spectrum was shifted by 0.75 eV toward the Fermi level. The agreement is again very good. Figures 14 and 16 demonstrate that the LUMO levels are not affected by the substitution of anhydride oxygens by methylimide groups. Most of the states are predominantly delocalized over the perylene core.

2.5. XPES Peak Structures

High-resolution X-ray photoelectron spectroscopy (HR-XPES) studies of large π-conjugated organic molecules[64]

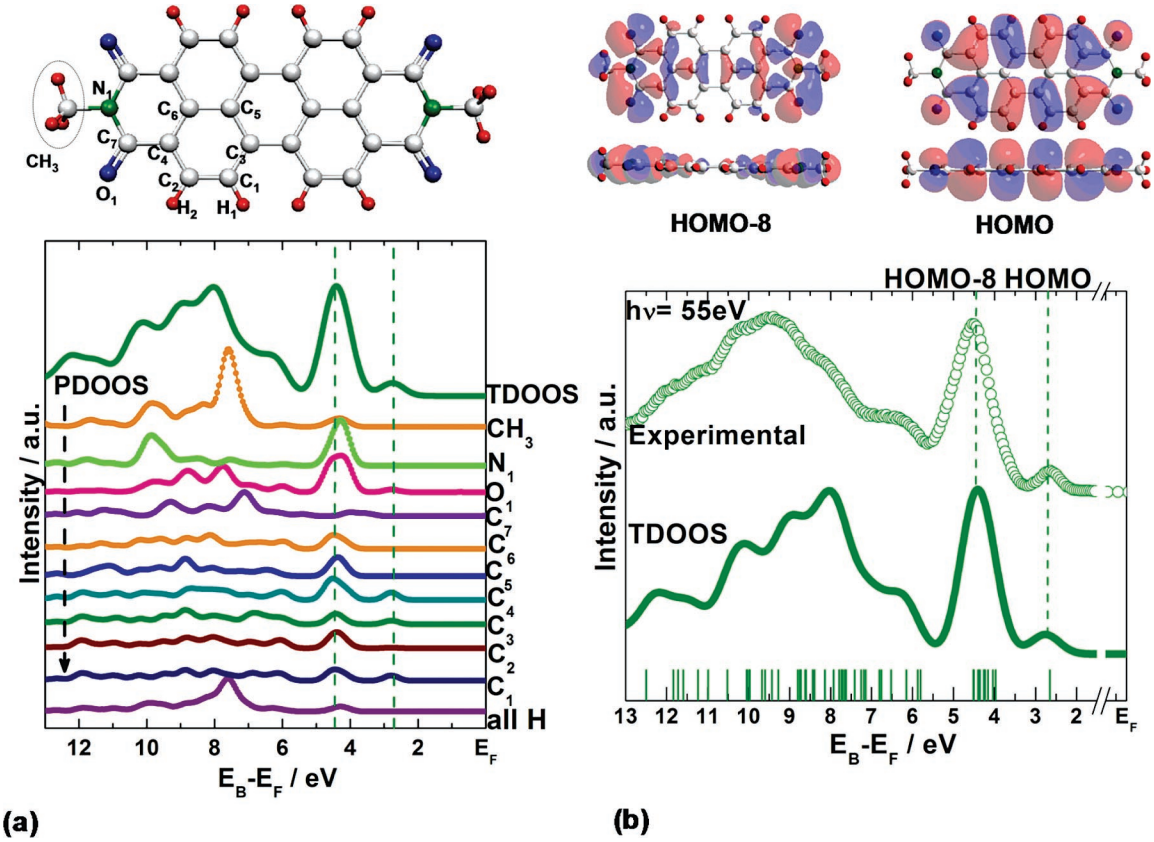

Figure 15. (a) PDOOS and TDOOS of DiMe-PTCDI. (b) Valence band spectrum of a DiMe-PTCDI thin film measured at 55 eV excitation energy and calculated TDOOS. The MO energies are shown by vertical bars. HOMO and HOMO − 8 are π- and σ-derived states, respectively. Top figure: left, geometry of DiMe-PTCDI with the labeled atoms that are contributing to TDOOS; right, charge density contours of the HOMO and HOMO − 8.

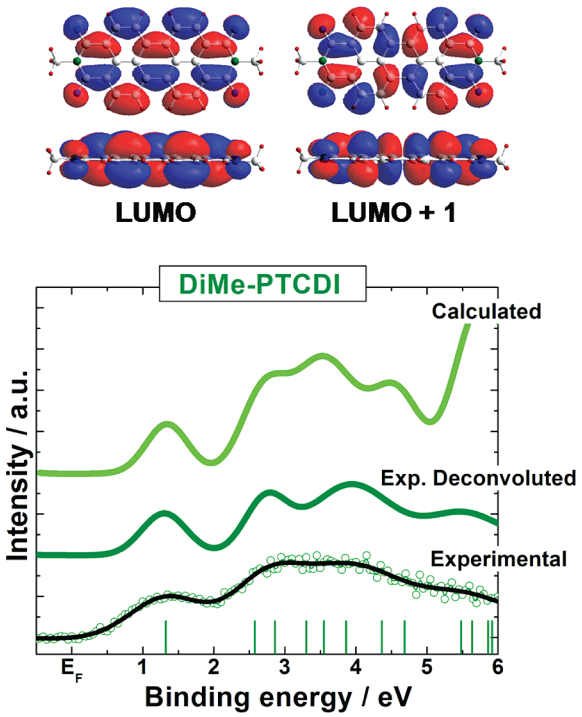

Figure 16. Experimental, deconvoluted, and calculated densities of unoccupied states of DiMe-PTCDI. Top: charge density contours of LUMO and LUMO + 1.

and/or of aromatic anhydride and imide perylene derivatives such as PTCDA and DiMe-PTCDI[65,66] were first presented in 2004. The high-resolution XPES spectra show complex peak structures of the C_{1s}, O_{1s}, and, to a lesser extent, N_{1s} core level emission. To get a deeper insight into the chemical interactions between organic molecules and at their interfaces with inorganic materials, a careful analysis of the core emission line shape is essential. Moreover, the peak intensity ratios cannot be simply explained by the different chemical states of the atoms, since they are strongly influenced by multielectron, so-called *shakeup excitations*. In order to analyze the various spectroscopic features, i.e., to distinguish and to assign the contributing components and the satellite features in detail and to define their energy positions, a peak fit analysis is essential.

Before fitting a core level spectrum, one should have a clear idea of how many components are present for which relative positions contribute to the spectrum. Each core level line shape/component is described by a convolution of Gaussian and Lorentzian (or Doniach−Sunjic type) contributions (the so-called Voigt profile function). The Lorentzian width (W_L) and the spin−orbit splitting, if present, are considered to be the same for all core level components in one core level spectrum. Absolute peak positions, Gaussian widths (W_G), and relative peak intensities were allowed to vary. A polynomial function combined with a Shirley background was usually chosen in order to obtain the best fit. The determination of the peak model parameters, e.g., W_G, W_L, peak positions, and intensities, proceeds iteratively by a nonlinear parameter fitting routine. The Levenberg−Marquardt algorithm has been chosen to minimize the mean square errors. The program used for fitting is UNIFIT for Windows, Version 2004, developed by Ronald Hesse, University of Leipzig. In this program, the areas of the

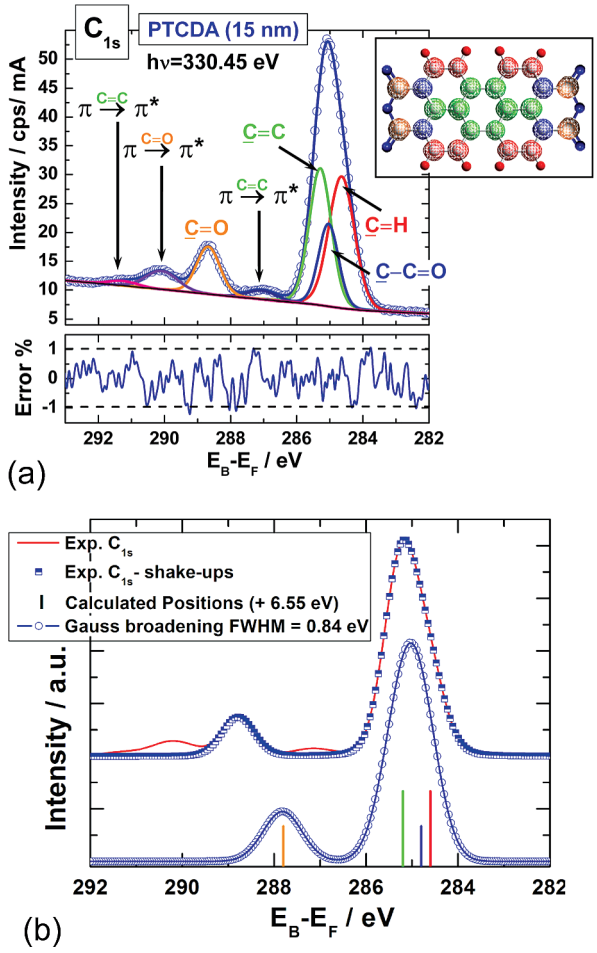

Figure 17. (a) Results of the peak fit analysis of the C_{1s} spectrum of a PTCDA thin film. For the main peaks C—H, *C*—C═O, C═C, and C═O, Voigt functions with a fixed W_L of 0.075 eV and variable W_G were used. The intensities are constrained by the stoichiometry of the atoms in PTCDA to 8:4:8:4. The individual components for the C_{1s} of PTCDA are assigned according to the color coding. (b) Calculated positions of C_{1s} (vertical bars), and experimental, experimental with shake-up contributions subtracted, and simulated (using a W_G of 0.84 eV) C_{1s} emission line shapes.

components are not fit parameters. They are calculated as a numerical integral of the peaks.

In the following, a detailed analysis of thin film spectra in comparison with the results of DFT calculations will be presented.

2.5.1. C_{1s} Core Level

Figure 17 shows the C_{1s} spectrum of 15 nm PTCDA deposited onto sulfur-passivated GaAs(001). The C_{1s} spectrum consists of two well-separated features. The main feature with its peak at about 285.3 eV stems from different carbon atoms of the aromatic part while the second peak located at 288.9 eV stems from the carbon atoms in the anhydride part. The contribution of the individual carbon sites cannot be easily separated, even though the weak asymmetry at the low binding energy side indicates a contribution due to a slightly different chemical environment in the aromatic part. Figure 17b shows the calculated C_{1s} spectrum for PTCDA using DFT under the assumption that the molecule is the same in the initial and final states. The results provide evidence for three distinct groups of C atoms which constitute the perylene core. The four C atoms involved in C═O bonds are characterized by their higher binding energy because of their highly electronegative oxygen environment.

Because of the short time scale of the photoelectron emission process, one normally assumes that the geometries in both the initial and the final states are identical. Under this assumption, we find that the calculated core level shift of C—H is underestimated by 6.6 eV compared to the experimental value. On the other hand, we find that the discrepancy with the experiment regarding this shift is not removed, but overestimated, if structural relaxation in the final state is allowed, i.e., in the presence of a core-hole. Moreover, the relative shifts between components appear to be less sensitive to the geometries assumed in the calculations. However, the real sample is not composed of isolated molecules and it could be that the intermolecular interaction in the real solid modifies the core levels significantly, for example by providing a modified screening environment.

At the high binding energy side of the main peak at 285.3 eV, three peaks with low intensity are also present and they are attributed to multielectron excitations: one at 287 eV, the second at 290 eV, and the third at 291.2 eV. During the fit, it was observed that the stoichiometric ratio of the carbon atoms in the aromatic part to those in the functional group, which is 5:1, is not reproduced by the corresponding peak areas. The molecular stoichiometry is reproduced only when the peaks at 287 and 291.2 eV are assigned to $\pi-\pi^*_{C=C}$ and the shoulder at 290 eV is assigned to $\pi-\pi^*_{C=O}$ shakeup satellites corresponding to core ionized final states in which an electron from the valence states is promoted from an occupied to an unoccupied level. The $\pi-\pi^*$ shakeup feature at 291.2 eV appears at a similar position as observed earlier[67,68] and is assigned to shakeup processes in the benzene ring. Therefore, it is reasonable to assign the shakeup feature with the highest binding energy to excitations in the aromatic ring.

On the basis of these observations, we used four components to fit the C_{1s} core level. These are assigned to (1) carbon atoms involved in C—H bonds, total number 8; (2) carbon atoms involved in *C*—C═O bonds (underlined), total number 4; (3) carbon atoms involved in *C*═C bonds, total number 8; (4) carbon atoms involved in *C*═O bonds, total number 4.

The main peaks (*C*—H, *C*—C═O, *C*═C, *C*═O) and satellites were described by Voigt functions having a constant W_L of 75 meV and variable W_G. The energy positions of all components were allowed to vary. The ratio of the peak areas was constrained according to the PTCDA stoichiometry. In Figure 17a, the result of the peak fit analysis of the C_{1s} of PTCDA is displayed. The corresponding residual plotted underneath the spectrum reveals the excellent quality of the fit. The energy positions, line widths, and relative areas of the peaks are summarized in Table 8.

The same fit procedure combined with DFT single molecule calculations was applied to the C_{1s} of DiMe-PTCDI (see Figure 18). The results of the fit for the C_{1s} core level of DiMe-PTCDI are summarized in Table 9.

Hardly any shift of the aromatic peak appears between PTCDA and DiMe-PTCDI. It has to be noticed, however, that the aromatic peak of DiMe-PTCDI presents a weak asymmetry at the high binding energy side. After a proper deconvolution, this can easily be assigned to the carbon atoms involved in the C—N bond.

As is the case for PTCDA, the well-separated features at higher binding energy can be attributed to the C atoms of

Table 8. Results of the Peak Fit Analysis of the PTCDA C_{1s} Spectrum in Figure 17a

	C-H	C-C=O	C=C	C=O	$\pi \rightarrow \pi^*_{C=C}$ (1)	π-$\pi^*_{C=O}$	$\pi \rightarrow \pi^*_{C=C}$ (2)
Energy / eV	284.6	285	285.3	288.6	287	290	291.2
W_G / eV	0.84	0.63	0.72	0.81	0.92	1.05	0.95
Rel. Area / %	33.4	16.7	30	11.5	2.4	5.9	1.3
W_L / eV	0.075	0.075	0.075	0.075	0.075	0.075	0.075
A_{C-H} : ($A_{C=C}$ + $A\pi$-$\pi^*_{C-C(1)}$ + $A\pi$-$\pi^*_{C-C(2)}$) : $A_{C-C=O}$: ($A_{C=O}$ + $A\pi$-$\pi^*_{C=O}$)= 8 : 4 : 8 : 4							

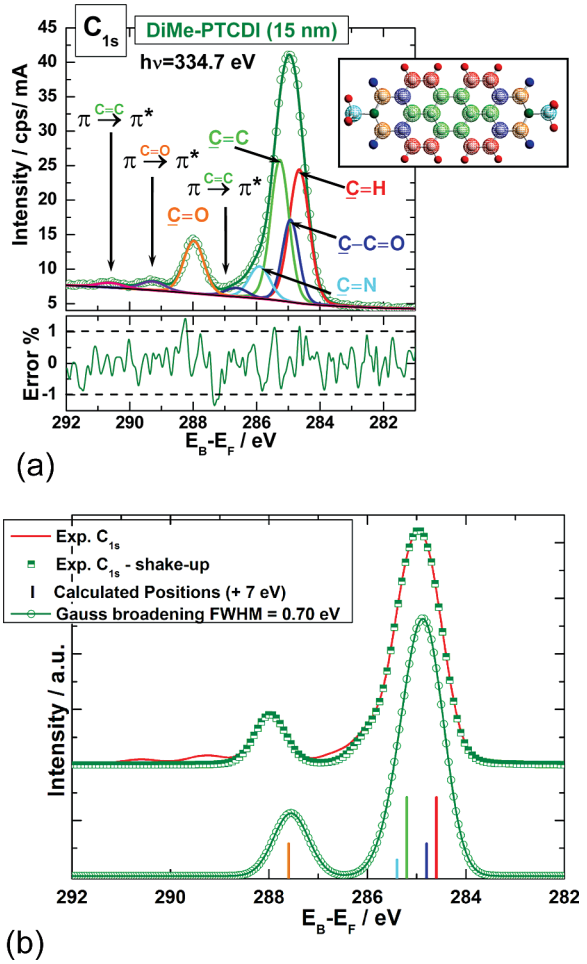

Figure 18. (a) Results of the peak fit analysis of the C_{1s} spectrum of DiMe-PTCDI thin films. The intensities are constrained by the stoichiometry of the atoms in DiMe-PTCDI to 8:4:8:2:4. The individual C_{1s} components of DiMe-PTCDI are assigned according to the color coding, and the corresponding residual is plotted underneath the spectrum. (b) Calculated positions of C_{1s} (vertical bars), and experimental, experimental with shake-up contributions subtracted, and simulated (using a W_G of 0.7 eV) spectra of C_{1s}.

the functional groups, i.e., the methylimide group in DiMe-PTCDI. Both the binding energy and the line shape of these structures, together with the corresponding shakeup features, vary significantly for the two molecules. From PTCDA to DiMe-PTCDI, the C=O peak maximum shifts by 0.6 eV toward lower binding energies. The replacement of the oxygen atom in the anhydride group by the less polar methylimide group leads to the smaller energy splitting between the components of the aromatic part and the functional group as a consequence of the higher electronegativity of oxygen compared to N−CH_3. Furthermore, it can be noticed that the satellite intensity strongly depends on the polarity of the functional group. The shakeup process is a result of an intramolecular charge transfer. Since in the $\pi-\pi^*_{C=O}$ shakeup process the charge is moved from the aromatic part acting like a donor to the accepting functional groups, the decrease in intensity of the $\pi-\pi^*_{C=O}$ satellite of DiMe-PTCDI compared to the $\pi-\pi^*_{C=O}$ one of PTCDA can easily be understood. In the case of PTCDA, the intensity of the $\pi-\pi^*_{C=O}$ is about 50% of the corresponding main line while, for DiMe-PTCDI, the intensity is decreased to about 30%.

2.5.2. O_{1s} and N_{1s} Core Levels

Additional information when analyzing XPES data is provided by the O_{1s} core level emissions of PTCDA and DiMe-PTCDI and by the N_{1s} core level emission of DiMe-PTCDI. The main lines and satellites of O_{1s} and N_{1s} were curve fitted using Voigt functions having a constant W_L of 120−160 meV and variable W_G. The energy positions of all components were allowed to vary. The ratio of the peak areas was constrained according to the PTCDA stoichiometry. In Figure 19, the result of the peak fit analysis of the O_{1s} of PTCDA is displayed. The corresponding residual is plotted underneath the spectrum. The energy positions, line widths, and relative areas of the peaks are summarized in Table 10a. The same fit procedure and DFT single-molecule calculations were applied to the O_{1s} emission of PTCDA as those for the C_{1s} emission, and the simulated O_{1s} emission is obtained using a W_G of 1.0 eV. The peaks at 531.5 and 533.5 eV are attributed to the main photoemission lines of the O=C and C−O−C atoms, respectively. At 533.2 eV an intense HOMO−LUMO shakeup satellite of the O=C peak is present.

Due to the replacement of the central oxygen atom in PTCDA by an N−CH_3 in DiMe-PTCDI, the O_{1s} spectra will exhibit only one contribution accompanied by a shakeup

Table 9. Results of the Peak Fit Analysis of the DiMe-PTCDI C_{1s} Spectrum in Figure 18a

	C-H	C-C=O	C=C	C-N	C=O	$\pi \rightarrow \pi^*_{C=C}$ (1)	π-$\pi^*_{C=O}$	$\pi \rightarrow \pi^*_{C=C}$ (2)
Energy / eV	284.6	285	285.3	285.9	288	287	290	291.2
W_G / eV	0.71	0.64	0.60	0.75	0.81	0.92	1.08	0.89
Rel. Area / %	30.7	15.6	27.5	7.7	11.8	2	3.4	1.2
W_L / eV	0.075	0.075	0.075		0.075	0.075	0.075	0.075
A_{C-H} : ($A_{C=C}$ + $A\pi$-$\pi^*_{C-C(1)}$ + $A\pi$-$\pi^*_{C-C(2)}$) : $A_{C-C=O}$: ($A_{C=O}$ + $A\pi$-$\pi^*_{C=O}$)= 8 : 4 : 8 :2: 4								

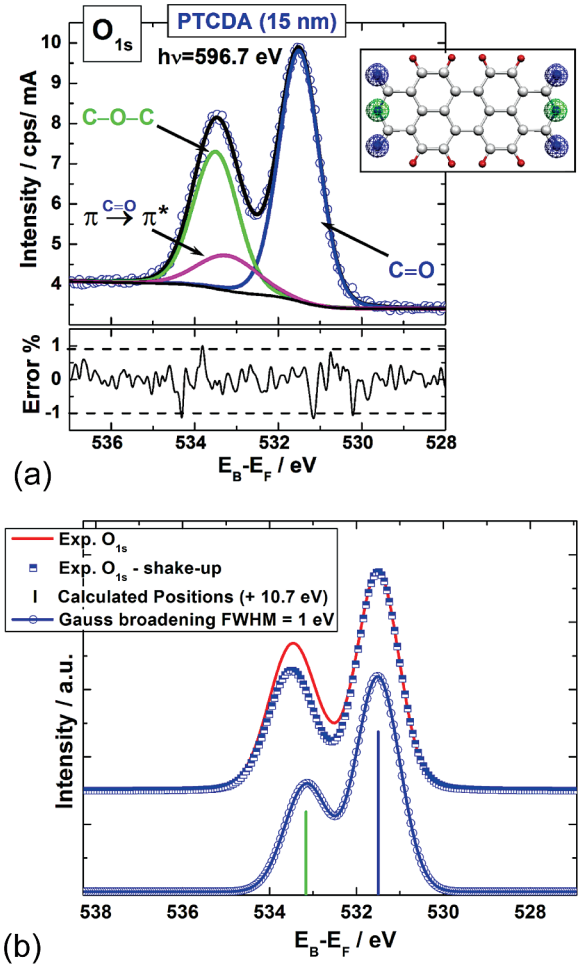

Figure 19. (a) Results of the peak fit analysis of the O_{1s} spectrum of PTCDA. The individual components of the O_{1s} core level emission of PTCDA are assigned according to the color coding, and the corresponding residual is plotted underneath the spectrum. (b) Calculated positions of the O_{1s} core levels (vertical bars) and the spectrum obtained by broadening each level with a Gaussian function with a fwhm of 1 eV (line plus open circles) compared to the experimental spectrum (continuous line) and to the experimental spectrum after subtracting the shake-up contributions (squares).

Table 10. Results of the Peak Fit Analysis of (a) the PTCDA O_{1s} Spectra in Figure 19a and (b) the DiMe-PTCDI O_{1s} and N_{1s} Spectra in Figure 20

(a)	C=O	C-O-C	π-π*C=O
Energy / eV	531.5	533.5	533.2
W_G / eV	1.06	1.16	1.63
Rel. Area / %	55	33	11
W_L / eV	0.12	0.12	0.12
$A_{C-O-C} : (A_{C=O} + A\pi-\pi^*_{C=O}) = 1 : 2$			

(b)	C=O	π-π*C=O
Energy / eV	531.5	533.2
W_G / eV	1.06	1.54
Rel. Area / %	85.7	14.3
W_L / eV	0.16	0.16

	C-N	π-π*C-N
Energy / eV	531.5	533.2
W_G / eV	1.01	1.4
Rel. Area / %	95	4.88
W_L / eV	0.14	0.14

satellite and the N_{1s} core level emission will appear. The core level emission spectra of N_{1s} and O_{1s} together with the peak fit analysis results are displayed in Figure 20a and b, respectively. The energy positions, line widths, and relative areas of the peaks are summarized in Table 10b.

As explained for the C_{1s} core level emission, the intensity of the $\pi-\pi^*_{C=O}$ shakeup satellite decreases from PTCDA to DiMe-PTCDI. Similar trends are observed for the shakeup satellites in the O_{1s} core level emission spectra. For the O_{1s} of PTCDA, the intensity of the $\pi-\pi^*_{C=O}$ shakeup is about

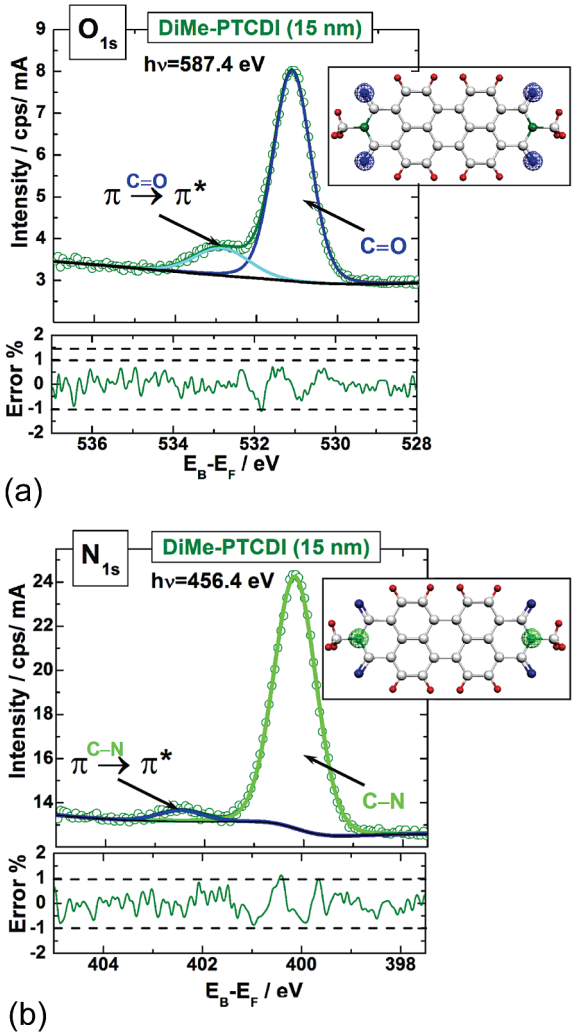

Figure 20. (a) Results of the peak fit analysis of the O_{1s} spectrum and (b) the N_{1s} spectrum of DiMe-PTCDI. The individual components for the O_{1s} and N_{1s} core level emission of DiMe-PTCDI are assigned according to the color coding, and the corresponding residual is plotted underneath the spectrum.

20% of the corresponding main line while, for DiMe-PTCDI, the intensity of the same shakeup is decreased to 16%. These results enforce the proposed interpretation that the intramolecular charge transfer during shakeup processes depends strongly on the strength of the electron-withdrawing functional groups. Moreover, these observations are consistent when compared with the core level emission of another perylene derivative, e.g., 3,4,9,10-perylenetetracarboxylic diimide (PTCDI),[66] where the central oxygen in the functional group is replaced by a somewhat more polar group than the methylimide group, namely an imide (i.e., N−H) group. Consequently, the analysis of these satellites may provide further information on multielectron excitations and can be taken into account for quantitative investigations.

High-resolution XPES spectra of condensed multilayers of five different molecules, including PTCDA, were reported by Schöll et al.[64] In their work, the size of the aromatic ring is systematically varied and the functional groups are identical, namely anhydride. The relative energy positions of the three different carbon atoms in the aromatic ring in ref 64 are different from the ones reported in this work. The energetic order with decreasing binding energy of the carbon lines in the C_{1s} peak proposed in ref 64 is C−C, C−H, and *C*═C═O while, in this review, we propose the following

order: C—H, *C*═C═O, and C═C. The difference may stem from the fact that the shakeup satellite intensities were not included in the fitting procedure performed in ref 64. The intensity of a shakeup satellite can be up to 20% of the corresponding intensity of the main line.[69] The appearance of shakeup satellites leads to a decrease in the intensity of the corresponding main line. The interpretation proposed here is supported by the DFT calculations presented above and by the calculations of the charges on the individual C atoms in the PTCDA molecule made by Chen et al.[70]

Similarly, in the O_{1s} spectra of PTCDA, the two clearly separated peaks were assigned to the two chemically different oxygen atoms in the anhydride functional group. The energy separation of the two peaks varies for different molecules, but a shakeup satellite is present at the side of the carboxylic oxygen toward higher binding energies. Even though the calculations clearly showed that the shakeup satellite is buried under the C—O—C photoemission peak, its energy position may be only ambiguously assigned. In this work, its energy position is taken at 2.32 eV relative to the C═O main line. However, a systematic study performed on different perylene derivatives with different functional end groups[66] revealed that the energy position of the same shakeup satellite is positioned at about 1.7 eV from the main line. Therefore, the value of 1.7 eV was considered for the $\pi-\pi^*_{C=O}$ satellite in this work.

2.6. Near-Edge X-ray Absorption Fine Structure (NEXAFS)

The NEXAFS spectra exhibit sharp structures below the ionization energy, IE, a steplike increase in absorption around the IE, and then broader structures above the IE. The sharp peaks observed below the IE correspond to transitions from a core level (e.g., 1s) to an π^* antibonding orbital of the molecule. Such transitions are named π^* *resonances*. A π^* resonance is only observed for the molecules with π bonding. In the π^* resonance, the final state lifetime is determined by the decay of the core-hole, which predominantly proceeds via Auger decay, accounted as a very short process. Above the IE, the K-shell spectrum exhibits the so-called σ^* resonances. The energy width of these resonances is related to the lifetime of the electronic state. The π^* resonances can be described by Lorentzian line shapes. Because of the increasing decay probability of the electron in the continuum states, σ^* resonances become broader the higher they lie in the continuum. Furthermore, these resonances are asymmetrically broadened by the vibrational motion of the atoms in the molecule. Since the σ^* orbitals are directed along the internuclear axis between two atoms, the energy position of these resonances is sensitive to the internuclear distance.

An interpretation of the NEXAFS spectral features of the molecules which are the object of this review can be given in comparison with NEXAFS data on NTCDA[71] and ANQ[72] and based on calculations for naphthalene.[73] Schöll et al.[74] explained the experimental spectrum of 1,4,5,8,-napthalenetetracarboxylic dianhydride (NTCDA) (see Figure 21) by various contributions of electronic transitions from the C_{1s} initial states of the four chemically different carbon atoms into the lowest unoccupied molecular orbitals (LUMO up to LUMO + 4). In Figure 21 the experimental spectra are plotted together with the result of a GSCF3 calculation for the electronic transitions of NTCDA. The calculated energies are shifted by −2.27 eV to align the first experimental and theoretical transitions. A comparison of the experimental and

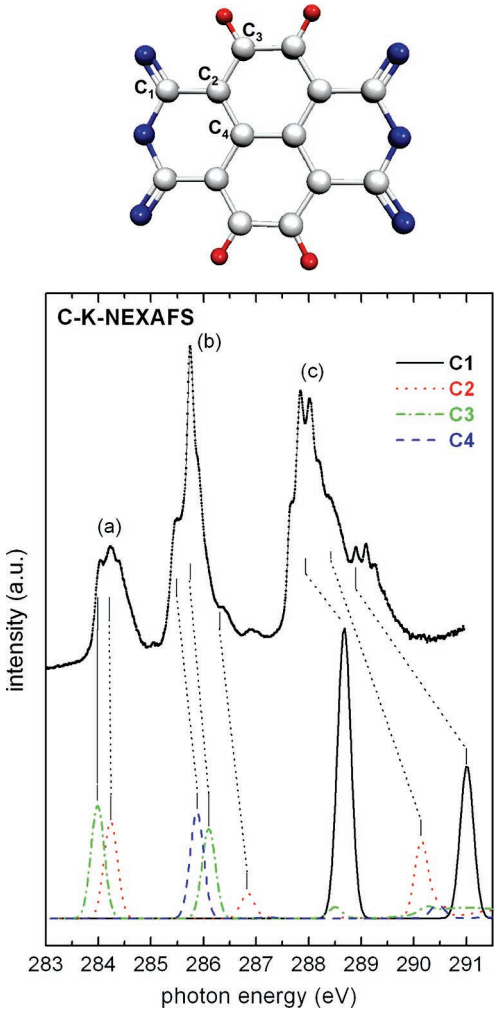

Figure 21. π^* region of the experimental C K-shell NEXAFS data of NTCDA compared with corresponding GSCF3 calculations (bottom). The calculated spectra were shifted in energy to align the transitions induced by the lowest photon energy. The inequivalent carbon atoms distinguished in the calculation are indicated in the inset, and their contributions to the spectrum are indicated by different line styles. Reused with permission from A. Schoell, Y. Zou, D. Huebner, S. G. Urquhart, Th. Schmidt, R. Fink, and E. Umbach, *Journal of Chemical Physics*, *123*, 044509 (2005). Copyright 2005, American Institute of Physics.

calculated data in Figure 21 reveals a "stretching" of the calculated energy scale, which is well-known for this and similar *ab initio* methods and originates due to overscreening of the core-hole in these calculations. Nevertheless, if the "energy stretch" is taken into account, the calculated spectra fit the experimental data very well and help to assign the different electronic transitions contributing to the observed spectral features. The assignment of the various calculated transitions to the different features in the experimental spectra is indicated in Figure 21 by different line styles. The first peak at about 284.05 eV corresponds to electronic transitions from the C—H and *C*═C═O 1s initial states into the LUMO. The next feature between 285.5 and 286 eV is attributed to electronic transitions from *C*═C and C—H 1s orbitals into LUMO + 1. The shoulder at 286.25 eV corresponds to electronic transitions from the *C*═C═O 1s initial state into LUMO + 1; therefore, the main feature can clearly be related to LUMO + 1.

As seen in Figure 22, π^* resonance structures similar to those of NTCDA are also observed for the C K-shell

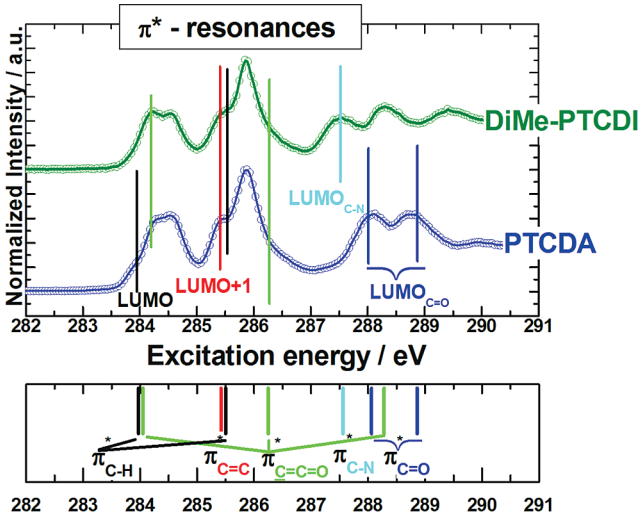

Figure 22. π^* resonance structures of PTCDA and DiMe-PTCDI together with the assignment of the features.

NEXAFS spectra of the molecules PTCDA and DiMe-PTCDI. For PTCDA transitions involving the carboxylic C atoms, contributions in the C K-edge can easily be recognized at 288 eV for $C_{1s} \rightarrow$ LUMO and at 288.9 eV for $C_{1s} \rightarrow$ LUMO + 1, respectively. It should be noted that the position and intensity of the C═O related features are slightly different for DiMe-PTCDI compared to PTCDA due to different contributions of anhydride groups attached to the C atoms in the carboxylic group. The transition present at 287.6 eV, labeled π^*_{C-N}, corresponds to the transition $C_{1s} \rightarrow$ LUMO involving the C atom bonded to the methylimide group. The lower energy position of this electronic transition can be understood by considering the higher electronegativity of O compared to that of $N-CH_3$.

3. Experimental Methods, Data Analysis, and Theoretical Calculations

3.1. Sample Preparation

3.1.1. Surface Preparation

The experiments described in this review focus on thin films of PTCDA and DiMe-PTCDI grown on GaAs(100) by organic molecular beam deposition.

Figure 23 schematically shows the procedures for the preparation of differently treated GaAs(100) surfaces. For the preparation of GaAs(100)-c(4×4) and Se-GaAs(100)-(2×1) surfaces, homoepitaxially grown n-type GaAs(100) layers (Si doped, $n = 1 \times 10^{18}$ cm^{-3}) capped with a thick amorphous As layer were used. By gentle annealing of the substrate at 380 °C in ultrahigh vacuum (UHV), the c(4×4) surface reconstruction was obtained. In order to prepare the Se-GaAs(100) surface, the GaAs(100)-c(4×4) surface was exposed to a beam of Se obtained by the decomposition of $SnSe_2$ from a Knudsen cell. During the Se exposure, the sample was kept at 400 °C. This treatment results in a (2×1) reconstructed surface.[75]

Te- or Si-doped n-type epi-ready GaAs(100) (Freiberger Compound Materials GmbH, $n = 2 \times 10^{17}$ or (1.8−2.7) ×

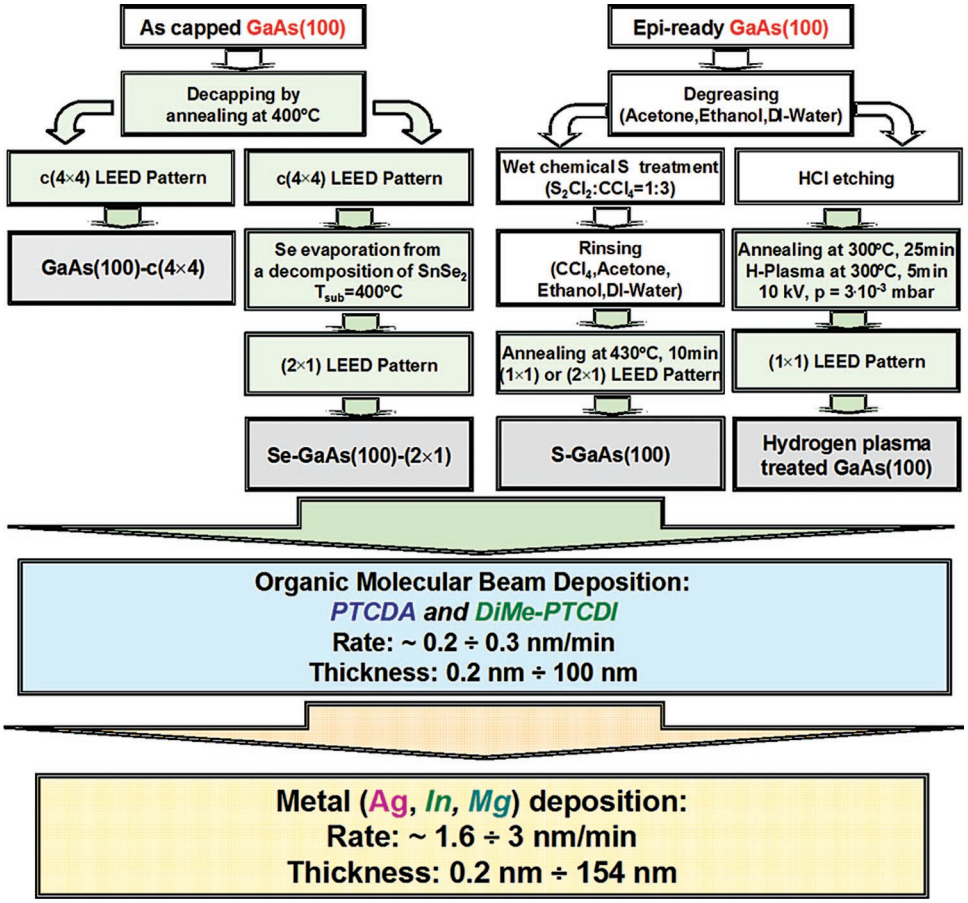

Figure 23. Schematic diagram of the procedures used for the preparation of differently treated/reconstructed GaAs(100) surfaces and the parameters used for the subsequent deposition of organic molecules and metals. Processes performed in UHV are represented by shaded boxes.

10^{18} cm^{-3}) was used for the preparation of S-GaAs(100) and H-plasma treated GaAs(100) surfaces. The samples were first degreased in an ultrasonic bath with acetone, ethanol, and DI-water in sequence for 5 min each and dried in a nitrogen flow. The sulfur-terminated GaAs(100) surfaces were obtained by dipping the GaAs wafers into a solution of $S_2Cl_2/CCl_4 = 1:3$, followed by rinsing first in CCl_4 and then again in acetone, ethanol, and DI-water. After the treatment, the sample was quickly introduced into the UHV chamber and annealed at 430 °C. The last step removes the excess sulfur. The resulting sulfur-passivated GaAs(100) surfaces, from now on denoted as S-GaAs, exhibit 2×1 surface reconstructions. For the hydrogen-plasma-treated GaAs(100) surface, after the degreasing process, the samples were first dipped into a 40% HCl solution in order to remove the native oxide from the surface. A H-plasma was obtained by the decomposition of H_2 gas under high voltage (10 kV) at 3×10^{-3} mbar pressure. The H-plasma treatment was performed for 5 min at a sample temperature of 300 °C.

3.1.2. Organic Molecular Beam Deposition (OMBD)

The PTCDA material was purchased from Lancaster Synthesis while the DiMe-PTCDI material was purchased from Sensient Imaging Technologies GmbH (former SynTec GmbH). Each material was further purified by double sublimation at 310 °C for PTCDA and 300 °C for DiMe-PTCDI under high vacuum (~10^{-6} mbar) and then filled into a quartz crucible mounted in a Knudsen cell. Before the evaporation of the organic material, the Knudsen cell was thoroughly degassed for a few hours at 200 °C. Organic thin films were prepared using OMBD from the Knudsen cells operated at approximately 280 °C for the two organic materials. During OMBD, the GaAs(100) substrates were kept at room temperature. The organic films were deposited at a rate of ~0.2 nm/min, as monitored by a quartz crystal microbalance located in the vicinity of the sample. A calibration of the microbalance was performed by correlating the frequency shift to the thickness determined by means of atomic force microscopy (AFM). The thickness of the organic coverage varies from submonolayer to 120 nm thick films. For the PES and IPES measurements, the thickness of the organic film did not exceed 15 nm. Such thickness was chosen in order to avoid sample charging effects. We define the thickness of one monolayer (ML) as the amount of PTCDA molecules (7.6×10^{13} cm^{-2}) that cover the entire surface, assuming flat-lying PTCDA molecules: 1 ML ≅ 0.32 nm.

3.1.3. Metal Deposition

The metals were evaporated from boron-nitride Knudsen cells kept at 380 °C for Mg, 830 °C for In, and 930 °C for Ag onto the organic films. Prior to use, all evaporation sources were thoroughly degassed. The metal was deposited at a rate of approximately 1.6 nm/min for Ag and 2 nm/min for In and Mg, in a stepwise manner. The amount of metal deposited onto the sample was monitored using a quartz crystal microbalance.

3.2. Experimental Methods and Data Analysis

3.2.1. Electron Spectroscopic Methods

The methods employed to obtain information about occupied and unoccupied states are outlined and illustrated schematically in Figure 24. Cases a and b involve prompt

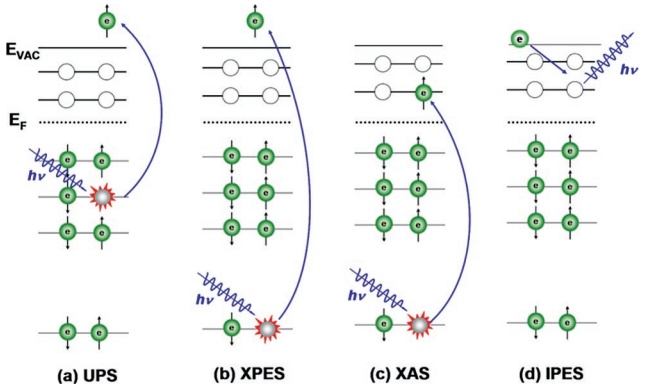

Figure 24. Schematic picture of radiation absorption and emission in the frame of a molecule as probed by the electron spectroscopic techniques involved in this review.

transitions from occupied states into continuum states. An ultraviolet (UV) (a) or X-ray (b) photon excites valence and core level electrons, respectively, to be emitted from the system as free electrons. The respective techniques are called valence band photoemission spectroscopy (VB-PES) or ultraviolet photoemission spectroscopy (UPES) and X-ray photoemission spectroscopy (XPES), respectively. The spectra are related to the density of occupied states (DOOS). The electronic transition displayed in Figure 24c takes place from a core state to an unoccupied state and is the keystone of X-ray absorption spectroscopy (XAS) experiments. In many cases, the spectra are directly related to the density of unoccupied states (DOUS). In principle, an XAS spectrum can be divided into two different regions.[76] The region interesting for us is the so-called "near-edge region" where the electron is excited into unoccupied states in the vicinity of the absorption edge. This region ranges from about 5 eV below the IE to about 15 eV above the IE and is called near-edge X-ray absorption fine structure (NEXAFS). A tunable X-ray source is required, and generally the experiments are performed using synchrotron radiation.

By variation of the photon energy $\hbar\omega$, the absorption into different unoccupied states is probed. The state-dependent absorption cross section σ_{NEXAFS} is described by eq 12:[76]

$$\sigma_{\mathrm{NEXAFS}} = \frac{4\pi e^2\hbar^2}{m^2}\frac{e^2}{\hbar c}\frac{1}{\hbar\omega}\left|\langle \mathrm{f}|\vec{e}\cdot\vec{p}\,|\mathrm{i}\rangle\right|^2\rho_{\mathrm{f}}(E)\,\delta(E_{\mathrm{f}} - E_{\mathrm{i}} - \hbar\omega) \propto \left|\frac{\vec{E}}{|\vec{E}|}\langle \mathrm{f}|\vec{p}\,|\mathrm{i}\rangle\right|^2\rho_{\mathrm{f}}(E)\,\delta(E_{\mathrm{f}} - E_{\mathrm{i}} - \hbar\omega) \quad (12)$$

Here, $|i\rangle$ and $|f\rangle$ denote the initial and final state, respectively, $\vec{p}$ is the linear momentum operator, $\vec{E}$ is the electric field vector, and $\rho_f(E)$ is the density of final states. The equation describes a number of characteristics of the method important for the interpretation of NEXAFS data: (1) The matrix element $\langle f|\vec{p}|i\rangle$ necessitates an overlap between the core level involved and the unoccupied orbital. Therefore, NEXAFS is a local probe; that is, it measures the unoccupied states at the site of the core level. (2) For NEXAFS, the dipole selection rule $\Delta l = \pm 1$ must be fulfilled. For excitations from the 1s orbital, only states with a component of p character at the excitation site are probed. (3) The scalar product of $\vec{E}$ and $\vec{p}$ gives rise to an angular dependence of the cross section that can be used to determine molecular orientation.

Hence, since the process is local and governed by dipole selection rules, NEXAFS probes the partial density of unoccupied states (PDOUS). A complementary technique to

NEXAFS is inverse photoemission spectroscopy (IPES), which samples all the unoccupied states.

In IPES, electrons from a monochromatic electron beam relax into unoccupied states with simultaneous emission of UV radiation. This process is depicted in Figure 24d.

In all the PES, NEXAFS, and IPES experiments, the sample preparation and the analysis are performed in separate UHV chambers (typical base pressure 2×10^{-10} mbar) which are interconnected such that the sample transfer takes place without breaking the vacuum. The measurements were performed either in Chemnitz or at the Berliner Elektronen-speicherring-Gesellschaft für Synchrotronstrahlung m.b.H (BESSY) in Berlin.

All soft X-ray PES, VB-PES, and NEXAFS experiments were performed at BESSY at the Russian-German Beam Line (RGBL) using a plane-grating monochromator. The angular resolved NEXAFS spectra of the DiMe-PTCDI/S-GaAs(100) system were recorded in total yield mode. The incidence angle was varied between normal incidence (0°) and near-grazing incidence (70°). For normalization purposes, spectra of GaAs substrates were used as reference.

The PES and NEXAFS experiments involving Mg and In deposition onto PTCDA and DiMe-PTCDI were performed at BESSY using the MUSTANG experimental station connected to RGBL. For a detailed description of this system, see ref 66. The station is equipped with a Phoibos 150 analyzer (SPECS GmbH). The photon energies for PES measurements were selected to enhance the surface sensitivity. The overall experimental resolution was 70 meV for the Mg_{2p} and In_{4d}, 85 meV for the C_{1s}, 100 meV for the N_{1s}, and 140 meV for the O_{1s} photoemission spectra at photon energies of 100, 335, 450, and 585 eV, respectively. The C K-edge NEXAFS measurements were performed by sweeping the excitation energy between 280 and 320 eV and recording the electrons having a selected kinetic energy of 6 eV.

The VB-PES experiments of the organic film growth were performed in Chemnitz using an ARUPS 10 system. The overall resolution of the spectrometer determined using a polycrystalline Ag(111) film grown on hydrogen-passivated Si(111) surfaces is 0.15 eV for the He I line (21.22 eV). All the VB-PES spectra taken using ARUPS 10 were recorded in normal emission mode.

The IPES experimental setup working in the isochromat mode is a "home"-built system. The IPES setup consists of two main components: the low-energy electron gun and the Geiger−Müller detector, which are mounted on a CF 160 mm flange. The fixed-energy photon detector[77] consists of a Geiger−Müller tube with a magnesium fluoride (MgF_2) window filled with a gas mixture containing ethanol and argon. The ionization energy of ethanol and the transmission function of the MgF_2 provide a value of 10.9 eV as the nominal detection energy of the detector. A low-energy electron gun[78] was used to produce a monoenergetic electron beam. The overall IPES instrumental resolution, estimated from the width of the Fermi edge measured on a clean polycrystalline nickel sample, is 0.4 eV. All the IPES spectra were recorded at normal incidence of the electron beam with a current density in the range of 10^{-6} A/cm^2. At these values of the current density, the reproducibility of the data taken from different samples was better than 98%. The IPES spectra were averaged over a large number of scans (i.e. 40 scans). A comparison between the average of the first scans and that of the last scans (i.e. 10 scans) showed no significant difference. Moreover, a comprehensive IPES study dealing with the characterization of the interface formation between phthalocyanine materials and hydrogen-passivated silicon[79−81] also shows a good reproducibility of data. All spectra were measured and reproduced at the range of the current density mentioned above, indicating that this value is low enough to cause no damage of the organic film.

3.2.2. Raman Spectroscopy

In its classical description, Raman scattering is treated as the radiation of light produced by a time-dependent dipole $M(t)$ which is induced in a molecule by the incident electromagnetic light and is modulated by the molecular vibrations. The highly monochromatic incident light required in Raman spectroscopy is provided by laser sources having a light frequency ν_L usually much larger than the vibrational frequency ν_j involving the motions of nuclei. Therefore, only electrons can respond to the external electromagnetic field. The dipole moment induced in the molecule can be written as

$$M(t) = \alpha(t)\, E(t) + {}^1/_2\beta(t)\, E^2(t) + ... \qquad (13)$$

Here $E = E_L \cos(2\pi\nu_L t)$ is the electric field component of the incident light (with the amplitude E_L), α is the electronic polarizability of the molecule (or susceptibility in inorganic crystals), and β is the hyperpolarizability, which is responsible for the hyper-Raman effect.

In general, the direction of the induced dipole M does not coincide with that of the electric field. Therefore, the polarizability in the relation $M = \alpha E$ must be a second-rank tensor:

$$\begin{pmatrix} M_x \\ M_y \\ M_z \end{pmatrix} = \begin{pmatrix} \alpha_{xx} & \alpha_{xy} & \alpha_{xz} \\ \alpha_{yx} & \alpha_{yy} & \alpha_{yz} \\ \alpha_{zx} & \alpha_{zy} & \alpha_{zz} \end{pmatrix} \begin{pmatrix} E_x \\ E_y \\ E_z \end{pmatrix} \qquad (14)$$

The matrix constructed with the elements of the polarizability tensor derived with respect to the normal coordinate q_j of vibration j is denoted as the Raman tensor or scattering tensor:

$$\delta\alpha^j = \begin{pmatrix} \alpha^j_{xx} & \alpha^j_{xy} & \alpha^j_{xz} \\ \alpha^j_{yx} & \alpha^j_{yy} & \alpha^j_{yz} \\ \alpha^j_{zx} & \alpha^j_{zy} & \alpha^j_{zz} \end{pmatrix} q_j \qquad (15)$$

Taking into consideration the wave−particle duality of light, Raman scattering processes involve at least two quanta acting instantaneously (scattering time is on the order of 10^{-14}−10^{-15} s) with the conservation of energy and momentum between the initial and final states of the light−matter system:

$$h\nu_L = h\nu_S \pm h\nu_j(k_j) \qquad \text{energy conservation} \qquad (16)$$

$$\vec{k}_L = \vec{k}_S \pm \vec{k}_j \qquad \text{momentum conservation} \qquad (17)$$

Here $h\nu_{L,S}$ and $\vec{k}_{L,S}$ are the energy and momentum of the incident (L) and scattered (S) light. $h\nu_j$ and $\vec{k}_j$ are the energy and momentum related to a transition between the vibrational states of a normal vibration j. For a visualization of the energy diagram of the processes, see Figure 25.

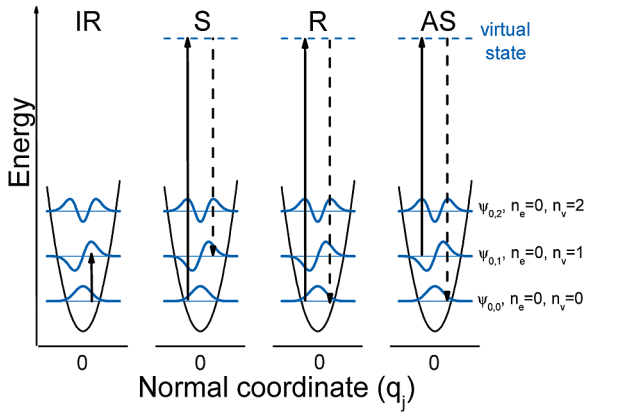

Figure 25. Comparison of energy diagrams for infrared absorption (left diagram), and scattering processes: Raman Stokes (S), Rayleigh (R), and Raman Anti-Stokes (AS). Each energy level of the harmonic oscillators is labeled with the electronic quantum number (n_e) and the vibrational quantum number (n_v).The energies of the exciting and emitted photons are indicated by a continuous arrow and by a dashed arrow, respectively.

In an elastic Rayleigh scattering process, a photon having the same energy as the incident one is emitted and the molecule/crystal remains in the initial vibrational state. In the case of an inelastic Raman process, the energy of the emitted photon is not the same as that of the impinging one and there is a net change in the vibrational state of the molecule. The Stokes process brings the molecule into a higher vibrational state, and the energy of the emergent photon is lower than ν_L (see Figure 25). During the anti-Stokes process, the molecule suffers a transition to a lower energy vibrational state and the emitted photon has a higher energy compared to the incident one. Typically, the intensity of the Rayleigh line is about 10^{-3} of the incident light intensity, while the Raman bands are at least another factor of 10^3 weaker. As the population of the ground vibrational state is higher by a Boltzmann factor compared to that of the first excited state, Stokes processes are more probable than anti-Stokes ones.[82] Therefore, the more intense Stokes Raman spectrum on the low-energy side of the exciting line is usually recorded.

The broadening of the Rayleigh band is dominated by the spectrometer resolution and can thus serve for the determination of the experimental resolution. The line shape of a Stokes/anti-Stokes band originates from the limited lifetime of the vibrations convoluted with the instrumental resolution. Generally, it can be described by a Lorentz function convoluted with a Gaussian function. When the width of the Gaussian function is small enough, the line shape of Raman bands can be approximated by a Lorentz function. Unless otherwise specified, the Raman spectra throughout this work were fitted with Lorentzian functions using a least-square error algorithm.

The samples investigated by means of Raman spectroscopy were prepared in a UHV chamber (base pressure of 2×10^{-10} mbar) that serves also as the analysis chamber. It is optically coupled to a Raman spectrometer, allowing *in situ* measurements and on-line growth monitoring to be performed. The Raman spectra shown in this work were excited with the 488 nm (2.54 eV) emission line of an Ar^+ laser. The scattered light was collected with a Dilor XY 800 triple monochromator operated in subtractive mode and equipped with a multichannel charge coupled device detector. The spectral resolution ranged from 2 to ~3.5 cm^{-1}, as determined from the fwhm of the Rayleigh line.

For the *in situ* measurements, the angle between the incident and scattered light is fixed by the position of the corresponding UHV windows. The sample surface was always oriented parallel to the collection window; that is, the scattered light was collected in the direction parallel to the sample normal. The incidence angle was 30°. The diameter of laser light focused on the sample was ~300 μm, and the collection angle was ~18°.

Ex situ measurements were realized in two back-scattering geometries: the *micro*- and *macro*-configurations. In the micro-configuration, an Olympus BH-6 microscope is used. This experimental setup realizes a backscattering geometry, with both the incident and the scattered beams passing the microscope objective. For the microscope objective used (×100), the focus size on the sample is ~0.8 μm^2. This geometry was employed for investigations of single crystals. In the *ex situ* macro-configuration geometry, the focus size on the sample is comparable to the one for the *in situ* macro-configuration. An advantage of the macro-configuration resides in a small collection angle (~18°), which reduces significantly the depolarization effects encountered in micro-Raman measurements.[83]

The laser power for the *in situ* measurements was measured in front of the UHV window. Typical power values were in the range from 50 to 100 mW for the *in situ* measurements and 30 mW for the *ex situ* macro-configuration. For micro-measurements, the power measured under the microscope objective was at most 0.1 mW. The power densities lie below the damage threshold of the absorbing PTCDA and DiMe-PTCDI films and crystals in all configurations used.

Two polarization configurations were used in the present work. The polarization of the analyzer was always kept the same, and only the polarization of the incident light was rotated. For example, in the *in situ* measurement case, "crossed polarization" means that the electric field vector of the incident light was in the plane of incidence and the electric field vector of the analyzed scattered light was perpendicular to it; "parallel polarization" means that both electric field vectors are perpendicular to the plane of incidence and, hence, parallel to the sample surface. If the polarization configuration is not specified in the text, it means that the polarization of the scattered light was not analyzed.

Since the incidence angle for the *in situ* measurements is rather small (30°) this quasi-backscattering geometry, the polarization configuration will be denoted in all cases according to the Porto notation, i.e., $z(yx)\bar{z}$ and $z(xx)\bar{z}$ for the parallel and perpendicular polarization configurations, respectively. Here z and $\bar{z}$ indicate that the directions of the incident and analyzed scattered light, respectively, are parallel to the sample surface normal, while x and y denote the directions of the electric field vectors of the incident and analyzed scattered light, respectively.

3.2.3. Data Analysis: Electron Spectroscopic Methods

Figure 26 shows an example of the procedure for the determination of energy level alignment at organic/inorganic interfaces. Typical VB-PES spectra of an inorganic (solid lines, top) and an organic (unfilled squares, bottom) solid are shown on the left side of Figure 26, while the right side of the same figure shows typical IPES spectra of an inorganic (solid lines, top) and an organic (unfilled squares, bottom) solid. The spectra consist of a number of well-defined features related to the density of occupied and unoccupied

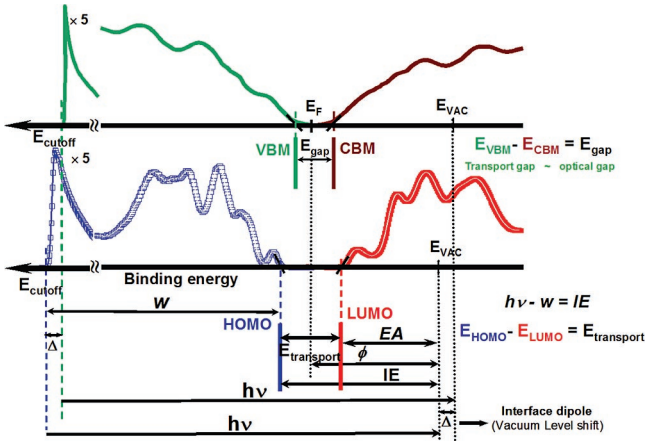

Figure 26. Exemplary VB-PE and IPE spectra of an inorganic solid (upper panel) and of a thin organic film (lower panel) used to define the quantities relevant for this review.

states of the solids and a low-energy secondary electron peak resulting from inelastically scattered electrons. E_{HOMO} corresponds to the edge of the HOMO peak toward lower binding energy, similar to E_{VBM}. E_{LUMO} corresponds to the edge of the LUMO peak toward higher binding energy, similar to E_{CBM}.

The position of the vacuum level E_{VAC} is determined from the low kinetic energy edge of the secondary electron peak when a bias of −10 V is applied to the sample. A shift in the photoemission cutoff at an interface provides information on interface dipoles between two materials. The ionization energy, IE, is determined by subtracting the total width of the spectra—measured from the low kinetic energy onset/cutoff E_{cutoff} to E_{HOMO} or E_{VBM}—from the photon energy.

The energy resolution of a VB-PES measurement is about 80 meV when using synchrotron radiation and 150 meV when using the He I discharge lamp. For the VB-PES spectra, no deconvolution of the instrumental broadening was performed, since the instrumental resolution is much smaller than the width of the spectral features.

Before fitting the IPES data, a background described by a cubic polynomial function was subtracted. The IPES data were then fitted with Gaussian functions using a nonlinear least-square fitting technique. Due to the rather poor instrumental resolution of the IPES ($\Delta E = 0.4$ eV), the widths of the fitted peaks were then corrected for the instrumental broadening using the following formula:

$$\mathrm{fwhm}_{\mathrm{deconv}} = \sqrt{\mathrm{fwhm}_{\mathrm{exp}}{}^2 - 0.4^2}$$

The HOMO and LUMO require special attention when evaluating their positions on the energy scale, and a detailed description is presented in section 5—Characterization of Thin Films. However, in analogy with inorganic semiconductors and after a proper deconvolution of the IPES spectra, the HOMO and LUMO energy positions (edges) are determined from the intercept of two linear extrapolations. One is describing the background, and the second one is a tangent to the most prominent band edge in the inflection point. From the edge-to-edge distance between the HOMO and LUMO features, the transport gap of an organic material can be obtained, as depicted on the left-hand side of Figure 27.

The following information on the electronic properties can be derived from the combination of direct and inverse photoemission measurements: (1) the position of the valence band maximum of an inorganic semiconductor and of the highest occupied molecular orbital (HOMO) of the organic semiconductor, as well as the ionization energy calculated as the difference between the vacuum level and the position of the VBM/HOMO; (2) the dipole between the two materials at their interface; (3) the position of the conduction band minimum of an inorganic semiconductor and the lowest unoccupied molecular orbital (LUMO) of the organic semiconductor and the electron affinity as the difference between the vacuum level and the position of the CBM/LUMO; (4) the energy offset between the HOMO (LUMO) and the VBM (CBM); (5) the transport gap of an inorganic semiconductor and of an organic semiconductor as the energy differences $E_{VBM} - E_{CBM}$ and $E_{HOMO(edge)} - E_{LUMO(edge)}$, respectively.

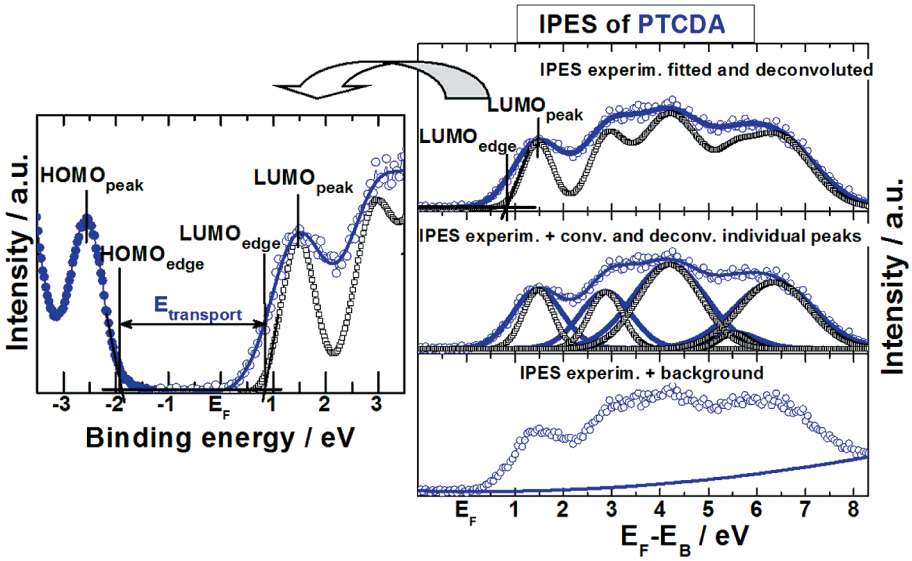

Figure 27. Schematic of the procedure used for the determination of the energetic transport gap from the PE (line plus full circles) and IPE (line plus empty circles) spectra on the example of a PTCDA thin film (left panel). The steps of the deconvolution process (see text for details) can be visualized in the right panel. The contribution of the individual peaks to the overall intensity of the measured IPES data is plotted with thick lines, and the deconvoluted contributions are plotted with open squares.

3.3. A Short Introduction to Density Functional Theory (DFT)

3.3.1. DFT Methods

In calculating the total energy of molecules, density functional theory (DFT) methods have become very popular due to the high level of accuracy in predicting observables at much lower computational cost compared with other methods such as Hartree−Fock theory. In density functional theory, the electron−electron interaction is described by the exchange-correlation functional, which includes terms accounting for both the exchange energy and the electron correlation. The latter one is entirely neglected in Hartree−Fock theory.

The exchange-correlation functional includes integrals of some function of the electron density (ρ), $E_{xc}(\rho)$. As Kohn and Sham pointed out,[84] these integrals have to be solved iteratively and the Kohn−Sham equations are exact only if $E_{xc}(\rho)$ is known precisely. Usually, this $E_{xc}(\rho)$ term is divided further into separate exchange $E_x(\rho)$ and correlation $E_c(\rho)$ components.[85]

One approximation which assumes that the exchange energy is only dependent on the charge density (ρ) and not its gradient is the local density approximation (LDA). An extension of the limits of this approximation by including the gradient dependence of the exchange energy was published by Becke in 1988.[86] His semiempirical approach leads to the so-called E_X^{B88}, a widely accepted and commonly used gradient-corrected exchange energy functional.

A more accurate approach to the correlation term $E_c(\rho)$ is based on the work by Colle and Salvetti, who expressed the correlation energy as a functional of the electron density and of the second-order Hartree−Fock density matrix.[87] Lee, Yang, and Parr then restated this as a functional of the charge density as well as of the gradient and the Laplacian of the density ρ.[88] The functional includes both local and nonlocal terms and is known as the correlation functional E_C^{LYP}.

Names for the various pure DFT models are given by combining the names for the exchange and correlation functionals. The combination of the Becke exchange functional and the LYP correlation functional into the Kohn−Sham formalism results in the BLYP theory. Nevertheless, for a given observable, the prediction by BLYP theory typically introduces a systematical error to the opposite direction from that in Hartree−Fock calculations. For example, BLYP tends to overestimate bond lengths while Hartree−Fock underestimates these. This motivated the development of hybrid density functionals which include a mixture of Hartree−Fock exchange and DFT exchange-correlation. Becke first proposed a half and half mixing ratio,[89] which was soon replaced by a three parameter mix, resulting in the B3LYP hybrid functional. The good accuracy at comparably low computational cost makes B3LYP probably the most commonly used functional of modern density functional theory.[90]

Pure DFT methods (i.e., without any Hartree−Fock exchange) tend to give HOMO−LUMO gaps that are too small. HF methods, on the other hand, overestimate the HOMO−LUMO gaps. Consequently, the accuracy of the calculations is increased when using the hybrid functionals. Nevertheless, the common drawback in predicting the band gap of materials, and along with it the energy positions, is still present.

As already mentioned in section 2.4—Electronic Properties: Valence Band Structures, the ground state electronic and vibrational properties of single molecules[57,91] such as PTCDA and DiMe-PTCDI using DFT on the B3LYP level can be calculated with rather good accuracy. Even though the calculated occupied and unoccupied electronic states were rigidly shifted to match the experimental data and the vibrational frequencies were slightly overestimated, the trends in the calculated values were found to be satisfactory for understanding some physical phenomena. Several quantum-chemical methods showed that a good accordance between the energy scales of the experimental and calculated data is not necessary for achieving a good match between the experimental and theoretical line shapes[92,93]

3.3.2. Basis Sets

A common approximation is the expression of the molecular orbitals as a linear combination of atomic orbitals (LCAO). These molecular orbitals are the weighted sum of the basis functions ϕ_μ:

$$\psi_i = \sum_{\mu=1}^{N} C_{\mu,i}\phi_\mu \tag{18}$$

with the molecular expansion coefficients C_μ. Nowadays, essentially two general classes of basis sets are used. The more accurate, but also the more costly in the computation of the integrals, is the one based on the atomic orbitals proposed by Slater.[94] A very successful compromise between computational cost and accuracy is offered when *contracted Gaussians* are used:

$$\psi_i = \sum_{\mu=1}^{N} C_{\mu,i}\left(\sum_p d_{\mu,p} g_p\right) \tag{19}$$

The contraction coefficients $d_{\mu,p}$ are usually fixed constants within a basis set while g_p are primitive Gaussian functions having different forms and used to approximate the molecular orbitals.[85] They are very flexible in the sense that if higher precision is needed, one can increase the degree of contraction (i.e., the number of primitive Gaussians per basis set) at the cost of increased computation time. An additional correction, which also comes at the cost of increased computational expense, is the usage of split-valence sets, meaning that a number of differently sized basis sets are used to describe the valence orbitals. As an example, for a given molecule composed only of hydrogen and carbon atoms, the MOs are described as follows: a set of three Gaussian functions is used to represent/describe the inner shells while the valence shells are represented by two sets, one of two Gaussians, and one of only one Gaussian function. The common notation for such a representation of MOs is 3-21G. The number of Gaussians representing the inner shells can be increased to six, and the split valence shells can be increased to sets of three Gaussians and one Gaussian. The notation for this type of basis set is 6-31G. Following the same principle, triple split valence sets such as 6-311G can further improve the precision of calculations. A further, commonly used improvement of the basis functions allows some degree of mixing between unfilled orbitals and the valence shells. The orbitals derived from such *polarized* basis sets are enabled to change not only in size, as in pure split valence basis sets, but in shape as well. The notation 6-311G-

(d,p) describes a basis set where p-like functions are added to hydrogen atoms and d-type functions are added to the heavier atoms. The last addition to the basis sets is the so-called *diffuse functions*. These are large size versions of s- and p-type functions. By adding these, one enables the valence orbitals to span larger areas in space. This addition is needed for systems with highly delocalized electrons.[86] Usually basis sets with added *diffusion functions* are referred to by 6-311G+(d,p) for diffuse functions added to heavier atoms and 6-311G++(d,p) for diffuse hydrogen and heavier atom sets.

3.3.3. Simulation of Occupied and Unoccupied Electronic Levels: TDOOS and PDOOS Formalism

In this review, the densities of states (DOS) are simulated using DFT molecular orbital calculations. These calculations were performed using the Gaussian 98 package[51] with the B3LYP method and the 6-311++G(d,p) basis set to describe the core orbitals and the inner and outer parts of the valence orbitals. The geometric structures of the molecules under study were determined by performing optimization with the standard gradient technique in the same Gaussian 98 package.[51] Moreover, the densities of states (DOS) were projected onto constituent atoms and atomic orbitals in order to deduce how the individual atoms contribute to the total electronic structure or total density of states (TDOS) in this case.

The total density of occupied states (TDOOS) is formulated as

$$N(E) = \sum_{p} N_p(E) \tag{20}$$

where $N_p(E)$ is the partial density of occupied states (PDOOS) in atom p and is given by

$$N_p(E) = \sum_{\mu \in \rho} N_{p,\mu}(E) \tag{21}$$

and $N_{p,\mu}(E)$ is

$$N_{p,\mu}(E) = \sum_{i} N^{i}_{p,\mu}(E) \tag{22}$$

where $N^{i}_{p,\mu}(E)$ is the contribution of the i-th molecular orbital from the μ-th atomic orbital of the p-th atom. Its value is proportional to the Mulliken population of the μ-th orbital. Analyzing the contribution of the electronic states from the individual atoms to a particular molecular orbital is a suitable method to obtain the localization of the states and the chemical properties of the atoms. The TDOOS and PDOOS were calculated, based on the output coefficient matrix of the wave functions from the Gaussian 98 package in combination with the AOMix[62] program.

The calculated binding energies of each MO state for a single molecule are convoluted using Gaussian functions with the fwhm adapted to the experimental line widths. Since the densities of states (DOS) can be projected onto constituent atoms and atomic orbitals using AOMIX, the photoelectron intensity at a certain photon energy can be calculated if the values of the photon energy-dependent cross section of the atomic orbitals tabulated by Yeh and Lindau[95] are included. However, for simplicity, no photoionization cross section is included in the calculations. The calculated spectrum is then rigidly shifted in order to match the HOMO or the LUMO energy with the first experimental peak.

3.3.4. Calculation of Vibrational Frequencies

Vibrational frequencies are computed by determining the second derivatives of the energy with respect to the Cartesian nuclear coordinates and then transforming to mass-weighted coordinates. In general, DFT methods slightly overestimate vibrational frequencies.[57] Therefore, it is common practice to introduce scaling factors for the frequencies of 0.95−0.99 in order to get a lower root-mean-square error between calculated and experimental modes. However, in some cases, calculated modes can match experimental values or even underestimate them slightly. As the situation is rather complicated for oxygen-containing compounds such as PTCDA and DiMe-PTCDI, no general scaling for the calculated mode frequencies was performed. The relative order of the Raman-active and IR-active modes calculated using the 6-31G(d) basis set corresponds better to the ordering of the experimental frequencies. However, the smaller 3-21G basis set results in the best agreement with the experimental findings in terms of the root-mean-square deviations.[57] Since it also requires less calculation time, in particular for larger systems such as PTCDA + Si (see section 4—Initial Adsorption of Molecules on Inorganic Semiconductor Surfaces), the 3-21G basis set was used for all the frequency calculations within this work.

4. Initial Adsorption of Molecules on Inorganic Semiconductor Surfaces

Early studies of organic molecule adsorption on the low-index faces of inorganic semiconductors such as GaAs(100) suggested that a passivated surface was necessary for ordered growth. It was found that, for example, PTCDA formed ordered layers on GaAs(100) if the surface had been passivated by a selenium (Se) monolayer, while the order was significantly poorer when the growth took place on clean GaAs surfaces.[96] It was proposed that the GaAs surface bonds are saturated by Se and the organic molecules attach through a weak van-der-Waals bonding to the surface. As a result of this weak interaction, the molecules have sufficient mobility on the surface to arrange into an ordered, quasi-epitaxial overlayer. It is thus expected that the quality of the passivated surfaces will influence the organic film structure. On the other hand, the molecular functional groups, *viz.* the anhydride and the methyl-imide groups, may also play a role in determining the strength of interaction with the passivated surface and the surface defects. In this section, the nature of the interface bonding and its role in determining the structure of the organic film as well as the energy band profile will be investigated by combining photoelectron spectroscopy (PES) and Raman spectroscopy (RS).

4.1. Initial Interface Formation between PTCDA Molecules and Differently Treated GaAs Surfaces

4.1.1. S-XPES Investigations

In order to achieve ordered growth of the organic film, the substrate needs to be passivated prior to organic deposition. Chalcogen atoms (e.g., Se, S) have been successfully used for the passivation of GaAs(100) surfaces. During the passivation of GaAs(100) surfaces with chalcogen atoms, an exchange reaction between the chalcogen atoms and the

group V atoms at the surface results in the formation of a thin Ga-chalcogenide-like layer terminated by a layer of chalcogen atoms. The passivated surfaces can be obtained by sulfur or selenium passivation using a treatment under ultrahigh vacuum (UHV) conditions or a wet chemical procedure. A detailed discussion of the preparation of passivated GaAs(100) surfaces and their characterization by photoemission spectroscopy is given elsewhere.[97] In this review, we will present only the structural model for the sulfur-passivated GaAs(100) surfaces together with the corresponding core level spectra.

On the basis of the theoretically calculated STM topography and photoemission data, the sulfur-passivated GaAs(100) surface is proposed to be terminated by single sulfur atoms[98,99] (see Figure 28). The surface layer is followed by

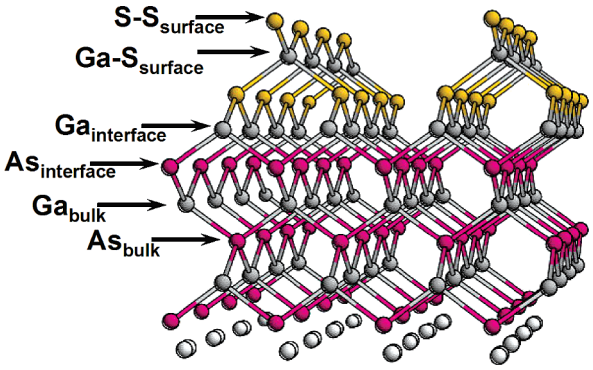

Figure 28. Structural model of chalcogen (S)-passivated GaAs(100)-(2×1) surfaces. The substrate is covered by a Ga-sulfide-like layer (Ga-$S_{surface}$) terminated by a sulfur layer (S-$S_{surface}$) followed by an intermediate layer of Ga and As atoms ($Ga_{interface}$ and $As_{interface}$) with slightly different chemical environments than those of the bulk atoms (Ga_{bulk} and As_{bulk}). Reprinted from *Applied Surface Science, 234*, B. Szucs, Z. Hajnal, R. Scholz, S. Sanna, and Th. Frauenheim, p 173, Copyright 2004, with permission from Elsevier.

a Ga layer and a second layer of sulfur atoms (Ga−$S_{surface}$). The fourth atomic layer contains an equal amount of Ga atoms ($Ga_{interface}$) and vacancies and is followed by the GaAs bulk, starting with an As layer ($As_{interface}$). The corresponding core level spectra of a clean GaAs(100)-c(4×4) surface and of S- and Se-passivated GaAs(100) surfaces are summarized in parts a−c, respectively, of Figure 29 , in the lowest spectra of each panel. The binding energies are given for the $d_{5/2}$ components of Ga_{3d}, As_{3d}, and Se_{3d} core levels and for the $p_{3/2}$ components of the S_{2p} core level.

For the clean, As-rich GaAs(100)-c(4×4) surfaces achieved after decapping a thick As layer, the As_{3d} core level spectrum exhibits three different components (see bottom spectra in Figure 29a). The most prominent feature in the spectrum with a binding energy of (40.88 ± 0.10) eV is attributed to As atoms in the bulklike surrounding of GaAs (As_{bulk}). The $As_{surface}$ surface component shifted by (0.59 ± 0.05) eV toward higher binding energy relative to As_{bulk} can be assigned to As atoms in a pure As surrounding representing the surface dimers. The $As_{interface}$ component can be attributed to As atoms in the second atomic layer, which are threefold-coordinated due to missing surface dimers. The energy position of $As_{interface}$ is shifted (0.56 ± 0.05) eV toward lower binding energy. On the other hand, the Ga_{3d} core level of the GaAs(100)-c(4×4) surface is characterized by a bulk component (Ga_{bulk}) at a binding energy of (19.16 ± 0.10) eV and a weak surface component ($Ga_{interface}$) shifted by (0.89

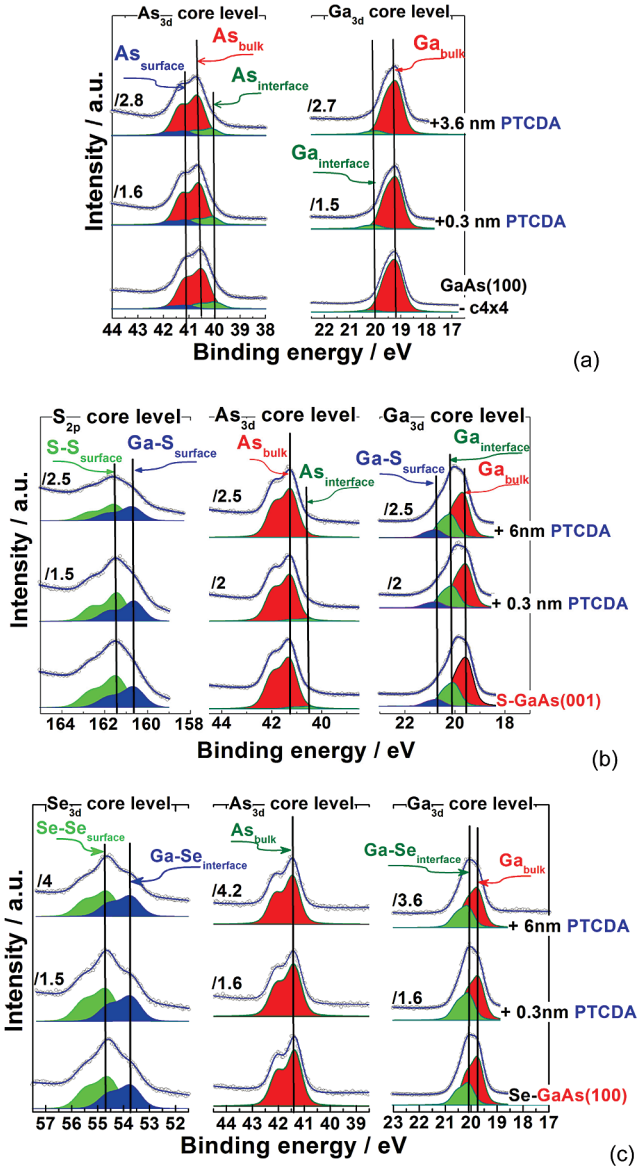

Figure 29. Core level spectra (Ga_{3d}, As_{3d}, S_{2p}, and Se_{2p}) of clean and passivated GaAs(001) surfaces (lower spectra in each panel) and upon deposition of PTCDA onto (a) GaAs(100)-c(4×4), (b) S-GaAs(100), and (c) Se-GaAs(100) surfaces. The surface, interface, and bulk components of the Ga_{3d}, As_{3d}, S_{2p}, and Se_{2p} core levels are labeled and indicated by arrows.

± 0.05) eV toward higher binding energies. The latter originates from Ga atoms situated at the interface of the bulk making bonds to the threefold-coordinated As atoms in the second layer.

For the chalcogen-passivated GaAs(100) (see bottom spectra in Figure 29b and c), the As_{3d} core level can be fitted using two components: one is a bulk contribution at (41.35 ± 0.10) eV binding energy, and the other one is an interface contribution stemming from the topmost layer of As ($As_{interface}$) and is shifted by (0.69 ± 0.05) eV toward lower binding energies. Instead, the Ga_{3d} core level has three contributions. The lower binding energy features at (19.5 ± 0.10) eV correspond to Ga atoms in the bulk (Ga_{bulk}). The higher binding energy peak ($Ga_{interface}$) at (19.9 ± 0.10) eV is a contribution from an intermediate layer between the topmost layer and the bulk which contains gallium vacancies. The highest binding energy peak ($Ga_{surface}$) at (20.5 ± 0.10)

Table 11. Gaussian Line Width of Core Level Spectra before and after Deposition of PTCDA on GaAs(100) Surfaces[a]

	PTCDA/ GaAs(100)-c(4×4)	PTCDA/ S-GaAs(100)	PTCDA/ Se-GaAs(100)
Ga_{3d}	0.54 → 0.50	0.50 → 0.50	0.41 → 0.44
As_{3d}	0.63 → 0.58	0.61 → 0.58	0.53 → 0.55
Se_{3d}			0.83 → 0.77
S_{2p}		1.07 → 0.97	

[a] The values after PTCDA deposition are averaged over the values obtained from the spectra at different PTCDA thicknesses.

eV is assigned to Ga atoms in a gallium sulfide/selenide (Ga_2S_3/Ga_2Se_3)-like environment.

Figure 29 also shows core level spectra of substrate components (Ga_{3d}, As_{3d}, S_{2p}, and Se_{3d}) upon deposition of PTCDA in a stepwise manner on the differently treated GaAs(100) surfaces. Upon deposition of PTCDA onto those surfaces, no dramatic changes were observed in the line shape of all the core level spectra, indicating the absence of a chemical reaction between the PTCDA molecules and the GaAs surfaces. However, taking a closer look at the core level spectra corresponding to the topmost atomic layer (As_{3d}, S_{2p}, and Se_{3d} for GaAs(100)-c(4×4), S-GaAs(100), and Se-GaAs(100) surfaces, respectively), subtle changes are revealed; namely, the valley originating from spin−orbit splitting in the As_{3d} core level spectra of PTCDA/GaAs-(100)-c(4×4) and the shoulders at both sides of S_{2p} and Se_{3d} core level spectra for PTCDA/S-GaAs(100) and PTCDA/Se-GaAs(100) become sharper.

Curve fitting of the core level is employed for a quantitative analysis. Table 11 shows changes in the Gaussian line width before and after PTCDA deposition for all the core levels of the three different samples. The values of the Gaussian line width after PTCDA deposition were averaged over the values obtained from spectra at different PTCDA thicknesses. While the energy positions of the core level components remain unchanged, the fitting results show that a pronounced reduction in the Gaussian line width occurs for the core level components corresponding to the topmost atomic layers. The decrease in the Gaussian line width is different for each core level. However, when corrected by the overall resolution at the corresponding photon energies for the core levels (0.25, 0.3, and 0.5 eV for As_{3d}, Se_{3d}, and S_{2p}, respectively), the decrease of the Gaussian line width for all core levels lies in a similar range. The line widths corresponding to deeper lying core levels also appear to decrease but to a lesser extent.

In order to understand the origin of the core level sharpening, much less than one monolayer of PTCDA was deposited onto a Se-GaAs(100) surface.

The thickness of the ultrathin layer ($^1/_3$ of a ML ≅ 0.1 nm) was estimated by the degree of the damping of the GaAs bulk core level components (Ga_{bulk}, As_{bulk}) upon PTCDA deposition. The sharpening of the Se_{3d} core level is still observed (see Figure 30), and therefore, it can be concluded that this behavior is related to the initial adsorption of PTCDA on the surface.

The Lorentzian line width of a core level accounts for the intrinsic lifetime of the core-hole while all other factors, such as the instrumental resolution, as well as disorder and potential variations across the surface, i.e., inhomogeneous band bending of the surface, contribute to the Gaussian broadening. In the absence of covalent bonding upon deposition of organic molecules on GaAs(100) surfaces, as

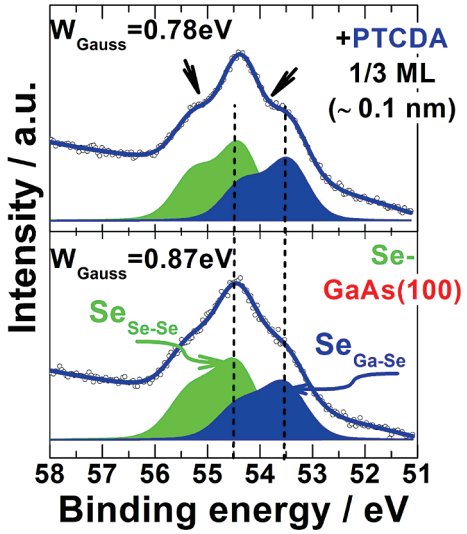

Figure 30. Se_{3d} core level spectra before and after deposition of $^1/_3$ of a ML of PTCDA on a Se-GaAs(100) surface. Values of the Gaussian broadening obtained from curve fitting are included. Arrows indicate the sharpening of the core level line shape upon PTCDA deposition.

evidenced by core level spectra, only changes in the inhomogeneous band bending can influence the broadening in the core level spectra since all other effects remain unchanged. In conclusion, the sharpening of the surface core level lines can be attributed to a reduction of inhomogeneous band bending of the surfaces.

The surface Fermi level pinning in the band gap for covalent semiconductors is commonly observed regardless of the type of surface, due to a large number of surface states. A STM study of GaAs(100) surfaces by Yamaguchi et al. reveals a density of surface defects in the range of 10^{12}−10^{13} cm^{-2}, depending on the doping concentration.[100] The situation is comparable to that of the Se−GaAs(100) surface, where two types of defects on the surface were observed in another STM study:[101] a few small holes from missing dimers and many bright features. The density of these bright features is approximately 10^{12} cm^{-2}. Considering the doping concentration used in this study (2×10^{17} to 1×10^{18} cm^{-3}), the number of dopant atoms on the surface would also be $\sim 10^{12}$ cm^{-2} among 6×10^{14} cm^{-2} surface atoms. In both cases, there is approximately one dopant atom in 300 surface unit cells, which can easily be covered by $^1/_3$ of a ML of PTCDA molecules. It is also known that the PTCDA molecules preferentially adsorb at defect sites due to an enhanced interaction.[1] Since no further change is observed upon subsequent PTCDA deposition, the sharpening of the core level spectra corresponding to the surface core level components is attributed to the preferential adsorption of PTCDA molecules on defect sites, leading to a removal of inhomogeneous Fermi level pinning.

The dopant atoms have different covalent radii (0.11 nm for Si, 0.14 nm for Te), and they may induce local distortion of the surface. Upon PTCDA deposition on top of the dopant atoms and/or any other defect sites of the GaAs(100) surfaces, geometrical distortions at the local surface may relax, accompanied by charge redistribution, resulting in more homogeneous surfaces. Even though no indication of covalent bond formation between PTCDA and GaAs(100) surfaces was observed in the core level spectra, it should be considered that a charge transfer may occur through defect sites and/or dopants, leading to a deformation of the

individual PTCDA molecules. Due to the low defect density, a more sensitive and higher resolution measurement technique would be needed to reveal the local charge transfer between dopant atoms and PTCDA molecules.

A comprehensive understanding of the interaction between molecules and various defect sites has been achieved from a combination of Raman spectroscopy and theoretical calculations. The related results are presented and discussed later in this section.

4.1.2. Valence Band Spectra and Interface Electronic Structures

In Figure 31, valence band (VB) spectra of PTCDA on differently treated GaAs(100) surfaces are shown as a function of the PTCDA thickness. For PTCDA/GaAs(100)-c(4×4) and PTCDA/Se-GaAs(100), synchrotron radiation ($h\nu$ = 24 eV) was used as a photon source while a He discharge lamp ($h\nu$ = 21.22 eV) was used for PTCDA/S-GaAs(100). The S-GaAs(100) surfaces show various IE_{GaAs} values from sample to sample depending on the details of the surface treatment. A thorough study revealed that the surface chemistry of sulfur-passivated GaAs(100) surfaces depends strongly on the annealing procedure during the passivation. Different annealing times, ramp rates, and pressure increases during annealing strongly affect the surface ordering and consequently the work function, ϕ, and IE_{GaAs} values of the surfaces. Here, only one representative deposition series is presented (Figure 31b). The bottom spectra in each panel of Figure 31 correspond to the substrate surfaces and are discussed elsewhere.[22] Even though IE_{GaAs} after an optimized sulfur surface treatment still varies between (6.28 ± 0.10) eV and (6.5 ± 0.10) eV,[102] the electronic properties of the wet chemically treated S-GaAs(100) surface are almost comparable with those of *in situ* passivated Se-GaAs(100) surfaces, which is an indication of a good surface ordering.

The deposition of PTCDA results in clear changes in the spectra. For a monolayer thickness of PTCDA, the features of the substrate surfaces are still present. Upon further PTCDA deposition, features characteristic of PTCDA become dominant. In the spectra of thick PTCDA films (above 10 ML), the features characteristic for PTCDA are clearly seen, in particular the feature labeled A attributed to the HOMO band at about 2 eV and the feature B at about 6 eV ascribed to contribution from the π orbital from the functional group.

In addition to the development of VB structures corresponding to PTCDA, a change in the energy position of the secondary electron onset is observed, as shown in the left panels of Figure 31. This indicates that the vacuum level, E_{VAC}, shifts, reflecting the formation of an interface dipole Δ at the PTCDA/GaAs(100) interfaces. The amount and direction of the shift are different when differently prepared GaAs(100) surfaces are used, as will be discussed later.

It should be noted that a saturation of the E_{VAC} shift occurs below 3 ML (~1 nm) PTCDA thickness for PTCDA/GaAs-(100)-c(4×4) and PTCDA/Se-GaAs(100), while a slower shift of E_{VAC} that lasts up to 6 ML (~2 nm) PTCDA thickness was observed for PTCDA/S-GaAs(100). This is related to the actual nominal thickness necessary for the completion of a monolayer, since an interface dipole layer can be thought of as a parallel plate capacitor and therefore results in an abrupt change in the electrostatic potential energy at the interface.[35] The slower saturation of the E_{VAC} shift for PTCDA/S-GaAs(100) is consistent with a stronger island formation.

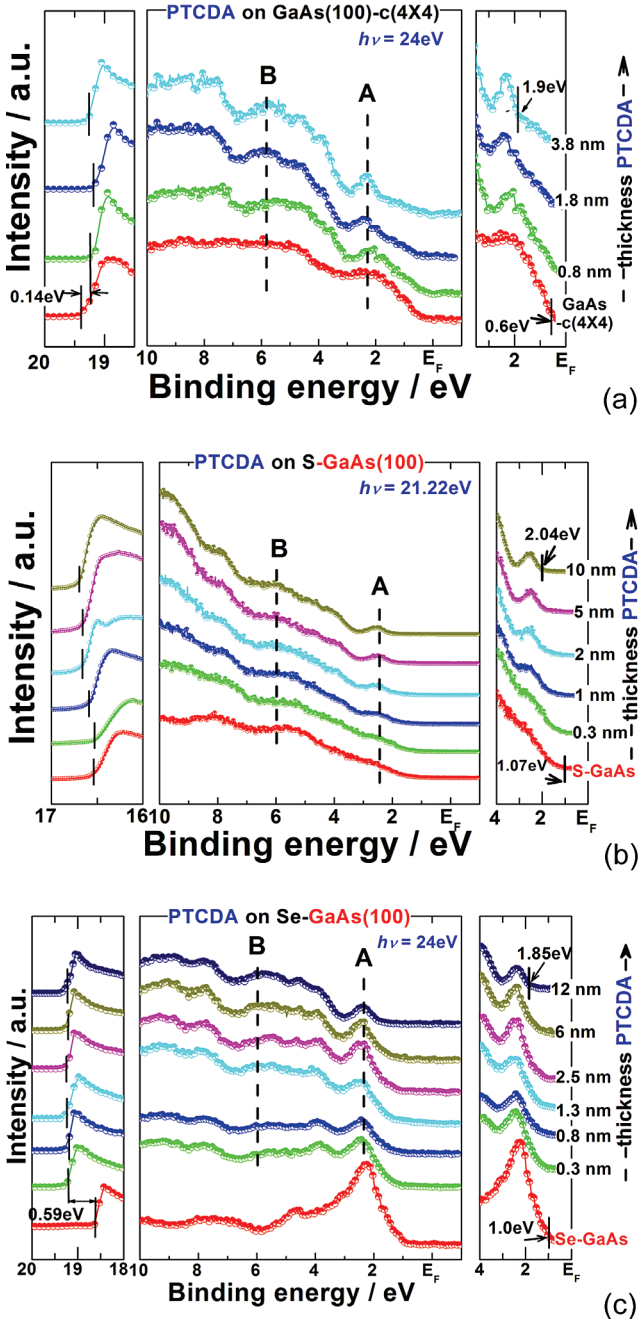

Figure 31. VB spectra upon deposition of PTCDA on (a) GaAs-(100)-c(4×4), (b) S-GaAs(100), and (c) Se-GaAs(100) surfaces. The spectra for the PTCDA/GaAs(100)-c(4×4) and PTCDA/Se-GaAs(100) surfaces were measured using a synchrotron radiation source ($h\nu$ = 24 eV) while a He discharge lamp ($h\nu$ = 21.22 eV) was used for the PTCDA/S-GaAs(100) surface. The bottom spectrum in each panel corresponds to the substrate surface. The energy positions of $GaAs_{VBM}$ and $PTCDA_{HOMO}$ are indicated as well. The dashed lines are guides for the eye.

The energy band diagram of the PTCDA films on the GaAs(100) surfaces having different electronic properties may provide a general rule for the energy level alignment at those interfaces. Before drawing the energy level scheme at PTCDA/GaAs(100) interfaces, it should be considered whether there is any energy level shift upon PTCDA deposition for features corresponding to the GaAs(100) surfaces and the PTCDA films. As can be seen in Figure 31, the energy position corresponding to the center of the PTCDA HOMO in the VB spectra for each sample does not appear to change during the stepwise deposition, despite the

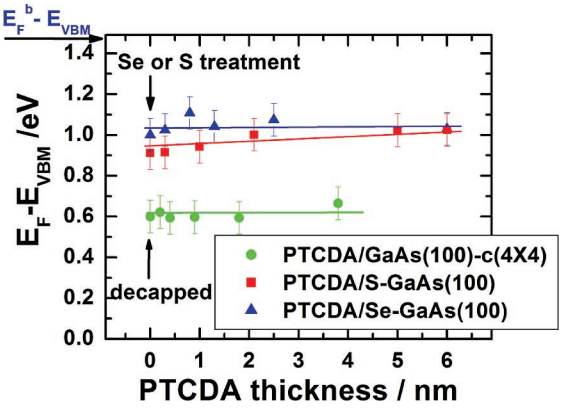

Figure 32. Evolution of the E_F position above VBM as a function of PTCDA thickness on different GaAs(100) surfaces. The solid lines indicate that the band bending of the substrate surfaces does not change upon PTCDA deposition.

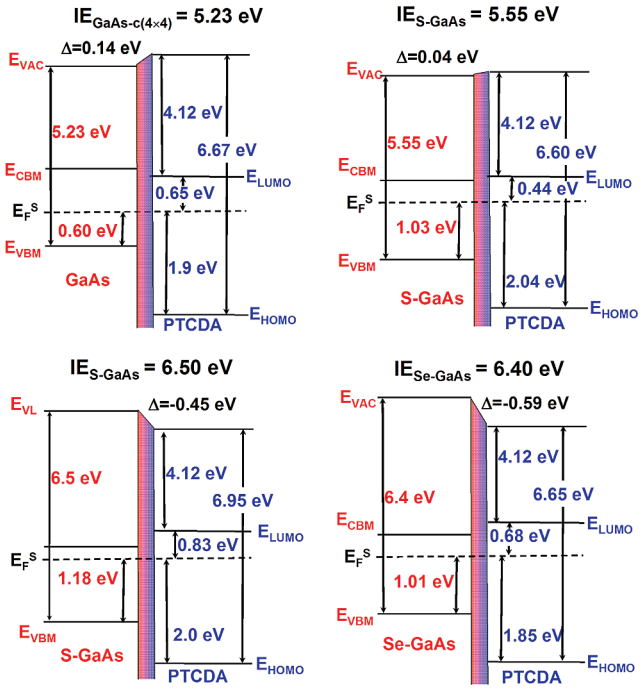

Figure 33. Energy level alignment at interfaces of PTCDA on differently treated GaAs(100) surfaces with different ionization energies IE.

fact that it is difficult to evaluate the energy shift below a PTCDA thickness of 1 nm due to the screening by the VB features of the substrates. After the determination of the energy distance between E_F and E_{VBM} from the VB spectrum before PTCDA deposition, the evolution of E_F is monitored by the binding energy shifts of the Ga_{3d} and As_{3d} bulk components. This is shown in Figure 32 as a function of PTCDA thickness. In all cases, the change in the energy position is negligible within the error of the measurement, indicating that the band bending of the substrate surfaces does not change upon PTCDA deposition.

The energy level alignment obtained from VB spectra between PTCDA films and differently treated GaAs(100) surfaces is displayed in Figure 33. For simplicity the band bending of the substrates is omitted, so that the energy levels are presented with respect to the Fermi level of the substrate surfaces, E_F^S. Note that the measured IE_{GaAs} ranges from (5.23 ± 0.10) eV for the GaAs(100)-c(4×4) surfaces to (5.55−6.5 ± 0.10) eV for the S-GaAs(100) surfaces to (6.40 ± 0.10) eV for the Se-GaAs(100) surfaces. The energy positions for the PTCDA films were obtained using the VB spectra of thin (4−12 nm) PTCDA films in order to prevent any influence due to sample charging. The measured IE_{PTCDA} fluctuates from 6.56 to 6.95 eV, probably due to variations in surface morphologies.[35] E_{HOMO} is found to be in the range of 1.85−2.04 eV, showing a weak dependence on IE_{GaAs}. This indicates that the ability of E_F to move within the HOMO−LUMO gap is low. A pinning of the Fermi level was also observed for PTCDA/metal interfaces.[103]

A strong correlation is found between the interface dipole and the relative energy position between E_{LUMO} and E_{CBM}, and, thus, the electron affinities of the PTCDA film (EA_{PTCDA}) and substrates (EA_{GaAs}). E_{HOMO} is always located well below E_{VBM}. At the PTCDA/GaAs(100)-c(4×4) interface where a positive interface dipole is formed, E_{LUMO} is located below E_{CBM}. The situation is reversed when a negative dipole is formed, as in the case of the PTCDA/Se-GaAs(100) interface. Consequently, the interface dipole formed at PTCDA/S-GaAs(100) varies from positive to negative depending on IE_{GaAs} (or EA_{GaAs}). As mentioned, for the optimized preparation of wet chemically treated GaAs surfaces, a smaller variation in IE_{GaAs} was observed. In this case, the interface dipole is always negative and varies between (0.3 ± 0.10) eV and (0.45 ± 0.10) eV. It can therefore be deduced that the formation of the interface dipole at PTCDA/GaAs(100) interfaces is most likely driven by the difference in EA_{GaAs} and EA_{PTCDA} and that, in general, the vacuum level alignment rule is not applicable for these interfaces.

At thermal equilibrium, the number of electrons and holes that are transported across the interfaces should be equal. Due to the difference in the EA and IE values between substrate surfaces and PTCDA films, each electron and hole transported undergoes an energy loss or gain. The net energy loss, therefore, depends on the electron and hole concentration that is transported across the interface and the energy difference of $EA_{GaAs} - EA_{PTCDA}$ and $IE_{GaAs} - IE_{PTCDA}$. The interface dipole is formed in order to compensate the net energy loss. In the case of PTCDA films on n-GaAs(100) surfaces, it is expected that the number of electrons transported across the interface is much higher than that of holes and, therefore, $EA_{GaAs} - EA_{PTCDA}$ can be proposed to be the determining driving force for the interface dipole formation.

In Figure 34 the interface dipole is presented as a function of EA_{GaAs}. It can be seen that the interface dipole formed at PTCDA/GaAs(100) interfaces is linearly dependent on EA_{GaAs}. Using a linear fit, the interface dipole is found to be zero at $EA_S = (4.12 \pm 0.10)$ eV. This value also represents EA_{PTCDA}, assuming that the formation of the interface dipole is driven by the difference in EA_{GaAs} and EA_{PTCDA}.

On the basis of these findings, the energy level alignment at the interfaces between PTCDA and differently treated GaAs(100) surfaces was established (see Figure 33). Moreover, the energy offset between E_{CBM} and E_{LUMO} at the interfaces can be estimated to be (−0.17 ± 0.10) eV for PTCDA/GaAs(100)-c(4×4), (0.05−0.41 ± 0.10) eV for PTCDA/S-GaAs(100), and (0.27 ± 0.10) eV for PTCDA/Se-GaAs(100) interfaces. In addition, we can estimate the HOMO−LUMO gap of PTCDA to be in the range of 2.44−2.83 eV.

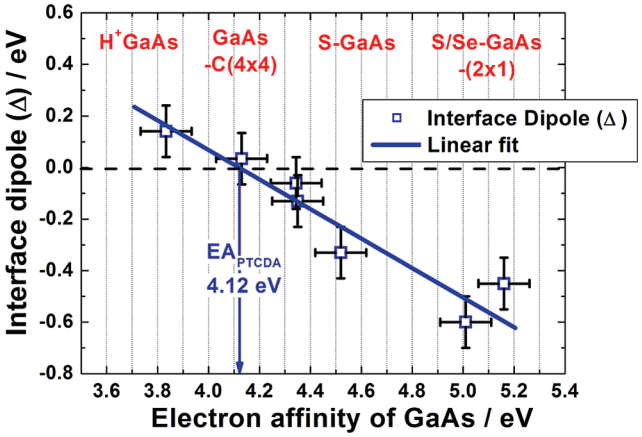

Figure 34. Interface dipole formed at PTCDA/GaAs(100) interfaces vs EA of GaAs(100) surfaces. Using a linear fit and by means of the interface dipole cancellation method, the electron affinity for PTCDA could be found as $EA_{PTCDA} = (4.12 \pm 0.10)$ eV.

4.1.3. Raman Investigations

In this subsection, the Raman spectra of sub-monolayer coverages of PTCDA on S-GaAs(100) surfaces are analyzed and compared with theoretical frequency calculations in order to explore the initial interface formation. Similar experiments were also performed for the PTCDA/Se-GaAs system. During the Raman monitoring of PTCDA deposition onto Se-passivated GaAs surfaces, the thickness-dependent spectra in the region of the most intense vibrational modes with C−H and C−C character resembled those of a single crystal.[53] Hence, the interaction between the PTCDA molecules and the Se-passivated GaAs substrate was proposed to be weak and comparable with intermolecular interaction. It must be noted, however, that the lowest investigated thickness was 1.8 nm, which corresponds to roughly 6 ML.

The evolution of PTCDA modes with contributions from C−C and C−H vibrations as a function of film thickness was recorded in the $z(y,x)\bar{z}$ polarization configuration (with $x = [001]$, $y = [010]$, $z = [100]$ defined by the main axis of the GaAs substrate) and is presented in Figure 35. All spectra are normalized to the height of the $\nu_{C-C} + \delta_{C-H}$ mode at 1572 cm^{-1}. Due to the low signal-to-noise ratio, each spectrum required an accumulation time of up to 3 h, a period for which the growth was interrupted.

The Raman spectrum of a 40 nm thick PTCDA/S-GaAs-(100) layer recorded *in situ* is considered as reference for line shape and frequency positions, since it resembles that of a PTCDA single crystal.

Several differences can be noticed when comparing the spectra of the 0.18 nm thick film with that of the 40 nm thick PTCDA film. A novel feature is observed with high intensity at 1290 cm^{-1}. The other modes are shifted toward lower frequencies, e.g., by ~2.4 cm^{-1} for the totally symmetric (A_g) C−C stretching mode at 1572 cm^{-1}. The amount of shift is reduced for the modes at 1303 cm^{-1} (C−H bending with A_g symmetry, 1302.3 cm^{-1} in crystal) and 1572 cm^{-1} upon increasing thickness to 0.45 nm. The intensities of these modes increase, while that of the 1290 cm^{-1} band remains almost constant. Obviously, there are molecules experiencing a different type of interaction in the initial phase of adsorption compared to the intermolecular interaction specific to thicker films and single-crystal PTCDA. The spectral contribution and hence the number of such molecules remains almost constant upon increasing the coverage above 0.18 nm.

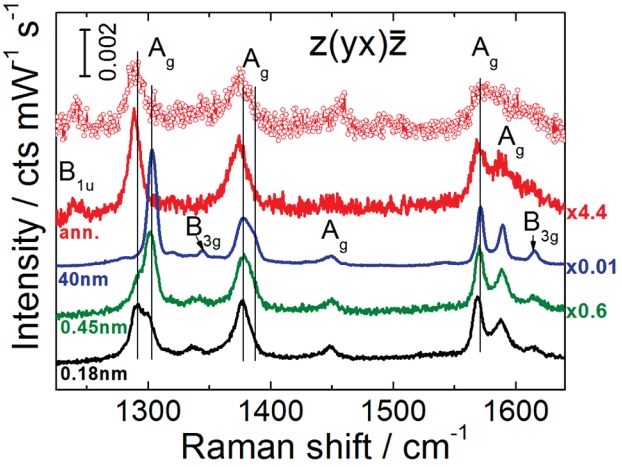

Figure 35. Raman spectra in the region of the C−C and C−H modes for several thicknesses of PTCDA films (from bottom to top: 0.18, 0.45, and 40 nm) on S-GaAs(100) and after annealing a 14 nm thick film for 30 min at 350 °C (second from the top), taken in crossed polarization. The topmost spectrum was recorded after annealing a 20 nm thick film grown on a H-Si(100) substrate at 410 °C for 15 min.

Further insight into the molecule−substrate interaction and the origin of the new band at 1290 cm^{-1} is obtained by annealing a 14 nm thick PTCDA film at 350 °C for 30 min. This temperature is higher than the desorption temperature for PTCDA multilayers, determined to be 325 °C for PTCDA on glass substrates.[104] Thus, only molecules experiencing a bonding to the substrate stronger than the intermolecular interaction should remain on the GaAs surface. The spectrum after annealing is shown in the upper part of Figure 35. By comparing the height of the C−C mode at 1572 cm^{-1} for the annealed and the as-deposited 0.18 nm films, a number of molecules corresponding to ~0.04 nm nominal coverage are evaluated as remaining on the surface, i.e., approximately $^1/_8$ of a ML. However, it must be noted that a precise determination of the absolute number of molecules from the Raman peak intensities may be limited by a number of parameters, e.g., the growth mode or the resonance conditions. The photoemission measurements have shown from the attenuation of the substrate core levels that, at room temperature on Se- as well as on S-passivated GaAs(100)[105] surfaces, the first PTCDA monolayer should be completed before the second one starts to form. Hence, the signal from a 0.18 nm film most probably originates only from molecules in direct contact with the substrate. In the following it will be shown that the interaction between the molecules and the surface after annealing does not involve the disruption of the molecule. It should thus not modify significantly the resonant conditions for Raman scattering and hence the relative intensities of the Raman modes. Therefore, the relative change in the intensity of the C−C mode when comparing the spectra of the as-deposited 0.18 nm thick film and the annealed film is expected to give a fairly reasonable estimate of the number of the molecules remaining on the surface after annealing.

At the doping level used in this experiment ($N_d = 2.7 \times 10^{18}$ cm^{-3}), the number of Si dopant atoms on the GaAs-(100) surface should be at least 10^{12} cm^{-2} among 6×10^{14} cm^{-2} surface atoms. Furthermore, previous investigations of ZnSe films grown on GaAs(100) have shown that, already upon annealing at 280 °C for 40 min, Si dopant impurities diffuse toward the GaAs surface, leading to the occurrence

of silicon clusters.[106] Considering the PTCDA molecules lying flat on the substrate when grown at room temperature as well as after annealing, the nominal coverage of $^1/_8$ of a ML (~0.04 nm) determined from the Raman spectra after annealing would correspond to $\sim 10^{13}$ cm^{-2}, i.e., sufficient to cover all surface defect sites induced by Si dopant atoms. Further evidence for the interaction of molecules mainly with the Si dopant atoms is provided by the similarities between the spectra recorded after annealing the 14 nm thick PTCDA film grown on S-GaAs(100) and after annealing of a 20 nm thick PTCDA film grown on an H-passivated Si(111) substrate (topmost spectrum in Figure 35). Additional defect sites such as missing S atoms, domain boundaries, and step edges[107] may also be present and can probably explain the large value of 10^{13} molecules/cm^2.

In the spectrum after annealing, the band at 1303 cm^{-1} is entirely replaced by the novel feature at 1290 cm^{-1}. This is a clear hint to the origin of the band at 1290 cm^{-1} being a shifted variant of the 1303 cm^{-1} mode, in agreement with the argument used for molecules adsorbed on Ag(111) substrates.[29] The band at 1290 cm^{-1} is thus proposed to be characteristic for molecules having direct contact with the surface defects, while the band at 1303 cm^{-1} is characteristic for molecules in a molecular crystalline-like environment.

The approximately $^1/_2$ of a ML (~0.18 nm) coverage of PTCDA corresponds to a number of molecules that is about four times larger than the number of molecules remaining on the surface after annealing. Thus, the corresponding Raman spectrum should contain three types of contributions: from molecules in contact with defects, from molecules in contact with the passivated surface, and from molecules also interacting with other molecules. The experimental spectrum, however, appears as a combination of the spectra of molecules interacting with defects and of the spectra of thick films. The intensity of the 1290 cm^{-1} mode is approximately equal to that of the 1303 cm^{-1} mode. The intensity ratio of these modes reflects that at least half of the molecules at the surface are not interacting exclusively with the surface defects. Consequently, the molecules interacting with the passivated surface must contribute to the spectrum in a similar way as the molecules involved in intermolecular agglomerations; hence, the strength of the interaction between the molecules and the passivated GaAs surface is likely to be comparable to that of the intermolecular interaction.

Considering the adsorption of the PTCDA molecules at surface Si dopant atoms (or other defects) at the GaAs surface, several mechanisms may be involved. The prediction of the Raman spectra corresponding to the PTCDA molecules interacting with Si defects requires the knowledge of the adsorption geometry as well as theoretical tools capable of handling systems with a large number of atoms comprising the PTCDA molecule and the topmost five layers of the S-GaAs substrate. To our knowledge, additional experimental evidence regarding the exact location of the Si defects with respect to the surface sites and the adsorption geometry of the PTCDA molecules on the defects is missing. The calculation of the Raman spectra within the Gaussian 98 package is possible only under coarse approximations of the interaction between single molecules and defects. Therefore, the calculated Raman spectra can be only qualitatively compared to the experimental ones.

Charge transfer between a molecule and one defect was first considered and approximated by charging an isolated

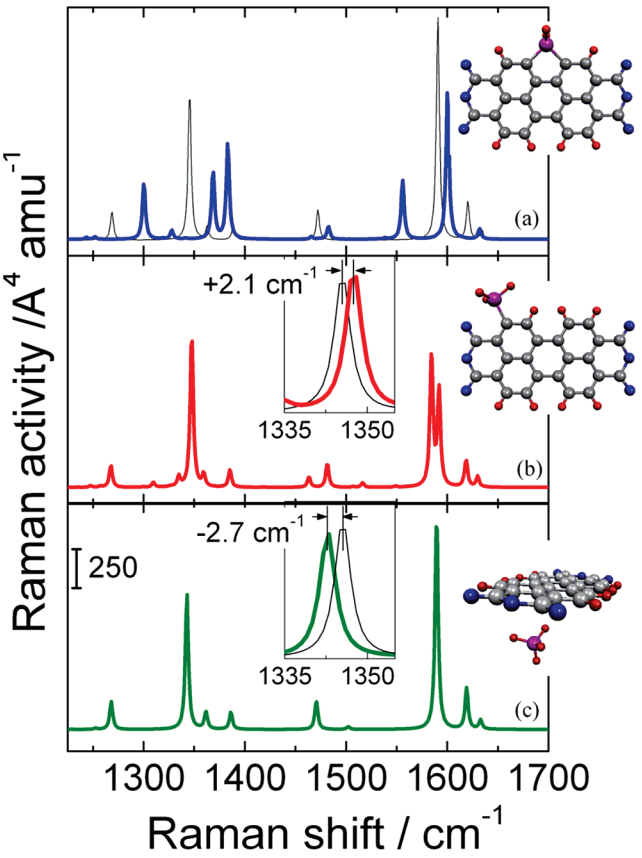

Figure 36. Calculated Raman spectra (thick lines) for a PTCDA molecule bonded to one Si atom via two σ-bonds (a) or via one σ-bond (b); and for a PTCDA molecule with a passivated Si atom below the molecular plane (c). The calculated spectrum of a neutral molecule is shown for comparison in part a and in the insets of parts b and c by the thin continuous lines. The Raman bands were modeled with Lorentz oscillators having a fwhm of 3.5 cm^{-1}.

PTCDA molecule with one positive or negative elementary charge. Frequency calculations with the B3LYP:3-21G functional predict dramatic shifts for the C−C stretching Raman modes[108] that are not detected in the spectra after annealing.

In a second approach, complexes consisting of a PTCDA molecule and one Si atom are considered and the corresponding Raman spectra are calculated with the same functional. The high affinity of Si atoms having dangling bonds to form σ-bonds with C atoms was experimentally proven by the chemisorption process of maleic anhydride onto clean nonpassivated Si(100):2×1 surfaces[109] accompanied by the rehybridization of the C atoms from sp^3 to sp^2. Therefore, complexes having σ-bonds between one Si atom and the carbon atoms of the perylene core of PTCDA were considered. As can be seen in the calculated Raman spectra in Figure 36a and b, the formation of two σ-bonds between Si and PTCDA also leads to dramatic shifts of all modes, while the C−H Raman modes of the complex with a single σ-bond are slightly shifted toward higher frequencies. Thus, none of the two complexes can explain the spectral changes observed upon annealing.

Finally, calculations for a single Si atom with all valence electrons saturated with H atoms situated below the molecular plane of PTCDA were performed. Most of the modes in the spectral region of interest shift to lower frequencies by at most 1.5 cm^{-1}, while the mode at 1346 cm^{-1} (calculated

for an isolated molecule, 1303 cm^{-1} in experiment) experiences the largest amount of shift (2.7 cm^{-1}) to lower frequencies (Figure 36c). This situation provides the best qualitative match to the experimentally observed shift, but the amount of shift is still lower than the experimentally observed one. The amount of accompanying static charge transfer from the PTCDA molecule is only 0.007 of an elementary charge. Besides strengthening the assignment of the mode at 1290 cm^{-1} as being a shifted variant of the 1303 cm^{-1} mode, these calculations also show that small changes in the molecular environment can lead to significant frequency shifts for modes with pure C−H deformation character.

An additional feature of the Raman spectra after annealing should be noted. A normally infrared active band ($B_{1u}(y)$, δ_{C-H}) occurs at 1243 cm^{-1}. Its presence can be explained either by a symmetry lowering to C_v for the molecules adsorbed at defect sites (by analogy with the case of D_{6h} molecules[110]) or by a dynamical charge transfer.[111] Therefore, the molecules are proposed to interact with surface defects due to Si dopant atoms via a charge transfer modulated by molecular vibrations and/or accompanied by a molecular deformation. This conclusion is supported by the observation of the mode at 1243 cm^{-1} along with the one at 1290 cm^{-1} in the spectra of Ag/PTCDA or In/PTCDA interfaces (see section 6—Metals on Organic Layers) or in the Raman spectra of PTCDA MLs on Ag(111).[28,29]

In summary, the molecules with a different spectral signature compared to those in a molecular crystalline environment are proposed to be adsorbed at defects mainly due to Si dopant atoms at the GaAs surface. The interaction involved is sufficiently strong to retain these molecules at the surface upon annealing above the desorption temperature of PTCDA. A comparison of the experimentally observed characteristic features and the calculated spectra excludes static transfer of an elementary charge or the formation of σ-bonds between the Si atom and the molecule as being responsible for this interaction. However, the observed breakdown of selection rules points to an interaction mediated by dynamical charge transfer. From the similarity between the spectral response of molecules arriving at the surface after the defects are saturated and that of molecules in a crystalline environment, the interaction between PTCDA molecules and the S-passivated surface is estimated to be comparable to the intermolecular one.

4.2. Initial Interface Formation between DiMe-PTCDI Molecules and Sulfur-Passivated GaAs Surfaces

Another interface formation assessed by means of PES and Raman spectroscopy is the DiMe-PTCDI/S-GaAs(100) interface.

4.2.1. S-XPES Investigations

The evolution of the core level spectra of substrate components (Ga_{3d} and As_{3d}) upon deposition of DiMe-PTCDI onto S-GaAs(100) surfaces in a stepwise manner is shown in Figure 37. Similar to the case of PTCDA, the adsorption of DiMe-PTCDI does not induce any dramatic changes in the line shape of the As_{3d} and Ga_{3d} core level spectra, strongly indicating the absence of any chemical reaction of the DiMe-PTCDI molecules with the substrate. Table 12 shows the changes in the Gaussian line width before and during DiMe-PTCDI deposition. Gaussian broadening

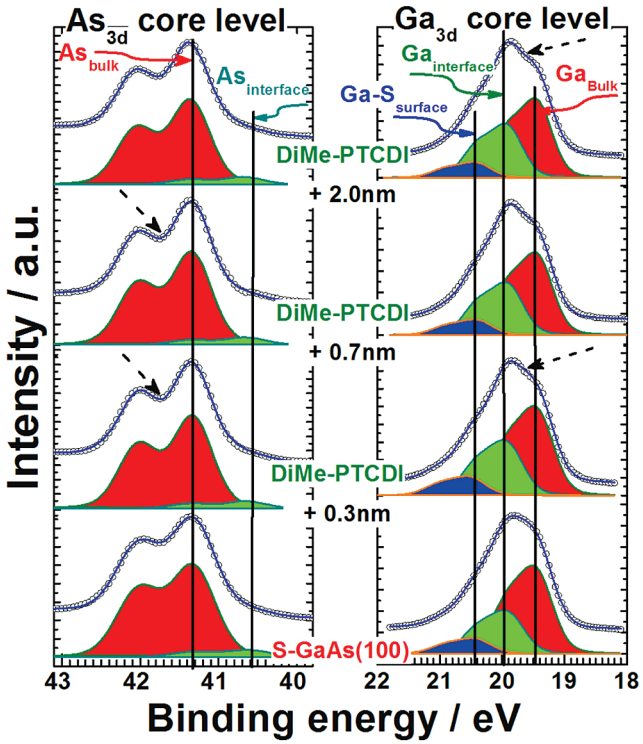

Figure 37. Evolution of As_{3d} and Ga_{3d} core levels of S-GaAs upon deposition of several thicknesses (0.3, 0.7, and 2.0 nm) of DiMe-PTCDI. The substrate components (surface, interface, and bulk) are labeled and indicated by arrows. The dashed arrows indicate the sharpening of the core level line shape upon DiMe-PTCDI deposition.

Table 12. Gaussian Line Width of the As_{3d} and Ga_{3d} Core Levels' Core Level Spectra before and after Deposition of DiMe-PTCDI on GaAs(100) Surfaces[a]

	W at the following thicknesses (nm)			
	0	0.3	0.7	2
$W^{As_{3d}}_{Gauss}$/eV	0.60	0.54	0.54	0.54
$W^{Ga_{3d}}_{Gauss}$/eV	0.56	0.55	0.52	0.51

[a] The uncertainty is 0.01 eV.

of the As_{3d} is reduced by 60 meV immediately after deposition of ∼1 ML of DiMe-PTCDI while for Ga_{3d} the sharpening of the core level amounts to 40 meV after deposition of ∼2 ML of an organic layer. For higher DiMe-PTCDI coverages, the Gaussian broadening remains constant. The observed reduction in the Gaussian broadening is explained in terms of an improvement of the surface properties after deposition of the organic layer. As was already observed for PTCDA, DiMe-PTCDI molecules are likely to stick preferably on defect sites, thereby reducing disorder and potential variations across the surface, which results in more homogeneous band bending on the surface. On the other hand, the energy positions of the core levels are not changed, indicating that the band bending of the substrate remains constant.

4.2.2. Valence Band Spectra and Interface Electronic Structures

Figure 38 displays the electronic structure of DiMe-PTCDI films grown onto H^+-plasma-treated GaAs(100) surfaces and two different S-GaAs(100) surfaces. The bottom spectrum in each panel corresponds to the GaAs(100) surfaces before

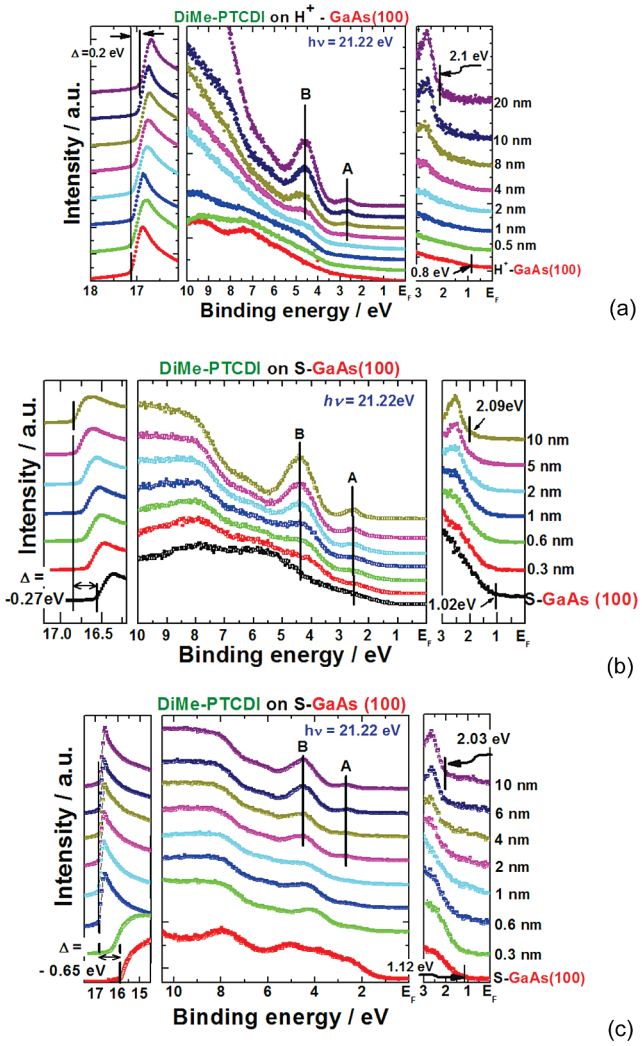

Figure 38. Evolution of the VB spectra upon deposition of DiMe-PTCDI in a stepwise manner onto H^+-plasma GaAs(100) (a), low IE S-GaAs(100) (b), and high IE S-GaAs(100) (c). The bottom spectrum in each panel corresponds to the substrate surface. The energy positions of $GaAs_{VBM}$ and $DiMe\text{-}PTCDI_{HOMO}$ are indicated as well. The solid lines labeled A and B indicate the positions of HOMO and HOMO − 1. The spectra were measured using a He discharge lamp ($h\nu = 21.22$ eV).

deposition. As mentioned, differently treated S-GaAs(100) surfaces lead to different surface ordering and consequently different electronic structure and properties. A noticeable difference can be very well seen in the lowest spectra of Figure 38b and c. The VB structures are better developed, resulting in an increase in IE_{S-GaAs} in case (c).

The spectral features characteristic of the DiMe-PTCDI film become dominant in the spectra as the film thickness increases. The VB feature labeled A is assigned to the HOMO while band B is attributed to a contribution from the π orbital of the methylimide and carboxylic groups. As in the core level spectra, no change in the energy position of these features is observed during the growth of the DiMe-PTCDI film, indicating the absence of band bending in the organic layer.

Valuable information on the growth mode can be obtained from the evolution of ϕ as a function of the thickness of the organic films or the change in the secondary electron onset. As shown in the left panels of Figure 38, the movement of the onset is slower for the first two cases. Moreover, there seems to be a correlation with IE_{GaAs}. This can be related to

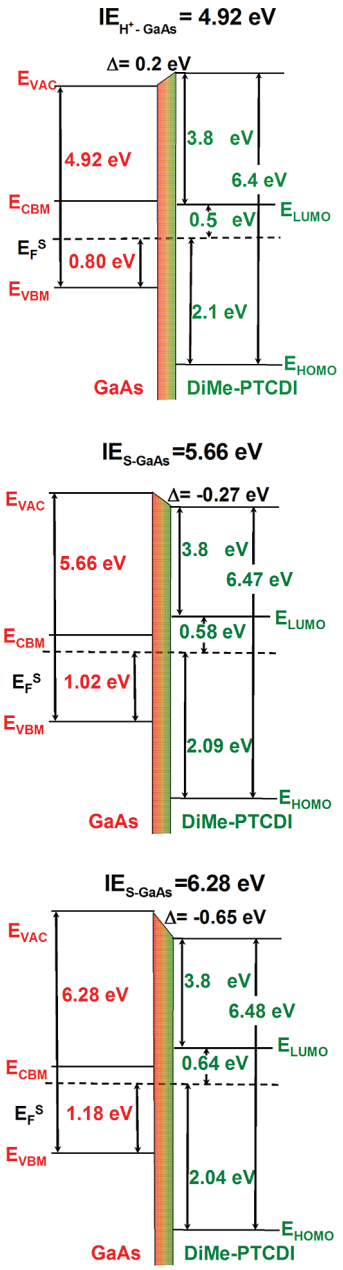

Figure 39. Energy level alignment at interfaces of DiMe-PTCDI on GaAs(100) surfaces with different ionization energies.

different rates of formation of a complete ML. On smoother surfaces, such as for example case (c), the organic layer starts to grow in a more homogeneous manner. A rapid saturation of the E_{VAC} shift was also observed for PTCDA grown onto passivated Se-GaAs(100) (see Figure 31c).

In Figure 39, the energy level alignment at the interface of DiMe-PTCDI with differently treated GaAs(100) surfaces is shown. The energy levels corresponding to DiMe-PTCDI are obtained from the VB spectrum of the 10 nm film. The measured $IE_{DiMe-PTCDI}$ fluctuates between (6.36 ± 0.1) eV and (6.6 ± 0.1) eV from sample to sample, due to slightly different morphologies of the films.

In Figure 40 the interface dipole is presented as a function of EA_{GaAs}. It can be seen that the rule of the energy level alignment driven by the EA difference also holds for the DiMe-PTCDI/GaAs(100) interfaces.

Assuming that the formation of the interface dipole is driven by the difference in EA_{GaAs} and $EA_{DiMe-PTCDI}$, a zero

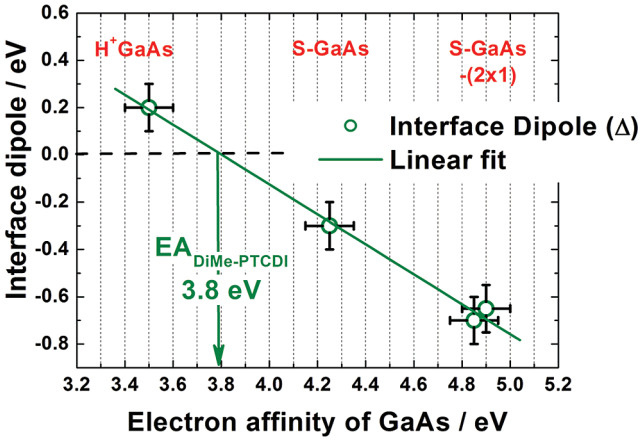

Figure 40. Interface dipole vs EA_{GaAs} formed at DiMe-PTCDI/GaAs(100) interfaces. It has a linear dependence, and by means of the interface dipole cancellation method, the electron affinity for DiMe-PTCDI can be determined.

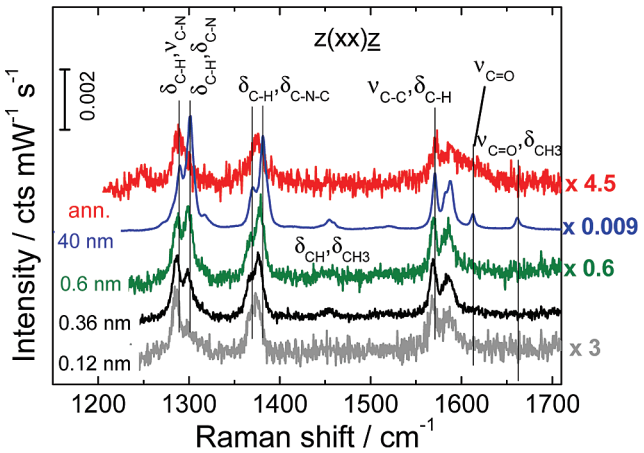

Figure 41. Raman spectra in the region of the C−C and C−H modes for several thicknesses of DiMe-PTCDI films on S-GaAs-(100) recorded in the parallel polarization configuration. Spectra are normalized with respect to the height of the mode at 1570 cm^{-1}.

interface dipole corresponds to $EA_{DiMe-PTCDI} = (3.8 \pm 0.10)$ eV. On the basis of these findings, the energy offset between E_{CBM} and E_{LUMO} at the interfaces between DiMe-PTCDI and differently treated GaAs(100) surfaces was established (see Figure 39). In addition, we can estimate the transport gap of DiMe-PTCDI to be between (2.6 ± 0.10) eV and (2.68 ± 0.10) eV.

4.2.3. Raman Investigations

The Raman spectra of DiMe-PTCDI on S-GaAs(100) starting from a sub-monolayer coverage are presented in Figure 41. The spectrum of a 40 nm thick film was taken as a reference for the frequency positions quoted below.

In order to verify if the DiMe-PTCDI molecules stick at the surface defect sites via interactions comparable to those between the PTCDA and the defects on S-GaAs(100), a ∼15 nm thick DiMe-PTCDI was annealed at 325 °C for 10 min. This was sufficient to leave a coverage of only 0.08 nm of DiMe-PTCDI on the substrate, which corresponds to a coverage fraction of $^1/_4$ of a ML. This value was estimated by comparing the intensity of the C−C stretching band at 1570 cm^{-1} with that in the spectrum of a 0.36 nm thick film (taken under the same experimental conditions).

The spectrum of the molecules remaining on the surface after annealing presents a B_u mode at 1248 cm^{-1} (Figure 41). The C−H modes at 1290 and 1300 cm^{-1} merge into one band, downshifted to 1287 cm^{-1}. The two modes at 1369 and 1380 cm^{-1} also merge into one band at 1375 cm^{-1}. The shift of the C−C stretch band at 1570 cm^{-1} is very small (0.5 cm^{-1}) and toward larger frequencies while the band at 1290 cm^{-1} shifts to lower frequencies.

Table 13. Frequency Positions (in cm^{-1}) of Several Modes in the Spectra of Annealed PTCDA and DiMe-PTCDI Films Recorded in Parallel Polarization

PTCDA/S-GaAs	PTCDA/H-Si	DiMe-PTCDI/S-GaAs
1243	1240.7	1247.8
1290	1289.8	1287.2
1373.9	1375.5	1375
1570	1571.9	1570.4

The number of bands, their broadening, and their relative intensities are very similar to those observed in the parallel polarization configuration for the annealed PTCDA/S-GaAs sample. The frequency positions in the spectra of the annealed DiMe-PTCDI and PTCDA films on S-GaAs differ by at most 4.8 cm^{-1} (Table 13), which might be an indication of molecular fragmentation with a loss of CH_3 groups. Fragmentation of molecules adsorbed on Ag(110) substrates with the desorption of CH_3 groups was detected by mass spectroscopy when annealing the substrate at 455 °C,[112] which is 100 °C higher compared to our experiment. We assume that the DiMe-PTCDI molecules remaining on the surface are involved in processes of fractional charge transfer with the defect sites, similar to the case of PTCDA, i.e., via the π orbitals. As a result, the N−CH_3 bonds are weakened, possibly enabling the molecular fragmentation already at 325 °C.

Let us consider now the spectrum of an as-deposited 0.12 nm thick film. Here, the B_u mode is not observed. If the first deposited DiMe-PTCDI molecules adsorb at superficial defects—following the interpretation proposed for PTCDA on S-GaAs(100) in the previous section—the defect sites must already be saturated at this coverage. Thus, the spectra of 0.12 nm and higher coverage should contain information about three types of molecules: molecules interacting with the surface defects, molecules interacting with the S-passivated GaAs(100):2×1 surface and molecules having additional interactions with other molecules. All bands except for the one at 1300 cm^{-1} (see Figure 9c for its vibrational pattern) are shifted to lower frequencies compared to the reference spectrum. The largest shift is observed for the band at 1290 cm^{-1}, which originates from the vibrational deformation of C−H bonds as well as CH_3 groups (Figure 9b). The band appearing in thicker films at 1300 cm^{-1} is very broad and has a lower height compared to the band at 1290 cm^{-1}. The frequency position of the $\delta_{CH} + \nu_{CC}$ mode at 1570 cm^{-1} in thicker films is shifted downward by −1.5 cm^{-1}, less than the corresponding band in PTCDA. Moreover, the B_u mode is not observed. This might indicate that the interaction between the perylene core and the passivated GaAs substrate is lower for DiMe-PTCDI than for PTCDA molecules. The umbrella deformation of CH_3 groups at 1454 cm^{-1} and the C═O deformations (Figure 9e,f) are not observed.

For a DiMe-PTCDI coverage of 0.36 nm, the mode at 1300 cm^{-1} becomes well resolved, probably due to the larger number of molecules interacting only with the passivated surface and with other molecules. The umbrella deformation of CH_3 groups at 1454 cm^{-1} is also resolved though its intensity relative to the band at 1570 cm^{-1} is lower compared to the case of thicker films. A broad band is observable at

the position of the C═O antisymmetric stretching at 1610 cm^{-1}, while the symmetric C═O stretching at 1688 cm^{-1} is still not resolved.

In the next section it will be shown that in thicker films the DiMe-PTCDI molecules are oriented with their molecular plane making an angle of ~56° with the substrate plane. Assuming the same orientation also for the molecules at the interface, this would mean that the interaction between the molecule and the substrate takes place via the CH_3 group at one side of the molecule. This situation could be achieved through the formation of C−H−S bridges, considering the high electron affinity of S. Such an adsorption geometry would explain the low activity of the CH_3 umbrella deformation and of the C═O vibrations in the Raman spectra of submonolayer coverages.

To summarize, the interface formation between the two perylene derivatives and differently treated GaAs(100) surfaces was assessed by means of PES and Raman spectroscopy. It was proposed that initially molecules adsorb at the defect sites of the passivated surfaces, leading to a reduction of an inhomogeneous band bending.

It was observed that the energy levels alignment at the interfaces is driven by the difference between the EA of the substrate and the EA of the organic films. From the interface dipole cancellation method, the transport gap of the two organic molecules was estimated. Moreover, by means of Raman spectroscopy, the strength of interaction between the molecules and the S-passivated surface is estimated to be comparable to the intermolecular one.

5. Characterization of Thin Films

5.1. Molecular Orientation

5.1.1. Angular Dependence in NEXAFS: Formalism

Due to its atomic sensitivity and its polarization dependence, NEXAFS allows the spatial orientation of the unoccupied π^*-type orbitals in terms of dipole selection rules to be determined. The orbital studied can be translated into the molecular geometrical orientation if the principal relationship between the relevant orbital and the atomic arrangement is known. For the molecules under investigation, PTCDA and DiMe-PTCDI, this is typically the case for the (lower energy) π^* resonances in the perylene core. In the following, the formalism used in the data analysis will be introduced.

In the case of well-ordered samples, the X-ray absorption signal often exhibits a strong dependence on the angle of the incoming light with respect to, for example, the surface normal. This dependence can be used to determine the molecular orientation.[76] Responsible for this angular variation is the scalar product of the electric field vector $\vec{E}/|\vec{E}|$ and the dipole matrix element $\langle f|\vec{p}|i\rangle$ in eq 12 for the X-ray absorption cross section. The main component of the electric field

$$\vec{E} = E^{\parallel}\cos(kz - \omega t) + E^{\perp}\sin(kz - \omega t) \qquad (23)$$

emitted by the synchrotron radiation sources lies in the plane of the electron orbit, while $E^{\perp}$ is the perpendicular component of the electric field. The degree of linear polarization is represented by the polarization factor

$$P = \frac{|E^{\parallel}|^2}{|E^{\parallel}|^2 + |E^{\perp}|^2} \qquad (24)$$

which is ~0.98 for the Russian−German beam line at BESSY II, a number which indicates a high degree of linear polarization.

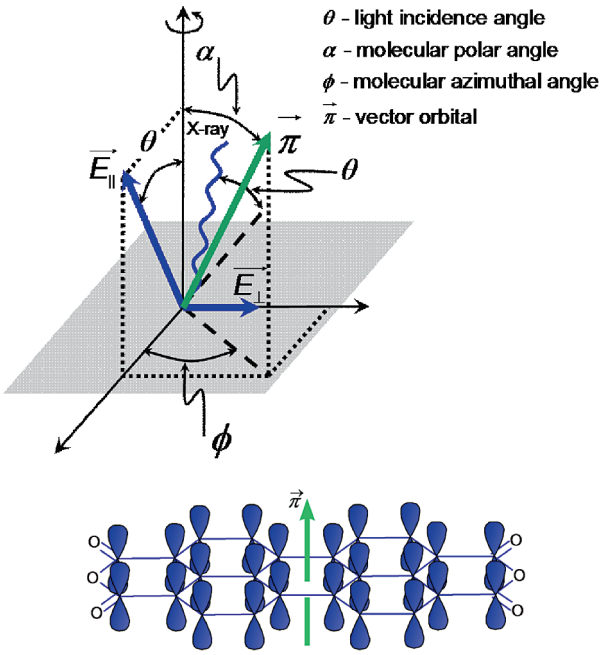

Figure 42. Orientation of a π-type molecular orbital, represented by the vector $\vec{\pi}$, characterized by a polar angle α and an azimuthal angle ϕ. The X-rays are incident in the (x,z) orbit plane of the storage ring which contains the major electric field component $E^{\parallel}$. The angle of incidence θ is changed by rotating the sample around the y-axis. On the right side, the molecular π-system of PTCDA is symbolized by π-orbitals at the carbon vertices and described by a vector $\vec{\pi}$ perpendicular to the molecular plane.

For the calculation of the dipole matrix element $\langle f|\vec{p}|i\rangle \propto \langle f|e\cdot\vec{r}|i\rangle$, the linear momentum operator $\vec{p}$ is re-expressed using the dipole operator $e\cdot\vec{r}$, taking into account the dipole selection rule $\Delta I = \pm 1$. For the measurements presented in the following, which employ excitation from the C_{1s} orbitals only, this means that the final state $|f\rangle$ has to contain a component of p-symmetry. For the perylene derivatives, the lowest energy final state stems from the ring π-orbitals which are described by a vector $\vec{\pi}$ perpendicular to the molecular plane. Thus, $\langle f|\vec{p}|i\rangle \propto \langle f|e\cdot r|i\rangle$ is directed along $\vec{\pi}$ (see Figure 42).

Therefore, the scalar product of $\vec{E}$ and the matrix element $\langle f|e\cdot\vec{r}|i\rangle$ is proportional to $\cos^2\delta$, where δ is the angle between the electric field vector and the direction $\vec{\pi}$ of the final state molecular orbital. The angle δ can be expressed by a different set of angles, namely the angle of incidence θ, the $\vec{\pi}$ orbital polar angle α, and the orbital azimuth ϕ. In the case of NEXAFS measurements, the angle of incidence, Θ, is defined with respect to the sample surface.

For a twofold substrate symmetry such as that of sulfur-passivated GaAs(100), the experimental intensities associated with the absorption cross section as a function of light incident angle can be expressed as

$$I(\theta) = A(P\{\cos^2(90° - \theta)\cos^2\alpha + \sin^2(90° - \theta)\sin^2\alpha\cos^2\phi\} + (1 - P)\{\sin^2\alpha\sin^2\phi\}) \qquad (25)$$

where A is an experimental constant that describes the absolute angle-integrated intensities and it should be the same for all different angles and P is the polarization factor defined by eq 24.

Figure 43 schematically illustrates the polarization dependence of π^* and σ^* resonances which can be observed in a

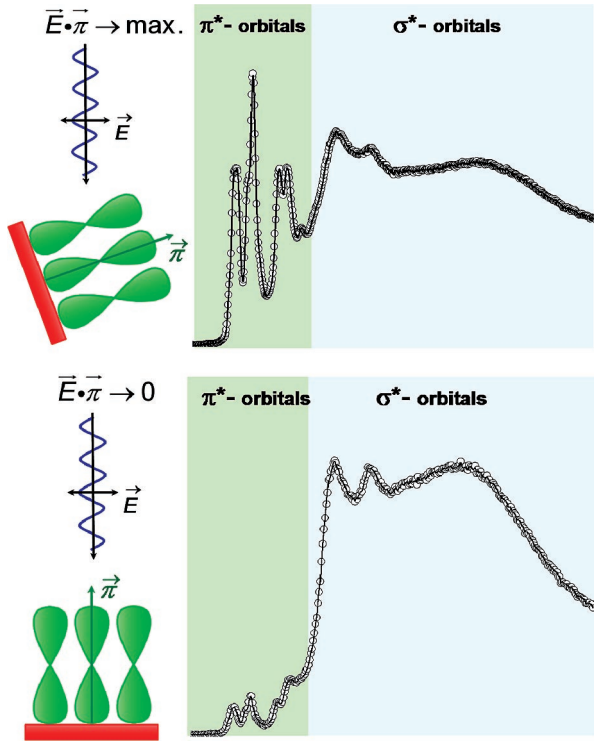

Figure 43. Sketch of the polarization dependence on the intensities of σ^* and π^* resonances for a planar π-conjugated molecule lying flat on the substrate surface.

planar π-conjugated molecule lying flat on a substrate surface. A transition from the K-shell to an unoccupied π^* orbital has maximum intensity when the electric field vector $\vec{E}$ of the linearly polarized X-ray beam is parallel to the orbital. The transition is dipole-forbidden when the polarization vector is perpendicular to the orbital.

In order to determine the orientation of $\vec{\pi}$ and consequently the molecular orientation, one has to measure the intensity dependence of a particular resonance on the incidence angle θ. A curve fitting procedure is employed for the determination of the parameters A, α, and ϕ from the intensity vs angle curves.

5.1.2. Angular Resolved NEXAFS of PTCDA Films on S-GaAs(100) Substrates

The C K-edge NEXAFS spectra of a 15 nm thick PTCDA film grown on a S-GaAs(100) substrate taken at different angles between the incident photon beam and the sample surface are shown in Figure 44. A thorough discussion of the spectral features is given in section 2.6—Near Edge X-ray Absorption Fine Structure (NEXAFS); here it is merely noted that the peaks below 289.4 eV are related to transitions from the C_{1s} core levels of C atoms in the perylene core into LUMO and LUMO + 1 states.

The photon energy interval from 280 to 318 eV was chosen to completely span the C K-edge and all π^* and σ^* transitions. For each sample, scans were taken at angles of incidence between 45° and 130°, as indicated in Figure 44. For normalization purposes, NEXAFS spectra of GaAs substrates were used as reference. To account for angle-dependent changes of the absorption path and the collection efficiency, the spectra were normalized such that they coincide for photon energies far below and far above the C K-edge absorption edge. This procedure effectively normalizes the signal to the number of carbon atoms sampled in the experiment.

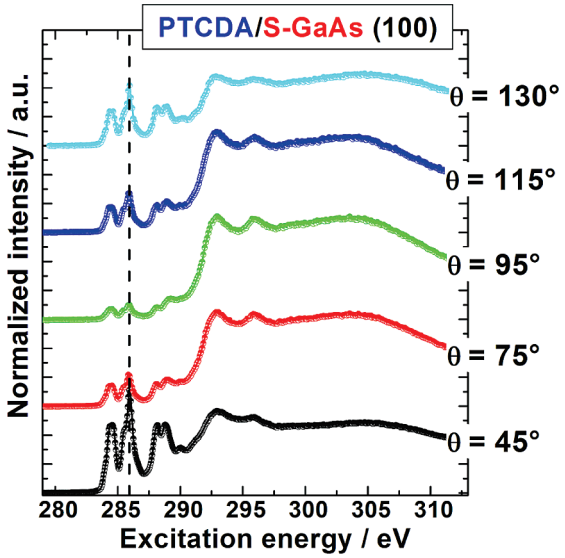

Figure 44. C K-edge NEXAFS of PTCDA as a function of θ, the angle of incidence; the lower energy features (284−290 eV) represent π^* resonances, while those features above 290 eV are related to σ^* resonances.

Focusing on the π^* resonance at 285.9 eV, the strongest π^* feature in the C K-edge spectra, a strong angular dependence is observed. The largest intensity for this resonance is reached at 45° and 130° while the minimum is observed around 95°.

Before proceeding further with the analysis of the angular dependence, an interesting point needs to be mentioned. If perfect order exists, the π^* intensity in Figure 44 should vary between 0 and I_{max} when the angle of the incident beam is changed by 90° from the angle where the intensity is 0. Because the electric field vector cannot be perpendicular to all molecules at a certain angle of incidence θ, the π^* resonances will not show a minimum when a degree of orientational disorder is present. The magnitude of the modulation decreases with the increase in the spread of orientations of molecules.

Quantitative analysis is performed by a curve fitting procedure of the difference intensities as a function of θ. Since the resolution of the monochromator is better than 10 meV, Lorentzian line shapes were chosen for curve fitting the π^* resonance features. The integrated area under the peaks was used to measure their intensities. A detailed description of the fitting procedure is given elsewhere.[66]

The angle of incidence q and the polarization factor P are known quantities, which only leaves the molecular orientation (e.g., polar angle α and azimuthal angle ϕ) and the normalization constant A unknown. These parameters can be determined by curve fitting the above equation to the relative intensities of the π^* resonances in the NEXAFS spectra.

The best fits to the experimental data are presented in Figure 45. An average tilt angle of $\alpha = 8° \pm 3°$ of the molecular plane was obtained with the azimuthal angle ϕ being 0°. This arrangement may be imposed by the herringbone structure that PTCDA usually tends to adopt. The ≈90° angle between the two molecules in the unit cell will average the azimuthal angle to 0°.

5.1.3. Angular-Resolved NEXAFS of DiMe-PTCDI Films on S-GaAs(100) Substrates

In contrast to the herringbone structure of the PTCDA molecules where the angle between the two molecules in a

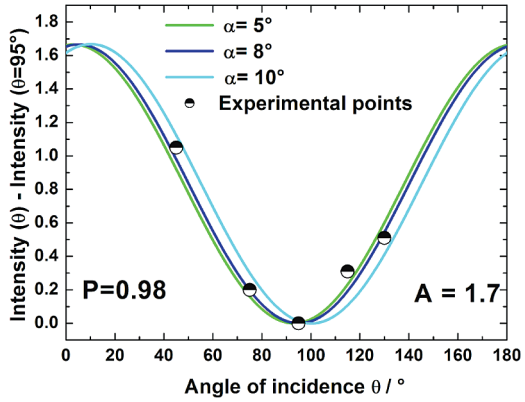

Figure 45. Intensities of the π^* resonance at 285.8 eV of PTCDA as a function of the incidence angle θ (symbols). Simulated curves using $A = 1.7$ for three different angles α are plotted with lines.

unit cell is almost 90°, the DiMe-PTCDI molecules in a unit cell align almost in the same direction (see section 2.2.2—Crystalline Structure). In order to reveal the molecular orientation within a DiMe-PTCDI film, both polar and azimuthal angular-dependent NEXAFS measurements were carried out.

The evolution of high-resolution NEXAFS spectra of DiMe-PTCDI as a function of angle of incidence for two different azimuthal directions of the S-GaAs(100) substrate, namely along [011] and [0−11], is shown in parts a and b, respectively, of Figure 46. The experiments employing different directions of the substrate are equivalent to using two azimuthal directions of the sample. In the first geometry, the plane of incidence contains the [011] direction of the S-GaAs(100) substrate while, in the second one, the plane of incidence is perpendicular to [011]; that is, it contains the [0−11] direction. For these two geometries, strong differences in the angular dependence of the intensities are observed. The normalized intensity of the features related to π^* resonances is presented in Figure 47 (symbols) as a function of incidence angle for two azimuthal directions of the sample. The best fits to the experimental data are also presented in Figure 47 (lines). An average tilt angle of $\alpha = 56° \pm 5°$ of the molecular plane is obtained while an angle of $\phi = -7° \pm 3°$ with respect to the [011] axis of the S-GaAs substrate is evaluated for the in-plane projection.

5.1.4. Molecular Orientation of PTCDA and DiMe-PTCDI Films on S-GaAs(100) Substrates Determined by Means of Infrared Spectroscopy

Infrared (IR) measurements on PTCDA/S-GaAs(100) samples reveal isotropy in the substrate plane. The ratio of the in-plane molecular modes with respect to the out-of-plane ones is similar to that observed for PTCDA/Si(111)[113] (see Table 14 for mode assignments). Quantitative analysis of this ratio reveals that the molecular planes of the PTCDA molecules form an average angle of ~9° with respect to the Si(111) substrate plane.[113] This value is in very good agreement with the one obtained by the analysis of NEXAFS spectra.

The results of infrared measurements for a 120 nm thick film of DiMe-PTCDI on S-GaAs(100) are shown in Figure 48.

Figure 48a shows the infrared reflectance spectra measured in s-polarization at a 20° angle of incidence with the [011] (thick line) and [0−11] (symbols) directions of the substrate parallel to the plane of light incidence; that is, the electric

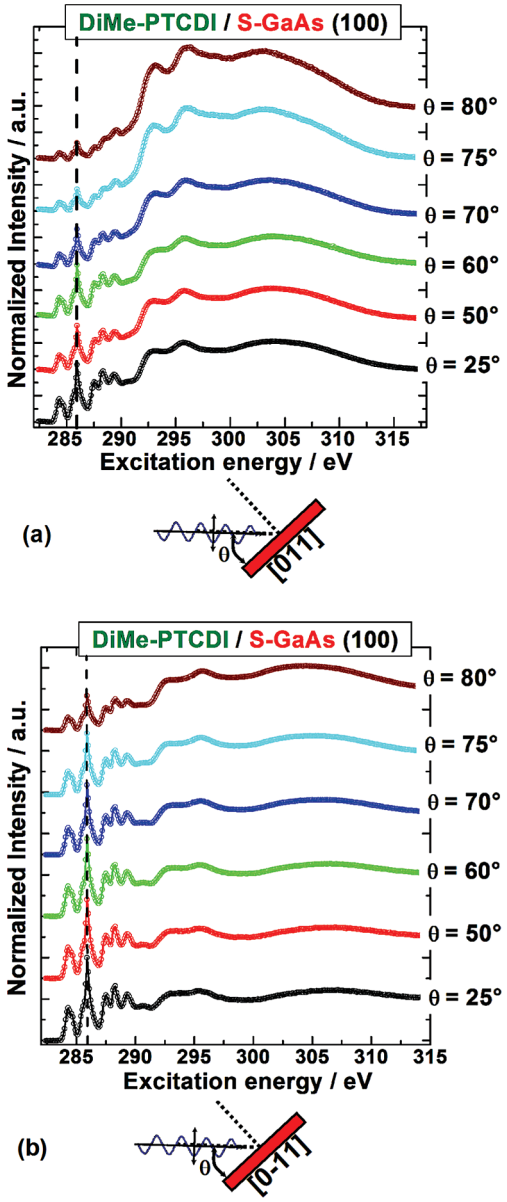

Figure 46. C K-edge NEXAFS of DiMe-PTCDI as a function of the angle of incidence θ when the plane of incidence contains the [011] (a) or [0−11] (b) directions of the S-GaAs(100) substrate.

field is parallel to the [0−11] and [011] directions. Here, the angle of incidence is defined with respect to the sample normal. The increasing background in the spectral region below 1200 cm^{-1} originates from the absorption of the GaAs substrate. The increase of the background is stronger for experiments measured at an incidence angle of 60°, since this angle is closer to the Brewster angle of GaAs. For near normal incidence, it is obvious that the s-polarized spectra in the [011] and [0−11] directions show totally different absorption features. From these spectra it can be derived without any calculation that the film has strong in-plane anisotropy.

By comparing the experimental frequencies and intensities with calculated ones (see Table 14), the strongest features measured along the [0−11] direction can be assigned to vibrations along the *x*-direction of the molecule. The contribution of features related to vibrations with dominant elongations along other molecular directions is small. Dominance of features related to vibrations with elongations along the *y*- and *z*-directions of the molecule, on the other

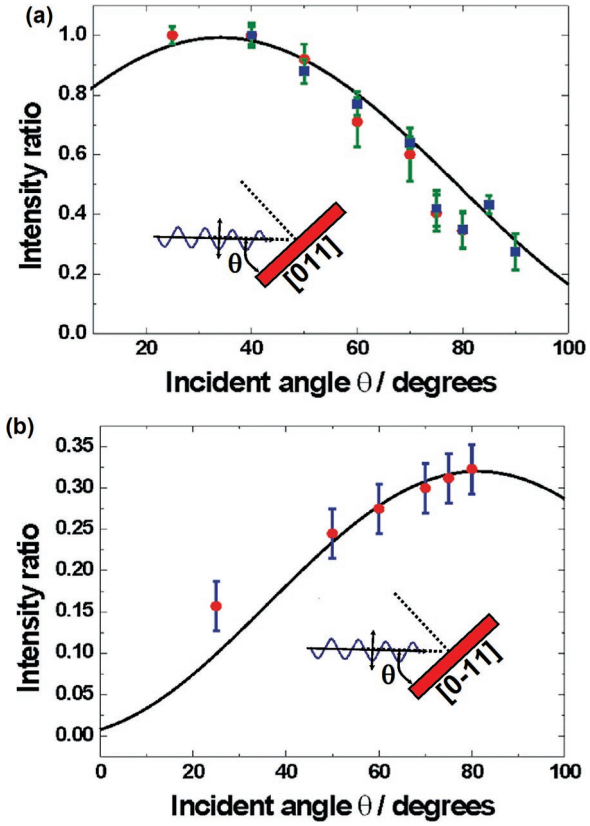

Figure 47. Experimental (symbols) and calculated (lines) intensity ratios of π^* resonances at 285.9 eV as a function of incidence angle. Different symbols indicate different samples.

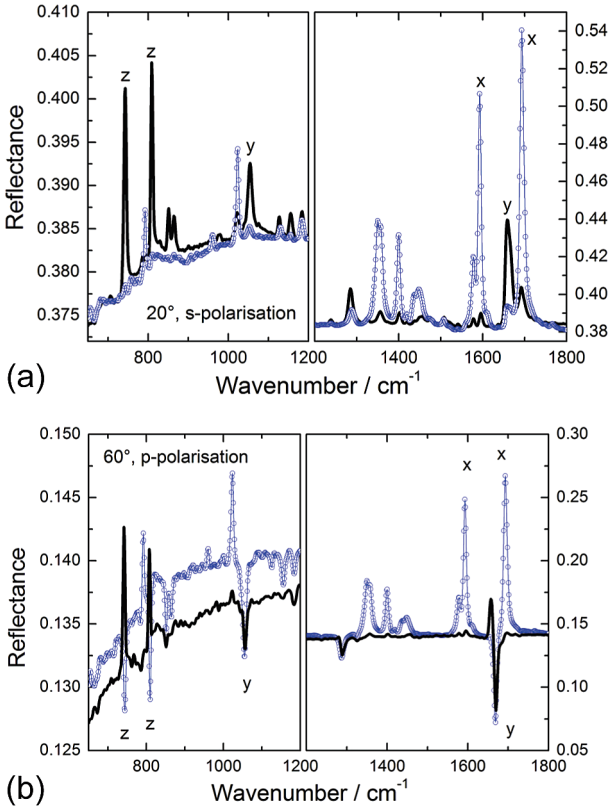

Figure 48. Infrared reflection spectra of a 120 nm thick DiMe-PTCDI film with the [011] direction (thick line) and [0−11] direction (symbols) of the S-GaAs(100) substrate parallel to the plane of incidence recorded at a 20° angle of incidence with s-polarized light (a) and at a 60° angle of incidence with p-polarized light (b). The bands labeled with *x*, *y*, and *z* originate from internal vibrations that induce a change in the molecular dipole along the respective molecular axes.

hand, is observed in the [011] direction spectra. Interestingly, for a 60° angle of incidence and p-polarized light, the *z* modes point downward. Such a behavior may occur in the vicinity of the Brewster angle for strongly absorbing modes that can couple well to the electric field component parallel to the sample normal (see, e.g., ref 114). However, for an accurate explanation of the observed behavior, a simulation taking into account the film thickness, the complex refractive index, and the optical anisotropy of the film is necessary.

From the spectra in Figure 48 we can derive that the DiMe-PTCDI molecules are preferentially arranged with their *x*-axis in the [011] direction. The measurements at a 60° angle of incidence for s-polarized light (not shown) are similar to those in Figure 48a and confirm the in-plane anisotropy.

Additional information about the vibrational modes along the [100] direction can be extracted from the 60° measurements using p-polarized light for which the electric field vector lies in the incidence plane. The spectra are presented

Table 14. Comparison between the Experimental Infrared Modes for PTCDA and DiMe-PTCDI Films on S-GaAs(100) and Calculated Properties for an Isolated Molecule[a]

experiment (cm^{-1})		B3LYP:3-21G (cm^{-1})		symmetry		dominant character	
PTCDA	DiMe-PTCDI	PTCDA	DiMe-PTCDI	PTCDA	DiMe-PTCDI	PTCDA	DiMe-PTCDI
733	743	764	786	$B_{3u}(z)$	$A_u(z)$	$\delta_{O=C-C} + \delta_{C-O-C} + \delta_{C-C-C,}$ oop	$\delta_{C-H} + \delta_{C-C-C}$, oop
809	809	853	859	$B_{3u}(z)$	$A_u(z)$	$\delta_{C-H} + \delta_{C-C-C}$, oop	$\delta_{CH3} + \delta_{C-C-C}$, oop
939		947		$B_{1u}(y)$		$\nu_{C-C} + \nu_{C-O}$	
1017, 1024	1022, 1053	1040	1032	$B_{1u}(y)$	$B_u(x)$	$\nu_{C-O} + \nu_{CC}$	$\delta_{C-H} + \nu_{ring} + \delta_{CH3}$
1236	1237	1256	1260, 1265	$B_{1u}(y)$	$B_u(y)$; $B_u(x)$	$\delta_{C-H} + \nu_{C-C}$	$\delta_{C-H} + \delta_{ring} + \delta_{CH3}$; $\delta_{C-H} + \delta_{C-N-C}$
1300	1285	1309	1317	$B_{2u}(x)$	$B_u(y)$	$\delta_{C-H} + \nu_{C-C}$	$\delta_{C-H} + \delta_{C-N-C} + \delta_{CH3}$
	1350, 1358		1346		$B_u(x)$		$\nu_{C-C} + \delta_{C-N-C} + \delta_{C-H} + \delta_{CH3}$
1407	1400	1439	1372	$B_{2u}(x)$	$B_u(x)$	$\delta_{C-C} + \nu_{C-C}$	$\delta_{C-H} + \delta_{CH3} + \nu_{C-N}$
	1436, 1449		1438, 1456; 1483		$B_u(x)$; $B_u(x)$, $B_u(x)$		$\delta_{C-H} + \nu_{C-C}$; $\delta_{C-H} + \delta_{ring} + \delta_{CH3}$ CH_3 umbrella def
1594	1577, 1593	1618	1617	$B_{2u}(x)$	$B_u(x)$	$\nu_{C-C} + \delta_{C-H}$	$\nu_{C-C} + \delta_{C-H}$
1731, 1743	1658, 1665	1756	1678	$B_{1u}(y)$	$B_u(y)$	$\nu_{C=O}$	$\nu_{C=O}$
1771, 1778	1692, 1696	1796	1715	$B_{2u}(x)$	$B_u(x)$	$\nu_{C=O}$	$\nu_{C=O} + \delta_{CH3}$

[a] The modes labeled with oop correspond to vibrational elongations that take place out of the molecular plane. For all other modes, the atoms move within the molecular plane.

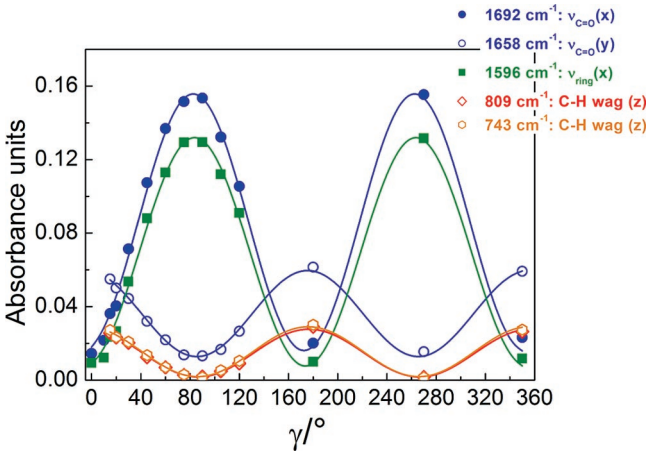

Figure 49. Intensity of *x*, *y*, and *z* IR features of a DiMe-PTCDI film with a thickness of 120 nm as a function of azimuthal angle γ for near normal incidence. Measurements are performed with s-polarized light.

Table 15. Dichroic Ratios Observed for Selected Infrared Modes of DiMe-PTCDI

		dichroic ratio	
wavenumber (cm^{-1})	character	I_a/I_b	I_b/I_a
743	*z*	15.8	
809	*z*	16.5	
1054	*y*	4.5	
1596	*x*		18.1
1658	*y*	4.7	
1692	*x*		10

in Figure 48b. For the measurement along the [011] direction (thick line), we see the *x* features pointing up and additional *y* and *z* features pointing down. In the [0−11] direction (symbols), the contribution of *x* features is negligibly small. Only *z* features pointing up and *y* features pointing down are perceptible. The p-polarized spectra in Figure 48b clearly indicate that the molecular planes are tilted with respect to the substrate surface.

Figure 49 shows the results of measurements performed at near normal incidence, turning the sample around its surface normal by an angle γ starting with the plane of incidence containing the [011] direction of the substrate. The behavior of the DiMe-PTCDI bands can be well described by a $\cos^2$ function shown by lines in Figure 49. The intensity maxima of the *y* and *z* features are shifted by an angle of about 90° with respect to those of the *x* features. Maxima are observed at the angles $\gamma_x = 7°$ and $\gamma_y = \gamma_z = 94°$. The ratios of the maximum and minimum in-plane intensity values are presented in Table 15.

With the minimum I_{ax} and maximum I_{bx} values of the *x* features, a coarse evaluation can be performed using the formula given by Turrell[115] for the determination of the dichroic ratio D_x. The formula derived for transmission spectra is applied here to reflection spectra of a 120 nm thick film showing absorption features similar to those which are characteristic for transmission spectra. We obtain

$$D_x = \frac{I_{bx}}{I_{ax}} = \frac{n_a}{n_b}\cot^2\phi \qquad (26)$$

Here, the refractive indices $n_b = 2.11$ and $n_a = 1.62$ determined previously by spectroscopic ellipsometry in the near-infrared range are employed.[116] The a and b directions defined via the minimum and maximum intensity values in Figure 49 almost coincide with the directions of the electric field vector during measurement. They correspond to the [011] and [0−11] directions of the substrate, respectively. Furthermore, we can estimate the ratios

$$D_y = \frac{I_{ay}}{I_{by}} \quad \text{and} \quad D_y = \frac{I_{ay}}{I_{by}} \qquad (27)$$

Under the assumptions that the long axes of the molecules are parallel to the sample surface and that the molecules have a good preferential orientation with their long axis parallel to the [011] direction of the sample, we can determine in a further approach an average tilt angle θ of the molecular plane with respect to the sample surface from the quotient of D_y and D_z:

$$\tan^2(1-\theta) = \frac{D_y}{D_z} \qquad (28)$$

With the quantities from Table 15, a tilt angle of $\theta = 62° \pm 6°$ is calculated. The angle is slightly larger compared to that from NEXAFS. Sources of error are the low intensity of infrared features, the angular spread of infrared light, and the assumption that the *x*-axis of the molecules lies parallel to the sample surface.

The angle θ determined from eq 26 should be the same for all *x* modes. However, with eq 26, different angles θ are calculated from the different dichroic ratios D_x of the ring band at 1596 cm^{-1} and the side group band at 1692 cm^{-1}. The deviation is too high to be explained by the experimental error alone. Further investigations are required for a better understanding.

5.1.5. Molecular Orientation of PTCDA and DiMe-PTCDI Films on S-GaAs(100) Substrates Determined by Means of Raman Spectroscopy

First of all, Raman spectroscopy provides evidence for the crystalline nature of films through the presence of external molecular modes (phonons). Dedicated studies were already carried out for PTCDA crystals[52] and thin films[11,117] as well as on DiMe-PTCDI crystals and thin films.[14,58] The number and frequency positions of these phonons in films correspond to those detected in a single crystal (see section 2.3—Vibrational Properties) for which XRD measurements proved a crystalline composition with monoclinic symmetry. Typical examples of phonon spectra of thin films are shown in Figure 50.

PTCDA films exhibit a very weak dependence of the Raman scattered intensity upon the azimuthal rotation of the sample around the substrate normal, supporting the in-plane isotropy found by IR.[113] For DiMe-PTCDI, the situation is entirely different. Considering the long-range ordering of DiMe-PTCDI films, a quantitative analysis of the polarization-dependent Raman spectra will be attempted in the following in order to assess the molecular orientation.

For this purpose, the 120 nm thick DiMe-PTCDI film was rotated clockwise azimuthally in steps of 10°. A fixed laboratory coordinate system (*x*,*y*,*z*) was defined such that the *z*-axis is parallel with the direction of the incident beam and perpendicular to the sample surface. The *x*-axis was defined to be parallel to the direction of the analyzed polarization. The electric field vector of the incident radiation was either parallel to *x* or perpendicular to it (parallel to the *y*-axis). The laboratory axes coincide with the substrate axes ($x = x_s$ = [011], $y = y_s$ = [0−11], $z = z_s$ = [100]) when γ

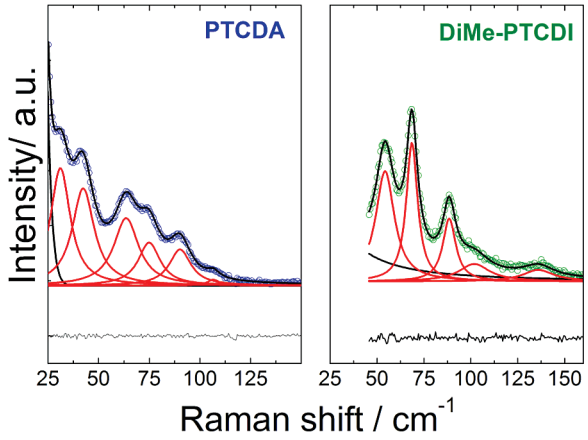

Figure 50. Phonon Raman spectra of PTCDA (left) and DiMe-PTCDI (right) thin films (40 nm) recorded at room temperature without analyzing the polarization of the scattered light.

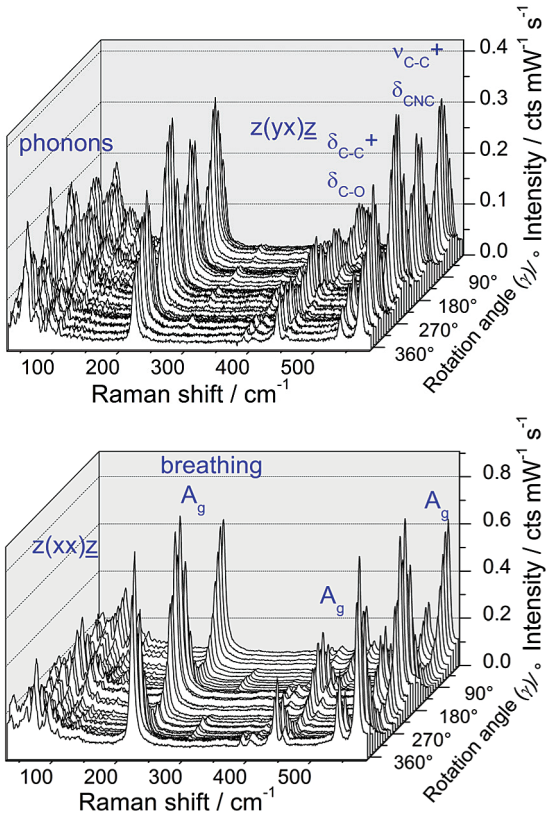

Figure 51. Low-frequency Raman spectra of a DiMe-PTCDI film with a thickness of 120 nm upon rotation of the sample around its normal (with angle γ). The spectra on the left and right are recorded in crossed and parallel polarization, respectively.

$= 0°$. Two polarization configurations were used for each sample position. In the Porto notation, $z(xx)\bar{z}$ and $z(yx)\bar{z}$ denote the cases when the incident electric field vector of scattered light is parallel/perpendicular to that of the analyzed light (parallel/crossed polarization configuration). The spectra obtained upon sample rotation are shown in Figure 51.

The Raman intensities of A_g modes vary with a period of 180° and 90° in parallel and in crossed polarization, respectively. The maximum response in parallel polarization for the A_g modes takes place when the electric field vectors are parallel to the [011] direction of the substrate ($\gamma = 0°$, 180°). This indicates a good ordering of the molecules with a preferred orientation of their x_m axis close to the [011] substrate axis, in agreement with the NEXAFS and IR results.

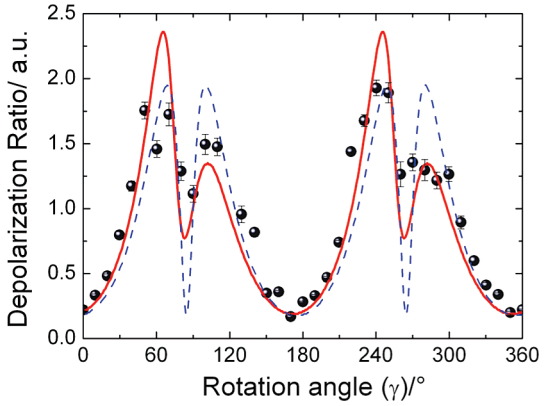

Figure 52. Experimental (symbols) and simulated (lines) depolarization ratios of the breathing mode at ~221 cm^{-1} obtained upon rotation around the sample normal to the angle γ for a DiMe-PTCDI film.

The density functional methods employed for the assignments of vibrational modes served also for determination of the Raman tensor specific for the A_g modes:

$$A_g^m = \begin{pmatrix} a & d & 0 \\ d & b & 0 \\ 0 & 0 & c \end{pmatrix} \tag{29}$$

As an example, the tensor components obtained for the molecular breathing mode at ~221 cm^{-1} have the following values: $a = 1$, $b = 0.04$, $c = 0$, and $d = -60$, with the tensor elements being normalized with respect to the a component. The considered mode elongates the molecule mainly along the long molecular axis x_m. One has to keep in mind that these values were calculated for an isolated molecule under nonresonant conditions.

As already mentioned in section 2.3—Vibrational Properties, the symmetry of the HOMO of DiMe-PTCDI is A_u, and that of the LUMO is B_g. Therefore, a resonant Raman effect involves a HOMO−LUMO transition with an electronic transition dipole oriented along the x_m axis. The effect of resonant excitation is taken into consideration by neglecting the off-diagonal components ($a = 1$; $b = 0.04$; $c = d = 0$). On the other hand, we have seen that the twofold Davydov frequency splitting expected due to the coupling of the two molecules in the unit cell is so small for the internal modes of DiMe-PTCDI that it lies at the experimental detection limit for both Raman and infrared active modes. Therefore, any perturbation of the molecular Raman tensor elements induced by intermolecular interactions can be neglected.

The depolarization ratio introduced in section 2.3—Vibrational Properties is a useful quantity for analyzing a sample polarization response.[46] The experimental values for the 221 cm^{-1} mode are shown as a function of rotation angle γ by symbols in Figure 52.

In order to extract the geometrical arrangement of the molecules from the depolarization ratios, there are three coordinate systems to be taken into account: molecular (x_m,y_m,z_m), substrate (x_s,y_s,z_s), and laboratory (x,y,z). Two consecutive transformations are required to transform the molecular Raman tensor to the laboratory reference. The first orthogonal transformation can be applied using the Euler angles (φ,θ,ψ). This method was previously employed by Aroca et al. for the Raman study of a highly symmetric molecular system (InPcCl, point group D_{4h}).[118] The transformation from the molecular to the substrate coordinate

system is described by

$$R = R(\varphi)\, R(\theta)\, R(\psi) \tag{30}$$

where

$$R(\varphi) = \begin{pmatrix} \cos\varphi & \sin\varphi & 0 \\ -\sin\varphi & \cos\varphi & 0 \\ 0 & 0 & 1 \end{pmatrix}$$

$$R(\psi) = \begin{pmatrix} \cos\psi & \sin\psi & 0 \\ -\sin\psi & \cos\psi & 0 \\ 0 & 0 & 1 \end{pmatrix}$$

and

$$R(\theta) = \begin{pmatrix} 1 & 0 & 0 \\ 0 & \cos\theta & \sin\theta \\ 0 & -\sin\theta & \cos\theta \end{pmatrix} \tag{31}$$

The molecular Raman tensor will be transformed according to

$$A_g^S = \mathbf{R} A_g^m \mathbf{R}^{-1} \tag{32}$$

where $\mathbf{R}^{-1}$ is the transpose matrix of $\mathbf{R}$.

The second transformation is from the substrate to the laboratory coordinate system and implies a clockwise rotation around the substrate normal (z_s) with the angle γ.

The corresponding rotation matrix is

$$R(\gamma) = \begin{pmatrix} \cos\gamma & \sin\gamma & 0 \\ -\sin\gamma & \cos\gamma & 0 \\ 0 & 0 & 1 \end{pmatrix} \tag{33}$$

and the transformation is described as

$$A_g = R(\gamma)^{-1} A_g^s R(\gamma) \tag{34}$$

The Raman intensity is then calculated as

$$I = (\vec{e}_i A_g \vec{e}_s)^2 \tag{35}$$

where $\vec{e}_i$ and $\vec{e}_s$ describe the directions of the electric field vectors for the incident and the scattered light, respectively.

A least-square fit of the experimental depolarization ratio was performed using a Levenberg−Marquardt algorithm. The closest match between the calculated depolarization ratios using the one-molecule approximation is presented in Figure 52 by the dashed line.

The corresponding set of Euler angles is ($\varphi = -70°, \theta = 53°, \psi = 51°$), which means that the molecular plane is tilted with respect to that of the substrate by 53° ± 5°, and the angle between the projection of x_m onto the substrate plane and [011] the substrate axis is −7° ± 5°. This set of angles is very close to those determined from the NEXAFS and infrared measurements (see previous subsections). However, even though the main maxima of the experimental data are reproduced well, the steep minima and the same height of all maxima indicate that a more complex model is required.

Considering the crystalline nature of the film reflected by the presence of phonons, a natural approach would be to consider two non-interacting molecules the Raman signals of which add up. The model was constructed such that the angles between the two molecules in the unit cell are maintained equal to the angles reported for the single crystal and only the unit cell is rotated with respect to the substrate by changing the Euler angles. The coordinate system of the unit cell (x_u, y_u, z_u) was chosen so that the x_u and y_u axes are contained in the (102) crystallographic plane. The molecular planes of the two molecules are tilted +8° and −8° with respect to the ($x_u y_u$) plane, and the long axes of the two molecules are rotated by +18° and −18° with respect to the x_u axis.

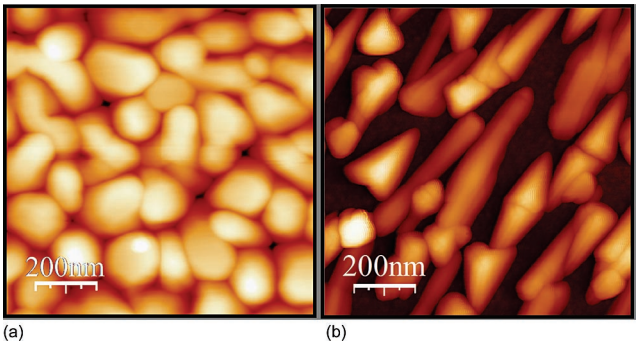

Figure 53. AFM images of a 30 nm PTCDA (a) and a 20 nm DiMePTCDI (b) film grown on S-GaAs(100).

The lowest deviation between the calculated and the experimental data is provided by the following set of Euler angles: $\varphi = 114° \pm 5°$; $\theta = 56° \pm 4°$, $\psi = 28° \pm 5°$. This means that the crystal (102) plane forms an angle of 56° with the substrate plane, and the projections of the long molecular axis deviate from the [011] direction of the substrate by $\phi_1 = -7° \pm 5°$ and $\phi_2 = -48° \pm 11°$, respectively.

It must be noted that in each of the two models the minima of the depolarization ratio should be very close to zero, assuming that the scattered light is totally polarized. In order to reproduce the experimental values in the minima, the scattered intensities in parallel and perpendicular configurations had to be mixed by a constant factor D:

$$\mathrm{Dep} = \frac{(1-D)I_{yx} + DI_{xx}}{DI_{yx} + (1-D)I_{xx}} \tag{36}$$

The parameter D was also optimized during the fitting procedure, and for both models, the resulting value was $D \sim 0.15$. This parameter describes a depolarization in the light scattered by the sample due to the surface roughness, thickness nonuniformity, angular spread of the collected beam,[119,120] and, eventually, spread in the orientation of some molecules from the preferential arrangement.

5.1.6. AFM Investigations

Deposition of PTCDA on S-passivated GaAs(100) at room temperature leads to PTCDA aggregates with an average diameter of 100 nm. Figure 53a shows a topographic AFM picture (1 μm × 1 μm) taken from a 30 nm thick PTCDA film. X-ray diffraction investigations performed on this sample revealed only one diffraction peak corresponding to the (102) plane of the PTCDA crystal, indicating a predominant orientation of these planes parallel to the substrate surface. In the case of DiMePTCDI, on S-passivated GaAs(100), deposition at room temperature leads to the formation of ribbon-like crystals. In Figure 53b, a topographic AFM picture (1 μm × 1 μm) corresponding to a nominal coverage of 20 nm is shown. The crystallites in the image are aligned with the [011] edges of the cleaved substrate. Their morphology supports the strong optical in-plane anisotropy of DiMe-

Table 16. Angles Defining the Orientation of the DiMe-PTCDI Molecules with Respect to the S-GaAs(100) Substrate as Determined from the Techniques Discussed in This Work[a]

			Raman	
	NEXAFS	IR	one molecule	two molecules
θ (deg)	56 ± 5	62 ± 6	53 ± 5	56 ± 4
ϕ (deg)	-7 ± 3	11.7 ± 3	-7 ± 5	$\phi_1 = -7 \pm 5$ $\phi_2 = -48 \pm 11$

[a] The angles θ and ϕ denote the tilt of the molecular plane with respect to the substrate plane and the angle made by the projection of the long molecular axis on the substrate plane with respect to the [011] direction of the substrate.

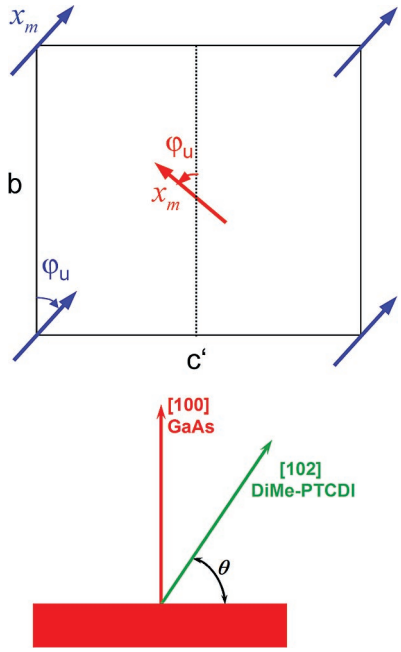

Figure 54. Schematic of the DiMe-PTCDI unit cell in the (102) crystalline plane (left) and of the relative orientation of the (102) planes with respect to the S-GaAs(100) substrate (right). Both planes are defined by the normal direction.

PTCDI films derived from NEXAFS, IR, and Raman spectroscopy.

To summarize, NEXAFS, IR, and Raman spectroscopies were applied for the determination of the molecular orientation in PTCDA and DiMe-PTCDI films grown on chalcogen-passivated GaAs(100) substrates. While the PTCDA molecules were found to lie flat on the substrate by means of NEXAFS, IR spectroscopy, and, previously, XRD, a large tilt angle of the DiMe-PTCDI molecular plane with respect to the GaAs(100) substrate plane and a preferential azimuthal orientation were determined. The tilt and azimuthal angles from NEXAFS, IR, and Raman spectroscopy are summarized in Table 16.

Figure 54 shows a sketch of the unit cell in the (102) DiMe-PTCDI crystal plane and the relative orientation with respect to the GaAs substrate. The good agreement between the tilt angles derived from different techniques indicates that each of them is a reliable method. However, the deviation in the azimuthal angle supports the thesis that a one-molecule model is too simple.

The AFM image displaying long-range ordering and the observation of molecular external modes in Raman spectroscopy provide evidence for the crystalline character of the films. Therefore, a model taking into account two molecules with the relative angular orientation as in a monoclinic crystal is expected to bring more accurate results. Up to now, only the Raman data were evaluated with the model taking both molecules in the unit cell into account.

Of the techniques applied, resonant Raman spectroscopy and NEXAFS are best suited to characterize the molecular orientation in very thin samples (~1 nm). Thicker samples (~100 nm) are required for the determination of molecular orientation by infrared spectroscopy. From the point of view of data evaluation, the mathematical formalism for NEXAFS is the simplest one. The strength of the Raman evaluation lies in the use of the depolarization ratio, which reduces the experimental errors affecting the absolute intensities. However, the weakness of the Raman evaluation is related to the complex formalism employing the knowledge of the Raman tensor. The strength of infrared spectroscopy lies in the simple detection of anisotropy. With the knowledge of optical constants, the azimuthal angle can be directly derived from the dichroic ratio. Due to the poor access to the direction perpendicular to the substrate surface, the IR accuracy for the determination of the tilt angle is comparatively low.

5.2. Energy Band Dispersion in Well-Ordered Thin Films

The electronic properties relevant for the device performance depend not only on the molecular structure but also on the molecular arrangement. In particular, well-ordered organic crystals or thin films are beneficial for achieving high carrier mobilities.[121−123] The ability of these materials to transport charges (holes and electrons) due to the π-orbital overlap of neighboring molecules defines their semiconducting and conducting properties. The self-assembling or ordering of these organic materials enhances this π-orbital overlap and is the key to improvement in carrier mobilities.

Many organic crystals are formed by regularly repeating a small unit along one direction. In such systems, the electronic energy levels of the units with the same energy may interact via the outermost orbitals, leading to a splitting of the respective energy levels. The width of the resulting energy band then depends on the magnitude of the interaction. For organic semiconductors, the width of the bands is expected to be very small due to the weak van-der-Waals interaction. Therefore, the observation of the intermolecular energy band dispersion is, to a certain extent, challenging.

Recently, the intermolecular energy dispersion of the HOMO band was measured for the archetypal organic semiconductor PTCDA deposited onto MoS_2 to be 0.2 eV.[124] Similarly, our own results revealed by means of energy-dependent VB-PES measurements an overall energy shift of 0.2 eV for the HOMO of DiMe-PTCDI on S-GaAs(100).

Figure 55 shows measured valence band spectra and their dependence on incident photon energy of 15 nm of DiMe-PTCDI grown onto S-GaAs(100) surfaces (a) and of 3 nm of PTCDA grown onto MoS_2[124] (b). The HOMO feature reveals a weak but clearly observable shift. The shift amounts to approximately 0.2 eV for both systems and is attributed to the intermolecular $\pi-\pi$ interaction. Moreover, for DiMe-PTCDI, the dispersion of the HOMO − 1 feature is much less pronounced when compared to the HOMO feature. This is explained by the higher binding energy and the predominant σ-character of the molecular orbitals contributing to HOMO − 1.[125]

Experiments conducted by measuring the energy dependence of the valence electrons emitted normal to the substrate surface reveal, if present, energy band dispersion for wave

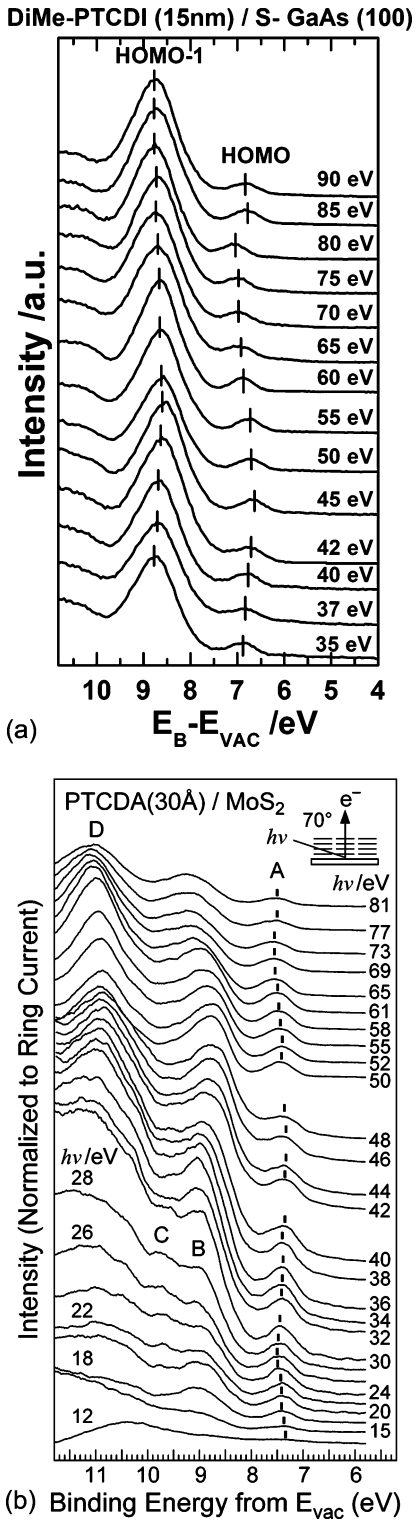

Figure 55. Energy band dispersion of a 15 nm film of DiMe-PTCDI grown onto S-GaAs(100) (a) and of 3 nm film of PTCDA grown onto MoS_2 (b). Reprinted with permission from H. Yamane, S. Kera, K. K. Okudaira, D. Yoshimura, K. Seki, and N. Ueno, *Physical Review B, 68,* p 033102, 2006 (http://link.aps.org/abstract/PRB/v68/p033102). Copyright 2006 by the American Physical Society.

vectors varied along the direction perpendicular to the sample surface. The perpendicular component of the initial state wave vector is usually determined assuming free electron-like final states and an inner potential V_0, which has to be determined. V_0 is treated as a fit parameter to obtain the expected periodicity of the dispersion in the reciprocal space. As reported in 2003 by Yamane et al.,[124] the tight binding model is a suitable approach to determine such an energy band dispersion. The approach is discussed in the following and applied to the DiMe-PTCDI case, taking into account the complementary results providing information on the intermolecular spacing.

The measured energy shift was converted into a dispersion relation assuming the three-step model[126] for the photoemission process as well as energy and momentum conservation before and after photoexcitation so that the following relations hold:

$$E_f = h\nu + E_j, \quad \vec{k}_f = \vec{k}_i + \vec{G}, \quad E_{Kin} = E_f \tag{37}$$

where E_i, E_f, $\vec{k}_i$, and $\vec{k}_f$ are the electron energies and the wave vectors before and after photoexcitation in the solid, and $\vec{G}$ is a reciprocal lattice vector. E_i and E_f are defined relative to the vacuum level such that E_f corresponds to the kinetic energy of the emitted electrons E_{Kin}. Determination of the final momentum $\vec{k}_f$ requires the knowledge of the final state band dispersion $E_f(\vec{k}_f)$, which is, however, generally unknown. Therefore, it is commonly assumed that the final state can be approximated by a free electron-like dispersion by applying an appropriate inner potential V_0:

$$E_f = \hbar^2 k^2 / 2m^* + V_0 \tag{38}$$

where m^* is the effective mass of the electron and V_0 is the constant inner potential in the solid for the final state free-electron-like parabola. Then, the following relations are used:

$$E_i = E_{Kin} - h\nu \tag{39}$$

$$k_i^{\perp} = k_f^{\perp} = [2m^*(E_f - V_0)]^{1/2}/\hbar = [2m^*(E_{Kin} - V_0)]^{1/2}/\hbar \tag{40}$$

where $k_i^{\perp}$ and $k_f^{\perp}$ are the normal components of the wave vector before and after the photoexcitation in the solid, respectively. These equations indicate that the values of E_i and $k_i^{\perp}$ can be determined from the measured E_{Kin} and $h\nu$. The effective mass of the excited electron m^* is approximated by the mass of the free electron m_0.

The energy band dispersion relation for DiMe-PTCDI is obtained by applying the one-dimensional tight-binding theory to the HOMO of the perylene core. For the formation of a 1D energy band, it is assumed that a unit, i.e., a molecule, is repeating along an axis x with a period a. The interaction only takes place with the nearest neighbors, with its strength being defined by the value t, the transfer integral. By analogy to the Hückel theory,[127] the energy E_B for the HOMO is expressed in terms of wave vector $k_\perp$ as[128]

$$k_\perp = [2m^*(h\nu - E_B - V_0)] \tag{41}$$

$$E_B(k_\perp) = E_B^0 + 2t\cos(a_\perp k_\perp) \tag{42}$$

Using the normal emission spectra and eqs 41 and 42, the energy of the highest valence band and its momentum can be calculated. However, for the experimental determination of the energy band dispersion, we need to determine the values of t, $a_\perp$, and V_0.

From the NEXAFS, infrared, and Raman spectroscopy results presented above, we learned that the DiMe-PTCDI molecules deposited onto S-GaAs(001) are tilted with respect to the substrate surface by an angle of (56° ± 4°) and are

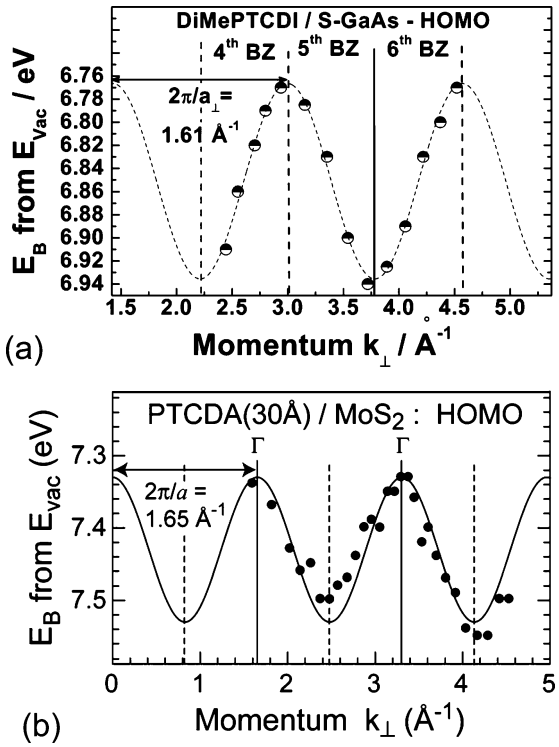

Figure 56. Experimental dispersion for the HOMO band (circles) of DiMe-PTCDI (a) and PTCDA (b) together with the best fit curve (line) in the tight-binding model. Figure 56b is reprinted with permission from H. Yamane, S. Kera, K. K. Okudaira, D. Yoshimura, K. Seki, and N. Ueno, *Physical Review B, 68*, p 033102, 2006 (http://link.aps.org/abstract/PRB/v68/p033102). Copyright 2006 by the American Physical Society.

predominantly oriented with their long axis parallel to the [011] direction. With the distance between the intermolecular planes of 3.21 Å, as experimentally determined,[43] we can calculate the length of the repeating unit (lattice spacing normal to the surface) as $a_\perp = 3.9$ Å.

The results of the best fit for the dispersion along with the experimental data are shown in Figure 56a. A cosine fit of the experimental data was performed where the inner potential V_0 and the transfer integral t are the two fit parameters. The best fit between calculated and experimental data is provided by the following set of parameters: inner potential $V_0 = -5.3$ eV and transfer integral $t = 0.04$ eV.

As shown in Figure 56a, the measured HOMO energy band dispersion for DiMe-PTCDI along the surface normal is extended over three Brillouin zones (fourth, fifth, and sixth zone) with a bandwidth of about 0.2 eV. These results clearly demonstrate the existence of an energy band dispersion similar to that for PTCDA[124] (see Figure 56b). The inner potential for PTCDA was found to be $V_0 = -5.1$ eV from the low-energy transmission spectrum for an estimated lattice spacing of 3.8 Å.[124]

As shown in section 2.4—Electronic Properties: Valence Band Structures, the HOMO for both perylene derivatives, DiMe-PTCDI and PTCDA, originates from a single molecular orbital with π character which is distributed predominantly over the perylene core. The observed HOMO band dispersion originates from $\pi-\pi$ interaction along the molecular stacking direction. The results for the transfer integral of 0.05 eV and the inner potential of −5.1 eV of PTCDA are quite close to the ones of DiMe-PTCDI. This is supporting the reliability of the results, since the interacting parts are the perylene cores of the molecules in both cases. The minor differences may be due to the difference of the intermolecular van-der-Waals interaction between the stacks of the two molecular films, considering that the lattice spacing is larger for DiMe-PTCDI than the one determined for PTCDA.

5.3. Transport Gap of PTCDA and DiMe-PTCDI

The charge carrier injection processes require promotion of an electron or a hole from the electrodes into one of the charge transport (HOMO or LUMO) states of the organic semiconductor. The most direct and successful methods for the determination of energy level positions and alignment are VB-PES and IPES. A complete picture of the electronic properties can only be achieved when VB-PES and IPES are employed in combination.

In section 3.2.3—Data Analysis: Electron Spectroscopic Methods, it is shown that the transport gap of the organic materials is evaluated from the distance of the HOMO and LUMO edges instead of the HOMO and LUMO peaks. In order to justify this approach, several aspects require consideration. First, the valence states of the gas-phase molecules show line widths that are typically less than 0.1 eV.[129,130] In this case, the energy positions of the HOMO and the LUMO are better represented by the peak centroids. In organic molecular solids, corrections related to the width of the observed peaks need to be taken into account.

In that respect, it is useful to briefly reconsider the inorganic semiconductor case and refer for the moment just to the uppermost valence states. Accurate determination of valence band maxima (VBM) for inorganic semiconductors is essential for determining the effectiveness of band offset engineering at heterojunctions. In order to determine the valence band offset of a semiconductor heterojunction, detailed knowledge of the energy positions of the VBM of two adjacent materials is necessary. Due to the strong dispersion of the uppermost valence band states, the VBM have to be determined at the correct points in k-space. This can be done by selecting suitable excitation energies and by employing a linear extrapolation of the VB edge.[131] This approach is experimentally justified by the excellent results obtained when using VB-PES and IPES to derive band edges for band gap determination.[132] The arguments which suggest that the linear extrapolation is the best approximation are as follows: First, a limited angular resolution leads to a nonsymmetric broadening toward higher binding energies due to the downward dispersion from the VBM in all k-directions. Second, inelastic scattering processes (such as phonon excitation) will also lead to a broadening which is more pronounced toward higher binding energies, because at room temperature an energy loss is more probable than an energy gain by such scattering processes. Third, due to the fact that photoemission probes the final state of the system with the presence of a hole, screening processes play an important role. Incomplete screening on the time scale of the photoemission process leads to a spectral shift toward higher binding energies. Hence, if the screening is spatially and/or temporally inhomogeneous, it is the spectral weight with lowest binding energy which most closely approximates the ground state.

In organic semiconductors, the above-discussed processes are also present. Moreover, the polaron formation driven by the electron−phonon interaction is particularly effective in organic solids, since they have both strongly coupled intermolecular phonons and many low energy intermolecular

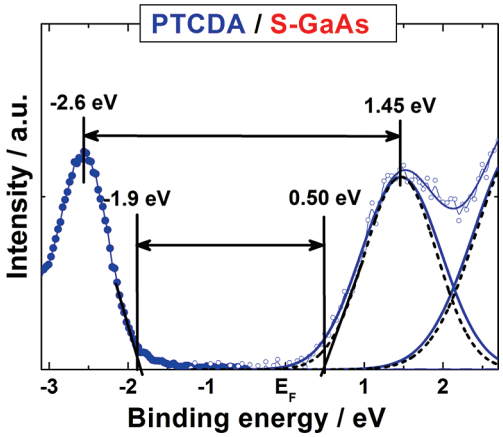

Figure 57. PES and IPES spectra of a 15 nm thick PTCDA film used for the determination of the transport gap.

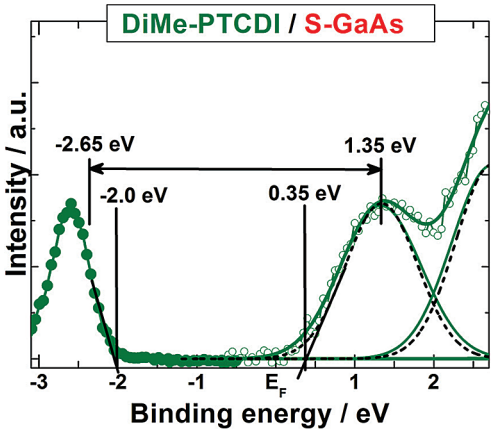

Figure 58. PES and IPES spectra of a 15 nm thick DiMe-PTCDI film used for the determination of the transport gap.

modes. Spatial variations in the electronic contributions to the intermolecular relaxation energies in the vicinity of the surface and local site-to-site variations in ion state energies due to the nonequivalent local environments in the nonsingle crystalline film can contribute to broadening as well. All processes discussed lead to nonsymmetric broadening toward higher binding energies, and in all cases, the spectral weight with lowest binding energy corresponds to the best approximation of the ground state properties.

In addition, as mentioned in the section 2.1.1—Organic Molecular Solids: Energy Levels, the VB-PES spectrum will show the HOMO shifted toward the vacuum level (E_{VAC}) (i.e., lower binding energies) by the polarization energy (P^+) induced by the presence of a molecular cation. Similarly, the IPES spectrum shows the LUMO shifted toward higher binding energies by the polarization P^- induced by the presence of the molecular anion. Moreover, VB-PES and IPES are surface sensitive techniques and, as such, provide information on electron states located predominantly in the surface molecules. The correction to obtain bulk values from the surface polarization was first experimentally estimated by Salaneck to be around 0.3 eV for the molecule of anthracene,[133] and theoretical methods to estimate the polarization energy in the bulk were developed by Soos et al.[134]

Under these considerations, when analyzing the VB-PES and IPES features, the positions corresponding to the HOMO and the LUMO, respectively, are better represented by the edges of these peaks after a proper deconvolution with the instrumental broadening.

VB-PES and IPES measurements of 15 nm PTCDA and DiMe-PTCDI films deposited onto sulfur-passivated GaAs-(100) are presented in Figures 57 and 58, respectively. The VB-PES data are depicted on the left side of the figures, while the IPES data are on the right side.

Contributions of the individual peaks to the overall intensities of the experimentally measured IPES data are plotted with lines while the deconvoluted contributions are plotted with dashed lines. The VB-PES and IPES spectra for both perylene derivatives were aligned on the energy scale with respect to the Fermi level.

The HOMO and LUMO energy positions (edges) are determined from the intercept of two linear extrapolations as described in section 3.2—Experimental Methods and Data Analysis. The results obtained for the two perylene derivatives are given in Table 17.

Table 17. Transport Gap of PTCDA and DiMe-PTCDI as Determined from Combined Measurements of VB-PES and IPES[a]

	$E_{transport}^{edge-to-edge}$ (±0.2 eV)	$E^{peak-to-peak}$ (±0.2 eV)	$E_{optical}$ (eV)
PTCDA	2.4	4.05	2.22
DiMe-PTCDI	2.35	4	2.16

[a] For comparison the optical gap values obtained from Figure 4 are presented as well.

The resulting transport gaps show a dependence on the functional groups. The addition of a more electronegative functional group to the perylene core leads to stabilization of both occupied and unoccupied energy levels. The replacement of the anhydride group by the less polar methylimide group leads to a smaller energy splitting between the energy levels, since the charge is moved from the aromatic part, acting like a donor, to the accepting functional groups. It seems that the electron-withdrawing groups strongly influence the energy positions, especially the LUMO levels. The trend observed for the transport gap is also preserved in the values for the optical gaps of these materials (see Figure 4).

It is now time to compare the VB-PES/IPES results with the results obtained using the interface dipole cancellation method presented in Figure 34 for PTCDA and in Figure 40 for DiMe-PTCDI of section 4—Initial Adsorption of Molecules on Inorganic Semiconductor Surface. There, the ionization energy for PTCDA fluctuates between (6.56 and 6.95) eV ± 0.1 eV while for DiMe-PTCDI it fluctuates between (6.36 and 6.6) eV ± 0.1 eV. Combining the VB-UPS and IPES measurements, a transport gap of (2.4 ± 0.2) eV for PTCDA and of (2.35 ± 0.2) for DiMe-PTCDI was determined. For the ionization energies of IE_{PTCDA}= 6.56 eV for PTCDA and $IE_{DiMe-PTCDI}$ = 6.36 eV for DiMe-PTCDI, values of (4.16 ± 0.2) eV for EA_{PTCDA} and (4.01 ± 0.2) eV for $EA_{DiMe-PTCDI}$ can be determined. These values are slightly larger than the ones derived by employing measurements of the interface dipole at inorganic/organic interfaces (i.e., $\Delta = f(EA)$), which are (4.12 ± 0.1) eV for PTCDA and (3.8 ± 0.1) eV for DiMe-PTCDI. The difference is even larger if the variation in the IE values of the two molecules is considered. Nevertheless, from the J-V characteristics, a value of (2.55 ± 0.1) eV for the band gap of PTCDA is expected,[135] and the value determined here by combination of VB-UPS and IPES is smaller but still in good agreement with the one expected when taking into account the experimental error of ±0.2 eV for the IPES. Conse-

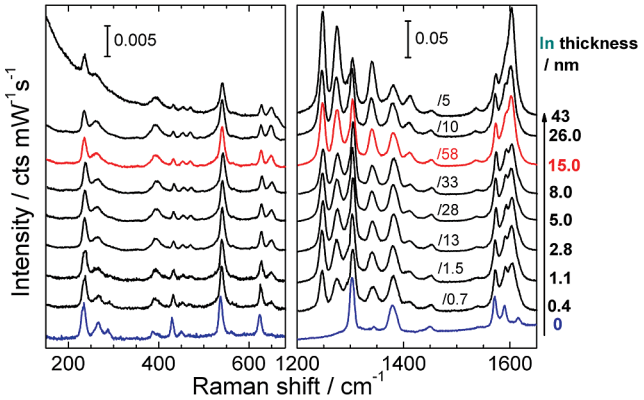

Figure 59. Raman spectra of PTCDA acquired upon successive deposition of In onto a 15 nm PTCDA film. The spectra normalization is done with respect to the intensity of the C−C stretch modes (1572 cm^{-1}).

quently, the *edge-to-edge* method for determining the transport gap is proposed to provide reliable values for the transport gap. Still, the error bar for the transport gap values is too large and further improvement in the experimental resolution is needed in order to make a precise prediction of energy level alignment at interfaces.

6. Metals on Organic Layers

6.1. Chemistry of Metal/Perylene Derivative Interfaces

6.1.1. Vibrational Spectroscopies

Metal deposition onto 15 nm thick films of PTCDA and DiMe-PTCDI was monitored by means of Raman spectroscopy in two spectral regions: below 600 cm^{-1}, where the interest is focused on the intermolecular phonon-like and intramolecular breathing modes, and between 1200 and 1650 cm^{-1}, where the C−H deformation and C−C and C═O stretching modes are located. The latter is the only region where a sufficient signal was obtained from a ML organic coverage. Figure 59 shows the Raman spectrum of a bare 15 nm PTCDA film and its evolution upon the stepwise deposition of indium.

The overall signal intensity increases with the In thickness up to 15 nm and decreases for higher metal coverages, as shown by the normalization factors in Figure 59. The same behavior is observed when Ag is deposited onto PTCDA and for both metals deposited onto DiMe-PTCDI.[136,137] This effect is known as surface-enhanced Raman scattering (SERS).[138−140] The SERS effect has been widely investigated for various molecules adsorbed on rough metallic surfaces or on metallic clusters in colloids. Reviews on this topic can be found in refs 140−143. The enhancement of normally Raman-active modes is a consequence of the enhancement of the electric field of the incoming and scattered radiation in the vicinity of a rough metal film upon coupling with the dipolar plasmon resonances in the metal clusters. This enhancement affects molecules located up to even 10 nm away from the metal surface.[139,140] The enhancement factors are essentially determined by the electronic properties of the metal and by the morphology of the metal film.

In addition to the enhancement of the totally symmetric modes, already the deposition of 0.4 nm In leads to the appearance of some modes in the higher frequency region.

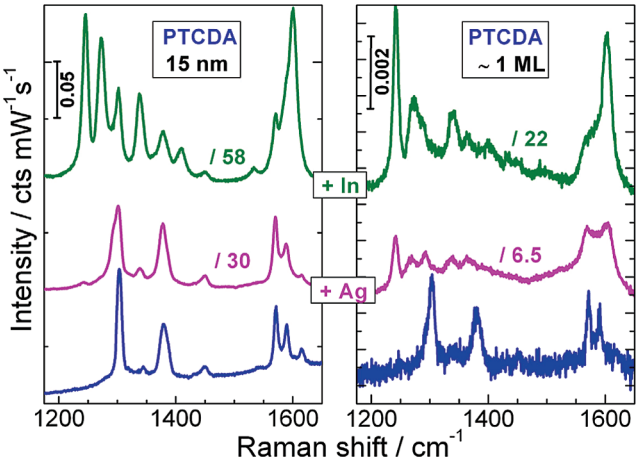

Figure 60. Raman spectra of a 15 nm (left) and a ML (right) PTCDA film clean (bottom) and covered with nominally 15 nm of silver (middle) and indium (top) each.

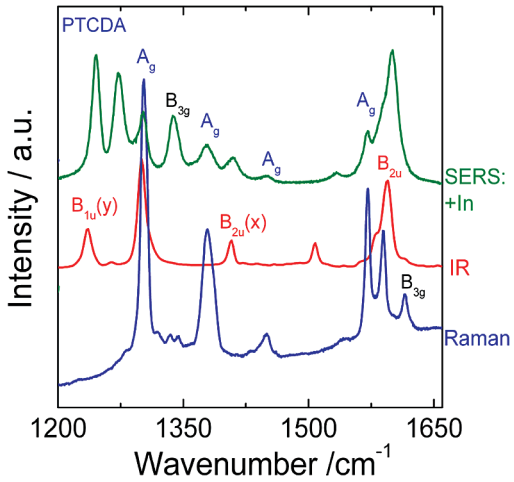

Figure 61. Example of the activation of infrared active modes in the Raman spectrum for the case of indium deposition onto PTCDA.

The same modes were also observed when depositing In or Ag onto a ML of PTCDA on S-GaAs, only with different relative intensities (Figure 60). They therefore must be a signature of the molecules in direct contact or in the very near vicinity of a metal surface. In general, such a breakdown of the selection rules accompanies the SERS effect and can be induced by several mechanisms: structural deformation of the molecule, charge transfer from the molecule into the metal or *vice versa*, or formation of new chemical bonds. Thus, the spectral changes induced by SERS can be used to extract information about chemical reactions at the interface, as well as about the morphology of the metal film.

The band at 1338 cm^{-1} was identified in ref 108 to be a B_{3g} band based on its frequency and intensity in the crystal spectra, while a band at 1292 cm^{-1} is likely to be a shifted variant of the C−H deformation A_g mode at 1303 cm^{-1} in the single crystal.[144] The other bands correspond to modes which normally show infrared activity (see Figure 61).

Considering that all the modes occurring upon In and Ag deposition are normal modes of the PTCDA molecule, the observed breakdown of the Raman-infrared selection rules was proposed to originate from a weak charge transfer between the molecules and the metal surface mediated by molecular vibrations.[137] This is in contradiction to previous findings of Hirose et al.[20] and Kera et al.,[21] who proposed the formation of a In_4PTCDA complex (for more details on

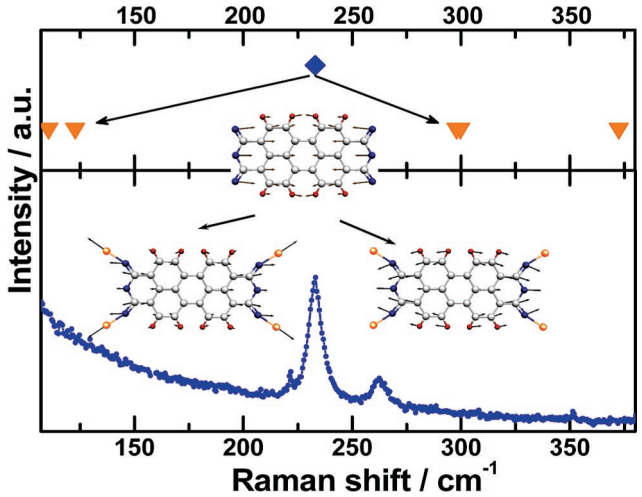

Figure 62. Raman spectrum of a PTCDA crystal along with calculated frequencies for a single molecule (rhombus) and for a In_4PTCDA complex (triangles).

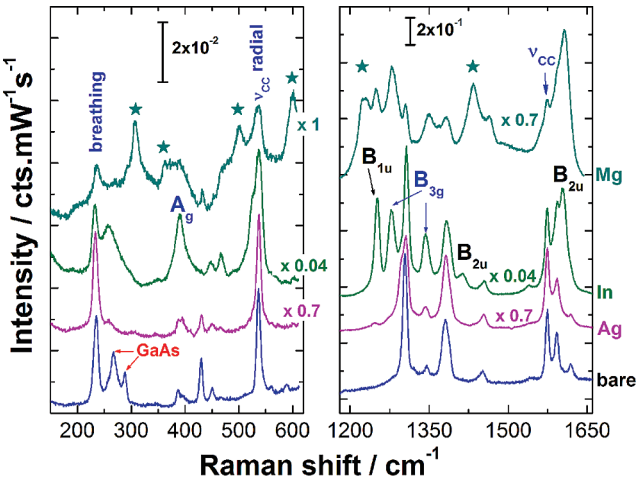

Figure 63. Raman spectra for In (5 nm), Ag (4.5 nm), and Mg (5 nm) coverages on 15 nm thick PTCDA films, compared with the spectrum of the bare PTCDA film in the spectral region of the internal breathing mode (left) and in the spectral region of the C—H deformation and C═C stretching modes (right).

their experiments, see section 6.1.2—High-Resolution Photoemission Spectroscopy).

In order to assess the effect of metal−PTCDA complex formation on the vibrational frequencies, theoretical calculations were preformed with the Gaussian 98 package on the In_4PTCDA complex using the B3LYP functional and the basis set LANL2DZ, which takes into account possible relativistic effects due to the presence of the heavy metal atoms.[51] Four In atoms were assumed to interact with the PTCDA molecule via the O atoms in the anhydride groups according to ref 21. The optimized geometry, the electronic levels, and the charge distribution over the complexes are similar to those reported in ref 21. Figure 62 shows the spectrum of a PTCDA single crystal together with the calculated frequencies for a single PTCDA molecule (rhombus) and for an In_4PTCDA complex (triangles).

The most dramatic effect of the complex formation resides in the 2-fold splitting of the breathing mode at 233 cm^{-1} (see the elongation patterns in Figure 62). The first component originates from a breathing of the whole complex, and the significant increment of mass compared to the single PTCDA molecule results in a dramatic shift toward lower frequencies (110 cm^{-1}). For the second component, the In atoms are fixed and constrain the breathing of the PTCDA molecule, increasing its frequency to 299 cm^{-1}. In the Raman experimental spectra (Figure 59) of the In/PTCDA heterostructure, the molecular breathing mode is still observed at 233 cm^{-1}, ruling out the possibility of this chemical reaction. This conclusion is further supported by infrared spectroscopy studies[137] and by recent high-resolution PES results to be presented later in this review.

In Figure 63 the Raman spectra of 15 nm films of PTCDA are shown for metal coverages of 5 nm of In, 4.5 nm of Ag, and 5 nm of Mg. The spectra in the low-frequency windows are normalized to the height of the molecular breathing mode at 233 cm^{-1}. The normalization in the high-frequency region is again performed with respect to the C═C stretch mode (1572 cm^{-1}).

The Raman spectra of the (5 nm) Mg/(15 nm) PTCDA system also exhibit the breakdown of selection rules, with the occurrence of the modes observed in the other two metal/organic heterostructures (see Figure 62). In addition, several modes with significant intensity (marked with asterisks in Figure 62) appear at 307, 502, 598, 696, 1088, 1225, and 1433 cm^{-1}. The assignment of these modes cannot yet be done unambiguously. The frequency of the mode at 598 cm^{-1} is very close to the calculated value of 592 cm^{-1} for a B_{3g} mode of an isolated PTCDA molecule.[57]

Frequency calculations performed with the same basis set and density functional methods in Gaussian 98 as in ref 57 but for a modified PTCDA molecule, in which the central O atom in the anhydride group is removed, deliver several frequencies that may be candidates for the assignment of the experimentally observed modes: 308, 500, 581, 702, and 1090 cm^{-1}. Raman active modes in MgO microcrystals[145] were observed at 595, 719, and 1096 cm^{-1}. Thus, the modes observed in the present work at 598, 696, and 1088 cm^{-1} may also indicate the formation of MgO as a result of the interaction between Mg and PTCDA. No modes of PTCDA or the modified molecule are found in the vicinity of 1225 cm^{-1}.

Whatever the final assignment of the new modes is, they are not activated in the molecules in contact with either Ag or In. Therefore, it can be concluded that the model of weak charge transfer is not sufficient to describe the interaction at the Mg/PTCDA interface.

To validate the model deduced from the results of these Raman spectroscopy experiments, detailed investigations of the Mg/PTCDA system by means of other methods that are highly sensitive with respect to the changes of the chemical environment and charge redistribution, such as photoemission spectroscopy, are required.

In Figure 64 the spectra of 15 nm DiMe-PTCDI films for metal coverages of 5 nm of In, 4.5 nm of Ag, and 5 nm of Mg are shown. The spectra in the low-frequency windows are normalized to the height of the breathing mode at 221 cm^{-1}. The normalization in the high-frequency region is performed with respect to the C−C stretching modes (1570 cm^{-1}).

In the case of DiMe-PTCDI, all the investigated metals, i.e., Ag, In, and Mg, lead to the breakdown of selection rules with the occurrence of normally infrared active modes at 1246 and 1606 cm^{-1}. The breathing mode at 221 cm^{-1} survives with increasing metal coverage. Thus, a chemical reaction between these metals and the O atoms of DiMe-PTCDI molecules can be ruled out. Interestingly, the features potentially assigned to MgO phonons do not appear in the

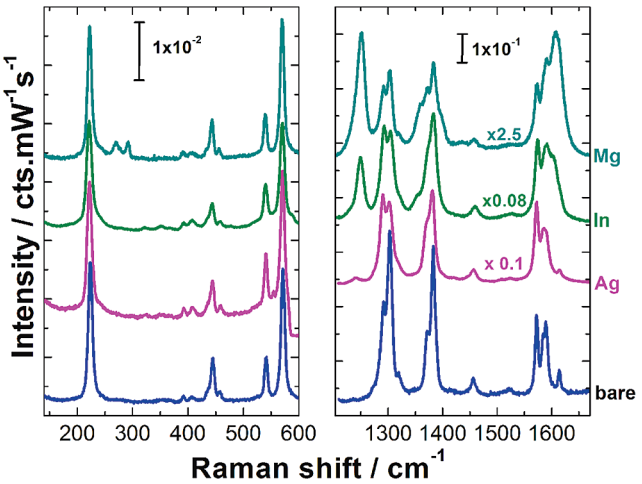

Figure 64. Raman spectra for In (5 nm), Ag (4.5 nm), and Mg (6 nm) coverages on 15 nm thick DiMe-PTCDI films, compared with the spectrum of the bare DiMe-PTCDI film.

spectra even for higher coverages of Mg. It can thus be concluded that the methylimide group in the DiMe-PTCDI molecule is less reactive compared to the O atoms in the anhydride group of PTCDA.

Raman spectroscopy showed that Ag and In behave similarly in terms of chemical reactivity when deposited onto PTCDA and DiMe-PTCDI. Both metals induced a breakdown of selection rules which was interpreted as a result of a dynamical charge transfer process. The vibrational signature of Mg deposited onto PTCDA is very different compared with those of the other metals, indicating that a strong chemical interaction between the two partners takes place. High-resolution photoemission measurements together with sophisticated core level line shape analysis can deliver a deeper insight into the physics and chemistry of the metal/organic interfaces.

6.1.2. High-Resolution Photoemission Spectroscopy

6.1.2.1. Mg on PTCDA. Figure 65a displays the C_{1s} core level spectra for bare PTCDA and for PTCDA with different Mg coverages. The C_{1s} emission spectrum of bare PTCDA is described in section 2—Properties of Organic Semiconductors: Perylene Derivatives. The contributions of the individual carbon sites evidenced by a careful fit are assigned according to the color coding at the left side of Figure 65a. The main lines (C—H, C—C, C—C═O, C═O) were curve fitted with Voigt profiles with a constant Lorentzian line width of 75 meV and a variable width for the Gaussian contribution. The ratio of the peak areas for carbon atoms in the perylene core was constrained according to the perylene stoichiometry.

For all Mg thicknesses, strong changes in the core level spectra are observed when compared to the spectrum of bare PTCDA. These include the appearance of new features and binding energy shifts, which are significantly different for the various atoms. First, we will assign the new features present in the spectra, and then, the shifts in binding energy will be explained and correlated with the appearance of the new features.

The nature of the reaction can be followed in more detail in Figure 65b, where the evolution of intensity and relative area resulting from the peak fitting analysis is presented. Upon deposition of 0.2 nm of Mg, all the components of the C_{1s} core level are significantly decreased in intensity. The strongest decrease is observed for the high binding energy components, indicating that the presence of Mg predominantly affects the carboxylic carbon (C═O) side of the molecule. Moreover, in the C_{1s} core level, two new components at 285.35 eV (C_1) and 287.45 eV (C_2) evolve on the low binding energy site of the C═O component. The C_1 component is present in the spectrum up to thicknesses larger than 13 nm while the C_2 component vanishes already at thicknesses above 3.2 nm. The occurrence of C_1 and C_2 indicates that at the initial stage of the reaction some molecules are in a higher oxidation state because of the formation of new bonds. Nevertheless, it is important to notice that if we integrate the area of these two peaks and calculate the total area, we find that this is very close to the stoichiometric ratio of 5:1 between the perylene ring (20) and functional group (4) carbon atoms. Therefore, the C_1 and C_2 structures can be attributed to intermediate phases derived from the carboxylic carbon at 289.5 eV.

In the low binding energy region, the spectra of C_{1s} show the same spectral features for all Mg coverages but with drastically different intensities and significant broadening. After the initial decrease in intensity upon deposition of 0.2 nm of Mg, the intensity of the aromatic carbon slightly increases at a coverage of 0.4 nm. We interpret the observed signal changes as a result of a redistribution of charges within the molecule. For thicknesses larger than 0.8 nm, no significant changes are observed except the attenuation in the intensity of all components as a function of Mg coverage. Moreover, the area ratio of the C_{1s} peaks in the perylene core remains constant above 0.8 nm of Mg thicknesses.

The remaining $\pi \rightarrow \pi^*$ shakeup satellites in the C_{1s} spectra, presented in the inset on the left side of Figure 65a, reveal that the organic compound preserves its aromatic structure. Therefore, one main finding from the C_{1s} fit analysis is that the modified organic molecule consists of the same number of carbon atoms as PTCDA.

A more thorough interpretation of the changes observed in the C_{1s} core level emission can be given when following the evolution of the O_{1s} and Mg_{2p} core level emission spectra. The evolution of the O_{1s} and Mg_{2p} spectra as a function of Mg thickness is presented in Figures 66a and 67a, respectively. The evolution of the intensities for different Mg coverages is summarized in Figure 66b for the O_{1s} core level and in Figure 67b for the Mg_{2p} core level.

The O_{1s} emission for bare PTCDA consists of two distinct components stemming from the different oxygen environments within the anhydride group corresponding to O═C (low binding energy) and C—O—C (high binding energy). The small intensity component at the higher binding energy side of the O═C component stems again from a $\pi \rightarrow \pi^*$ shakeup satellite.

The first major change observed in the O_{1s} core level at low Mg coverage (0.2 nm) is the significant decrease in intensity of all O_{1s} components compared to the spectrum of bare PTCDA. The second major change is the shift of the high binding energy component toward even higher energies. This change is another indication that a chemical interaction between Mg and PTCDA occurs involving predominantly the C—O—C group. At the same coverage of 0.2 nm, the Mg_{2p} signal can be fitted using three components: one component at 50.45 eV labeled Mg_1, another strong component at 51.20 eV labeled Mg_2, and a high binding energy component at 51.95 eV labeled Mg_3.

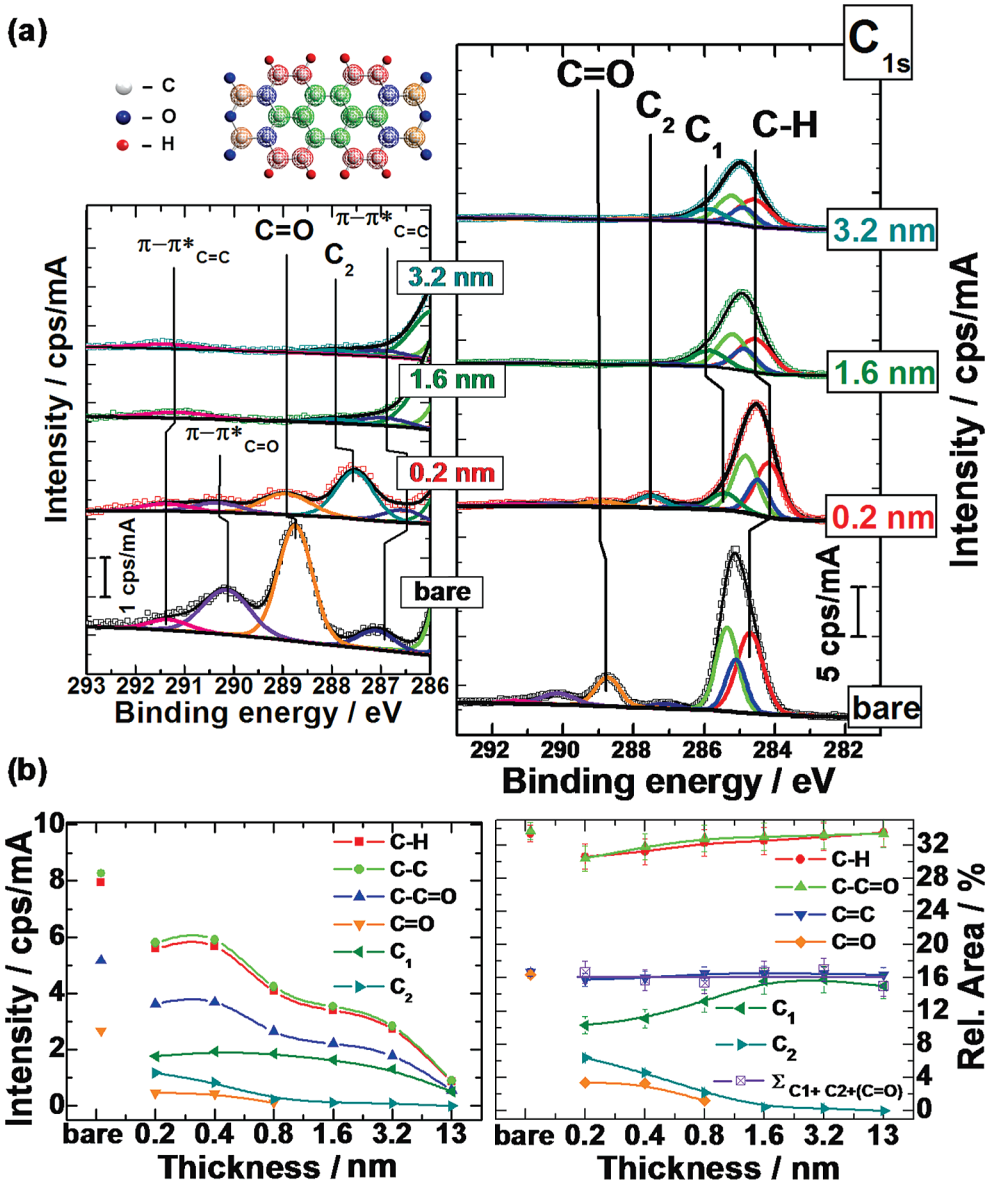

Figure 65. (a) C_{1s} core level spectra and contribution of the individual peaks to the overall intensities of the C_{1s} for bare PTCDA and upon Mg deposition. The individual components for the C_{1s} of PTCDA are assigned according to the color coding (the inset at the left shows the magnified shake up structures and the C═O contribution). (b) Evolution of fit parameters (intensity and relative area) of the C_{1s} core level as a function of Mg thickness for the original components and the new components.

In the O_{1s} spectra at a coverage of 1.6 nm, corresponding to an equivalent of about four monolayers of Mg, two new strong features, one feature at a binding energy of 530.9 eV (O_1) and another feature at 533.4 eV (O_2), are present while the C−O−C component vanishes. At the same coverage, one more component at 49.8 eV assigned to metallic Mg[146,147] occurs in the Mg_{2p} core level emission.

Literature data for the characterization of different Mg chemical states by XPES analysis[148−151] show that binding energies of 51.2 eV for the Mg_{2p} core level and 530.6 for O_{1s} core level indicate the presence of oxidized magnesium. Similarly, films containing relatively large amounts of magnesium hydroxide $Mg(OH)_2$ and/or $MgCO_3$ species are characterized by the appearance of the (51.9 ± 0.4) eV peak in the Mg_{2p} core level and of the (533.1 ± 0.4) eV peak in the spectrum of the O_{1s} core level. With these details we can easily assign the components Mg_2 and O_1 to MgO. The Mg_3 and O_2 components have a broad fwhm, indicating a rather undefined environment: a hydroxide or carboxide environment of magnesium cannot be assigned unambiguously. Consequently, the high binding energy components may be attributed to the adsorption of isolated Mg atoms on different sites of the organic layer: near hydrogen atoms or/and between the molecular planes. The component at 50.45 eV, labeled Mg_1, might be due to a hydrated Mg^{1+} or a suboxide species.[152]

At 1.6 nm of Mg, it seems that the reaction is almost complete. Further Mg deposition decreases the intensities of the O═C component of the O_{1s} core level and of the Mg_2 (MgO) component of the Mg_{2p} core level, in agreement with the appearance of the strong metallic Mg component. However, the presence of the Mg_3 and O_2 components and their increase as a function of Mg coverage suggests that some of the Mg atoms may still adsorb near hydrogen atoms and/or between the molecular planes. The presence of MgO obviously prevents diffusion of Mg into the organic film. On top of the reacted layer, the morphology of the metallic Mg overlayer is island-like, as revealed by the persistence of the C_{1s} main peak, of the O_{1s} (O═C) peak, and of the oxidized Mg peak up to a coverage of at least 13 nm.

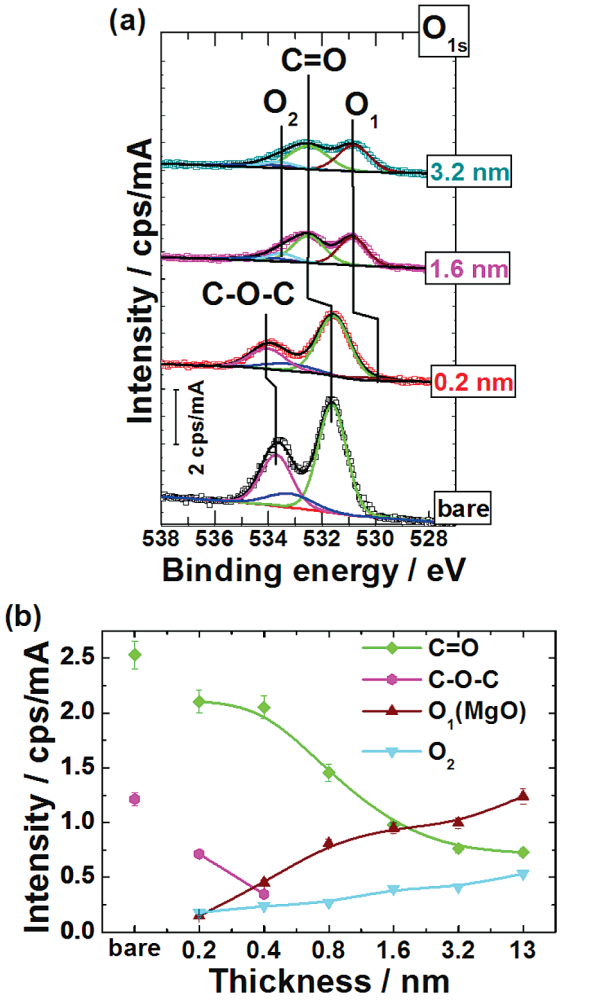

Figure 66. (a) O_{1s} core level spectra and contribution of the individual peaks to the overall intensities of the C_{1s}, for bare PTCDA and upon metal deposition. (b) Evolution of intensity of the O_{1s} core level as a function of Mg thickness for the original and the new components.

Besides the changes in the spectral line shape, shifts in binding energies were also observed. Initially, a gradual shift of ~(−0.7 eV) for C_{1s}, in particular of the perylene core components, and of ~(+0.25 eV) for O_{1s} (C−O−C) is observed. After the reaction is initiated by the presence of Mg, the C−O−C bond is strongly affected, most probably broken. Due to these changes, the charges will redistribute mainly over the perylene core. This hypothesis agrees very well with the increase in intensity of the aromatic carbon at a coverage of 0.4 nm of Mg. An additional contribution of screening due to the photogenerated core-hole upon deposition of Mg cannot, however, be excluded. At thicknesses larger than 0.8 nm, the C_{1s} and O_{1s} features shift toward higher binding energies by ~(+0.6 eV) and ~(+1 eV), respectively. Above the same thickness (0.8 nm), the C−O−C component vanishes. This is an indication that the reaction between Mg and PTCDA is almost complete with the apparent formation of MgO and a modified organic molecule with properties different from those of PTCDA. Due to MgO formation, the C_{1s} and O_{1s} photoemission lines cannot be efficiently screened, consequently, a shift toward higher binding energies occurs. We notice that at about the same thickness the Mg_3 component decreases dramatically in intensity and relative area.

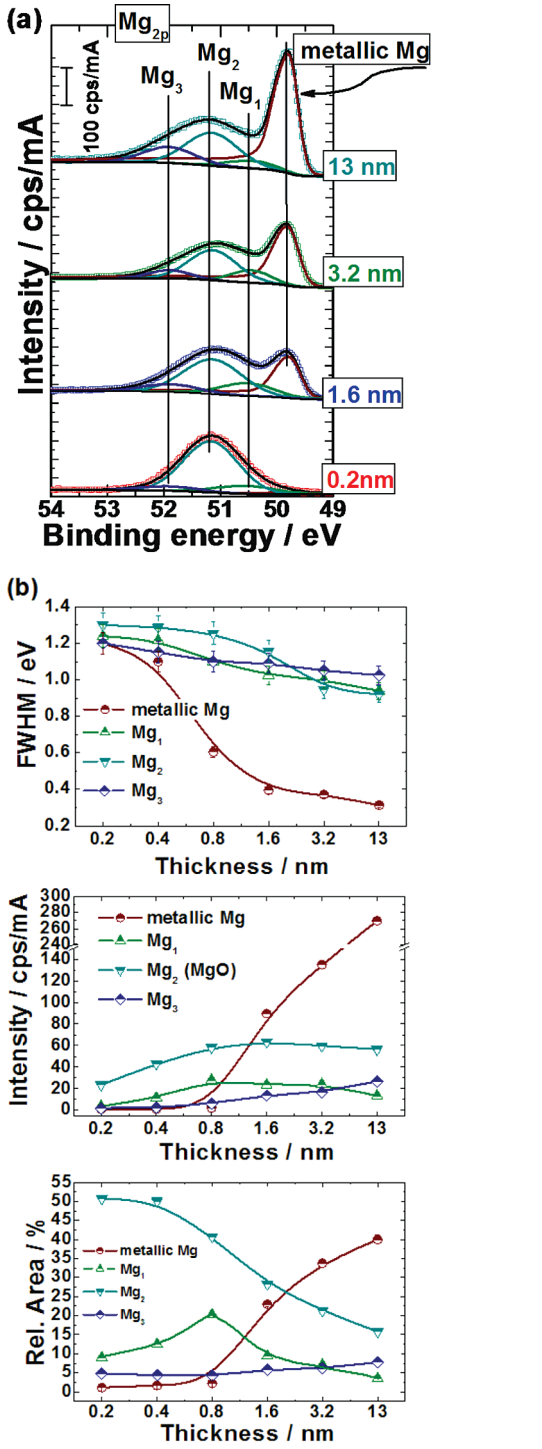

Figure 67. (a) Mg_{2p} core level spectra evolution with the Mg thickness upon deposition onto a PTCDA film; the contribution of the individual peaks to the overall intensities of Mg_{2p} was obtained by fitting. (b) Evolution of the fit parameters (fwhm, intensity, and relative area) of the Mg_{2p} core level components as a function of the Mg thickness.

Moreover, the formation of MgO is also supported by the valence band measurements. Figure 68a shows the valence band spectra of bare PTCDA (bottom), of 0.8 nm of Mg on a 15 nm film of PTCDA (middle), and of MgO, with the latter being measured using a He discharge lamp (21.22 eV) (top). The well separated peak at ~2.5 eV corresponds to the HOMO and is distributed over the perylene core while the feature at ~6 eV is mainly attributed to the O_{2p} derived molecular orbitals (see section 2—Properties of Organic

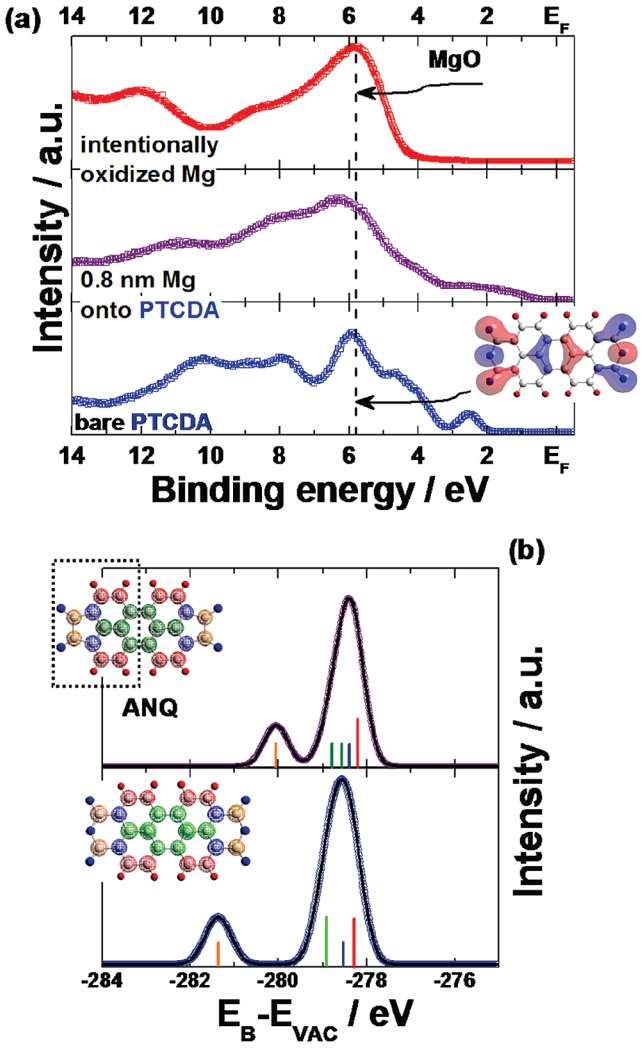

Figure 68. (a) Comparison between the valence band spectra of bare PTCDA (bottom), 0.8 nm Mg on a PTCDA film (middle), and intentionally oxidized Mg (top). (b) Calculated C_{1s} core level of the pristine PTCDA (bottom) and of the modified molecule (top) using Gaussian 98 B3LYP/6311-G(d,p). The individual components (vertical bars) are assigned according to the color coding.

Semiconductors: Perylene Derivatives). By comparison with the valence band spectra corresponding to MgO, the change in the HOMO and of the feature at ~6 eV is explained by the strong intermixing between Mg atoms and the organic material resulting in MgO, a modified organic molecule, and charge transfer to the molecule. Moreover, the formation of MgO is consistent with the delay of the appearance of the density of states at the Fermi level due to metallic Mg.

On the basis of the changes observed in the core levels, the molecular structure of the modified "new" molecule is proposed. The modified molecule consists of two quinone (O═C—C═O) groups attached to the opposite ends of a perylene core. The structure of the new molecule is shown in Figure 68b. It is worth mentioning that studies of a similar π-conjugated organic molecule (e.g., acenaphthenequinone (ANQ)) via high-resolution X-ray photoelectron spectroscopy and near-edge X-ray absorption spectroscopy were already reported.[64,74]

DFT single molecule calculations using the Gaussian 98 package[51] with the B3LYP method and 6-311G(d,p) basis set were performed to describe the C_{1s} core orbitals of the pristine PTCDA and of the modified molecule. The obtained core level spectrum is displayed and compared to the one of PTCDA in Figure 68b. The simulated C_{1s} was obtained by Gaussian broadening of each calculated energy position of C_{1s} (vertical bars) with a fwhm of 0.84 eV. The calculated data support the experimental results; namely, the C═O component of the C_{1s} core level shifts toward lower binding energies.

6.1.2.2. Mg on DiMe-PTCDI. The changes in the C_{1s} core level spectra of DiMe-PTCDI as a function of Mg coverage are displayed in Figure 69. The assignment of the C_{1s} core level components for bare DiMe-PTCDI is described in detail in section 2—Properties of Organic Semiconductors: Perylene Derivatives. To recall, the C_{1s} peak consists of five main components. The main peak with maxima at about 285.3 eV ($C_{perylene}$) stems from different carbon atoms of the aromatic part and consists of three components (C—H, C—C═O, and C═C). The small peak at 286.2 eV is attributed to the C—N bond while the high binding energy component at 288.3 eV corresponds to the anhydride group. The area ratio of these peaks is 8:4:8:2:4 when the shakeup component areas are taken into account.

Together with the bare C_{1s} core level, the peak fit analysis for three different Mg thicknesses is displayed in the same figure.

Upon deposition of 0.2 nm of Mg, the main spectral change is a shift toward lower binding energies for all C_{1s} components. The shifts are significantly different for the various components. The components attributed to the perylene core and its shakeup satellites are shifted by ≈0.15 eV toward lower binding energies while the C═O component and its shakeup satellite are shifted by about 1 eV. Two processes or their combination can be responsible for the origin of these changes: charge transfer from the metal to the molecule and/or a change in the final state screening due to the metal presence. From this we can conclude that a larger amount of charge is transferred from the metal to the carboxylic carbons compared with the perylene ones.

For larger Mg coverages, the spectral features remain basically the same but with drastically different intensities and significant broadening. It is worth noticing that, unlike the Mg/PTCDA case, no new components are evolving as a function of Mg coverage. Therefore, a reaction between Mg and DiMe-PTCDI can be ruled out.

Additional information on the type of interaction can be gained from the shakeup satellites of the photoemission lines. The shakeup structure magnified in the left panel of Figure 69a corresponds to the core ionized final states in which an e^- from the valence band is promoted to an unoccupied level. Therefore, it is linked to the convolution of occupied and unoccupied states. The broadening of these structures could indicate the strength of interaction between the involved partners. For Mg/DiMe-PTCDI, these features are rather sharp, and thus, a weak chemical interaction can be deduced. Moreover, the area ratio of the C_{1s} peaks reflects the preservation of the stoichiometry of the DiMe-PTCDI molecule for all Mg thicknesses. Therefore, one main finding from the C_{1s} fit analysis is that the interaction of Mg with DiMe-PTCDI is rather weak and can be described by a charge transfer from the metal to the organic molecules.

On the other hand, when the O_{1s} core level was curve fitted, two new components were revealed. The deconvolution of the O_{1s} emission spectra for several selected Mg thicknesses is illustrated in Figure 70a. The relative positions of the new components (labeled O_1 and O_2) were found to be identical for all Mg thicknesses. The component O_1 was

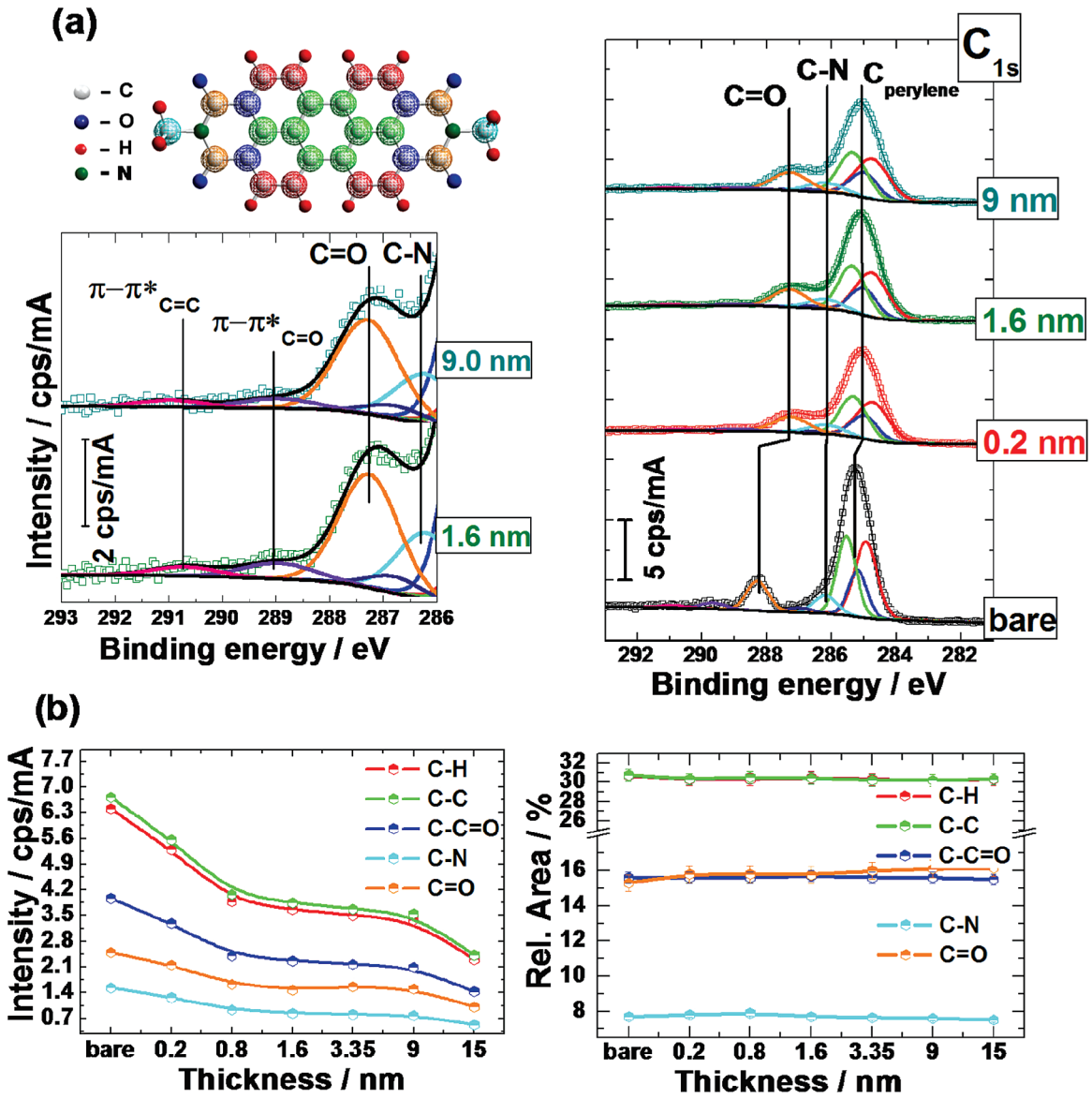

Figure 69. (a) C_{1s} core level spectra and contribution of the individual peaks to the overall intensity for bare DiMe-PTCDI and upon Mg deposition (The inset at the left shows the magnified shake up structures and the C═O contribution. The individual components for the C_{1s} of DiMe-PTCDI are assigned according to the color coding used for the DiMePTCDI molecule at the top of the inset). (b) Evolution of the fit parameters (intensity and relative area) of the C_{1s} core level as a function of Mg thickness for the original and the new components.

found to be at 530.45 eV, i.e., a binding energy lower by 0.45 eV than that for MgO; therefore, this peak cannot be assigned to the formation of MgO. The nature of this feature, that should indicate a lower oxidation state of O_{1s} atoms, is unclear. One explanation could be the presence of free Mg atoms that are located close to oxygen and/or carbon atoms. The second component, labeled O_2, was found to be at 532.75 eV. Similar to the case of Mg on PTCDA, this component may be attributed to the adsorption of isolated Mg atoms on different sites of the organic layer: near hydrogen atoms or/and between the molecular planes. The shift of about 0.2 eV toward higher binding energies of the main peak is in complete agreement with the observations in the C_{1s} core level emission spectra. The electron charge transfer from the metal to the carboxylic carbon will induce a deficit of electrons at the O atoms leading to an increase in binding energy. However, the intensities of the high, middle, and low binding energy components behave very similarly as a function of Mg thickness, as shown in Figure 70b. They are continuously increasing up to a nominal coverage of 1.6 nm. For larger thicknesses, the intensity of all components starts to decrease, consistent with the appearance of metallic Mg in the Mg_{2p} core level emission spectra (see Figure 71). In contrast, the fwhm and relative area of these components are not changing for all Mg thicknesses. This implies that the chemical environment of the O_{1s} species does not change significantly as the Mg coverage is increased.

Figure 71 describes the evolution of the Mg_{2p} signal after decomposition into several components. As shown in Figure 71a, the core level is initially dominated by a high binding energy component at 51.40 eV, labeled Mg_2. Its intensity is followed by the highest binding energy component labeled Mg_3, possibly associated with $Mg(OH)_2$ and/or $MgCO_3$,[148] and by one component at 50.55 eV labeled Mg_1 and attributed to Mg^+. All the peak intensities increase with Mg deposition until a nominal coverage of 3.35 nm of Mg is reached. Beyond 3.35 nm of Mg, the intensity of the high binding energy component saturates rapidly, increasing only slightly upon further Mg deposition. At about the same thickness, a low binding energy component starts to evolve.

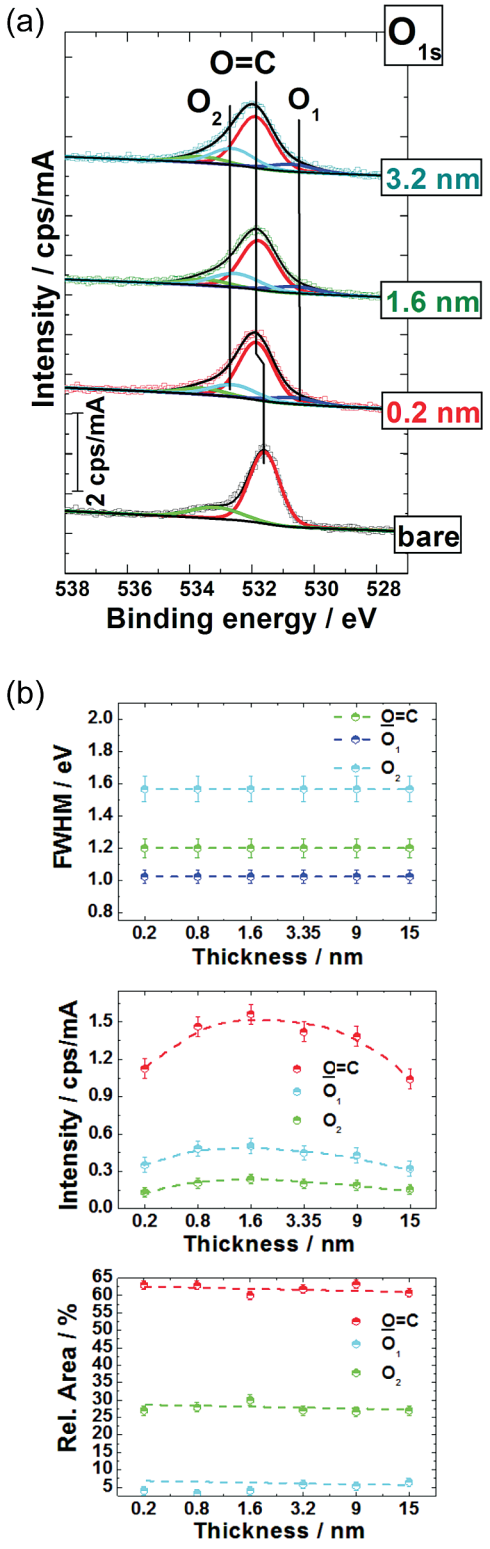

Figure 70. (a) O_{1s} core level spectra and contribution of the individual peaks to the overall intensities of the O_{1s} for the bare DiMe-PTCDI thin film and upon Mg deposition. (b) Evolution of the fit parameters (fwhm, intensity, and relative area) of the O_{1s} core level as a function of the Mg thickness.

Its intensity increases with the coverage, finally surpassing the high binding energy component in intensity at 15 nm coverage. This low binding energy component is assigned to metallic Mg species (49.8 eV).

The assignment of the component labeled Mg_2 is not clear. It can well correspond to an oxidized form of Mg as a result of electron transfer from the metal to the organic molecules.

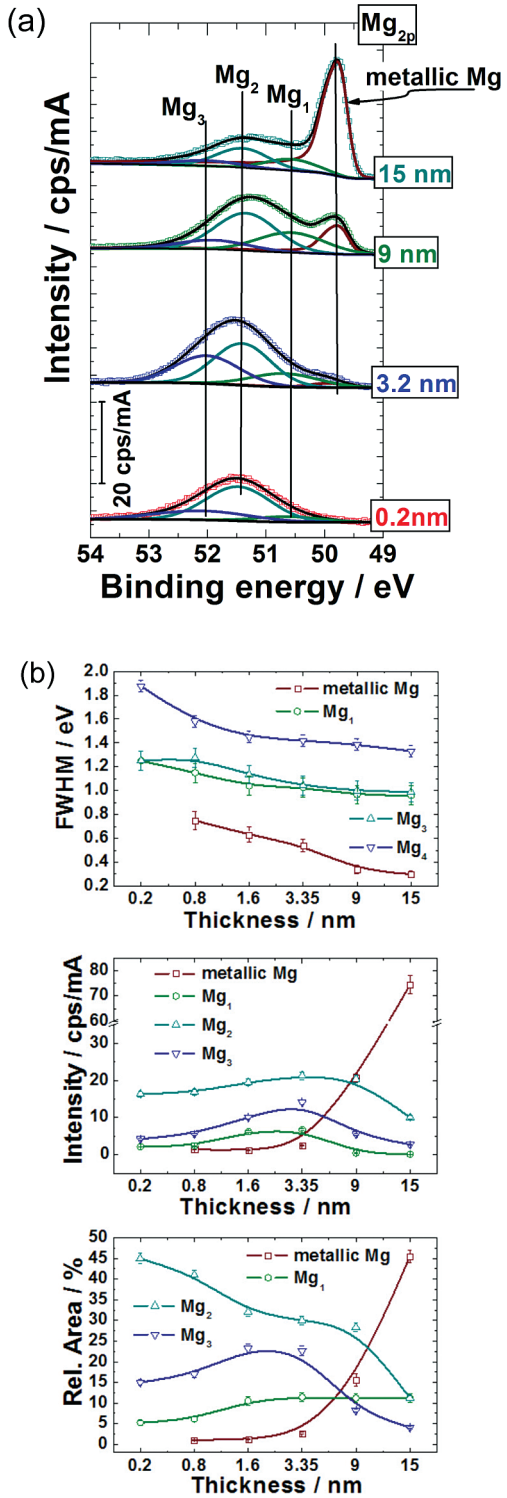

Figure 71. (a) Mg_{2p} core level spectra and contribution of the individual peaks to the overall intensity of the Mg_{2p} upon Mg deposition onto DiMe-PTCDI. (b) Evolution of the fit parameters (fwhm, intensity, relative area) of the Mg_{2p} core level components as a function of the Mg thickness.

The chemical shift with respect to the metallic component, as deduced from the peak separation, amounts to 1.65 eV. This separation nearly equals the chemical shift of 1.7 eV between MgS and metallic Mg.[75] At a DiMe-PTCDI thickness of 15 nm, which is used in our photoemission studies, the organic crystalline domains do not cover the substrate entirely (see Figure 53). Therefore, a reaction of Mg with the sulfur-passivated substrate cannot be excluded in this

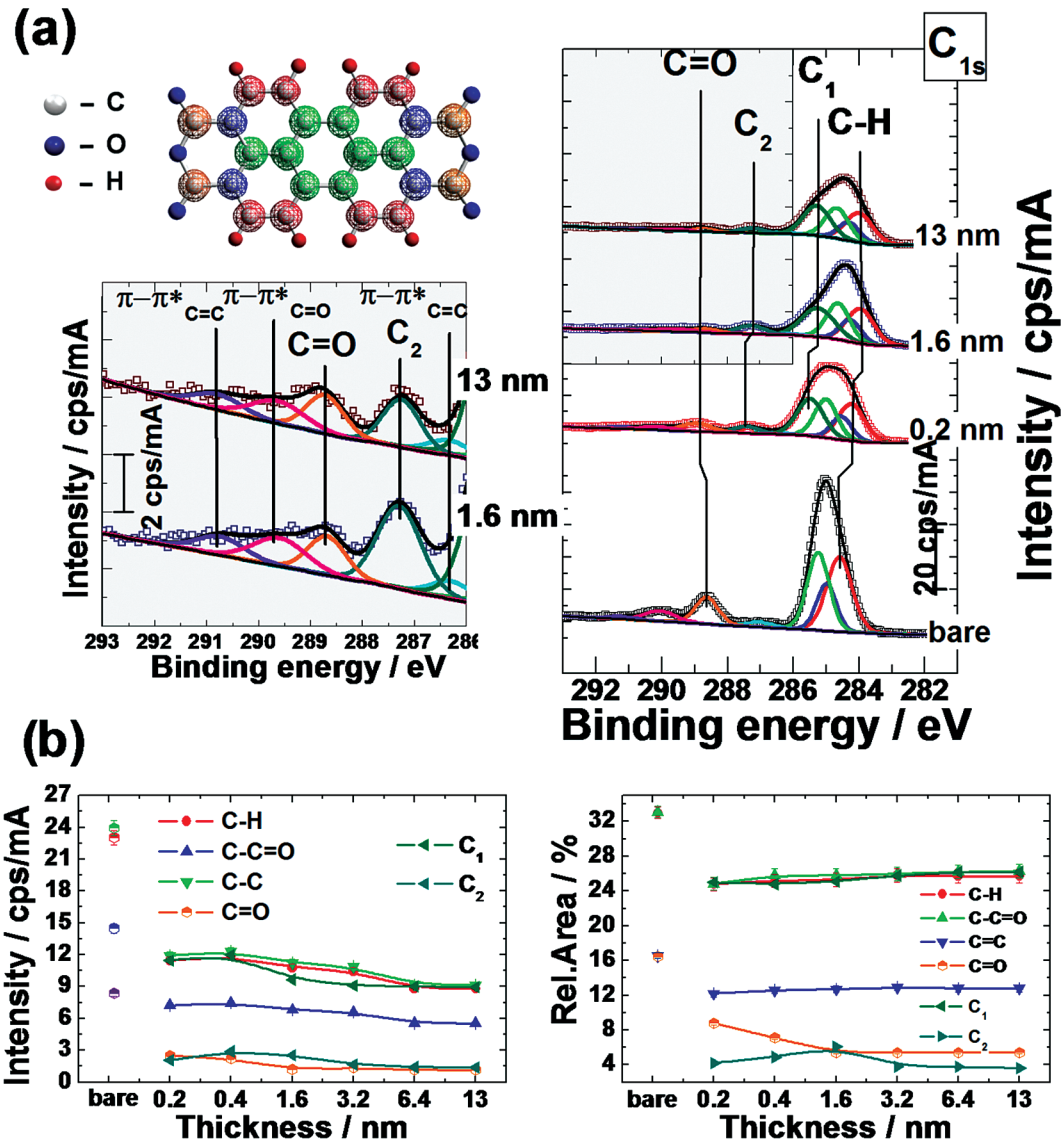

Figure 72. (a) C_{1s} core level spectra and contribution of the individual peaks to the overall intensity of the C_{1s}, for the bare PTCDA film and upon In deposition. The inset shows the shake up structures and C═O contribution magnified in the high binding energy region. (b) Evolution of fit parameters (intensity and relative area) of the C_{1s} core level as a function of In thickness.

particular case and it may be the reason for the appearance of this Mg_{2p} component.

From the persistence of the C_{1s}, O_{1s} (O═C) peak as well as of the oxidized Mg up to a coverage of at least 3.35 nm, an island-like growth can be inferred. Above 3.35 nm, the Mg clusters start to grow. The metallic character is gained above a nominal coverage of 9 nm when the metallic component is surpassing the other components. Less dramatic changes observed in the C_{1s}, O_{1s}, and N_{1s} peaks upon Mg deposition onto DiMe-PTCDI indicate a less reactive nature of this interface compared to that of PTCDA. This can be easily related to the molecular structure of DiMe-PTCDI. The existence of a methylimide group as a side group controls the chemical nature of this interface.

6.1.2.3. In on Perylene Derivatives. The first PES study of In deposition onto PTCDA was reported by Hirose et al. in 1996.[20] Here it was first suggested that there is a chemical reaction between In atoms and the carboxylic group in PTCDA on the basis of the observation of a new valence state formed close to the Fermi level. Later, the In/PTCDA system was studied using angle-resolved ultraviolet photoelectron spectroscopy (ARUPS),[153] a combination of metastable atom electron spectroscopy (MAES) with ultraviolet photoelectron spectroscopy (UPES),[21] low-energy electron diffraction (LEED),[154] and high-resolution electron energy loss spectroscopy (HREELS).[23] From these studies, it was concluded that, as a result of a chemical reaction between In and PTCDA, In_4PTCDA is formed at the interface[153] and that the new HOMO state appearing close to the Fermi level originates from a widely spread π molecular orbital mixed with the In-$5p_z$ atomic orbital.

Our Raman spectroscopy results on In/PTCDA evidenced that formation of In_4PTCDA can be ruled out. Formation of such an organometallic complex should lead to strong Raman shifts of the molecular vibrations, a situation which is obviously not encountered. To solve this apparent contradiction, more details about the chemistry at this interface will be extracted from the high-resolution photoemission measurements in combination with the core level fit procedure.

Figure 72a presents the evolution of the C_{1s} core level spectra for bare PTCDA and for PTCDA with different In coverages. For all In thicknesses, strong changes in the C_{1s} spectra as compared to those for the bare PTCDA are observed. The changes are more pronounced at the initial

stage of In deposition. In Figure 72b, the evolution of the parameters resulting from the peak fitting analysis is presented.

Upon deposition of 0.2 nm of In, all components of the C_{1s} core level are significantly decreased in intensity and broadened. A larger broadening, however, and a stronger decrease are observed for the high binding energy component, indicating that the carboxylic carbon is most strongly affected by the presence of In. Moreover, two new components at 285.55 eV (C_1) and 287.45 eV (C_2) evolve on the low binding energy site of this peak. These new components are present in the spectrum up to thicknesses larger than 13 nm, and a tentative assignment will be given later.

After an initial decrease in intensity above an In coverage of 0.4 nm, the intensity of the aromatic carbon slightly increases as a result of a redistribution of charges in the molecule. The area ratio of the C peaks related to the perylene core remains constant for all In thicknesses. Also, the presence of well defined $\pi \rightarrow \pi^*$ shakeup satellites in the C_{1s} spectra (see the left side of Figure 72a) indicates that the aromatic structure is preserved. Furthermore, since the broadening of these structures defines the strength of interaction between the organic molecule and the metal, a weak chemical interaction can be deduced.

Another change observed is a shift in binding energies for all C_{1s} components. The shift is 0.4 eV toward lower binding energies for the perylene components and 0.2 eV toward higher binding energies for the C═O component. The process responsible for this behavior is a charge transfer from the metal to the molecule. The charge is likely to be transferred from the metal to the perylene core. At the same time, the C═O component shifts to higher binding energy, reflecting that the charge redistribution over the molecule induces a deficit of electrons on the C═O bonds. For thicknesses larger than 0.8 nm, a shift toward lower binding energies is observed, in particular for the perylene core components. Similar shifts at the same thickness were observed, as we shall see later, in the O_{1s} core level and in the valence band spectra, and attributed to a change in the final state screening due to the metal presence.

Raman measurements (section 6.1.1) and, in addition, the evolution of the C_{1s} core level spectra of DiMe-PTCDI upon In deposition showed that DiMe-PTCDI experiences a similar interaction with In as PTCDA. A thorough analysis of the In/DiMe-PTCDI system is presented elsewhere.[66] A deeper insight into the chemistry between In and the two perylene derivatives can be delivered by the analysis of the O_{1s} core level emission spectra of PTCDA and DiMe-PTCDI, respectively.

The evolution of the O_{1s} spectra of PTCDA and DiMe-PTCDI as a function of In thickness is presented in parts a and b, respectively, of Figure 73. The gradual shifts of the C═O main line in the O_{1s} spectra are in complete agreement with what we observed in the C_{1s} spectra. The shift at 1.6 nm appears concomitantly with metallic In formation in the In_{4d} core level emission spectra. The most relevant fit parameters of the O_{1s} spectra as a function of In thickness are presented in Figure 73 at the bottom of each spectrum.

In the PTCDA case for 0.2 nm of In, the intensity of the O_{1s} components decreases significantly compared to that of bare PTCDA. The fwhm of the C═O component of the O_{1s} signal is significantly broadened. The fitting procedure shows that under this peak we can introduce two components: one component attributed to the original O═C bond and one

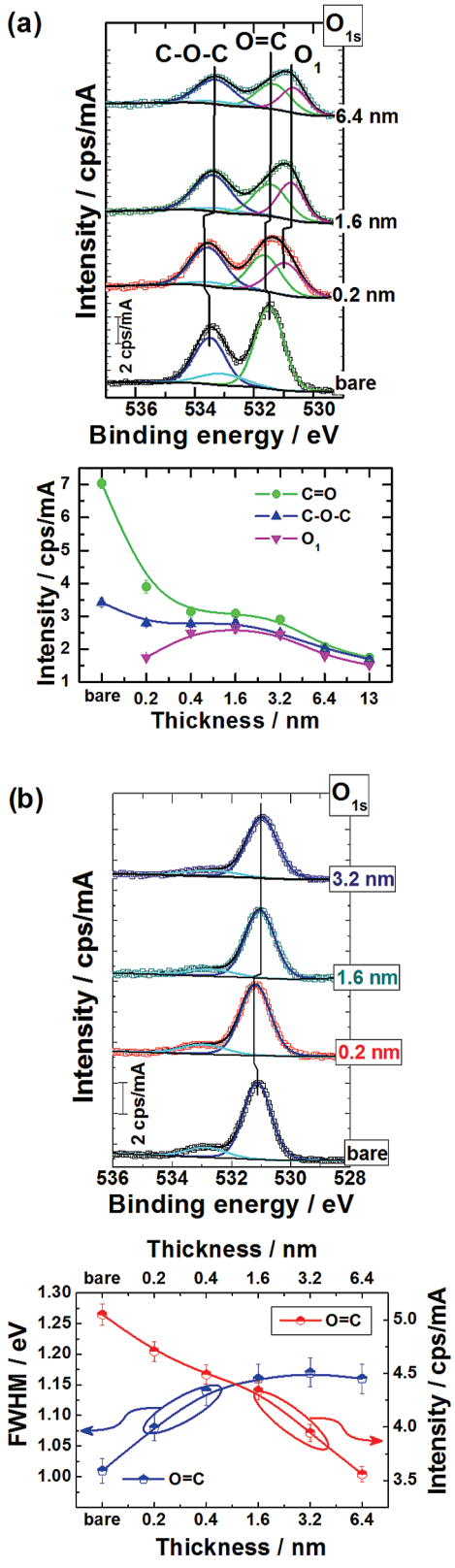

Figure 73. (a) O_{1s} core level spectra of PTCDA and contribution of the individual peaks to the overall intensity of the O_{1s}, for the bare organic film and upon In deposition (top), together with the evolution of the intensity as a function of In thickness for the original and new components (bottom). (b) O_{1s} core level spectra of DiMe-PTCDI and contribution of the individual peaks to the overall intensities of the O_{1s}, for the bare organic film and upon In deposition (top), together with the evolution of the intensity and fwhm as a function of In thickness (bottom).

component derived from the interaction of the organic molecule with In. Note that, as a function of coverage, the intensities of the three components change and the intensity ratio approaches 1:1 at a nominal thickness of 1.6 nm. This indicates that the C═O bond feels two different chemical environments; that is, the degeneracy of the C═O component is lifted. As the In coverage increases, the C−O−C peak and the new C═O peak decrease in intensity at the same rate, in good agreement with the intensity increase of metallic indium in the core level spectra of In_{4d} (see Figure 74a).

Contrary to the case of PTCDA, no changes are observed in the line shape of the O_{1s} core level emission spectra of DiMe-PTCDI except a decrease in intensity upon In deposition (see Figure 73b). The gradual decrease in intensity is accompanied by a slight increase in the fwhm.

Figure 74 shows the evolution of various components of the In_{4d} spectra upon metal deposition onto PTCDA and DiMe-PTCDI. Supported by the changes in the spectral line shape of C_{1s} and O_{1s} together with the evolution of In_{4d} components, an unambiguous assignment of the new components observed in the C_{1s} and O_{1s} spectra of PTCDA can be given.

During the fitting procedure, the spin−orbit splitting was kept fixed at 0.86 eV and the branching ratio was 0.65. The energy positions of all components were allowed to vary. For a reliable fit, the same initial parameters were used for all In thicknesses. At low coverage, three new components are observed at a higher binding energy than that of metallic In.[152] For both materials, these components dominate the In core level spectra up to about 13 nm when the metallic component is surpassing the high binding energy ones. Below this coverage, all components are increasing in intensity. At a thickness of 1.6 nm, the metallic component emerges. Its fwhm is substantially narrower than those of the high binding energy components. Its asymmetric line shape (asymmetry parameter = 0.2) is characteristic for emission from a metallic phase.

The high binding energy components are due to isolated In atoms physisorbed on the organic surface: on top of the perylene core and near the carboxylic oxygen. The widths reflect a broad distribution of inequivalent absorption sites. This assignment is supported by the following observations: First, for example in the PTCDA case, the energy separations between the high binding energy components and the metallic one are (1.6 ± 0.05) eV for In_1, (2.1 ± 0.05) eV for In_2, and (3.8 ± 0.05) eV for In_3. These values are much higher than the energy difference of 1.1 eV between metallic In and In covalently bonded to oxygen.[155] Second, the intensity of metallic In increases significantly above 1.6 nm, indicating the formation of In clusters. Examination of the coverage dependence of the core electron photoemission intensity and the binding energy for simple, noble metals and transition metal clusters on amorphous carbon has shown that very small atom clusters, containing less than 30 atoms, are not fully metallic and the final state core-holes are screened by polarization of the neighboring atoms. Consequently, the binding energy depends only weakly on the cluster size.[156] In larger metallic clusters, conduction electrons screen the hole, with the missing charge appearing at the surface of the clusters. In this regime, the core electron binding energy shifts to lower values in binding energy with increasing cluster size. The variation in binding energy of the In_{4d} components after 1.6 nm of In falls in the latter regime. Another interesting point

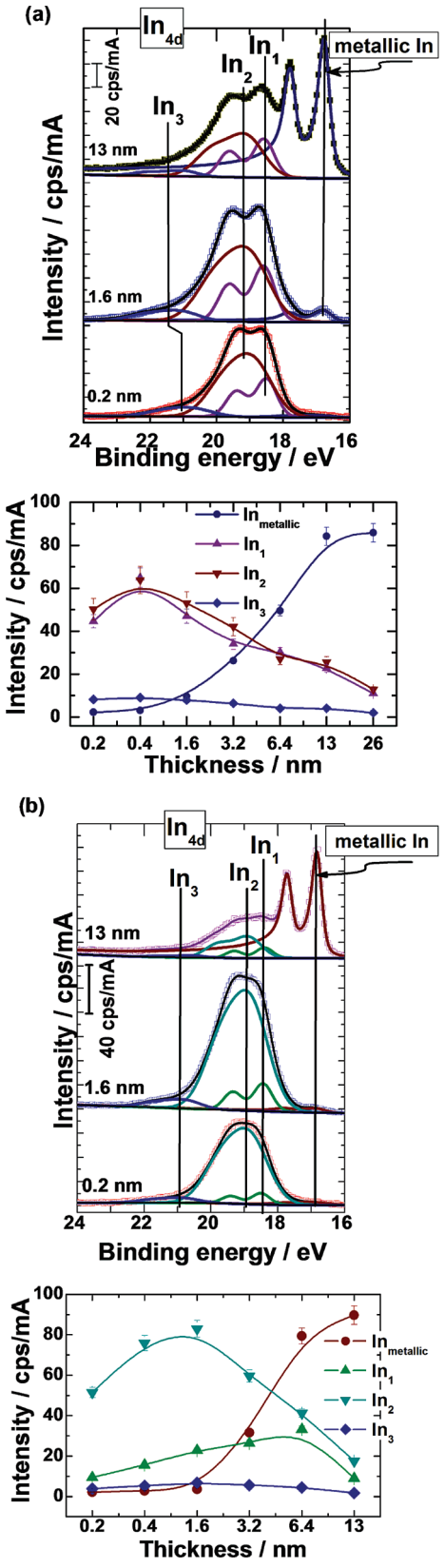

Figure 74. (a) In_{4d} core level spectra and contribution of the individual peaks to the overall intensity of the In_{4d} core level emission upon metal deposition onto PTCDA together with the evolution of the intensity of the In_{4d} core level components as a function of the In thickness. (b) In_{4d} core level and contribution of the individual peaks to the overall intensity of the In_{4d} core level emission upon metal deposition onto DiMe-PTCDI together with the intensity evolution of the In_{4d} core level components as a function of In thickness.

Table 18. Energy Difference between In_1, In_2, and In_3 Components and the Metallic Component at (16.85 ± 0.05) eV

	In_1	In_2	In_3
PTCDA	(1.6 ± 0.05) eV	(2.1 ± 0.05) eV	(3.8 ± 0.05) eV
DiMe-PTCDI	(1.55 ± 0.05) eV	(2.07 ± 0.05) eV	(3.9 ± 0.05) eV

to mention is that the Fermi level of the cluster "moves" toward larger binding energy with decreasing cluster size, as was previously found for Au cluster formation on amorphous carbon.[157] This is easily understood if one assumes that the emitted photoelectron is not quickly replaced, so that the cluster is left with an elementary positive charge in the photoemission final state. Since this final-state charge occurs whenever a photoelectron is emitted, the entire spectrum appears shifted to higher binding energies.

The evolution of the core level emission spectra of C_{1s}, O_{1s}, and In_{4d} leads to the following conclusions. At the initial stages, In coordinates weakly with the oxygen of the carboxylic group and adsorbs on the perylene core, leading to the formation of a weak bond between In and two of the carboxylic oxygens. This explains the lifting of degeneracy of the C═O component in O_{1s} with the appearance of the C_2 component in the C_{1s} core level spectra. In addition, the In_{4d} core level spectra exhibit high oxidation states (In_1 and In_2). These components are related with different adsorption sites of In and are linked to the new components observed in the core levels of C_{1s} and O_{1s}. The In_1 component is assigned to free In atoms in the vicinity of O═C, while In_2 is attributed to In situated near carbons in the perylene core or between the molecular planes. Since their intensity evolution as a function of In thickness is quite similar, the evolution of the fwhm as a function of In thickness is the criterion used to make the first tentative assignment. It is observed that the fwhm of In_1 is smaller than that of In_2 as a consequence of a more homogeneous environment. The fwhm of O_1 is decreasing faster as a function of In thickness, much faster than the fwhm of C_1. Therefore, In_1 is obviously linked to O_1.

A straightforward assignment of the In_{4d} individual components can be delivered when comparing the peak positions for the In/PTCDA and In/DiMe-PTCDI cases. The energy differences between high binding energy components and the metallic one presented in Figure 74 are summarized in Table 18. These components may be attributed to In atoms adsorbed on different sites of the molecule as follows: the In_1 component is attributed to In adsorbed near the functional group—anhydride or methylimide, respectively. Its energy position in DiMe-PTCDI is located at somewhat lower values than that of In_1^{PTCDA}, in good agreement with the fact that $EA_{anhydride} > EA_{methylimide}$. Moreover, its fwhm has the lowest value; therefore, its chemical environment is much better defined compared to the chemical environments of the other components. Similarly, the C_2 component of the C_{1s} core level develops into a sharp peak that reflects a well-defined environment. Therefore, it is likely to be linked to In_1. In_2, on the other hand, is attributed to the In atoms adsorbed on the perylene core or between the molecular planes. This assignment is supported by the intensity evolution of the C_1 component in the C_{1s} core level. In_3 is a very weak component that does not vary significantly in intensity and can be attributed to additional shakeup losses of the photoemission lines.

The presence of C_{1s} and O_{1s} core levels at thicknesses larger than 13 nm and the absence of density of states at the Fermi level (see Figure 90a) demonstrate that In diffuses into the organic film. It is reasonable to assume that, at the initial stages (up to 1.6 nm), In atoms form small clusters on the surface and diffuse into the organic film. Above 1.6 nm, the diffusion continues even if the cluster size may grow.

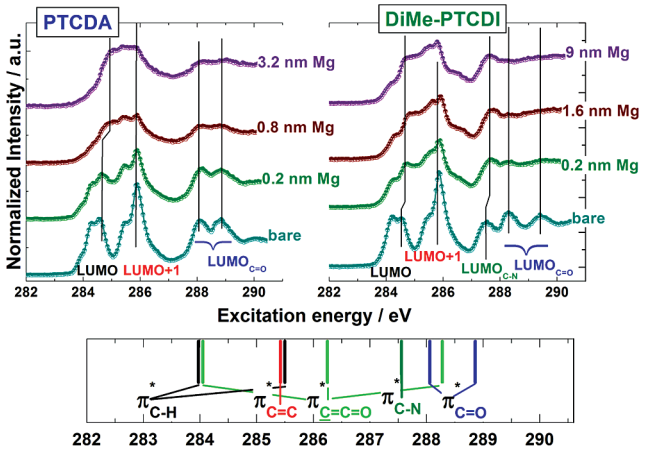

Figure 75. NEXAFS C K-edge of PTCDA and DiMe-PTCDI as a function of Mg coverage. Bottom: assignment of π^* resonance features.

6.1.3. High-Resolution NEXAFS

NEXAFS resonances are usually more affected than XPES peaks by a metallization process or by substrate bonding.[158] Due to interaction with metal atoms, the molecular orbitals are more strongly modified compared to the core levels and the identification of the molecular subunits involved in the chemical interaction is more straightforward.

It should be emphasized that there are significant differences in absorption energies and photoemission energies of a final state. This is due to quite different final states when using these two spectroscopies. Photoemission leaves an ionized excited state with a continuum final state. The binding energy depends on the image screening conditions of the core-hole. On the other hand, in NEXAFS, the final state is close to a neutral excited state and the excitation into localized final states is independent of any screening conditions. Unlike core level spectra, in which the peaks may undergo strong shifts due to better core-hole screening and/or a charge transfer, in NEXAFS, such shifts can hardly be observed. However, if a charge transfer toward molecules is present, the NEXAFS features may experience changes in intensities.

Furthermore, for a molecule in contact with a metal, the creation of the core-hole pulls the LUMO and LUMO + 1 resonances toward the Fermi level. The presence of density of states at the Fermi level leads to a charge transfer from the metal into the unoccupied states. The stronger the mixing between the LUMO and the metal states, the shorter the lifetime of the electron in the LUMO, which results in broadening of the corresponding NEXAFS feature.

The assignment of the different electronic transitions was discussed in detail in section 2—Properties of Organic Semiconductors: Perylene Derivatives. Here, for simplicity, they are indicated by lines at the bottom of each figure.

6.1.3.1. Mg/Perylene Derivative Interfaces. In the following, NEXAFS results are presented for the two perylene systems on S-GaAs for different Mg thicknesses. The results are shown in Figure 75 for the C K-edge of PTCDA (left) and DiMe-PTCDI (right). The large number of resonances

in the C K-edge spectra indicates the existence of various, non-interacting π^* orbitals with different energies and different spatial distributions.

The NEXAFS resonances show remarkable changes of their fine structure upon Mg deposition. These changes indicate a considerable modification in the electronic structure. They also prove the high sensitivity of this technique to such modifications.

Upon deposition of 0.2 nm of Mg, all π^* resonance features change severely relative to that of the bare thick film. The spectra become quite different for the two molecules, but common for all is the decrease in intensity. The most significant decrease in intensity is observed for the feature at about 286 eV that corresponds to a transition of an electron from the perylene core carbon(s) into LUMO + 1. We relate these spectral changes to a charge transfer from the metal to the perylene core, in very good agreement with the results from C_{1s} and O_{1s} core level spectra discussed above. Additional information about the amount of charge transfer and molecular subunits involved can be gained by analyzing the shifts of the LUMO feature. It can be seen that for both molecular systems this feature broadens and undergoes a shift toward higher excitation energy of about +0.1 eV. The core level fit result showed that the C_{1s} shifts in the same direction.

Upon increasing the Mg coverage, the LUMO and LUMO + 1 features are broadened and decreased significantly in intensity. Unlike the case of PTCDA, the LUMO and LUMO + 1 resonance features for DiMe-PTCDI are rather well resolved even at thicknesses larger than 9 nm Mg. There are different possible reasons for the change in the π^* structures. These can be attributed to a low degree of disruption in the molecular film or in the molecular structure due to the Mg presence and/or formation of Mg clusters. The pronounced changes in the line shape in the C K-edge of PTCDA at very low thicknesses indicate that the molecular disruption is stronger compared to that for DiMe-PTCDI. Together with the observations made at very thin coverages of Mg, we can conclude that the preservation of features in the case of DiMe-PTCDI may suggest a low degree of film disruption, indicating that Mg atoms do not react and do not diffuse into the molecular film. The VB-PES measurements show that the density of states at the Fermi level is present for thicknesses larger than 15 nm. This can be understood if one recalls that the DiMe-PTCDI film structure presents huge voids between the organic islands.

6.1.3.2. In/Perylene Derivative Interfaces. Figure 76 displays the NEXAFS results for the C K-edges of PTCDA and DiMe-PTCDI for different In coverages. Deposition of 0.2 nm of In leads to remarkable changes of the NEXAFS features. The most affected feature is the one labeled as LUMO + 1. As in the Mg/perylene case, the changes are related with the charge transfer from the metal into LUMO + 1. Above 0.8 nm of In coverage, the LUMO and LUMO + 1 features can no longer be resolved. The peaks derived from these characteristic resonances are practically developing into two broad features. The changes observed in the width of the C K-edge may be assigned to an increased hybridization degree between the molecular orbitals of core excited molecules and the metal. Consequently, the broadening of the LUMO and LUMO + 1 features can be attributed to the formation of metallic In clusters. Such a broadening could also occur due to the disruption of the molecular film and/or of the molecular structure caused by In atoms/clusters.

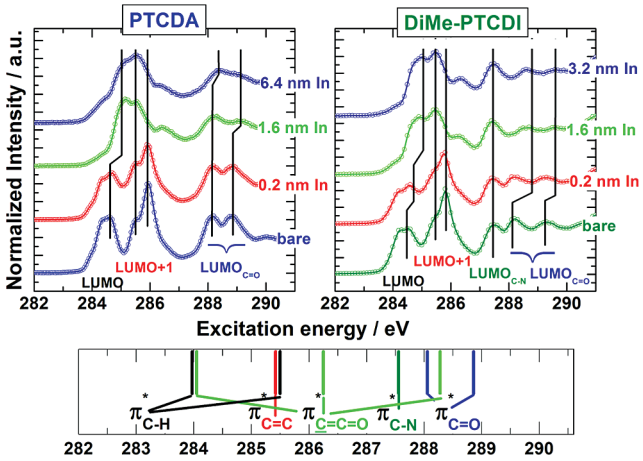

Figure 76. NEXAFS C K-edge of PTCDA and DiMe-PTCDI as a function of In coverage. Bottom: assignment of π^* resonance features.

However, for thicknesses equal to or larger than 1.6 nm, the broadening is accompanied by a shift of the LUMO feature toward higher excitation energies, which is a clear indication of charge transfer. Therefore, a disruption of the organic film is excluded.

6.2. Morphological Properties and Indiffusion of Metals at the Interfaces with Organic Semiconductors

6.2.1. Vibrational Spectroscopies

Besides the occurrence of internal modes related to molecules in direct contact with the metal, the totally symmetric modes are also enhanced (as shown by the normalization factors in Figure 77) in the spectra of Ag, In, and Mg on 15 nm thick PTCDA and DiMe-PTCDI films. The latter effect originates from the coupling of the incident and scattered radiation with localized and/or collective plasmon resonances in the rough metal film. Therefore, the intensity of the totally symmetric A_g modes is very sensitive to the morphology of the metal film.

For a quantitative determination of the enhancement factors, curve fitting of each set of spectra recorded during silver, indium, and magnesium deposition onto PTCDA and DiMe-PTCDI was performed using Lorentzian peaks. The dependence of the relative area on metal coverage is plotted in Figure 77 for a representative totally symmetric mode and for a normally infrared active mode of each organic material. The relative intensities were calculated by dividing the intensities in the spectra at a given coverage by the initial intensities in the spectrum where the mode occurs for the first time. For example, the reference spectrum for the totally symmetric Raman band is that of the pure organic film, while the reference spectrum for the normally infrared active band is that taken after the first metal deposition.

The intensities of the A_g modes initially increase upon Ag and In deposition, reflecting an increase in number and size of the metal clusters as their plasmon energy approaches the energy of the laser electromagnetic field. When Mg is deposited onto PTCDA, the intensities initially decrease, reflecting a reduction in the number of Raman active PTCDA molecules. This is in good agreement with the conclusion drawn in the previous sections regarding the disruption of PTCDA molecular structure upon reaction with Mg. In the next deposition step, i.e., at 2.8 nm of Mg nominal coverage,

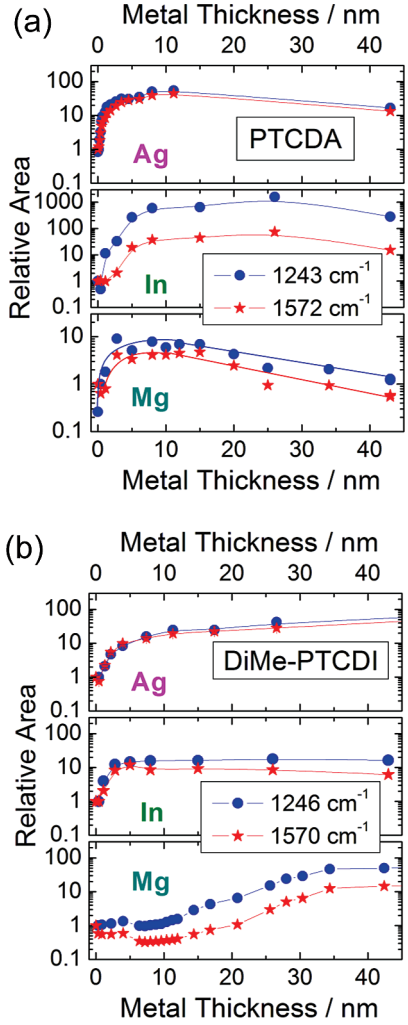

Figure 77. Enhancement factors of the B_u mode (1243 cm^{-1} in PTCDA and 1246 cm^{-1} in DiMe-PTCDI) and of the C−C stretching A_g mode (1572 cm^{-1} in PTCDA and 1570 cm^{-1} in DiMe-PTCDI) for PTCDA (a) and DiMe-PTCDI (b) as a function of the metal coverage.

the A_g Raman modes start to be enhanced, indicating the formation of metallic clusters. The enhancement of the totally symmetric modes of DiMe-PTCDI occurs only above 15 nm of Mg nominal thickness.

The PES studies (see the Mg_{2p} core level spectra in Figures 67 and 71) showed that the metallic character of Mg clusters occurs at coverages above 1.6 nm for PTCDA and between 9 and 15 nm for DiMe-PTCDI. The large difference in the nominal thickness for which the metallic character of Mg clusters is formed on the two molecules is probably related to the different morphologies of the underlying organic layers. The DiMe-PTCDI films have very large voids between the organic islands, while the PTCDA films are much more compact (see Figure 53).

The maximum enhancement of PTCDA modes for the Ag/PTCDA (15 nm) system is observed around 11 nm of Ag nominal coverage (Figure 77a) and corresponds to the optimum cluster size for the dipolar plasmon resonance. The In film thicknesses yielding the maximum enhancement for PTCDA and DiMe-PTCDI films are 26 and 5 nm, respectively. Further increase in the metal thickness leads to an increasing size of the metal clusters associated with a decreasing strength of the plasmon coupling with the incident and scattered radiation. Furthermore, the absorption in the metal film also plays an important role in decreasing the Raman signal for higher nominal coverages, when the clusters start to percolate.

Table 19. Skin Depth of Smooth Metallic Films: Apparent Penetration Depth of 488 nm Light in In, Ag, and Mg Films Grown on DiMe-PTCDI and PTCDA

	In	Ag	Mg
$\delta_{l=488nm}$(smooth metal film)	8 nm	2.5 nm	14 nm
$\delta_{l=488nm}$(DiMe-PTCDI)	49 nm	50 nm	15 nm
$\delta_{l=488nm}$ (PTCDA)	98 nm		24 nm

The signal from PTCDA and DiMe-PTCDI internal modes remains visible even for a metal coverage of 43 nm, with higher intensity compared to that for the pure organic film. For Ag deposition onto DiMe-PTCDI, no saturation of the signal intensity was observed up to a coverage of 263 nm.

Considering that I_0 is the intensity of the light incident on the sample, d is the nominal thickness of the metal coverage, and δ is the light penetration depth in the metal, the light intensity I scattered by the sample can be described by

$$I \propto I_0 e^{-2(d/\delta)}$$

A summary of the values obtained from the fitting of the experimental decay of the enhancement factors for the totally symmetric C═C stretching mode in all investigated heterostructures is given in Table 19. The obtained values are much larger compared to the penetration depth of 488 nm light into smooth closed metal films. This is a clear indication that In and Ag films grown on PTCDA and DiMe-PTCDI are not closed and have a high degree of roughness. The apparent light penetration depth in Mg films grown on PTCDA and DiMe-PTCDI estimated from the decrease in intensity of the C═C stretching mode has values comparable with the penetration depth in a closed smooth Mg film. This indicates that the Mg film is smoother and that the efficiency of the 488 nm radiation in exciting dipolar resonances is lower for Mg. The AFM topographic images in Figure 78 confirm the higher roughness of In compared to that of Mg films.

To recall, the A_g modes are enhanced via the long-range electromagnetic effect, while the activation of B_u modes is characteristic for the molecules in intimate contact with the metal. Therefore, the intensity of B_u modes relative to that of A_g modes will be considered in the following to extract the metal diffusion depth into the organic films.

In the case of Ag/PTCDA and Ag/DiMe-PTCDI, the intensity of B_u modes is relatively low, indicating that only a few molecules have intimate contact with Ag. This leads to the conclusion that Ag atoms diffuse very little into PTCDA layers. On the other hand, the B_u bands are stronger compared to the A_g modes in the spectra of In/PTCDA. This suggests that a large number of PTCDA molecules have intimate contact with the metal, indicating a strong diffusion of In into PTCDA layers. In/DiMe-PTCDI represents an intermediate case between Ag/PTCDA and In/PTCDA.

The ratio between the area of the B_u mode at 1243 cm^{-1} (1246 cm^{-1}) and that of the A_g mode at 1572 cm^{-1} (1570 cm^{-1}) in PTCDA (DiMe-PTCDI) is shown as a function of metal thickness in Figure 79. In the case of Ag/DiMe-PTCDI, the maximum value is observed for the first Ag deposition, i.e., 0.4 nm Ag, whereas for PTCDA it increases up to a 1.3 nm nominal coverage of Ag. For In deposition onto both organics, this ratio shows a saturation tendency only above

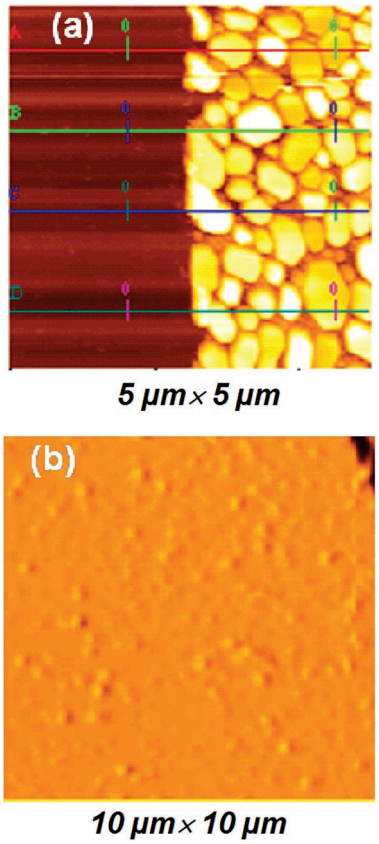

Figure 78. AFM topographic images of a 30 nm thick In film on PTCDA (a) (the left part of the image corresponds to the GaAs substrate, and the right part of the image corresponds to the In film grown on PTCDA) and of a 113 nm thick Mg film on PTCDA (b).

15 nm of In nominal coverage, but its value is lower for In/DiMe-PTCDI. It is proposed that a maximum in the above-defined ratio can be directly related to the metal diffusion length in the organic film. Thus, the Ag atoms arriving at the organic film surface diffuse into the PTCDA islands up to a nominal Ag coverage of 1.3 nm.

For metal coverages at which the enhancement of the Raman signal due to dipolar plasmon resonances is observed, the B_u bands at around 1606 cm^{-1} (in both PTCDA and DiMe-PTCDI) become asymmetric toward the low-frequency side in all the investigated systems except for Mg/PTCDA. This line-shape asymmetry is likely to be related to a Fano resonant coupling between the molecular electronic levels and the plasmons in the metallic clusters modulated by the molecular vibrations.[159] Interestingly, the mode at 1606 cm^{-1} stems from a breathing mode of the carbon rings. This observation reinforces the conclusion that the interaction between the considered metals and PTCDA (DiMe-PTCDI) takes place via the perylene core.

The conclusions regarding diffusion of the metal atoms into the organic polycrystalline layers drawn from the enhancement factors of the internal modes are further confirmed by the spectral changes in the region of the external modes of the organic layers. The external modes of PTCDA disappear almost completely already after depositing 0.4 nm of In, while they only get broader and decrease in intensity after Ag and Mg deposition (Figure 80).

In Figure 81 the spectra of the external modes are shown upon stepwise metal deposition onto 15 nm of PTCDA. For a quantitative evaluation, the spectra of Ag/PTCDA and Mg/PTCDA were fitted using Lorentzian functions.

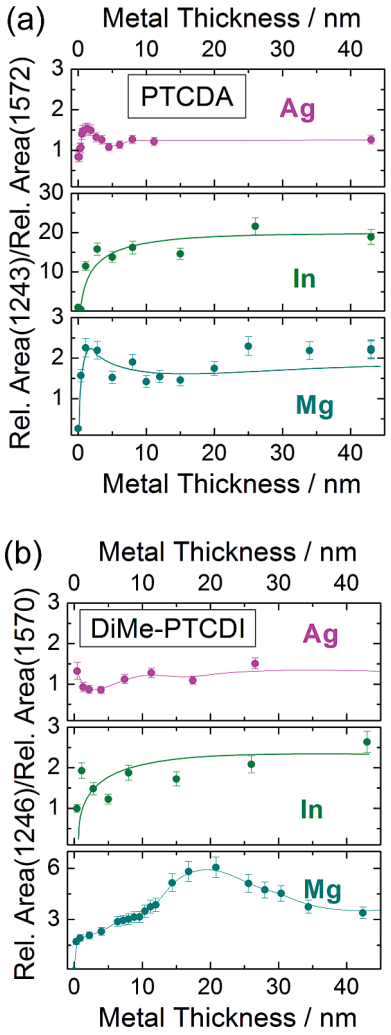

Figure 79. Ratio between the enhancement factor of the B_u mode (1243 cm^{-1} in PTCDA and 1246 cm^{-1} in DiMe-PTCDI) and that of the C−C stretching A_g mode (1572 cm^{-1} in PTCDA and 1570 cm^{-1} in DiMe-PTCDI) as a function of the metal coverage.

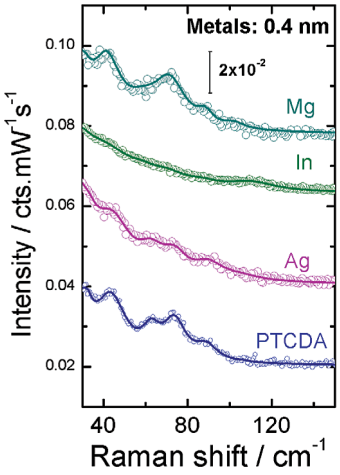

Figure 80. Raman spectra of 15 nm thick PTCDA films covered with Ag, In, and Mg in the region of the external modes.

The evolution of the fwhm as a function of Ag and Mg thickness is plotted in Figure 82 for the external mode at 41 cm^{-1}. This mode is fairly well separated from its neighbors, and hence, the fitting parameters of the corresponding Lorentzian function are less correlated. As the metal thickness increases, the fwhm of the external modes

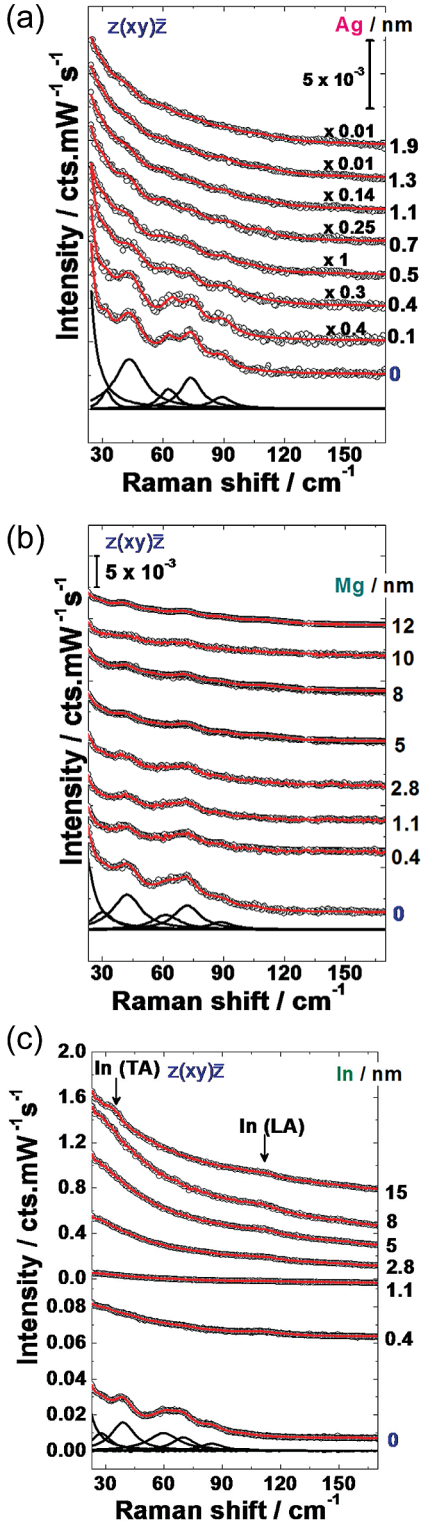

Figure 81. Raman monitoring in the external mode region upon metal deposition: Ag (a); Mg (b); In (c). The experimental spectra are shown by open symbols, and the fitted spectra, by red lines. The Lorentzian functions used for curve fitting of the Raman spectrum of the pure PTCDA film are shown by lines in the lower part of each graph. The spectra are normalized for Ag/PTCDA for a better observation of the phonons.

increases faster in Ag/PTCDA compared to Mg/PTCDA.

For Mg the external modes are still visible at 12 nm coverage, whereas they are almost completely smeared out at 1.3 nm of Ag. This is a clear indication that the crystalline structure of the organic layers is less affected by the Mg deposition compared to Ag. However, it should be noted that

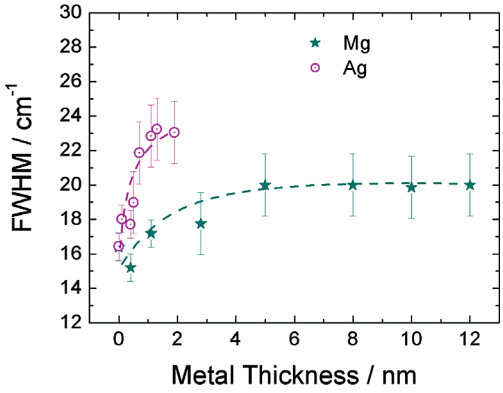

Figure 82. Evolution of the fwhm of the external mode at 41 cm^{-1} as a function of the metal coverage relative to the initial values before the metal deposition: for Ag (a) and Mg (b). The dashed lines are guides for the eyes.

curve fitting of the spectra in the case of Ag/PTCDA is complicated by the significant increase in the low-frequency background (which was already subtracted in Figure 80). The background evolution reflects an increasing degree of roughness, which is consistent with an increasing number of metallic clusters that diffusely scatter the light. A strong increase in the low-frequency background is also observed for the case of In deposition onto PTCDA, while it hardly affects the spectra of Mg/PTCDA, supporting the conclusion that the roughening due to Mg is lower compared to that of the Ag and In.

While the external molecular modes disappear already in the first deposition stages for In/PTCDA, two new modes develop at 33 and 112 cm^{-1} above In coverages of 2.8 nm. They may correspond to the transverse acoustic and longitudinal acoustic phonons located at 34 and 114 cm^{-1}, respectively, in bulk indium[160,161] activated due to the low dimension of the In clusters. This observation corroborated by the concomitant increase in the low-frequency background indicates the formation of metallic In clusters. Moreover, the enhancement of the internal modes also increases dramatically above 2.8 nm of In, supporting the conclusion of metallic cluster formation.

In the case of Mg deposition onto DiMe-PTCDI, the external modes are attenuated only for a Mg nominal coverage above 21 nm, i.e., similar to the case of Mg/PTCDA, indicating that the Mg atoms do not protrude into the crystalline molecular islands (Figure 83). However, the ratio between the area of the B_u mode at 1246 cm^{-1} and that of the A_g mode at 1570 cm^{-1} (Figure 79) continuously increases up to about the same coverage. These two observations might seem contradictory when recalling the previous discussion on the correlation between the evolution of this ratio and the diffusion of the metal atoms. On the other hand, the relative intensities of the GaAs related features change already for low Mg coverages (Figure 83), reflecting a change in the GaAs band bending. This can only occur if the Mg atoms reach the GaAs surface in the large voids between the DiMe-PTCDI islands and react with it, as also learned from the PES results.

6.2.2. Valence Band Photoemission

Additional information regarding the electronic properties of the metal/organic interface and evidence of metal indiffusion during the growth is provided by the valence band photoemission spectra.

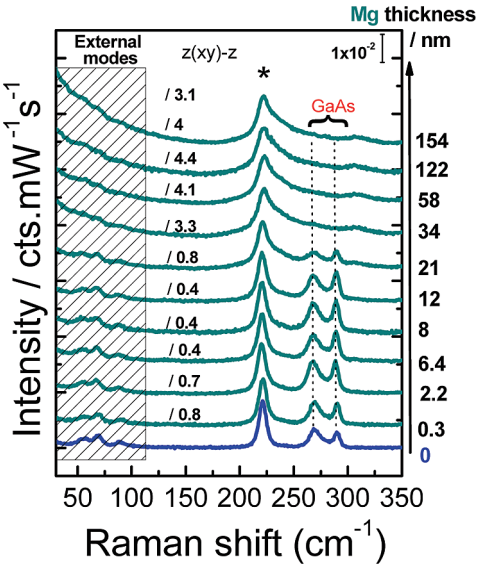

Figure 83. Raman spectra of DiMe-PTCDI upon Mg deposition in the region of external modes of the organic film and GaAs phonons. The spectra are normalized with respect to the intensity of the breathing mode at 221 cm^{-1}.

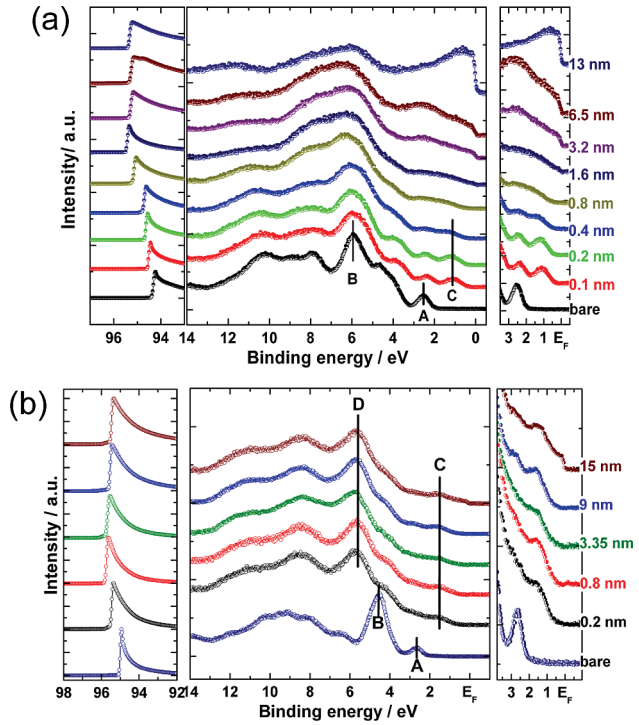

Figure 84. Evolution of the valence band spectra of 15 nm films of PTCDA (a) and DiMe-PTCDI (b) upon Mg deposition.

6.2.2.1. Mg on Perylene Derivatives. Figure 84 shows the valence band spectra of 15 nm films PTCDA (a) and DiMe-PTCDI (b) upon deposition of Mg. The bottom spectrum in this figure corresponds to the bare organic film.

Upon deposition of Mg, the center and right-hand panels clearly show the appearance of filled states in the gap of the organic material (feature C) at about 1.3 eV above the HOMO. The nature of the feature in the band gap is related to the charge transfer from the metal to the organic molecule resulting in an occupation of LUMOs, in good agreement with the S-XPES and NEXAFS observations.

In Figure 84a, at higher thicknesses, feature A shifts slightly toward lower binding energy while feature C does not change its binding energy position. In connection with the core level spectra, the change in features A and C can be explained by the strong interaction between Mg atoms and the organic material (see Figure 68) resulting in MgO charge transfer to the molecule and the modified organic molecule (see section 6.1.2.1—Mg on PTCDA). At 1.6 nm the formation of the Fermi edge is observed.

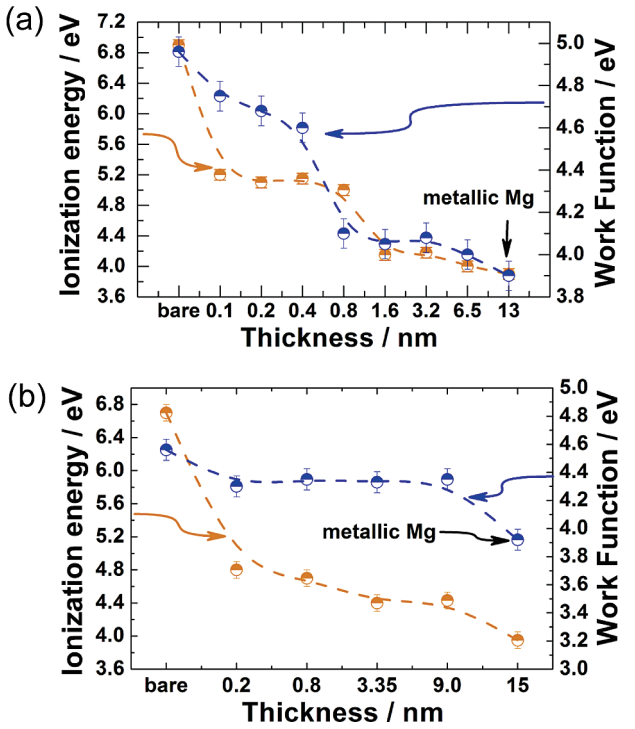

Figure 85. Evolution of IE and ϕ as a function of Mg thickness for PTCDA (a) and DiMe-PTCDI (b) films.

In Figure 84b the characteristic line shapes of the bulk seem to be significantly broadened and hardly distinguishable. In addition, a new feature (D) which develops at about 6 eV is related with the presence of the oxidized state in the Mg_{2p} spectra and with the shift toward higher binding energies of the O_{1s} core level.

The evolution of the ionization energy and of the work function as a function of Mg thickness is shown in Figure 85. An interesting point to mention before discussing the evolution of the work function is the origin of changes in ϕ and IE after metal coverage. As observed in the core level spectra, at low metal coverages the metal atoms diffuse into the underlying organic film and some metal clusters are formed. These metal atoms can influence the electronic properties of the organic films in two ways. First, in the presence of a charge transfer, either accompanied or not by the formation of covalent bonds, the energy levels of the organic film close to the surface will change according to the amount of charge transferred to the molecules. Second, even if there is no charge transfer, metal atoms between organic molecules in the film can disturb the crystalline structure of the organic layer and consequently change the polarization energy, which is defined as the energy difference of the IE (EA) values of the isolated molecules and the film. This effect can also lead to a change in the energy levels.

At low metal coverage, the electronic properties of the organic films are dramatically influenced. After the first deposition of Mg, there is an abrupt decrease in ϕ followed by a slower decrease. For thicknesses larger than 0.8 nm,

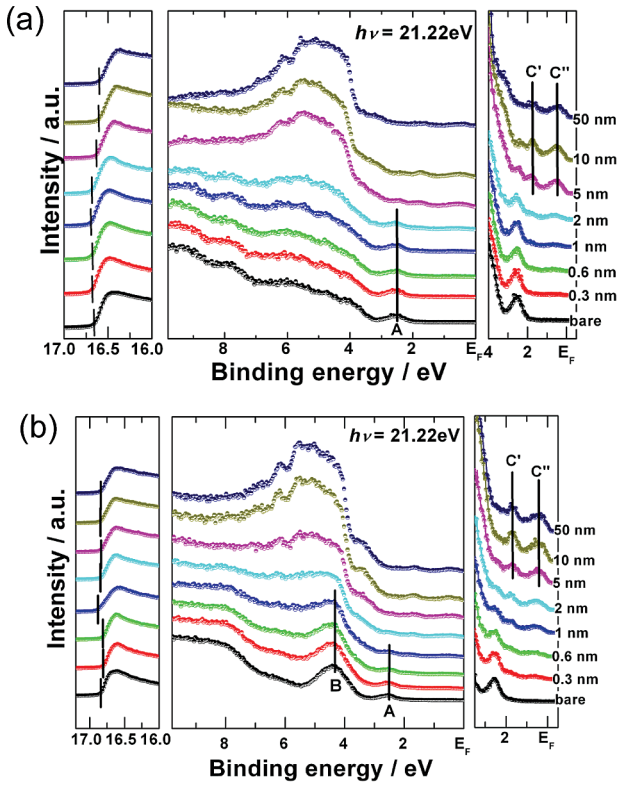

Figure 86. VB spectra as a function of Ag thickness on 10 nm PTCDA (a) and 10 nm DiMe-PTCDI (b) films for a photon energy of $h\nu = 21.22$ eV.

both IE and ϕ show a gradual decrease, reaching a final value of (3.9 ± 0.07) eV at about 1.6 nm of Mg. The latter value is closer to the value corresponding to metallic Mg. The presence of a Fermi edge at 1.6 nm for PTCDA clearly indicates that the formation of MgO prevents diffusion of Mg into the organic film and that the metal clusters grow on top of the reacted layer. For DiMe-PTCDI, ϕ reaches a final value of (3.9 ± 0.07) eV at a thickness of about 15 nm. Again, the occurrence of the Fermi edge at 15 nm indicates the accumulation of metal clusters at the surface of the organic film. The plateau observed in ϕ above 0.2 nm is a clear indication that the organic film is not disturbed upon Mg deposition.

6.2.2.2. Ag on Perylene Derivatives. The valence band spectra measured during deposition of Ag onto 10 nm films of PTCDA and DiMe-PTCDI are shown in Figure 86.

At Ag thicknesses below ~1 nm, all features corresponding to PTCDA and DiMe-PTCDI can be seen, with their line shapes and energy positions remaining unchanged. In addition, two small features (C′, C″) appear in the HOMO−LUMO gap of the organic film. The energy positions of these features are ~0.5 eV and ~1.7 eV. The origin of these two bands is arguable. PES studies of Ag/phthalocyanine interfaces showed that the feature located at about 0.5 eV from the Fermi level is the result of a charge transfer from Ag to the organic molecules. In this thickness range, the Fermi edge from metallic Ag is not clearly visible, indicating that clustering of Ag atoms does not occur due to diffusion into the organic layer.

Upon further Ag deposition, the new features C′ and C″ become stronger and the emission from the Ag_{4d} band is seen between 4 and 7.5 eV while all the bands corresponding to the organic films become attenuated. The Fermi edge becomes visible above 2 nm, in good agreement with the

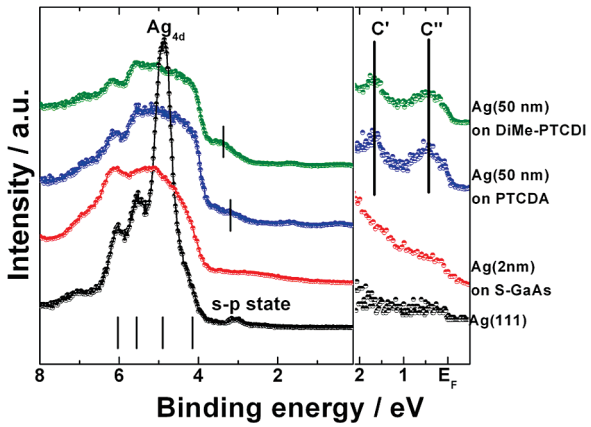

Figure 87. Comparison of VB spectra of different Ag films: the spectra from bottom to top correspond to Ag(111) film on Si(111), 2 nm Ag film on S-GaAs(100), and 50 nm Ag films grown on PTCDA and DiMe-PTCDI layers.

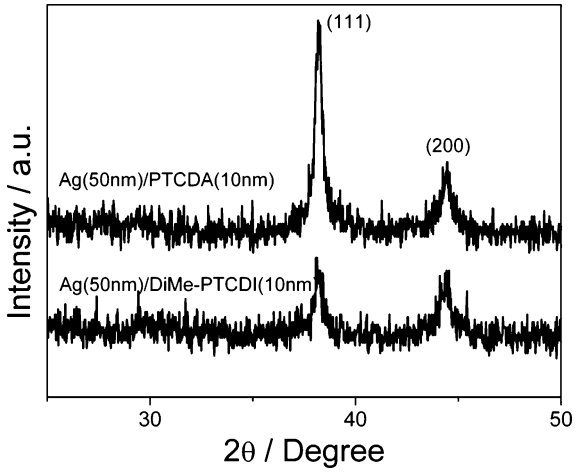

Figure 88. XRD spectra of 50 nm Ag films grown on 10 nm PTCDA and DiMe-PTCDI films.

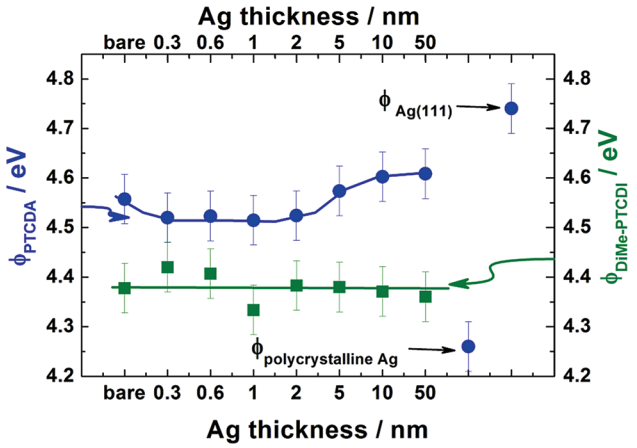

Figure 89. Evolution of ϕ as a function of Ag thickness for the Ag deposition onto 10 nm films of PTCDA (left scale) and DiMe-PTCDI (right scale). For comparison reasons, the values of ϕ for the polycrystalline Ag film[164] and single crystalline Ag(111)[163] are included.

1.3 nm of Ag coverage determined from Raman measurements for which the Ag diffusion stops.

It is known that the line shape of the Ag_{4d} band strongly depends on the bulk crystallographic directions, the surface morphology of the Ag film, and whether or not there is adsorbate on the surface.[162] The VB spectra of 50 nm Ag

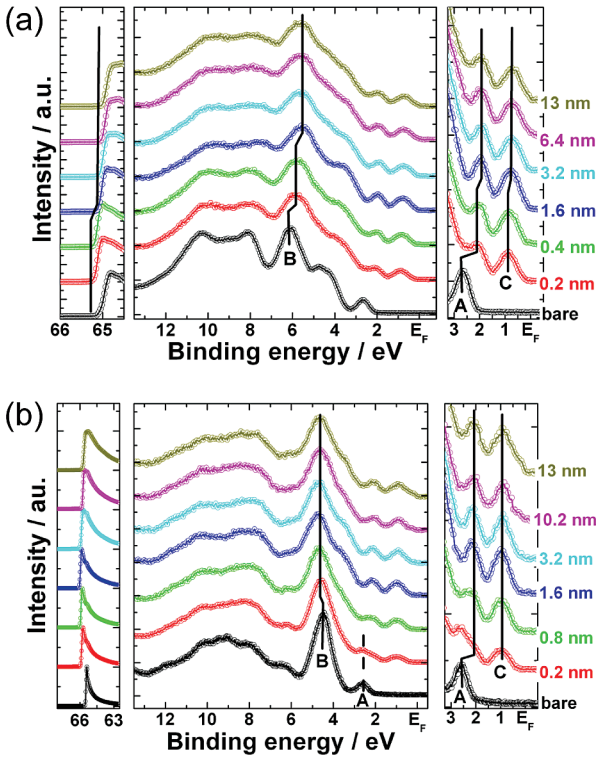

Figure 90. Evolution of the valence band spectra of 15 nm thick films of PTCDA (a) and DiMe-PTCDI (b) upon In deposition.

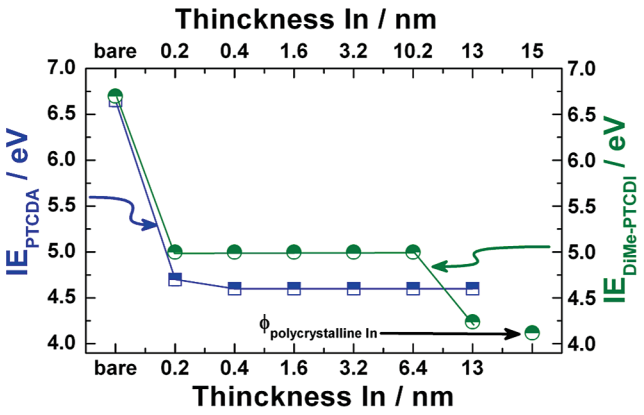

Figure 91. Evolution of IE as a function of In thickness for 15 nm thick PTCDA (left scale) and DiMe-PTCDI (right scale) films. For comparison reasons, the values of ϕ for the polycrystalline In film are included.[165]

on the PTCDA and DiMe-PTCDI films are compared with those of Ag(111) and Ag on S-GaAs(100), which are shown in Figure 87.

The VB spectra of the Ag films on the two organic films look similar to that of the Ag film on S-GaAs(100). However, the relative intensities between the sub-bands differ, reflecting different crystalline structures. Additional X-ray diffraction (XRD) experiments reveal two peaks corresponding to the (111) and (200) directions, the relative intensity of which depends on the organic film (Figure 88). The (111) peak is much stronger for Ag/PTCDA than for Ag/DiMe-PTCDI. This is an indication that the crystalline structure of Ag films is strongly affected by the morphology of the underlying organic films, such as the crystalline structure and the degree of packing.

The evolution of ϕ is shown in Figure 89 as a function of the thickness of Ag. The literature values for the single Ag-

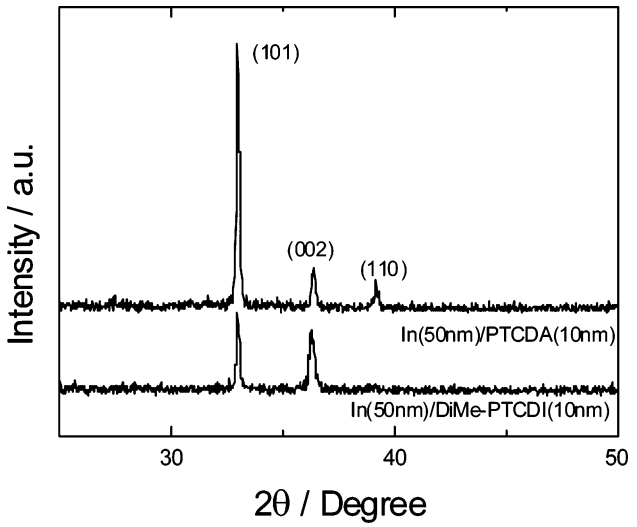

Figure 92. XRD spectra of 50 nm In films grown on 10 nm PTCDA and DiMe-PTCDI films.

(111) crystal[163] and the polycrystalline Ag films[164] are included. Before Ag deposition, the ϕ values of PTCDA and DiMe-PTCDI are (4.56 ± 0.05) and (4.38 ± 0.05) eV, respectively. Upon deposition of Ag onto PTCDA, a slight decrease of ϕ is observed up to 1 nm, and ϕ then begins to increase gradually to reach a final value of (4.61 ± 0.05) eV. On the other hand, ϕ does not change over the whole Ag deposition onto DiMe-PTCDI. The difference in ϕ for thick Ag films on PTCDA and DiMe-PTCDI can be understood when comparing the ϕ values of Ag having different crystalline orientations. The ϕ value of the Ag film on PTCDA is closer to the value corresponding to a single Ag(111) crystal. This agrees very well with the observation of a stronger (111) peak in the XRD experiment.

The combined results of the XRD and PES experiments indicate two important characteristics of the metal growth on organic substrates. First, the crystallinity of the metal films strongly depends on the morphology of the underlying organic film. Better crystalline metal films can be grown on organic films with a lower roughness. Second, in order to interpret or predict electrical properties for organic electronics, the work function values that were obtained for other systems cannot be used.

6.2.2.3. In on Perylene Derivatives. The evolution of valence band spectra of 15 nm films of PTCDA and DiMe-PTCDI upon deposition of In is presented in parts a and b, respectively, of Figure 90. The center and the right panels of both parts of the figure show the appearance of the filled states (feature C) in the gap of the organic film at about 0.9 eV from Fermi level.

From Figure 91 it can be seen that the molecular level separations remain constant as a function of metal coverage. Moreover, the bulklike molecular features are preserved.

These observations are consistent with the fact that In induces an electron transfer from the metal to the lowest unoccupied molecular orbitals and consequently a reconformation of the molecule but does not undergo a strong chemical interaction with PTCDA.

In Figure 90a, above 1.6 nm a shift of 0.25 eV is observed and attributed to the increase of the cluster size thus improving the core-hole screening. This result is in complete agreement with the observations in the C_{1s} and O_{1s} core levels. Even if the In thickness is increased, no states at the

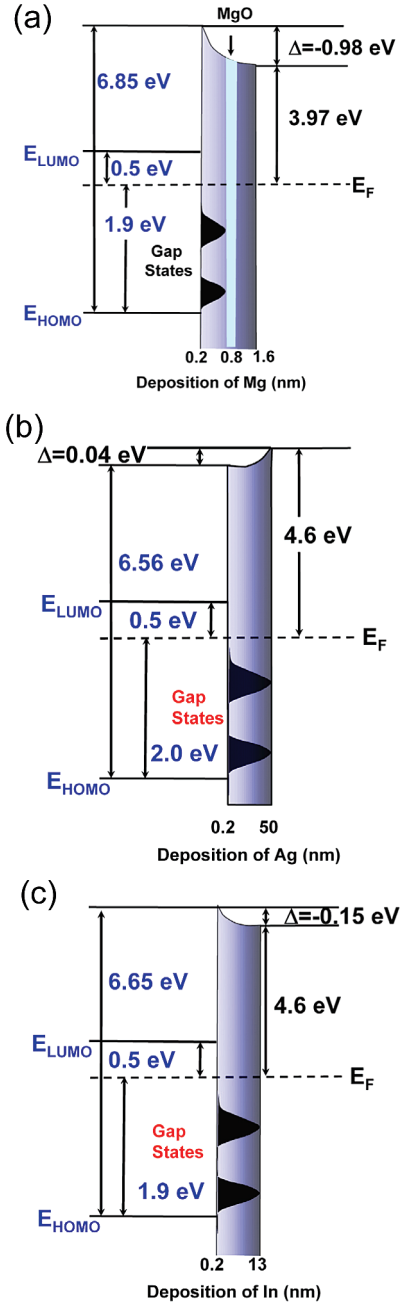

Figure 93. Energy level alignment at the metal/PTCDA interfaces: (a) Mg; (b) Ag; (c) In. The E_{LUMO} position is taken from IPES measurements.

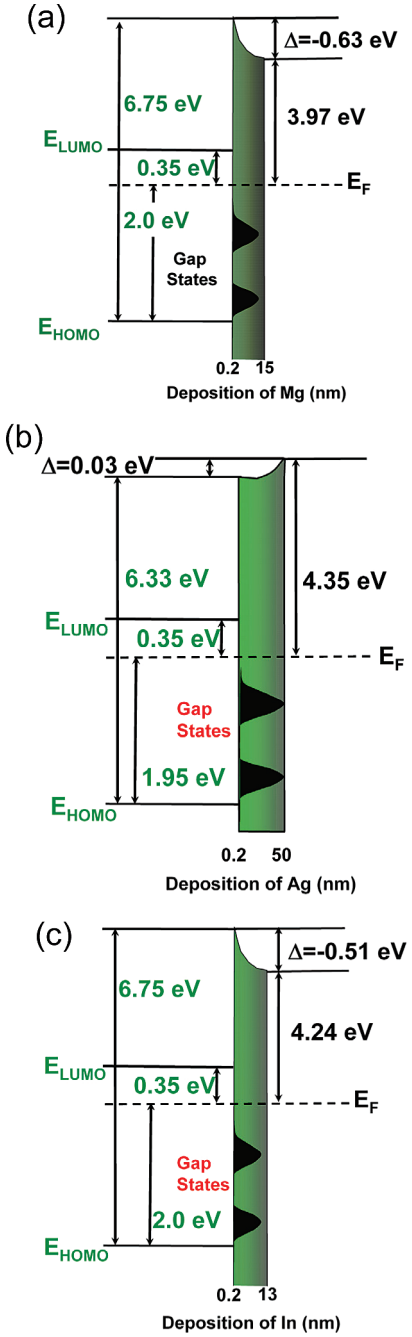

Figure 94. Energy level alignment at the metal/DiMe-PTCDI interfaces: (a) Mg; (b) Ag; (c) In. The E_{LUMO} position is taken from IPES measurements.

Fermi level were observed, indicating that the cluster sizes are small and clusters do not coalesce. This finding supports the conclusion drawn from Raman experiments on the high diffusion of In.

Contrary to PTCDA, in the DiMe-PTCDI case, densities of states at the Fermi level are observed at thicknesses above 13 nm, demonstrating that In does start to accumulate at the surface of the organic film (see Figure 90b). Moreover, the gradual shift toward lower binding energy associated with the increase of the cluster size is not observed. This can be attributed to different rates of the formation of In clusters and is an indication that the morphology of the In layer depends on the underlying organic materials.

The XRD measurements for a 50 nm In film on PTCDA and DiMe-PTCDI (Figure 92) also reveal different morphologies. For the In film on PTCDA, three peaks, corresponding to the (101), (002), (110) crystallographic directions, are revealed, while only the (101) and (002) peaks are visible for In on DiMe-PTCDI. The intensity of the (101) peak is found to be much stronger for In/PTCDA. Considering also the stronger (111) diffraction peak for Ag/PTCDA compared to that for Ag/DiMe-PTCDI, it can be concluded that metal films on PTCDA have higher crystallinity than those on DiMe-PTCDI.

In summary, Mg, Ag, and In deposition onto 15 nm thick PTCDA and DiMe-PTCDI films on S-GaAs(100):2×1 was characterized by Raman spectroscopy and electron spectroscopies.

A process of dynamical fractional charge transfer modulated by molecular vibrations is proposed to be responsible for the enhancement of modes and for the breakdown of

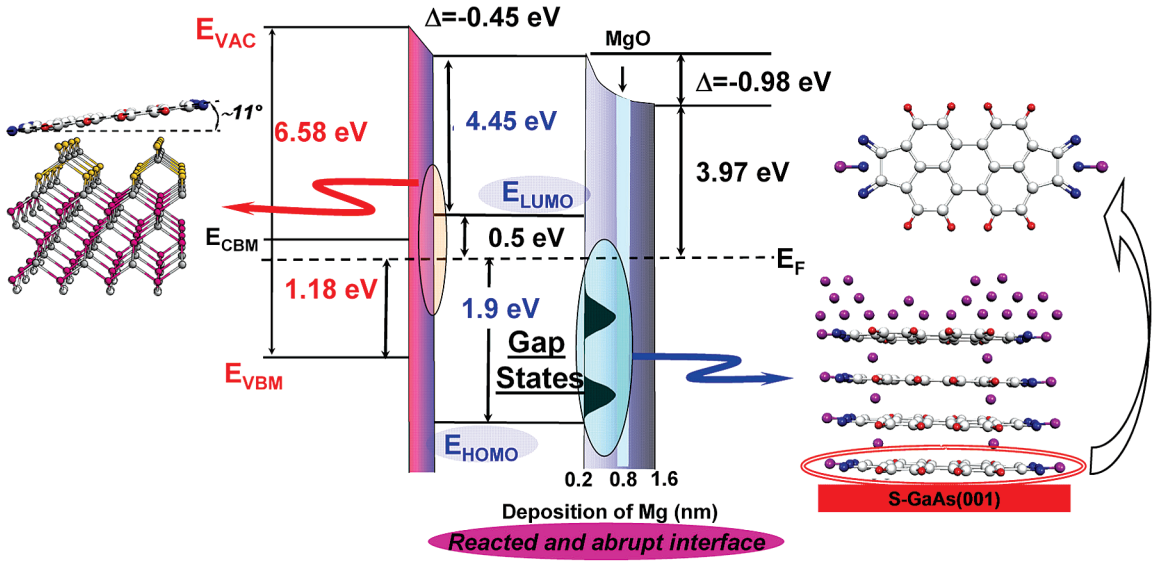

- Molecular orientation of PTCDA onto S-GaAs(001)
- Energy level alignment at the S-GaAs / PTCDA interface
- $E_{transport}=(E_{HOMO}-E_{LUMO})=(2.4 \pm 0.2)$ eV
- Strong reaction of Mg with the anhydride group → formation of MgO and a modified molecule
- Energy level alignment at the PTCDA / Mg interface

Figure 95. S-GaAs/PTCDA/Mg heterostructure.

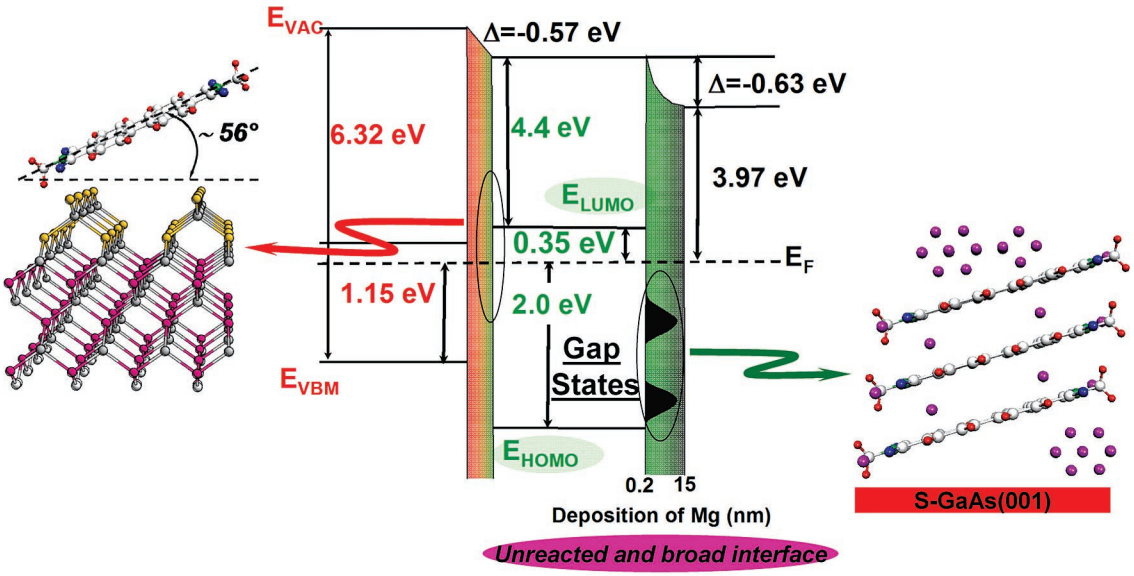

- Molecular orientation of DiMe-PTCDI onto S-GaAs(001)
- Intermolecular energy band dispersion Δ = 0.2 eV
- Energy level alignment at the S-GaAs / DiMe-PTCDI interface
- $E_{transport}=(E_{HOMO}-E_{LUMO})=(2.35 \pm 0.2)$ eV
- Mg prefers to adsorb between the crystalline grains → methyl group controls the chemical reaction
- Energy level alignment at the DiMe-PTCDI / Mg interface

Figure 96. S-GaAs/DiMe-PTCDI/Mg heterostructure.

selection rules in the Raman spectra of metal/(ML) organic heterostructures, particularly for Ag/organic and In/organic heterostructures. In the spectra recorded during the Mg deposition onto PTCDA, bands assigned to MgO develop, indicating a reaction of Mg with PTCDA molecules that causes the loss of the central O atom of the anhydride groups.

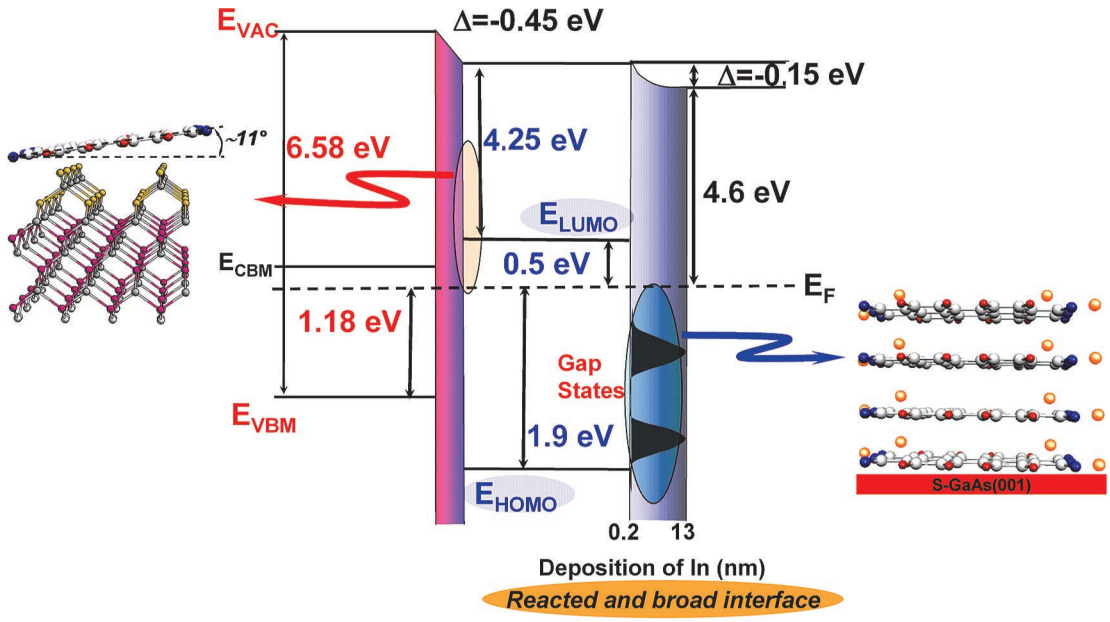

❖ In prefers to adsorb at the side of carboxylic group of PTCDA

❖ Energy level alignment at the PTCDA / In interface

Figure 97. S-GaAs/PTCDA/In heterostructure.

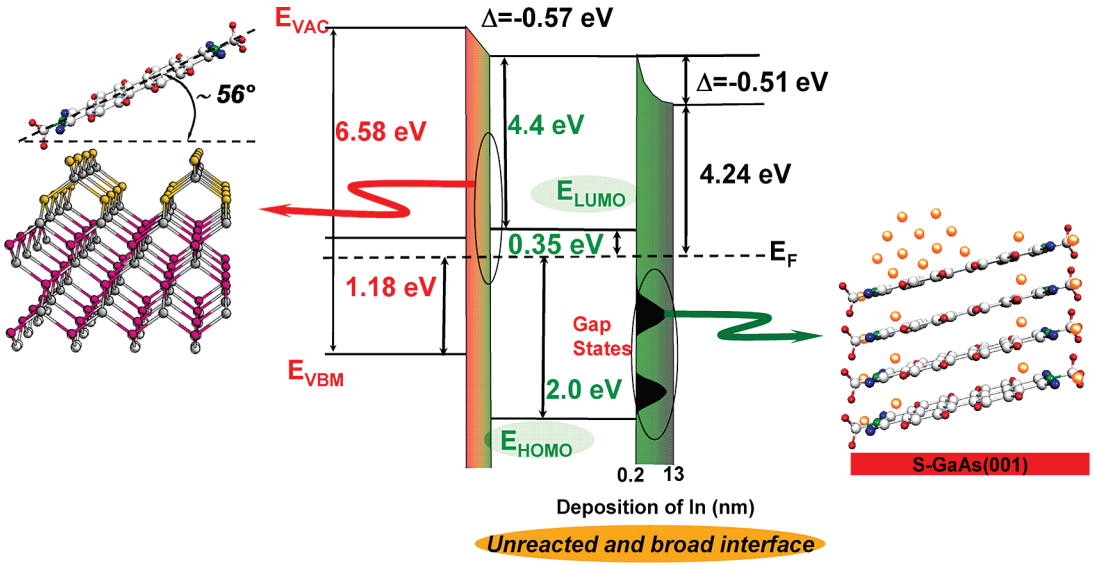

❖ Energy level alignment at the DiMe-PTCDI / In interface

❖ *Apparent* adsorption of In at the side of carboxylic group ➡ methyl group controls the chemical reaction

Figure 98. S-GaAs/DiMe-PTCDI/In heterostructure.

The features potentially assigned to MgO phonons do not appear in the spectra during deposition of Mg onto DiMe-PTCDI. Thus, a chemical reaction between Mg and DiMe-PTCDI was ruled out.

In metal/organic heterostructures with 15 nm thick organic films, analysis of the enhancement factors of the signal from the organic molecule as a function of metal coverage can indicate the level of roughness of the metal overlayer. Upon Mg, Ag, and In deposition, the totally symmetric modes are initially strongly enhanced. Subsequently, the signal is attenuated exponentially with an exponent that is much smaller than the exponent corresponding to the penetration depth of the incident radiation in a smooth closed metal film. The degree of roughness increases from Mg toward Ag over In for both organic films.

Moreover, the intensities of the normally infrared active modes relative to those of the Raman modes provide information on the metal diffusion depth in the organic films. Complementary information on the metal diffusion depth in the organic layers is provided by the attenuation rate of the

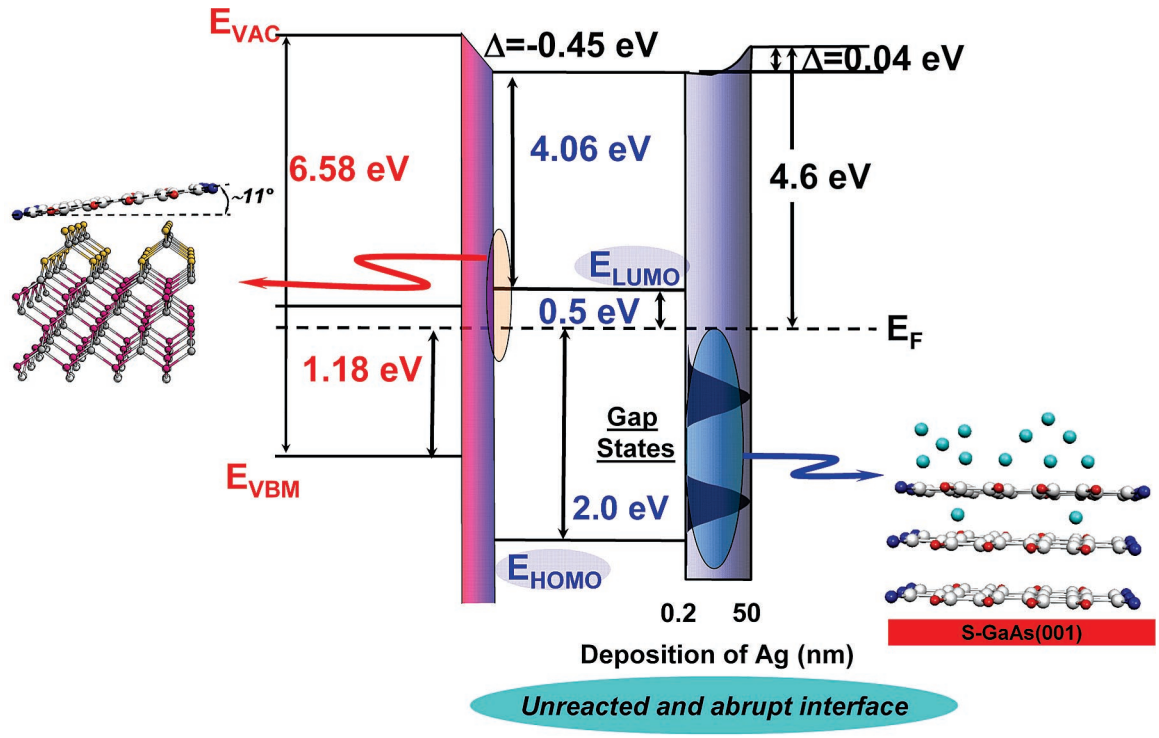

Figure 99. Energy level alignment at the S-GaAs/PTCDA/Ag interface.

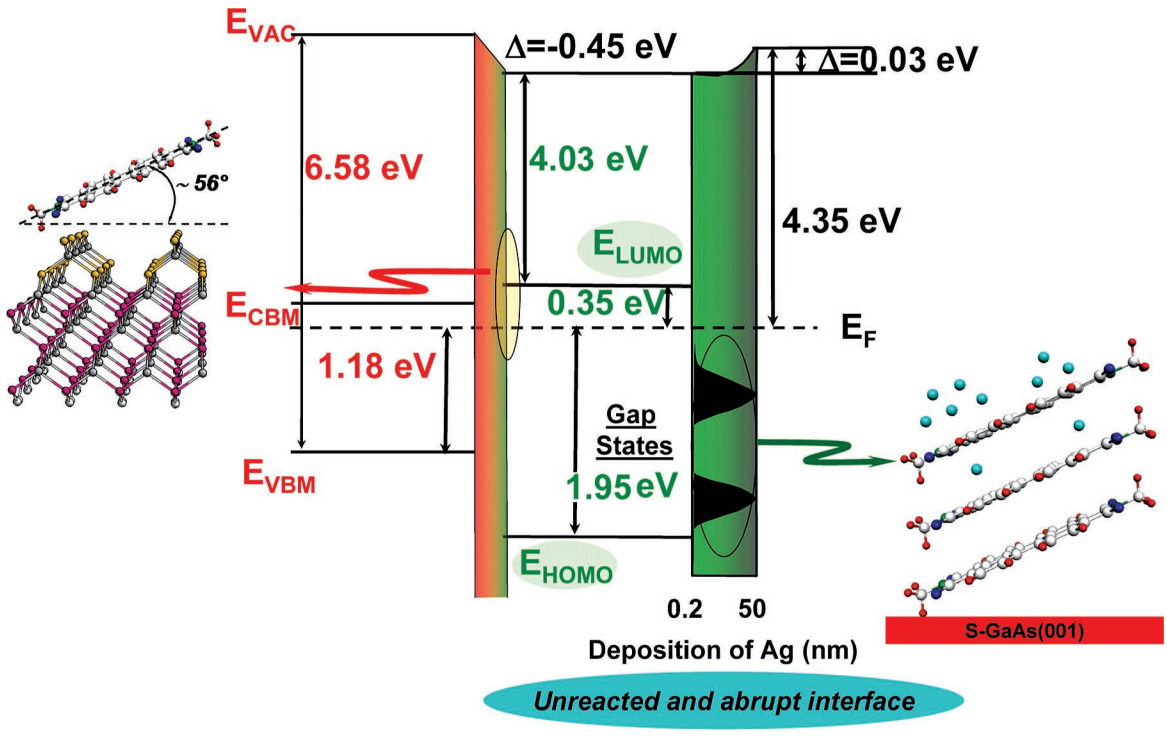

Figure 100. Energy level alignment at the S-GaAs/DiMe-PTCDI/Ag interface.

external mode intensities as a function of the metal coverage. While Mg and Ag form abrupt interfaces, In strongly diffuses into the organic layers.

Complementary information about the chemistry and indiffusion at the metal/organic interface was gained when electron spectroscopic methods were employed. The chemistry of these interfaces was established after a detailed analysis of the evolution of C_{1s}, O_{1s}, and metal core levels as a function of metal coverage.

When Mg is deposited onto PTCDA, new features are observed in the O_{1s} and Mg_{2p} core level emission spectra of PTCDA, indicating a strong chemical interaction between Mg and the single bonded oxygen atoms (side groups) of PTCDA. This interaction leads to the formation of MgO and

a modified organic molecule with different properties than those of PTCDA. The less dramatic changes observed in the C_{1s}, O_{1s}, and Mg_{2p} core level emission spectra upon Mg deposition onto DiMe-PTCDI indicate a less reactive nature of this interface compared to the Mg/PTCDA interface. This can be easily related with the molecular structure of DiMe-PTCDI. The existence of a methylimide group as a side group controls the chemical reactivity of this interface.

When In is deposited onto PTCDA, the carboxylic oxygen (C═O) of the O_{1s} core level emission spectra of PTCDA evolves into two different environments; in other words, the degeneracy of the C═O is lifted and the O_{1s} core level emission spectra as a function of the In coverage are strongly affected. Therefore, when In is grown onto PTCDA, its molecular structure is preserved but the In atoms will absorb near the carboxylic oxygen without a chemical bond formation. The changes observed in the O_{1s} and N_{1s} core level emission spectra upon In deposition onto DiMe-PTCDI are less dramatic, indicating that at this interface the interaction is weak. This is explained again by the presence of the methylimide group. Moreover, an assignment of the In_{4d} components was possible, and consequently, we could recognize the adsorption sites of In. The main difference between the two interfaces is the degree to which the In atoms diffuse into the organic film. Together with the XRD results, this could be related with the morphology of the organic film, in particular with the size of the organic crystals and/or the smoothness of the surface.

NEXAFS results showed that molecular and structural changes are accompanied by a charge transfer from the metal to the organic film. Such an electronic interaction reflects the partial occupancy of the LUMO and LUMO + 1, with the formation of gap states. The charges are redistributed mainly over the perylene core.

The evolution of valence band structures provides additional information about the degree of diffusion of the metal into the organic film. The VB-PES results corroborate the Raman results. For Mg differences are related with the formation of MgO, which prevents the diffusion of Mg into PTCDA. The energy level alignment between metal/PTCDA and metal/DiMe-PTCDI interfaces was established and is presented in Figures 93 and 94, respectively.

7. Conclusions

In this review we illustrate the complementary nature of electron and vibrational spectroscopies for studying organic/inorganic interfaces. This was done by utilizing the examples of two semiconducting organic molecules, viz. PTCDA and DiMe-PTCDI, deposited on GaAs surfaces. Thin films of these molecules later served as substrates for metal deposition and the study of metal/organic interface formation. In detail it was shown that both molecules preferentially adsorb on defect sites in the initial phase of interface formation with GaAs involving a reduction of inhomogeneous band bending of the substrate. In this case Raman spectroscopy was proven to possess sub-monolayer sensitivity. The energy level alignment between VBM(CBM) and HOMO(LUMO) was determined from photoemission spectroscopy. For thin films the transport gap was determined using the combination of direct and inverse photoemission spectroscopy. Owing to the high order in the organic layers, it was also possible to determine dispersions of HOMO bands. The molecular orientation in highly ordered films was evaluated using various techniques, including NEXAFS, Raman, and IR spectroscopies. In this context it is noteworthy to mention that the minor change in the molecular structure from the anhydride group in PTCDA to the methylimide group in DiMe-PTCDI induces a drastic change in molecular orientation. The complementary nature of vibrational and electron spectroscopies becomes most evident when considering the interface formation of metals deposited onto organic layers. Here, Raman spectroscopy turned out to be extremely interface sensitive due to the surface-enhanced Raman scattering effect. The Raman results provide information about interfacial reactivity as well as metal indiffusion while the details thereof are clarified by employing core level emission spectroscopy. A pictorial summary of this review together with the essential conclusions related to the organic/inorganic semiconductor and metal/organic semiconductor interface formation as well as to the structural properties of the organic thin films is outlined in Figures 95−100.

8. Acknowledgments

The authors are indebted to Sung Gook Park, Mihaela Gorgoi, Henry Mendez, Beynor Paez, Marion Friedrich, Cameliu Himcinschi, Nicoleta Nicoara, Axel Fechner, Mike Sperling, Denis Vyalikh, Walter Braun, Reinhard Scholz, Andrei Kobitski, and Hartmut Kupfer for their contribution in obtaining the experimental results presented in this review. The work was financially supported by the EU funded Human Potential Research Training Network DIODE (Contract No. HPRN-CT-1999-00164), the Deutsche Forschungsgemeinschaft within the OFET-SPP (Project No. SPP1121/Za146/14-2), and the BMBF (No. 05KS10CA/1, MUSTANG 05KS40C1/3).

9. References

(1) Forrest, S. R. *Chem. Rev.* **1997**, *97*, 1793.
(2) Glöcker, K.; Seidel, C.; Soukopp, A.; Sokolowski, M.; Umbach, E.; Böhringer, M.; Berndt, R.; Schneider, W.-D. *Surf. Sci.* **1998**, *405* (1), 1.
(3) Seidel, C.; Awater, C.; Liu, X. D.; Ellerbrake, R.; Fuchs, H. *Surf. Sci.* **1997**, *371*, 123.
(4) Kendrick, C.; Kahn, A.; Forrest, S. R. *Appl. Surf. Sci.* **1996**, *586*, 104−105.
(5) Hirose, Y.; Chen, W.; Haskal, E. I.; Forrest, S. R.; Kahn, A. *J. Vac. Sci. Technol. B* **1994**, *12*, 2616.
(6) Stephens, P. J.; Devlin, F. J.; Chabalowski, C. F.; Frisch, M. J. *J. Phys. Chem.* **1994**, *98*, 11623.
(7) Bitzer, T.; Richardson, N. V. *Appl. Surf. Sci.* **1999**, *144−145*, 339.
(8) Mönch, W. *Semiconductor Surfaces and Interfaces*; Springer-Verlag: New York, 1993.
(9) Le Thanh, V.; Bouchier, D.; Hincelin, G. *J. Appl. Phys.* **2000**, *87* (8), 3700.
(10) Möbus, M.; Karl, N. *Thin Solid Films* **1992**, *215*, 213.
(11) Salvan, G.; Tenne, D. A.; Das, A.; Kampen, T. U.; Zahn, D. R. T. *Org. Electron.* **2000**, *1*, 49.
(12) Chen, Q.; Rada, T.; Bitzer, Th.; Richardson, N. V. *Surf. Sci.* **2003**, *547*, 385.
(13) Kampen, T. U.; Salvan, G.; Tenne, D. A.; Scholz, R.; Zahn, D. R. T. *Appl. Surf. Sci.* **2001**, *175−176*, 326.
(14) Salvan, G.; Silaghi, S.; Paez, B.; Baumann, G.; Kampen, T. U.; Scholz, R.; Zahn, D. R. T. *J. Cryst. Growth* **2005**, *275* (1−2), e1155.
(15) Glockler, K.; Seidel, C.; Soukopp, A.; Sokolowski, M.; Umbach, E.; Bohringer, M.; Berndt, R.; Schneider, W.-D. *Surf. Sci.* **1998**, *405* (1), 1.
(16) Chkoda, L.; Schneider, M.; Shklover, V.; Kilian, L.; Sokolowski, M.; Heske, C.; Umbach, E. *Chem. Phys. Lett.* **2003**, *371* (5−6), 548.
(17) Kilian, L.; Umbach, E.; Sokolowski, M. *Surf. Sci.* **2004**, *573* (3), 359.
(18) Marchetto, H.; Groh, U.; Schmidt, Th.; Fink, R.; Freund, H. J.; Umbach, E. *Chem. Phys.* **2006**, *325* (1), 178.
(19) Zou, Y.; Kilian, L.; Schöll, A.; Schmidt, Th.; Fink, R.; Umbach, E. *Surf. Sci.* **2006**, *600* (6), 1240.
(20) Hiroshe, Y.; Kahn, A.; Aristov, V.; Soukiassian, P.; Bulovic, V.; Forrest, S. R. *Phys. Rev. B* **1996**, *54*, 13748.

(21) Kera, S.; Setoyama, H.; Onoue, M.; Okudaira, K.; Harada, Y.; Ueno, N. *Phys. Rev. B* **2001**, *63*, 115204.
(22) Park, S. Ph.D. Thesis, Technische Universität Chemnitz, 2002; http://archiv.tu-chemnitz.de/pub/2002/0004/index.html.
(23) Nakamura, T.; Iwasawa, K.; Kera, S.; Azuma, Y.; Okudaira, K. K.; Ueno, N. *Appl. Surf. Sci.* **2003**, *515*, 212−213.
(24) Tautz, F. S.; Sloboshanin, S.; Schäfer, J. A.; Scholz, R.; Shklover, V.; Sokolowski, M.; Umbach, E. *Phys. Rev. B* **2000**, *61*, 16933.
(25) Tautz, F. S.; Eremtchenko, M.; Schäfer, J. A.; Sokolowski, M.; Shklover, V.; Umbach, E. *Phys. Rev. B* **2000**, *65*, 125405.
(26) Shklover, V.; Tautz, F. S.; Scholz, R.; Sloboshanin, S.; Sokolowski, M.; Schäfer, J. A.; Umbach, E. *Surf. Sci.* **2000**, *60*, 454−456.
(27) Tautz, F. S.; Eremtchenko, M.; Schäfer, J. A.; Sokolowski, M.; Shklover, V.; Glöckler, K.; Umbach, E. *Surf. Sci.* **2002**, *176*, 502−503.
(28) Wagner, V.; Muck, T.; Geurts, J.; Schneider, M.; Umbach, E. *Appl. Surf. Sci.* **2003**, *212*−*213*, 502.
(29) Wagner, V. *Phys. Status Solidi A* **2001**, *188*, 1297.
(30) Guhatathakurta-Gosh, A.; Aroca, R. *J. Phys. Chem.* **1989**, *93*, 6125.
(31) Aroca, R.; Rodriguez-Llorente, S. *J. Mol. Struct.* **1997**, *17*, 408−409.
(32) Rodriguez-Llorente, S.; Aroca, R.; Duff, J. *Spectrochim. Acta A* **1999**, *55*, 969.
(33) Zahn, D. R. T.; Salvan, G.; Gavrila, G.; Paez, B. A. *Adv. Solid State Phys.* **2005**, *45*, 313.
(34) Ibach, H.; Lüth, H. *Solid State Physics*; Springer: Berlin Heidelberg, 1993; p 7.
(35) Hill, I. G.; Kahn, A.; Soos, Z. G.; Pascal, R. A., Jr. *Chem. Phys. Lett.* **2000**, *327*, 181.
(36) Knupfer, M.; Fink, J.; Zojer, E.; Leising, G.; Fichou, D. *Chem. Phys. Lett.* **2000**, *318*, 1055.
(37) Tsiper, E. V.; Soos, Z. G. *Phys. Rev. B* **2001**, *64*, 195124.
(38) Tsiper, E. V.; Soos, Z. G.; Gao, W.; Kahn, A. *Chem. Phys. Lett.* **2002**, *47*, 360.
(39) Weaver, J. *J. Phys. Chem. Solids* **1992**, *53*, 1433.
(40) Wu, C. I.; Hirose, Y.; Sirringhaus, H.; Kahn, A. *Chem. Phys. Lett.* **1997**, *43*, 272.
(41) Suzuki, H. *Electronic absorption spectra and geometry of organic molecules*; Academic Press: New York, 1967.
(42) Möbus, M.; Karl, N.; Kobayashi, T. *J. Cryst. Growth* **1992**, *116*, 495.
(43) Hädicke, E.; Graser, F. *Acta Crystallogr., C* **1986**, *42*, 189.
(44) Scholz, R.; Yu. Kobitski, A.; Kampen, T. U.; Schreiber, M.; Zahn, D. R. T.; Jungnickel, G.; Elstner, M.; Sternberg, M.; Frauenheim, Th. *Phys. Rev. B* **2000**, *61*, 13659.
(45) Yu. Kobitski, A. Ph.D. Thesis, Technische Universität Chemnitz, 2003; http://archiv.tu-chemnitz.de/pub/2003/0055/index.html.
(46) Ferraro, J. R.; Nakamoto, K. *Introductory Raman Spectroscopy*; Academic Press: San Diego, CA, 1994.
(47) Hoffmann, M. Ph.D. Thesis, Dresden, 2000.
(48) Wewer, M.; Stienkemeier, F. *Phys. Rev. B* **2003**, *67*, 125201.
(49) Scholz, R.; Vragovic, I.; Yu. Kobitski, A.; Salvan, G.; Kampen, T. U.; Schreiber, M.; Zahn, D. R. T. *Proceedings of Enricon Fermi School*; Varenna, 2001.
(50) Akers, K.; Aroca, R.; Hor, A. M.; Loutfy, R. O. *J. Phys. Chem.* **1987**, *91* (11), 2954.
(51) Frisch, M. J.; Trucks, G. W.; Schlegel, H. B.; Scuseria, G. E.; Robb, M. A.; Cheeseman, J. R.; Zakrzewski, V. G.; Montgomery, J. A.; Stratmann, R. E.; Burant, J. C.; Dapprich, S.; Millam, J. M.; Daniels, A. D.; Kudin, K. N.; Strain, M. C.; Farkas, O.; Tomasi, J.; Barone, V.; Cossi, M.; Cammi, R.; Mennucci, B.; Pomelli, C.; Adamo, C.; Clifford, S.; Ochterski, J.; Petersson, G. A.; Ayala, P. Y.; Cui, Q.; Morokuma, K.; Malick, D. K.; Rabuck, A. D.; Raghavachari, K.; Foresman, J. B.; Cioslowski, J.; Ortiz, J. V.; Stefanov, B. B.; Liu, G.; Liashenko, A.; Piskorz, P.; Komaromi, I.; Gomperts, R.; Martin, R. L.; Fox, D. J.; Keith, T.; Al-Laham, M. A.; Peng, C. Y.; Nanayakkara, A.; Gonzalez, C.; Challacombe, M.; Gill, P. M. W.; Johnson, B. G.; Chen, W.; Wong, M. W.; Andres, J. L.; Head-Gordon, M.; Replogle, E. S.; Pople, J. A. *Gaussian 98*, Revision A.1; Gaussian, Inc.: Pittsburgh, PA, 1998.
(52) Tenne, D. A.; Park, S.; Das, A.; Kampen, T. U.; Zahn, D. R. T. *Phys. Rev. B* **2000**, *61*, 15464.
(53) Kampen, T. U.; Salvan, G.; Friedrich, M.; Tenne, D. A.; Park, S.; Zahn, D. R. T. *Appl. Surf. Sci.* **2000**, *166*, 387.
(54) Kosic, T. J.; Schosser, C. L.; Dlott, D. D. *Chem. Phys. Lett.* **1983**, *96*, 57.
(55) Muck, T.; Schneider, M.; Umbach, E.; Wagner, V.; Geurts, J. *DPG-Frühjarstagung proceedings*; 2002.
(56) Guhatathakurta-Gosh, A.; Aroca, R. *J. Phys. Chem.* **1989**, *93*, 6125.
(57) Yu Kobitski, A.; Scholz, R.; Zahn, D. R. T. *THEOCHEM* **2003**, *625*, 39.
(58) Kampen, T. U.; Salvan, G.; Paraian, A.; Himcinschi, C.; Yu. Kobitski, A.; Friedrich, M.; Zahn, D. R. T. *Appl. Surf. Sci.* **2003**, *501*, 212−213.
(59) Hasche, T.; Canzler, T. W.; Scholz, R.; Hoffmann, M.; Schmidt, K.; Frauenheim, Th.; Leo, K. *Phys. Rev. Lett.* **2001**, *86* (18), 4060.
(60) Yu. Kobitski, A. Private communication.
(61) Spiro, V.; Enkvist, O.; Soldan, P.; Selzle, H. L.; Schlag, E. W.; Hobza, P. *J. Chem. Phys.* **1999**, *111* (2), 572.
(62) Gorelsky, S. L. *AOMix program*, Rev.9.24; 2004; http://www.sg-chem.net.
(63) Fuggle, J. C.; Inglesfield, J. E. *Topics in Applied Physics: Unoccupied electronic states*; Springer-Verlag: Berlin Heidelberg, 1992; Vol. 69.
(64) Schöll, A.; Zou, Y.; Jung, M.; Schmidt, Th.; Fink, R.; Umbach, E. *J. Chem. Phys.* **2004**, *121*, 10260.
(65) Gavrila, G.; Gorgoi, M.; Zahn, D. R. T.; Braun, W. *Bessy Annual Reports*; 2004; p 190.
(66) Gavrila, G. Ph.D. Thesis, Technische Universität Chemnitz, 2005; http://archiv.tu-chemnitz.de/pub/2006/0004.
(67) Nordfors, D.; Nilsson, A.; Mårtensson, N.; Svensson, S.; Gelius, U.; Lunell, S. *J. Chem. Phys.* **1998**, *88*, 2630.
(68) Enkvist, E. C.; Lunell, S.; Sjögren, Bo.; Brühwiler, P.; Svensson, S. *J. Chem. Phys.* **1995**, *103*, 6333.
(69) Sjögren, B.; Svensson, S.; Naves de Brito, A.; Correia, N.; Keane, M. P.; Enkvist, C.; Lunell, S. *J. Chem. Phys*. **1992**, *96*, 9, 6389.
(70) Chen, Q.; Rada, T.; Bitzer, Th.; Richardson, N. V. *Surf. Sci*. **2003**, *547*, 385.
(71) Schöll, A.; Zou, Y.; Kilian, L.; Hübner, D.; Gador, D.; Jung, C.; Urquhart, S. G.; Schmidt, Th.; Fink, R.; Umbach, E. *Phys. Rev. Lett.* **2004**, *93*, 146406.
(72) Schöll, A.; Hübner, D.; Schmidt, Th.; Urquhart, S. G.; Fink, R.; Umbach, E. *Chem. Phys. Lett.* **2004**, *392*, 297.
(73) Minkov, I.; Gel'mukhanov, F.; Friedlein, R.; Osikowicz, W.; Suess, C.; Öhrwall, G. O.; Sorensen, S. L.; Braun, S.; Murdey, R.; Salaneck, W. R.; Ågren, H. *J. Chem. Phys.* **2004**, *121*, 5733.
(74) Schöll, A.; Zou, Y.; Hübner, D.; Urquhart, S. G.; Schmidt, Th.; Fink, R.; Umbach, E. *J. Chem. Phys.* **2005**, *123*, 44509.
(75) Hohenecker, S. Ph.D. Thesis, Technische Universität Chemnitz, 2001, http://archiv.tu-chemnitz.de/pub/2002/0026.
(76) Stöhr, J. *NEXAFS Spectroscopy*; Springer-Verlag: Berlin Heidelberg, 1996; Corrected Printing.
(77) Prince, K. C. *Rev. Sci. Instrum.* **1988**, *59*, 741.
(78) Erdman, P. W.; Zipf, E. C. *Rev. Sci. Instrum.* **1982**, *53*, 225.
(79) Gorgoi, M.; Zahn, D. R. T. *Org. Electron.* **2005**, 6 168.
(80) Zahn, D. R. T.; Gorgoi, M.; Gordan, O. *Sol. Energy J*. **2006**, *80*, 707.
(81) Gorgoi, M. Ph.D. Thesis, Technische Universität Chemnitz, **2007**, http://archiv.tu-chemnitz.de/2007/0021.
(82) Debe, M. K. *Prog. Surf. Sci.* **1987**, *24*, 1.
(83) Turrell, G. *J. Raman Spectrosc.* **1984**, *15* (2), 103.
(84) Kohn, W.; Sham, L. J. *Phys. Rev. A* **1965**, *140*, 1133.
(85) Foresman, J.; Frisch, A. *Exploring Chemistry with Electronic Structure Method*; Gaussian Inc.: Pittsburgh, PA, 1996.
(86) Becke, A. *Phys. Rev. A* **1988**, *38*, 3098.
(87) Colle, R.; Salvetti, O. *Theor. Chim. Acta* **1975**, *37*, 329.
(88) Lee, C.; Yang, W.; Parr, R. *Phys. Rev. B* **1988**, *37*, 785.
(89) Becke, A. *J. Chem. Phys.* **1993**, *98*, 1372.
(90) Adamson, R. D. Ph.D. Thesis, Cambridge University, 1998.
(91) Ong, K. K.; Jensen, J. O.; Hameka, H. F. *THEOCHEM* **1999**, *459*, 131.
(92) Cornil, J.; Vanderdonckt, S.; Lazzaroni, R.; Dos Santos, D. A.; Thys, G.; Geise, H. J.; Yu, L. M.; Szablewski, D. L.; Bloor, D.; Lögdlund, M.; Salaneck, W. R.; Gruhn, N. E.; Lichtenberger, D. L.; Lee, P. A.; Armstrong, N. R.; Brédas, J. L. *Chem. Mater*. **1999**, *11*, 2436.
(93) Hill, I. G.; Kahn, A.; Cornill, J.; dos Santos, D. A.; Brédas, J. L. *Chem. Phys. Lett.* **2000**, *317*, 444.
(94) Slater, J. C. *Phys. Rev*. **1930**, *36*, 57.
(95) Yeh, J. J.; Lindau, I. *At. Data Nucl. Data Tables* **1985**, *32*, 1,
(96) Hirose, Y.; Forrest, S. R.; Kahn, A. *Phys. Rev. B* **1995**, *52*, 14040.
(97) Park, S. Ph.D. Thesis, Technische Universität Chemnitz, 2002, http://archiv.tu-chemnitz.de/pub/2002/0004/.
(98) Kampen, T. U.; Zahn, D. R. T.; Braun, W.; Gonzáles, C.; Benito, I.; Ortega, J.; Jurczyszyn, L.; Blanco, J. M.; Pérez, R.; Flores, F. *Appl. Surf. Sci.* **2003**, *212*, 850.
(99) Szucs, B.; Hajnal, Z.; Scholz, R.; Sanna, S.; Frauenheim, Th. *Appl. Surf. Sci.* **2004**, *234*, 173.
(100) Yamaguchi, H.; Horikoshi, Y. *Phys. Rev. B* **1996**, *53* (8), 4565.
(101) Pashley, M. D.; Li, D. *J. Vac. Sci. Technol., A* **1994**, *12* (4), 1848.
(102) Gavrila, G.; Méndez, H.; Kampen, T. U.; Zahn, D. R. T. *Appl. Surf. Sci.* **2004**, *234*, 126.
(103) Hill, I. G.; Rajagopal, A.; Kahn, A.; Hu, Y. *Appl. Phys. Lett.* **1998**, *73* (5), 662.
(104) Heutz, S.; Salvan, G.; Jones, T. S.; Zahn, D. R. T. *Adv. Mater*. **2003**, *15*, 131109.

(105) Park, S.; Querner, T.; Kampen, T. U.; Braun, W.; Zahn, D. R. T. *Appl. Surf. Sci.* **2000**, *166*, 376.
(106) Schneider, A.; Drews, D.; Zahn, D. R. T.; Wolfframm, D.; Evans, D. A. *J. Cryst. Growth* **1996**, *159*, 732.
(107) Kendrick, C.; Kahn, A. *Appl. Surf. Sci.* **1998**, *123*−*124*, 405.
(108) Yu Kobitski, A.; Salvan, G.; Scholz, R.; Tenne, D.; Kampen, T. U.; Wagner, H. P.; Zahn, D. R. T. *Appl. Surf. Sci.* **2002**, *190*, 386.
(109) Bitzer, T.; Rada, T.; Richardson, N. V. *J. Phys. Chem. B* **2001**, *105*, 4535.
(110) Moskovits, M.; DiLella, D. P. *J. Chem. Phys.* **1980**, *73*, 6068.
(111) Lippitsch, M. E. *Phys. Rev. B* **1984**, *25* (6), 3101.
(112) Seidel, C.; Schäfer, A. H.; Fuchs, H. *Surf. Sci.* **2000**, *459*, 310.
(113) Scholz, R.; Friedrich, M.; Salvan, G.; Kampen, T. U.; Zahn, D. R. T. *J. Phys.: Condens. Matter* **2003**, *15*, S2647.
(114) Tolstoy, V. P.; Chernyskova, I. V.; Skryshevsky, V. A. *Handbook of infrared spectroscopy of ultrathin films*; Wiley-Interscience: Hoboken, NJ, 2003; p 92.
(115) Turrell, G. *Infrared and Raman Spectra of Crystals*; Academic Press: London, 1972; Chapter 5.
(116) Friedrich, M.; Gavrila, G.; Himcinschi, C.; Kampen, T. U.; Kobitski, A. Y.; Méndez, H.; Salvan, G.; Cerrilló, I.; Méndez, J.; Nicoara, N.; Baró, A. M.; Zahn, D. R. T. *J. Phys.: Condens. Matter* **2003**, *15* (38), S2699.
(117) Salvan, G.; Silaghi, S.; Paez, B.; Kampen, T. U.; Zahn, D. R. T. *Synth. Met.* **2005**, *154* (1−3), 165.
(118) Aroca, R.; Jennings, C.; Loutfy, R. O.; Hor, A. M. *J. Phys. Chem.* **1986**, *90*, 5255.
(119) Woollam, J. A.; Johs, B.; Herzinger, C. M.; Hilfiker, J. N.; Synowicki, R.; Bungay, C. *SPIE Proc.* **1999**, CR72.
(120) Johs, B.; Herzinger, C. *Guide to using WVASE32*; J.A. Woolan Co., Inc.: Lincoln, NE, 1995.
(121) Dimitrakopoulus, C.; Brown, A.; Pomp, A. *J. Appl. Phys.* **1996**, *80*, 2501.
(122) Meyer zu Heringdorf, J.; Reuter, M. C.; Tromp, R. M. *Nature* **2001**, *412*, 517.
(123) Horowitz, G.; Hajllaoui, R.; Fichou, D.; Kassmi, El. *J. Appl. Phys.* **1999**, *85*, 3202.
(124) Yamane, H.; Kera, S.; Okudaira, K. K.; Yoshimura, D.; Seki, K.; Ueno, N. *Phys. Rev. B* **2003**, *68*, 033102.
(125) Gavrila, G. N.; Mendez, H.; Kampen, T. U.; Vyalikh, D. V.; Braun, W.; Zahn, D. R. T. *Appl. Phys. Lett.* **2004**, *85* (20), 4657.
(126) Seki, K.; Ueno, N.; Karlson, U. O.; Engelhardt, R.; Koch, E. E. *Chem. Phys.* **1986**, *105*, 247.
(127) Pireuax, J. J.; Riga, J.; Caudano, R.; Verbist, J. J.; Andre, J. M.; Delhalle, J.; Delhalle, S. *J. Electron Spectrosc. Relat. Phenom.* **1974**, *5*, 531.
(128) Narioka, S.; Ishii, H.; Edamatsu, K.; Kamiya, K.; Hasegawa, S.; Ueno, N.; Seki, K. *Phys. Rev. B* **1995**, *52*, 2362.
(129) Anderson, J. D.; McDonald, E. M.; Lee, P. A.; Anderson, M. L.; Ritchie, E. L.; Hall, H. K.; Hopkins, T.; Mash, E. A.; Wang, J.; Padias, A.; Thayumanavan, S.; Barlow, S.; Marder, S. R.; Jabbour, G. E.; Shaheen, S.; Kippelen, B.; Peyghambarian, N.; Wightman, R. M.; Armstrong, N. R. *J. Am. Chem. Soc.* **1998**, *120*, 9646.
(130) Slattery, D. K.; Linkous, C. A.; Gruhn, N. *Polym. Prepr.* **2000**, *41*, 866.
(131) Gleim, Th.; Heske, C.; Umbach, E.; Schumacher, C.; Gundel, S.; Faschinger, W.; Fleszar, A.; Ammon, Ch.; Probst, M.; Steinrück, H.-P. *Surf. Sci.* **2003**, *531*, 77.
(132) Gleim, Th.; Heske, C.; Umbach, E.; Schumacher, C.; Faschinger, W.; Ammon, Ch.; Probst, M.; Steinrück, H.-P. *Appl. Phys. Lett.* **2001**, *78*, 1867.
(133) Salaneck, W. R. *Phys. Rev. Lett.* **1978**, *40*, 60.
(134) Soos, Z. G.; Tsiper, E. V.; Pascal, R. A., Jr. *Chem. Phys. Lett.* **2001**, *342*, 652.
(135) Zahn, D. R. T.; Gavrila, G.; Gorgoi, M. *Chem. Phys.* **2006**, *325*, 99.
(136) Salvan, G.; Tenne, D. A.; Kampen, T. U.; Scholz, R.; Jungnickel, G.; Frauenheim, Th.; Zahn, D. R. T. *Appl. Surf. Sci.* **2001**, *179*, 113.
(137) Zahn, D. R. T.; Salvan, G.; Paez, B. A.; Scholz, R. *J. Vac. Sci. Technol., A* **2004**, *22*, 1482−1487.
(138) Brouers, F.; Blacher, S.; Lagarkov, A. N.; Sarychev, A. K.; Gadenne, P.; Shalaev, V. M. *Phys. Rev. B* **1997**, *55*, 13234.
(139) Creighton, J. A. In *Spectroscopy of Surfaces*; Clark, R. J., Hester, R. E., Eds.; John Wiley and Sons Ltd.: Chichester, 1988.
(140) Otto, A.; Mrozek, I.; Graborn, H.; Akemann, W. *J. Phys.: Condens. Matter* **1992**, *4*, 1134.
(141) Kneipp, K.; Kneipp, H.; Itzkan, I.; Dasari, R. R.; Feld, M. S. *Chem. Rev.* **1999**, *99*, 2957.
(142) Otto, A. *Phys. Status Solidi A* **2001**, *188* (9), 1455.
(143) Otto, A.; Mrozek, I.; Graborn, H.; Akemann, W. *J. Phys.: Condens. Matter.* **1992**, *4*, 1134.
(144) Salvan, G.; Zahn, D. R. T. *Europhys. Lett.* **2004**, *67* (5), 827.
(145) Böckelmann, H. K.; Schlecht, R. G. *Phys. Rev. B* **1974**, *10* (12), 5225.
(146) Fuggle, J. C.; Mårtensson, N. *J. Electron Spectrosc. Relat. Phenom.* **1980**, *21*, 275.
(147) Wagner, C. D.; Riggs, W. M.; Davis, L. E.; Moulder, J. F. *Handbook of X-ray photoelectron spectroscopy*; Perkin-Elmer Corporation: Eden Prairie, MN, 1979.
(148) Briggs, D.; Seah, M. P. *Practical surface analysis*; J. Willey & Sons: Chichester, 1993; Vol. 1.
(149) Yao, H. B.; Li, Y.; Wee, A. T. S. *Appl. Surf. Sci.* **2000**, *158*, 112.
(150) Fournier, V.; Marcus, P.; Olefjord, I. *Surf. Interface Anal.* **2002**, *34*, 494.
(151) Bouvier, Y.; Mutel, B.; Grimblot, J. *Surf. Coat. Technol.* **2004**, *180*−*181*, 169.
(152) *XPS Handbook of the Elements and Native Oxides*; XPS International, Inc.: Mountain View, 1999.
(153) Azuma, Y.; Akatsuka, S.; Okudaira, K. K.; Harada, Y.; Ueno, N. *J. Appl. Phys.* **2000**, *87*, 766.
(154) Azuma, Y.; Iwasawa, K.; Kurihara, T.; Okudaira, K. K.; Harada, Y.; Ueno, N. *J. Appl. Phys.* **2002**, *91*, 5024.
(155) Tanaka, I.; Mizuno, M.; Adachi, H. *Phys. Rev. B* **1997**, *56*, 3536.
(156) Wertheim, G. K.; DiCenzo, S. B. *Phys. Rev. B* **1988**, *37*, 844.
(157) Wertheim, G. K.; DiCenzo, S. B.; Buchanan, N. E. *Phys. Rev. B* **1986**, *33*, 5384.
(158) Gador, D.; Buchberger, C.; Fink, R.; Umbach, E. *J. Electron. Spectrosc.* **1988**, *96*, 11.
(159) Paez, B. A.; Salvan, G.; Scholz, R.; Zahn, D. R. T. *Phys. Status Solidi C* **2005**, *2* (12), 4048.
(160) Fleischer, K.; Chandola, S.; Esser, N.; Richter, W.; McGilp, J. F. *Phys. Rev. B* **2003**, *67*, 235318.
(161) Bakulin, A. S.; Overhauser, A. W.; Kaiser, H.; Werner, S. A.; Fernandez-Baca, J. A.; Smith, H. G. *Phys. Rev. B* **2001**, *63*, 052301.
(162) Sekiba, D.; Nakamizo, H.; Ozawa, R.; Gunji, Y.; Fukutani, H. *Surf. Sci.* **2000**, *449*, 111.
(163) Dweydari, A. W.; Mee, C. H. B. *Phys. Status Solidi A* **1973**, *17*, 247.
(164) Dweydari, A. W.; Mee, C. H. B. *Phys. Status Solidi A* **1975**, *27*, 223.
(165) Peisner, J.; Roboz, P.; Barna, P. B. *Phys. Status Solidi A* **1971**, *4*, K187.

CR050141P